PhD Thesis

Crystalline Molecular and Nanoparticle Assemblies with Optoelectronic Application Potential

Submitted By

Arin Bhakat

Under the supervision of

Prof. Arun Chattopadhyay

Department of Chemistry

Indian Institute of Technology Guwahati

Guwahti-781039, Assam, India

April 2024

Crystalline Molecular and Nanoparticle Assemblies with Optoelectronic Application Potential

A thesis submitted by Arin Bhakat

Roll No. 186122002

To

Indian Institute of Technology Guwahati

for the award of the degree of

Doctor of Philosophy

Department of Chemistry

Indian Institute of Technology Guwahati

Guwahti-781039, Assam, India

April 2024

Statement

This thesis entitled **"Crystalline molecular and nanoparticle assemblies with optoelectronic application potential"** is a work of research and investigation carried out by me under the supervision of Prof. Arun Chattopadhyay, Professor, Department of Chemistry, Indian Institute of Technology Guwahati. This thesis has been submitted by me to the Department of Chemistry, Indian Institute of Technology Guwahati for the award of Doctor of Philosophy. I further declare that this work has not been submitted by anywhere else for the award of any degree in any Institute or university to the best of my knowledge.

Arin Bhakat
Department of Chemistry
IIT Guwahati,
Guwahti-781039, Assam, India

Date: 03-04-2024

Place: Guwahati, Assam

Statement on Software

In the thesis entitled **"Crystalline molecular and nanoparticle assemblies with optoelectronic application potential"** submitted by me to the Department of Chemistry, Indian Institute of Technology Guwahati for the award of Doctor of Philosophy, the software used for drawing the structures are mentioned experimental section. They are available freely online. For any of the structures or texts of the thesis, I have not used any artificial intelligence-based software.

Arin Bhakat
Department of Chemistry
IIT Guwahati,
Guwahti-781039, Assam, India

Date: 03-04-2024

Place: Guwahati, Assam

Certificate

It is certified that the thesis entitled **"Crystalline molecular and nanoparticle assemblies with optoelectronic application potential"** being submitted to the Indian Institute of Technology Guwahati by Arin Bhakat (Roll. No. 186122002) for the award of the degree of Doctor of Philosophy in Chemistry, is a bona fide record of research work carried out by him. The information and data reported by him are solely the results of his original finding. He has meticulously carried out the investigations and followed the guidelines of the laboratory. This work has not been submitted elsewhere for any degree or diploma.

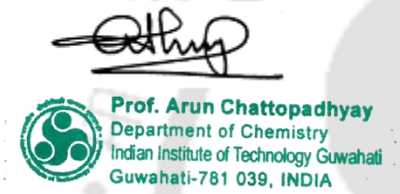

Prof. Arun Chattopadhyay

Thesis Supervisor

Professor,

Department of Chemistry, IIT Guwahati,

Guwahti-781039, Assam, India

Date: 03-04-2024

Place: Guwahati, Assam

Dedicated to

My Parents (Mr. Arun Kumar Bhakat, Mrs. Dipali Bhakat), Brother (Aninda Bhakat), Family members and Loved ones.

Acknowledgment

I want to thank my supervisor, Prof. Arun Chattopadhyay, for his leadership, unwavering support, encouragement, and invaluable advice throughout my PhD studies. His diligence, sincerity, dedication to research work, and convincing innovative ideas influenced me much during my studies. He taught me that, besides research, a researcher should care for their physical and mental well-being. He encourages me to dive deep into the ocean of research with curiosity and enthusiasm. Aside from scientific studies, he assisted me in personal growth in various ways, including how to be kind and grateful, how to manage a situation, when to take the lead or action, and many more. I am thankful to him for providing me with an outstanding research atmosphere.

I acknowledge my doctoral committee chairman, Prof. Chandan Mukherjee, and other committee members, Prof. Achalkumar Ammathnadu Sudhakar and Dr. Akshai Kumar Alape Seetharam, for their valuable suggestions and advice regarding research works.

I sincerely thank my collaborators, Dr. Ayan Pal, Sujay paul, Dr. Debadrita Bhattacharya, Dr. Raveesh S, and Ujjala Dey, for their invaluable contributions to my research.

I acknowledge the Department of Chemistry, the Central Instruments Facility, the Centre for Nanotechnology, the PARAM-ISHAN and PARAM-KAMRUPA supercomputing facilities, and, most importantly, IIT Guwahati.

I am grateful to my previous and current lab mates for their assistance and for creating a welcoming environment in the lab.

I am thankful to my hostel buddies Aritra, Anjishnu, Anindya, Santanu, Sanket, Surajit, Alik, Partha, Aritra, Tanay and Adri for making my hostel life joyful and cheerful, as well as for their assistance, support, and discussion on many topics.

Last, I want to express my deepest gratitude to my parents, Rashmita, and family members for their unwavering support, sacrifice, and unconditional love.

Thank you

Arin

Table of Contents

Abstract

The current thesis describes the production and prospective use of molecular crystals and crystallization-induced nanomaterial assembly. The current thesis reveals that the surface of molecular crystals can serve as an appropriate SERS platform. The surface functionality of molecular crystals can participate in non-covalent interactions with the deposited analyte molecules, allowing for efficient photoinduced charge transfer. The current thesis also shows that inorganic molecular crystals can exhibit metallic characteristics and cause surface plasmon. These molecular crystals may be exploited as a possible SERS substrate due to their excellent spectrum stability, simplicity of synthesis, outstanding environmental stability, biocompatibility, target molecule selectivity, and molecular cooperativity. The thesis also depicts the tuning of NC characteristics as a dopant inside molecular crystals, which sheds light on the methods for inducing tuneable phosphorescence features on simple metal NCs via ordered packing structures inside molecular crystals by altering the surrounding environment and electronic confinements. Furthermore, we used the intermolecular interaction-based surface complexation approach that causes molecular crystal formation to self-assemble nanomaterials into the crystalline superstructure.

The thesis is divided into six chapters, with the kernel of each underlined below.

Chapter 1 surveys the literature on various features resulting from the crystalline assembly of molecules and nanomaterials, including surface properties, potential applications, and possible intermolecular interactions within the crystalline assembly.

Chapter 2 shows that a microcrystal of π-conjugated copper 8-hydroxyquinolinate (CQ) is an appropriate platform for surface-enhanced Raman scattering (SERS). We also showed that such a microcrystal possesses metallic properties along all crystallographic axes and may increase molecule-specific Raman signals through plasmonic and charge-transfer mechanisms.

Chapter 3 shows that the organic compound terephthalic acid microcrystals display molecule-specific and cooperative Raman scattering of surface-deposited analyte molecules, resulting in a million-fold signal increase. Photo-induced charge transfer transitions and the idea of hybrid orbitals via noncovalent contacts in the combined system shed light on the cooperative, molecule-specific intense SERS performance.

Chapter 4 portrays that doping inside molecular crystals can be used as a easy generalized route colour tuneable solvent-processable persistent fluorescence to phosphorescence switching at room temperature. They provide significant insight on the tunability of PL

property of dopant i.e., aggregated metal nanoclusters, depending on the surrounding crystalline environment and compactness of the confinement.

Chapter 5 describes the surface complexation process between zinc ions and phosphate, which can assemble colloidal zinc oxide (ZnO) quantum dots (Qdots) into three-dimensional crystalline superstructures. Crystalline assembly was begun by the controlled growth of zinc phosphate tetrahydrate complexes across the Qdot surface, resulting in assembly formation. Crystalline networks in the ZnO Qdot-phosphate nanosensor film enhanced electron mobility across the structure, allowing for selective and sensitive electrochemical gas detection.

Chapter 6 summarises the thesis and discusses possible next directions. I have also included experimental evidence illustrating the synthesis of moiré superlattices of non-van der Waals 2D crystals as a future promise.

Chapter 1

Introduction

Crystalline Molecular self-assembly is a natural phenomenon that scientists have used to create unique supramolecular designs. Molecular self-assembly is the spontaneous organisation of molecules under near-thermodynamic equilibrium into structurally well-defined and stable configurations via non-covalent interactions.[1] Non-covalent interactions such as Coulombic forces (ionic bonds),[2] hydrogen bonds,[3] hydrophobic and hydrophilic forces,[4,5] water-mediated hydrogen bonds,[6] and van der Waals attraction[7] and repulsion[8] play crucial roles in effective molecular self-assembly. These individual weak forces can collectively interact to generate structurally and chemically stable structures. Molecular recognition and chemical and structural compatibilities are the driving forces for molecular self-assembly. Molecular components assemble into diverse forms through complimentary features such as surface wettability, surface charge, polarizability, mass, and surface functionality. Molecular self-assembly provides pathways to a wide range of structures, including liquid crystals, molecular crystals, and semicrystalline polymers. It provides a generic technique for assembling nanostructure ensembles and purification. Furthermore, the solid-state chemistry has made great leaps in recent past bolstered by computational support.[9,10] These developments have made it possible to anticipate the crystal structures of inorganic and organic materials using materials modelling; precisely characterize a variety of viable crystal structures along with the corresponding electronic or supramolecular properties in the solid state. The goal of creating materials with perfect precision is hindered by even seemingly insignificant modifications to their molecular structures—like switching H/F atom—frequently causes essential and unpredictable changes to the crystal packing, and more significant modifications—like adding hydrogen-bonding groups—may even have an impact on the topology and morphology of assembled solid-state system.[11,12] These assembled structures can have potential applications in electrochemistry,[13] smart materials,[14] protein binding,[15] corrosion resistance,[16] DNA assembly,[17] molecular electronics,[18] cell interactions,[19] and biological arrays.[20] As a result, self-assembly is valuable in many fields, including physics, chemistry, biology, nanoscience, and materials.

1.1 Interplay of Forces in Crystallization

Crystallization is a thermodynamic process; in the preliminary stage, there is a propensity for the most directed contacts to form synthon initially in solution because they are the longest-ranged and to stay locked in where as later connections are more isotropic .[21] It is defined as a supramolecular synthon because of the permanent pattern that is preserved in solution and that continues through the various phases of crystallization.[22] Prompt identification events between molecules result in a synthon. However, one must comprehend the characteristics of the intermolecular interactions that serve as the main drivers of particular recognition to appreciate which synthon might or might not emerge. The hydrogen bond, notably its weakest form, the C-H···π interaction, van der Waals contacts, metal ligand interactions, dipole–dipole interactions, steric repulsion, and more recently, the halogen bond, are examples of specific interactions in the realm of crystal design and crystalline assembly. [23,24] Interactions like the cation···π interaction and aurophilic, coprophilic and argentophilic interactions can also be present in a crystallization process.[25,26]

1.2. Properties of crystalline molecular assembly

1.2.1. Surface of molecular crystals

Crystals, with their fascinating geometric arrangement and various qualities, have captivated humans for millennia. Beyond their faceted elegance, there is a secret world: the crystal surface. This smooth surface is actually a frontier where atomic layout, intermolecular, and external interactions create a complex and dynamic image. The main core of a crystal is composed of an ordered arrangement of atoms, ions, or molecules, but the exterior disrupts this precise structure; disrupted atomic bonding results in dangling bonds and bare ionic charges.[27]

Crystal surfaces aren't merely flat surfaces; they frequently have well-defined facets or flat patches with specified directions. These facets result from the interaction between surface energy and crystal structure. The positioning of atoms at the surface is governed by a thermodynamic driving force known as surface energy minimization. Different crystal planes minimise energy to various extents, resulting in the predominance of specific facets.[28]

Crystal surfaces are not separate units; rather they interact with the environment. Components of gases or liquids can get adsorbed onto the interface, creating a new boundary. According to the characteristics of the adsorbate and the surface, several intermolecular interactions come into action. Weak affinity between molecules, such as London dispersion forces, may end up

in physisorption or ionic or polar substance can be drawn to oppositely charged places on the surface, leading to chemisorption; and a stronger bond including electron sharing or a particular kind of dipole-dipole interaction can form strong and directed surface-adsorbate bonds. The involvements of these forces determine the behaviour of adsorbed molecules; they affect everything from surface reaction to degradation.[29]

Crystal surfaces frequently serve as hosts of chemical activity. Hanging bonds and exposed ions can serve as reactive sites, enabling surface processes such as oxidation, reduction, and catalysis (Figure 1.1).[30] Understanding these interactions is critical in disciplines such as catalysis, where surfaces control major industrial processes. Crystal surfaces, in addition to being reactive, may alter radiation in intriguing ways. Surface plasmons, or synchronized undulation of electrons restricted to the surface, can bend and scatter photons, resulting in increased light harvesting, colour effects, and even negative refraction. These features have uses for solar cells, optical sensors, and metamaterials.[31] The versatility of crystal surfaces is what makes them so appealing. We may change their structure, shape, and functionalization to

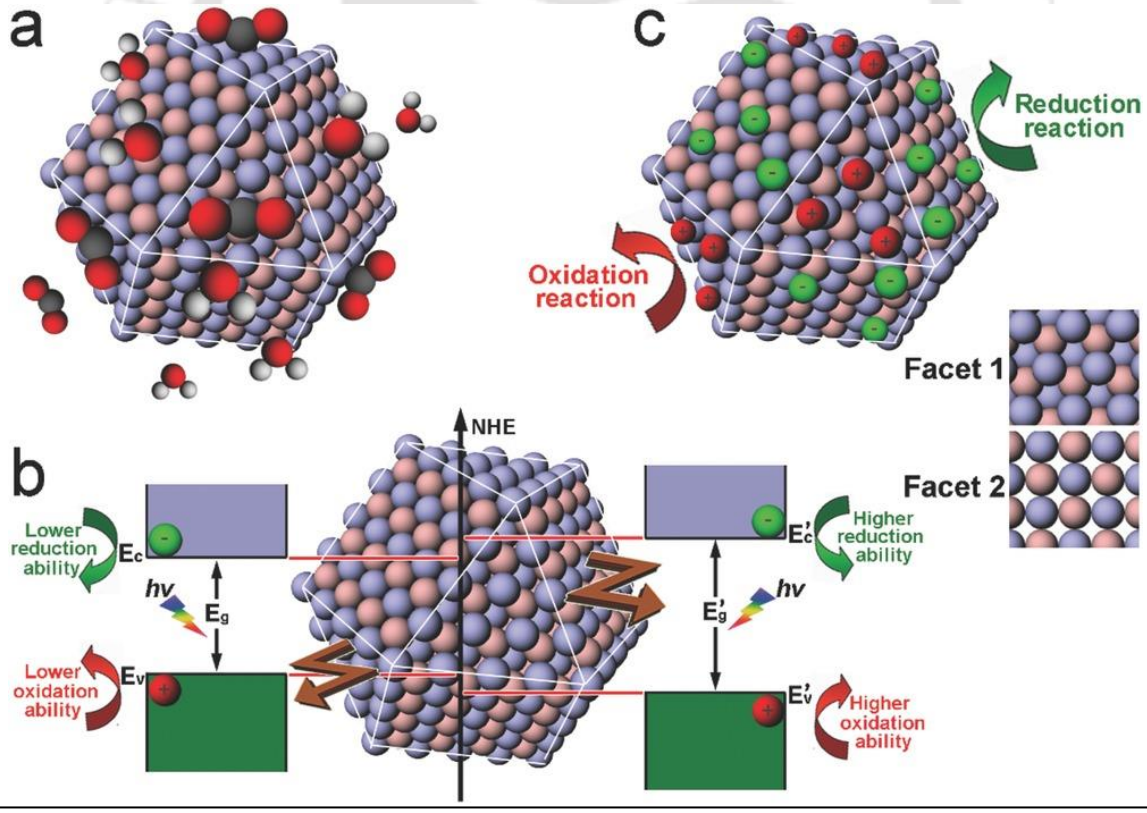

Figure 1.1 Schematics illustrate the importance of facets in catalysis and surface engineering. a) The adsorption and activation of reactant molecules on various surfaces. b) The surface electronic band structures of various aspects influence the redox properties of photogenerated charge carriers. b) The formation of photogenerated excitons on various surfaces.[30] Reprinted with permission from reference 30. Copyright 2017 John Wiley and Sons.

adapt their qualities to certain purposes. Doping, carving, and surface cladding methods are useful for introducing novel functions, increasing reactivity, and controlling surface adhesiveness. This brings up fascinating novel opportunities in disciplines such as electronics, biomaterials, and nanotechnology. Exploration of crystal surfaces is central to their applications, where atomic configurations create a dynamic tapestry of forces, catalysis, and light interactions. A crystal's surface is more than simply a barrier; it is a stage where the excitement of physics, chemistry, and materials science play out, and waiting to happen.

1.2.2 Crystal exciton

Excitons are excited electronic states that appear as quasiparticles in crystals. They develop when a positively charged "hole" is left in the valence band after an electron in the valence band in the presence of radiation (often from a photon) moves to the conduction band. The Coulomb force draws the electron and hole together, creating a bonded state like that of an atom's proton and electron.[32]

The exciton may travel along the lattice sites, transmitting energy to the electrically active or luminescent centres, because of the crystal's translation symmetry.[33] Therefore, most activities involving photoconductivity and light emission depend heavily on excitons. Within the crystals, two different kinds of excitons can be produced: Frenkel excitons: firmly bonded,[34] restricted to a small number of atomic locations, frequently present in organic compounds and Wannier-Mott excitons: more loosely connected,[35] they span many unit cells and are typically of inorganic semiconductors.

The optical characteristics of molecular crystals are defined by their many electronic and intra/intermolecular excitations. Tuneable molecular conformations and packing modes of crystals result in different intermolecular interactions, which provide a rational framework for investigating photophysical properties and exploring/designing structures that successfully emit light while avoiding the complications of structural defects and grain boundaries. However, crystallinity is frequently cited as a source of changes in photochemical characteristics such as Stokes shift, polarization, and quantum efficiency of illumination.[36]

Understanding exciton mechanics in materials is made harder by an intricate structure of excitonic couplings (up to three dimensions) that cannot be represented by basic low-dimensional approximations. More specifically, the limitation of the excitonic bandwidth, a vital factor, which has a considerable influence on exciton coherence characteristics, is still among the relevant topics being pursued in the area.[37] Excitonic bandwidths can reach ~0.8-1

eV, according to reliable calculations and experimental results.[38] Excitonic phenomena are particularly noticeable when the coupling between excitations localized on distinct molecules is significant. These strong couplings are mostly due to Coulombic affinity and include coupling between optically permitted (bright) excited states. Frenkel excitons, which are closely bound and localized, have bandwidths narrower than Wannier-Mott excitons, which are more delocalized and have wider bands. Wider bandwidths often indicate quicker exciton diffusion across the crystal, which aids in exciton-based transmission of energy and light harvesting. Bandwidth regulates the interaction of excitons and phonons (crystal vibrations), which can affect exciton relaxation.[39] Crystal excitons are intriguing quasiparticles with several applications in optoelectronics and nanoscale events. Understanding their features and influencing their behaviour is critical for developing technologies like as efficient light emission, solar energy conversion, and quantum electronics. The subject of exciton research is constantly evolving, introducing novel experimental and theoretical approaches promising interesting findings and potential applications.

1.2.3 Crystal phonons

In condensed matter physics, a phonon is a unit of vibrational energy produced by vibrating atoms inside a crystal. Any solid crystal, including regular table salt (sodium chloride), is made up of atoms arranged in a periodic three-dimensional spatial arrangement known as a lattice.[40]

Phonons can be produced by in-phase and out-of-phase collective oscillation of atoms. The study of phonons is an essential component of condensed matter physics. They play an important role in many of the physical characteristics of condensed matter systems, such as thermal conductivity and electrical conductivity, as well as in predictions of neutron scattering and associated phenomena.[41] it can couple strongly with photons, having an important role in Raman scattering and infrared absorption. Tuning phonon scattering can enhance thermal control in devices like heat sinks and thermoelectrics. Furthermore, the inelastic scattering of light by phonons offers insights into vibrational modes and points out defects and strains in the crystal structure. Excitons in molecular crystals disappear by fluorescence, heat deterioration, or photochemical reactions.[42] In the latter two stages, heat and chemical transformation, all or part of the exciton's energy returns in the shape of intermolecular (lattice) vibrations, demonstrating that excitons are coupled to lattice phonons. The coupling can be linked to the absorbance band profiles observed in the UV-vis spectrum. Progressively diving further into the universe of phonons, we reinvent the laws of material tuning, paving the stage for a future

in which sound waves interact with light. The song of the crystal lattice lies ahead and its tune has the potential to transform our technological world.[43]

1.2.4 Doping of Crystals

The pervasive colours of natural gems, mostly caused by impurity doping in crystals, continue to inspire efforts to create synthetic methods of producing customised crystals with different physical and chemical characteristics. Dopant atoms may be delicately woven into the flawless fabric of a crystal to fine-tune its electrical, optical, magnetic, and biological capabilities. Doping changes the harmony of a perfectly ordered crystal—a network of tightly packed atoms bound together by interatomic interactions. These dopants, carefully chosen for their distinct features, become permanent inhabitants of the crystal lattice, introducing fresh energy states and altering electron transport (Figure 1.2).[44,45]

The guest molecules are incorporated into the crystals by several means, such as adhering to facet surfaces, being uniformly distributed either as single entities or as aggregates inside the crystals, or creating their solid phase as a second precipitate during crystallization. Throughout crystal growth and nucleation, molecular crystals can contain numerous guest molecules and interactions between crystal and the guest molecules or guest-guest molecules inside the crystal environment might induce features not shared by both. Doping an atomic/ionic or molecular

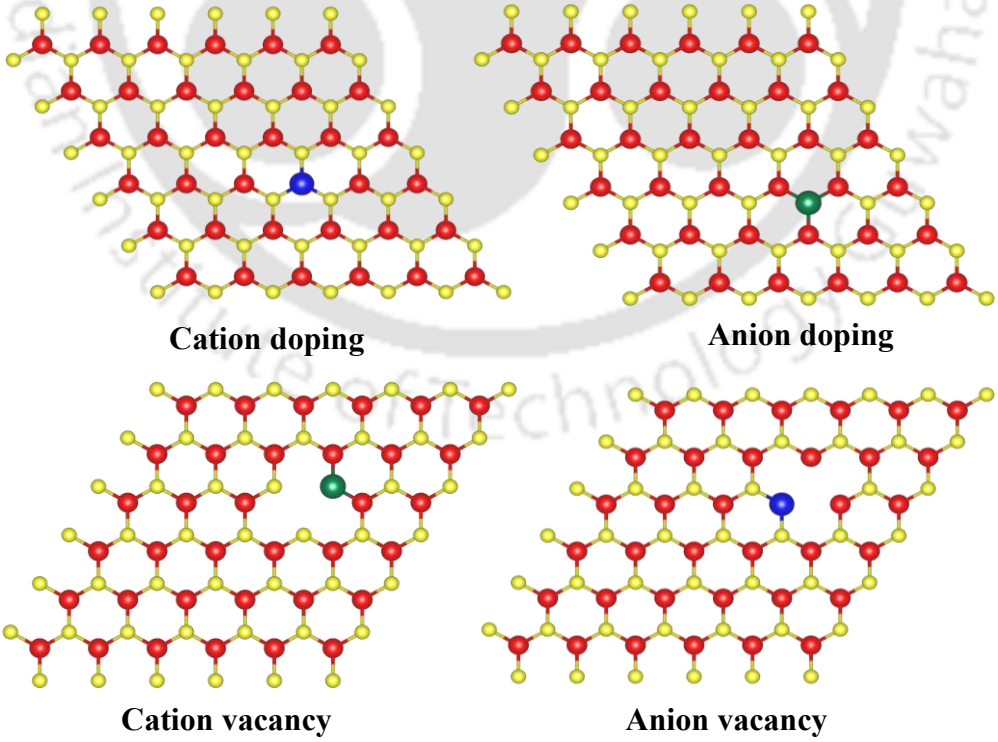

Figure 1.2 Schematic representation of different typers of crystal doping. Software used VESTA.

crystal with a different atom/ion or molecule (as applicable) may cause changes in the characteristics of either the atom/ion or molecule, the crystal, or both. For example, introducing certain dopants such as phosphorus or boron into silicon results in n-type or p-type electrical conductivity, which is the cornerstone of contemporary electronics. Doping crystals with rare earth elements such as europium or terbium gives them luminous qualities, allowing them to shine in brilliant LED lights and lasers. Doping some crystals with transition metals such as manganese or iron gives them magnetic superpowers, allowing for usage in data storage, magnetic sensors, and potentially quantum computing. Doping can increase materials' conductivity, optical transparency, and even catalytic activity, allowing them to be used in a variety of disciplines such as energy harvesting, catalysis and biomaterials.[46] Understanding the complex interaction between dopants and crystal structure allows us to design materials with previously imagined capabilities. This voyage of discovery continues, promising to revolutionise various disciplines and shape the next generation of technology.

1.3 Super-crystalline Nanoparticle Assembly Induced by Molecules

The captivating realm of nanoparticles calls out changing matter at the atomic level revealing a wealth of features and uses. Crystallisation, or the coordinated tango of atoms and molecules generating ordered structures, is the key to creating these microscopic masterpieces. But underneath the seemingly calm crystallising surface, there is a complicated dance of interactions that determines the nanomaterial's construction and eventual shape.

The molecular-interaction-based super-crystalline assembly of colloidal nanoparticles provide novel structural and functional properties that are missing in the component units.[47] Furthermore, the science underpinning assembly formation may bring fresh insights into the aspects that impact the well-defined assembly of the building components. Fortunately, several chemical techniques have been discovered in recent decades for the colloidal synthesis of nanomaterials with precise dimensions, form (e.g., core-shell), and surface functionalization.[48,49] These cornerstones are crucial for organising uniform nanocrystals (NCs) into superlattices. The ligands on the surfaces of nanoparticles play a crucial role in assembly development. The realm of nanomaterials, where matter moves at the atomic and molecular levels, has enormous potential to revolutionise a variety of areas. At the centre of this complicated minuet is the interesting occurrence of nanoparticle assembly caused by molecules (Figure 1.3).

Various assembly processes result in distinct nanomaterial structures. Nanoparticles suspended in a solvent self-assemble when the solvent disappears or achieved by tuning temperature or pressure. Solvent evaporation,[50] solvent destabilisation,[51] and assembly at the liquid-liquid interface are some of the most common assembly formation processes.[52] One easy method is to pour a dilute solution of NC onto a solid platform and let it dry. For instance, organic ligated PbSe NCs dispersed in a hexane/octane (9:1 v/v) mixture are evaporated into long-range-periodic superlattices.[53] However, using a two-layer phase dispersion approach with a thin film of ethanol atop the PbS NC dispersion in toluene resulted in the creation of a 3D crystalline assembled structure on the glass tube's exterior and top of a silicon platform positioned vertically within the tube.[54] Such destabilization-based ordered structures appear more substantial when solvent fusing in the NC surface ligand is less desirable than functional group, interwinding on the NC surface, which promotes NC clustering.[55] Furthermore, the assembly of nanoplates at liquid boundaries are shown to produce long-range positioning and orientational symmetry. The prominent 101 diffraction peak suggested that gadolinium trifluoride (GdF3) nanoplates selectively aligned in the edge-on fashion. The optical characteristics of Eu^{3+}-doped GdF3 nanoplates varied depending on their structure and orientation.[56] Furthermore, exterior forces or templates direct the nanoparticles into precise configurations, resulting in sophisticated and complicated nanostructures. Block copolymers have portions that selectively engage with distinct nanoparticle faces, directing their spacing and assembling them into predetermined patterns. Certain surfaces or facets of nanomaterials engage in gradual development and periodic positioning, resulting in 2D layers or superstructures. Small molecules may fill interparticle gaps, stabilise crystal structures, and even serve as templates for particular assembling forms. Surface complexation of nanoparticles might be a significant option for forming programmable assemblies using chemical bonds between surface constituents on the particles.[56] Furthermore, the complexes existing on the exterior may give unique and extra features in the assembly that are not found in either the nanoparticles or the complexes. Additionally, the variety of inorganic complexes and their characteristics might be exploited to identify probable surface complexation, allowing for hierarchy structures.[57] Such a method requires substantial development before becoming a viable choice. We may fine-tune the qualities of the resultant nanomaterial by adjusting the assembly choreography based on the molecules and surroundings. Ordered construction improves charge transfer, resulting in extremely conductive nanoparticles for electronics and energy-related uses. Specific crystal formations may influence light, resulting in tuneable colours, higher photon consumption, or even inverse refraction. Controlled construction

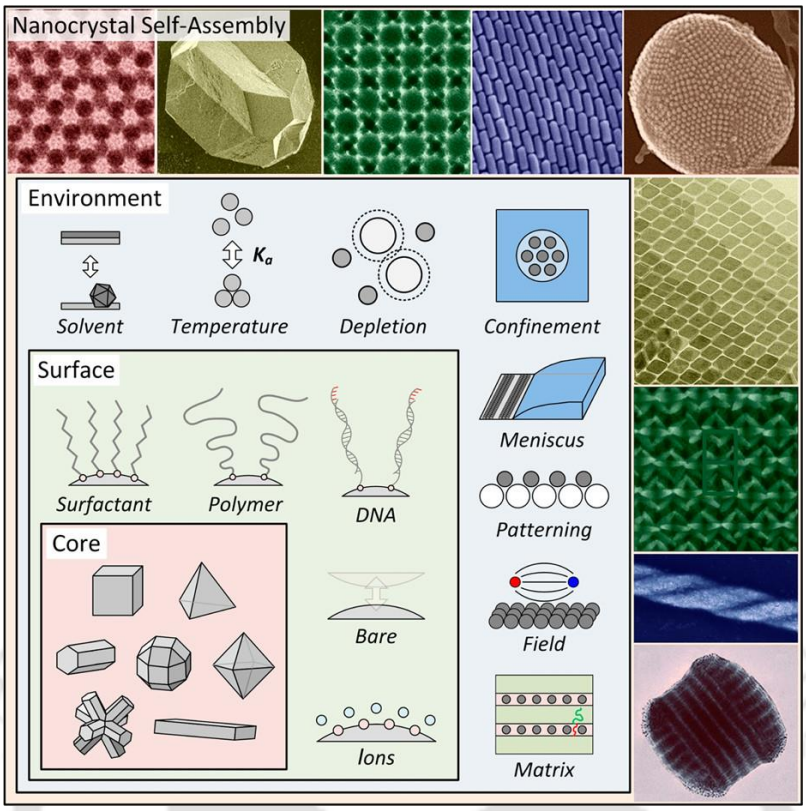

Figure 1.3 Pictorial representation of nanocrystal self-assembly process with different parameters that take part in assembly process.[47] Reprinted with permission from reference 47. Copyright 2016 American Chemical society.

exposes particular active areas on nanoparticles, improving their catalytic activity in chemical processes.

1.4 Application of crystalline assembly of molecules and nanomaterials

1.4.1 Light Emitting Diodes (LED)

LEDs are powered by electroluminescence, a process in which electrons and holes reunite in a semiconductor, emitting energy as light. Crystalline assemblies of organic molecules (OLEDs) or inorganic nanomaterials (QLEDs) efficiently organize these recombination sites, resulting in brighter, more energy-efficient LEDs. High-definition, flexible displays for smartphones, TVs, head-worn devices such as augmented reality (AR) and virtual reality (VR), and wearables use LEDs due to improved efficiency, extended longevity, and minimal operating voltage. LEDs are classed according to their emission properties:[58]

- Fluorescent substances (first generation)
- Metal phosphorescent structures (second generation)
- Thermally activated delayed fluorescence (TADF) semiconductors (third generation).

In 1987, Tang and VanSlyke reported on the first bilayer vacuum-deposited device that used Alq3 as an emitter and an electron carrier.[59] Following that, researchers have created numerous metal-containing substances with photophysical and luminescence characteristics, such as iridium(III),[60] platinum(II),[61] palladium(II),[62] gold(III),[63] silver(I),[64] copper(I),[65] ruthenium(II),[66] osmium(II),[67] and zinc (II) complexes.[68]

Crystallization-induced sustained luminescence was observed in single-component organic compounds, including halogenated benzophenones and esters.[69] Changing the luminous characteristics of molecular materials by manipulating and tweaking the configuration, alignment, and interatomic forces of fluorophores in solids is critical in attaining consistent light. Ordered hierarchical construction of multi functionalised materials by combining two or more units has emerged as an alternate way for producing adjustable long-lived photoemission. Wei et al. demonstrated the illumination of N-phenyl-naphthalen-2-amine (PNA) and its derivatives doped in crystal dibromobiphenyl (DBBP).[70] The co-crystals of 1,4-diiodotetrafluorobenzene (1,4-DITFB) with aromatic hydrocarbons (such as naphthalene and phenanthrene) exhibit brilliant green (naphthalene DITFB) and bright orange (phenanthrene-DITFB) room temperature phosphorescence.[71] Utilizing a familiar co-crystal method, they created a variety of consistently luminous co-crystals involving aromatic compounds (such as fluorine, pyrene, dibenzofuran, carbazole, and dibenzothiophene) as well as halogenated systems (such as 9-halo phenanthrene).[72] Crystalline inorganic phosphors that produce white light as pure or doped by metal ions (Eu2+, Mn2+, Ce3+, Yb3+) in single phases also gained widespread interest, for example, $SrAlSi_4N_7$, $BaSrMg(PO_4)_2:Eu^{2+}$, $K_2Ca(PO_4)F:Eu^{2+}$, $Sr_5(PO_4)_{3-x}(BO_3)_xCl:Eu^{2+}$, $Sr_2AlSi_2O_6N_2:Eu^{2+}$ and $Ba_3P_5N_{10}Br:Eu^{2+}$.[73]

1.4.2 LASERs

Several molecular crystals show high nonlinearities, allowing for frequency transformation (e.g., second-harmonic generation) and light manipulation, which is helpful for laser applications. Researchers are investigating these goals using crystals such as beta-barium borate (BBO) and potassium dihydrogen phosphate (KDP).[74,75] When stimulated with an external input, certain molecular crystals exhibit adjustable emission features, which might benefit the development of lasers. Studies on organic crystals such as 9,10-diphenyl anthracene (DPA) show potential in organic lasers.[76] Customised molecular crystals operate as functional waveguide constituents, changing light intensity or phase via electro-optic or other phenomena.

1.4.3 Photocatalysis and Solar energy

Photo-induced charge transfer (PICT) in crystals is an exciting event in which light absorption causes electrons to travel between various regions of the crystal lattice. Like a chain reaction, this movement has fascinating applications in multiple sectors, including harnessing sunlight and biomimetic catalysis. Crystals like TiO_2 are employed to induce light catalysed pollutant degradation or water splitting, thus, generating clean energy.[77] Traditional solar cells are built on a single-crystalline silicon substrate. Visible light excited crystalline photocatalysts such as $BiVO_4$,[78] Ta_3N_5,[79] and TaON[80] have also been created to harness solar power efficiently. Crystalline assemblies of quantum dots, perovskites, or metal nanoparticles have also shown promise in photocatalysis and solar cells, hydrogen and oxygen evolution, CO_2 reduction, and other forms of renewable energy generation.

1.4.4 Development of SERS Platforms

Devices with self-assembled plasmonic nanoparticles (NPs) have a high molar absorption cross-section (1×10^8 to 1×10^{10} M^{-1} cm^{-1}) and are commonly employed in sensing experiments.[81] The close-packed ordered assembly of NPs causes significant plasmonic coupling and induces hot spots, which reduce the detection threshold of probe molecules stuck between the NPs.[82] Therefore, substantial research has been conducted to develop and apply robust self-assembled NPs as platforms for various sensing potentials (Figure 1.4). For example, Klajn and colleagues created sheets of non-close-packed self-assemblies incorporating AuNPs for surface-enhanced Raman scattering (SERS) detection.[83] Again, careful etching of the superlattice portions allowed fine control of the inter-nanoparticle spacing between AuNPs. The NP superlattice with tightly packed AuNPs produced the most robust SERS response. In another report, Plasmonic designs using hexagonally packed AuNP super-crystals with uniform periodicity were prepared.[84] The plasmonic structures' absorbance was controlled from visible to NIR by altering the NP ordering and lattice units of the super-crystals. Depending on the application, it allows for greater flexibility in using various probe lasers. Furthermore, when the quantity of NPs in the self-assembled structure increased, the SERS signal improved, eventually increasing thrice compared to solitary NPs or random assemblies. Liz-Marzán and colleagues, for example, used template-mediated self-assembly to create Au nanorod supercrystals that can sense quorum in biofilms and microcolonies via surface-enhanced resonance Raman scattering (SERRS).[85] This technique is promising for researching cell-to-cell transmission using SERRS signals from tiny particles.

AuNP superstructure surface covered with metal-organic framework (ZIF-8) layers can detect lung cancer by capturing tumour-specific metabolite gas molecules using SERS. The pores in ZIF-8 led the passage of gaseous aldehydes to the surface of AuNP superstructures.[86]

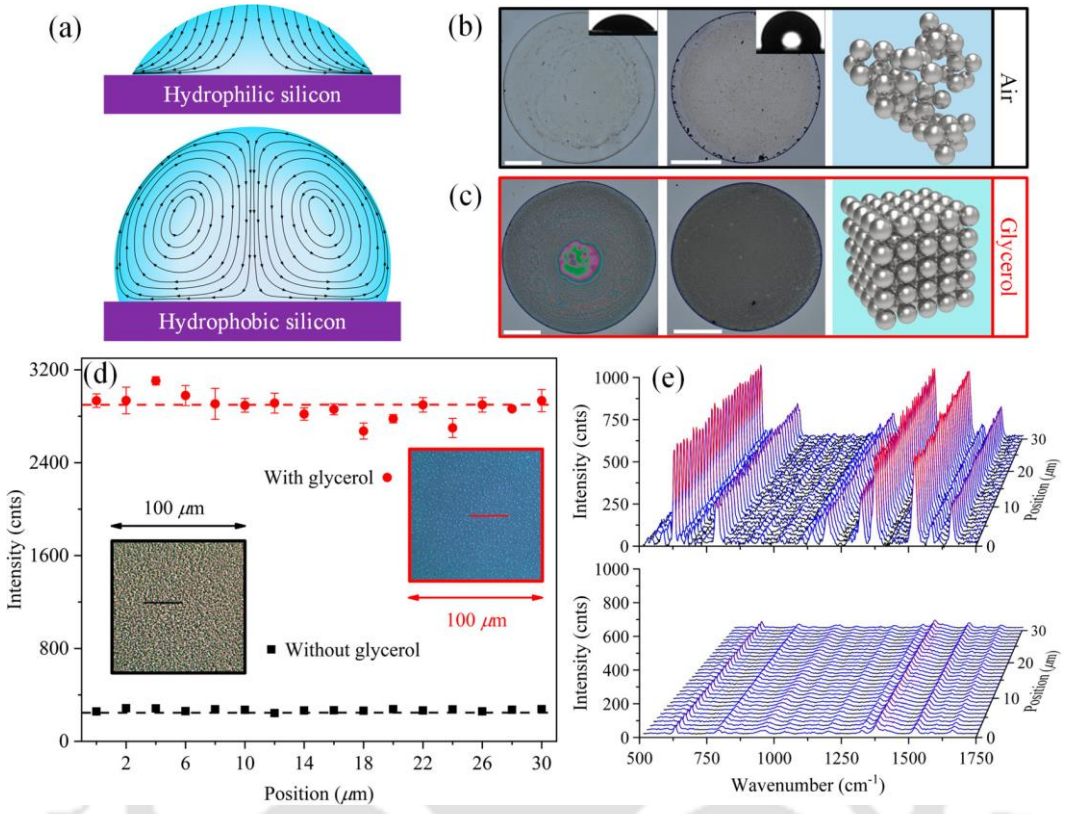

Figure 1.4 The diversity of NP assemblies as a reliable SERS platform with sensing potential. AgNPs were dried and deposited as droplets on hydrophilic and hydrophobic surfaces. Non-close-packed AuNP self-assembled arrangements with different inter-nanoparticle spacings. The SERS spectra from these AuNP self-assembled ensembles are displayed on the top.[81] Reprinted with permission from reference 81. Copyright 2019 American Chemical society.

Further, The SERS of a superhydrophobic and ivy-like nanostructured π-conjugated organic semiconductor film of α,ω-diperfluorohexylquaterthiophene (DFH-4T) resulted in hypersensitive molecular detection when coated with gold.[87] In absorbing irradiation, molecular crystals can display molecule-specific SERS properties and offer a plasmonic field and the ability to generate excitons. These crystals would be simple to manufacture, using recognized chemical concepts at various scales. Single-crystalline microstructures of molecules have the advantages of a long-range structured lattice, delocalized orbitals for electron transmission, and a surface area that facilitates analyte deposition and processing while preserving the crystal's consistency.

1.4.5 Electronic Devices

Due to their distinctive characteristics, single crystals are essential in contemporary electronics and sensors. Unlike polycrystalline substances with disorganised atomic frameworks, crystals have a homogeneous, ordered arrangement of atoms throughout, which has various advantages. Due to its controlled resistivity and flexibility with improved production methods, single-crystal silicon is the foundation of integrated circuits (ICs) (Figure 1.5). Several semiconductors, such as gallium arsenide (GaAs) and gallium nitride (GaN), provide higher efficiency for high-frequency devices and power electronics.[88,89] Quartz, lithium niobate, and gallium phosphate crystals display the piezoelectric effect, which converts mechanical strain into electrical impulses and vice versa.[90] They are essential for ultra-sensitive resonators, filtration systems, detectors in data transmission, accelerometers, and ultrasonic equipment. Barium titanate (BaTiO3) and lead zirconate titanate (PZT) crystals have convertible polarisation, making them suitable for memory chips, capacitors, and tuneable filters.[91] Organic single crystals have become revolutionary developments in flexible electronics, with several benefits over standard inorganic materials. Single-crystal rubrene transistors demonstrate greater electrical mobility and durability on flexible substrates, opening the path for efficient,

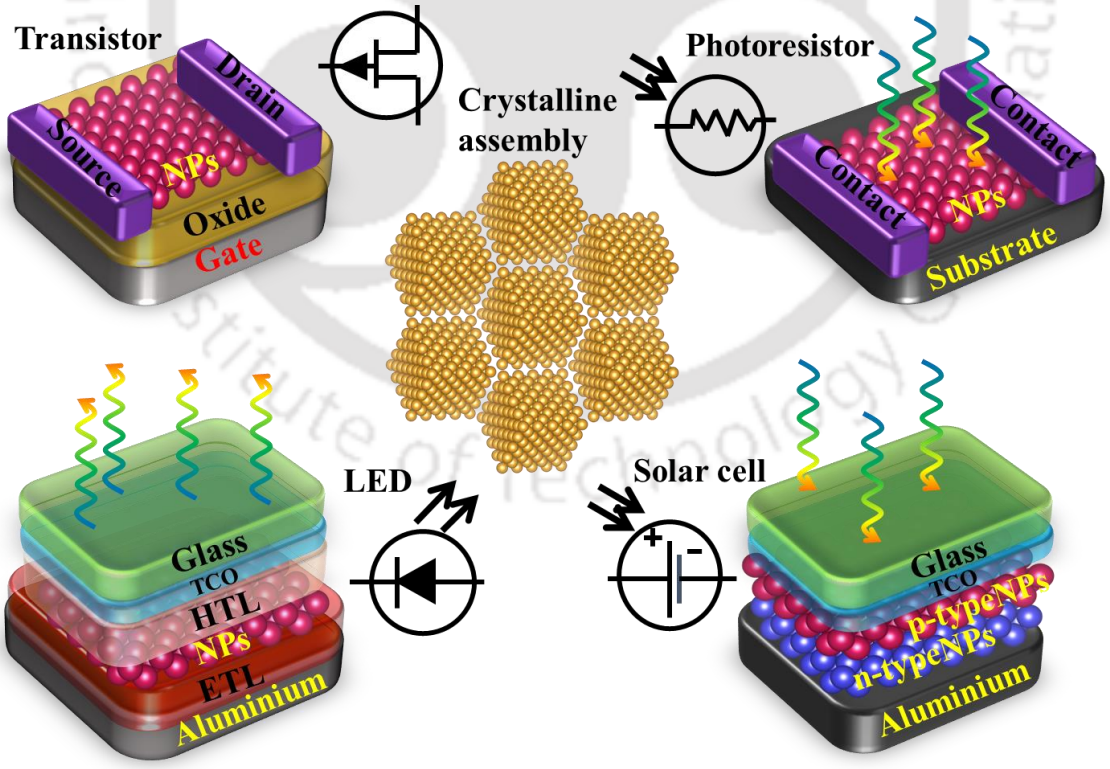

Figure 1.5 A pictorial illustration of integrated thin films of crystalline molecular and nanoparticle assemblies in various electronic and optoelectronic devices that alter and carry charges and generate light and electricity. Software used VESTA and MS PowerPoint.

foldable screens. Single-crystal pentacene-based organic photovoltaics (OPVs) have a high light-to-electricity transfer rate and mechanical flexibility, making them suitable for portable energy harvesting devices. Crystalline arrays of solution-deposited colloidal QDs may be incorporated into devices that regulate and transfer charge under bias and produce and control an electrical current, converting an optical flux to electrical power, similar to bulk semiconductors. The most dynamic carrier mobility has been found in the crystalline assembly of QDs encapsulated by inorganic ligands such as $Sn_2S_6^{4-}$, $In_2Se_4^{2-}$, $CdTe_2^{2-}$ $PbCl_3^-$, $InCl_4^-$, S^{2-}, Cl^-, I^-, SCN^- and N_3^-.[92]

1.4.6 Pharmaceuticals and Drug delivery

Most medicines are combined with molecular crystals for their stability, controlled release, and convenience of manufacture. Tailoring crystal packing and intermolecular interactions can impact medication solubility, dissolution rate, and bio-absorption.[93] Crystals can be programmed to release medications in specific locations or over time, enhancing selectivity and potency. Cocrystal generation can considerably improve solubility and dissolution rates by combining an active pharmaceutical ingredient (API) with another molecule (conformer) in a crystal lattice. This results in higher oral absorptivity. Adding water molecules to an API crystal can increase its solubility and longevity. This method is very effective for sparingly soluble medicines. The stability and shelf-life of the same medicine differs depending on its crystal form. Choosing a more inert polymorph can help avoid deterioration and maintain drug quality.[94]

1.5 Motivation

The introduction section of the thesis covers several aspects of the crystalline assembly of molecules and nanomaterials, including hidden characteristics and intriguing possibilities. The crystalline assembly of molecules, known as molecular crystals, can have characteristics different from their building components and can be utilised to create tuneable possible materials. These crystals' surfaces can interact with light or surrounding molecules or be a suitable chemical transformation substrate. These assemblies provide insight into the underlying forces and methods governing self-assembly at the molecular and nanoscale. These crystals with exquisite properties may be used to assemble nanomaterials (Qdots, metal clusters, or nanoparticles) successfully. The potential for creating innovative materials with specific characteristics, understanding fundamental self-assembly methodology, exploring new

scientific phenomena, and developing advanced technologies across numerous sectors motivate research on crystalline molecular and nanoparticle assemblies.

1.6 Overview of the thesis

The present thesis represents the synthesis and potential application of molecular crystals and crystallization-induced assembly of nanomaterials. We have demonstrated that the surface of molecular crystals can be used as a suitable SERS platform. The surface functionality of molecular crystals can take part in non-covalent interaction with the deposited analyte molecules and also facilitate effective photoinduced charge transfer. We have also demonstrated that inorganic molecular crystals can have metallic properties and induce weak surface plasmon. These molecular crystals can be used a potential SERS substrate with high spectral stability, ease of synthesis, exceptional environmental stability, biocompatibility, and target molecule specificity and molecular cooperativity in the SERS. Further, we applied the intermolecular interactions which are responsible for molecular crystal formation, which can also be applied to confined nanomaterials inside the crystal and self-assembled them into the crystalline superstructure for potential applications.

The thesis is divided into six chapters, with the kernel of each underlined below.

Chapter 1 describes the literature review on different properties arising from the crystalline assembly of molecules, its surface properties, and possible applications and probable intermolecular interactions inside the crystalline assembly (crystals). Molecule-induced crystalline assembly of nanomaterials and its intriguing properties and potential applications is also incorporated.

Chapter 2 demonstrate that microcrystal of π-conjugated copper 8-hydroxyquinolinate (CQ) is a suitable platform for surface enhanced Raman scattering (SERS). We further demonstrated that such a microcrystal has the combined benefit of plasmonic and charge-transfer-based amplification, which provides the foundation of selectivity between the host crystal and the analyte molecule. Rhodamine-6G (R6G), rhodamine B (RhB), and an in situ copper-(II)-picolinate complex (CuPA) deposited on microcrystals were taken as probe analytes. We also demonstrated that Raman signals of binary mixtures can exhibit analyte-specific amplification, allowing for molecule-specific detections. Computational investigations indicated that π-electron-rich CQ microcrystals are exceedingly electron-dense, and band structure computations revealed metallic characteristics along all crystallographic axes. Metallicity and

high electron density in a metal complex microcrystal produced novel properties such as strong analyte selectivity and efficient SERS activity.

Chapter 3 demonstrate that microcrystals of organic molecule terephthalic acid exhibits surface enhanced Raman scattering with a million-fold signal enhancement that is comparable to metal substrates. Rhodamine-6G (R6G), rhodamine B (RhB) and eosin yellowish, deposited on the solid microcrystals, were used as target analytes and probed using a 785 nm laser excitation. Importantly, the crystalline surface supports molecule-specific and cooperative Raman scattering for binary mixtures of analyte molecules. The density functional theory (DFT) based electronic structure of the crystals, photo-induced charge transfer transitions and the concept of hybrid orbitals through noncovalent interactions in the combined system gave insights into the cooperative, molecule-specific intense SERS performance.

Chapter 4 portrays that the aggregation of water-soluble gold nanocluster (AuNCs) doped inside an organic crystal can induce reversible fluorescence to phosphorescence switching with an excitation tuneable emission at room temperature. In addition, if the host crystal has an emissive state, there can be an energy transfer from long-lived singlet or triplet state to the triplet state of the acceptor NCs via a delay sensitization process. For a test case, we have doped histidine-stabilised AuNCs (HIS-AuNCs) inside histidine crystals (HIS-AuNCs-HIS) and isophthalic acid crystals (HIS-AuNCs-IPA) respectively and glutathione-stabilised gold nanoclusters (GSH-AuNCs) inside histidine crystal (GSH-AuNCs-HIS). These doped AuNCs showed solvent-processable phosphorescence. Upon dissolution of crystal with appropriate solvent, phosphorescence property vanished and a weak delayed fluorescence was observed. In case of HIS-AuNCs-HIS and HIS-AuNCs-IPA composite crystals the phosphorescence lifetime was in millisecond whereas for GSH-AuNCs-HIS phosphorescence life time was in microsecond. The possible energy states and interactions involved in agglomerated NCs was accounted by DFT calculation.

In **chapter 5** we introduce a simple method to assemble colloidal zinc oxide (ZnO) quantum dots (Qdots) into three-dimensional superstructures via surface complexation reaction between zinc ions and phosphate. Crystalline assembly was initiated by addition of aqueous solution of disodium hydrogen phosphate into the in situ ZnO reaction mixture resulting in controlled growth of zinc phosphate tetrahydrate structures over Qdot surface leading to the assembly formation. Further, the so-generated ZnO Qdot-phosphate crystalline assembly was successfully applied to devise a highly sensitive gas sensor. The presence of crystalline

networks in the ZnO Qdot-phosphate nano sensor film assisted in superior electron mobility throughout the structure, resulting in improved conductance. The as-prepared Qdot assembly film was highly sensitive and selective towards CO_2 gas.

Chapter 6 contains the summarization and plausible future prospects of the thesis. I have also included experimental results demonstrating synthesis of moiré superlattices of non van der Waals 2D crystals as a part of the future prospect.

Reference

1. Fung, S. Y.; Hong, Y.; Keyes-Baig, C.; Chen, P. 12 - Self-Assembly of Peptides and Its Potential Applications. In *Molecular Interfacial Phenomena of Polymers and Biopolymers*; Chen, P., Ed.; Woodhead Publishing, 2005; pp 421–474.
2. Bian, T.; Gardin, A.; Gemen, J.; Houben, L.; Perego, C.; Lee, B.; Elad, N.; Chu, Z.; Pavan, G. M.; Klajn, R. Electrostatic Co-Assembly of Nanoparticles with Oppositely Charged Small Molecules into Static and Dynamic Superstructures. *Nat Chem* **2021**, *13* (10), 940–949.
3. Corradi, E.; Meille, S. V.; Messina, M. T.; Metrangolo, P.; Resnati, G., Halogen Bonding versus Hydrogen Bonding in Driving Self-Assembly Processes Perfluorocarbon-hydrocarbon self-assemble. *Angew. Chem. Int. Ed.* **2000,** *39* (10), 1782-1786.
4. Aakeröy, C. B.; Seddon, K. R. The Hydrogen Bond and Crystal Engineering. *Chem Soc Rev* **1993**, *22* (6), 397–407.
5. Robertson, Craig. C.; Wright, J. S.; Carrington, E. J.; Perutz, R. N.; Hunter, C. A.; Brammer, L. Hydrogen Bonding vs. Halogen Bonding: The Solvent Decides. *Chem Sci* **2017**, *8* (8), 5392–5398.
6. Batys, P.; Kivistö, S.; Lalwani, S. M.; Lutkenhaus, J. L.; Sammalkorpi, M. Comparing Water-Mediated Hydrogen-Bonding in Different Polyelectrolyte Complexes. *Soft Matter* **2019**, *15* (39), 7823–7831.
7. Bondi, A. Van Der Waals Volumes and Radii. *J Phys Chem* **1964**, *68* (3), 441–451.
8. Pauling, L. The Nature of the Chemical Bond: An Introduction to Modern Structural Chemistry; Cornell University Press: Ithaca, United States, 1960.
9. Scanlon, D. O.; Dunnill, C. W.; Buckeridge, J.; Shevlin, S. A.; Logsdail, A. J.; Woodley, S. M.; Catlow, C. R. A.; Powell, Michael. J.; Palgrave, R. G.; Parkin, I. P.; Watson, G. W.; Keal, T. W.; Sherwood, P.; Walsh, A.; Sokol, A. A. Band Alignment of Rutile and Anatase TiO2. *Nat Mater* **2013**, *12* (9), 798–801.

10. Lewis, D. W.; Willock, D. J.; Catlow, C. R. A.; Thomas, J. M.; Hutchings, G. J. De Novo Design of Structure-Directing Agents for the Synthesis of Microporous Solids. *Nature* **1996**, *382* (6592), 604–606.
11. Corpinot, M. K.; Stratford, S. A.; Arhangelskis, M.; Anka-Lufford, J.; Halasz, I.; Judaš, N.; Jones, W.; Bučar, D.-K. On the Predictability of Supramolecular Interactions in Molecular Cocrystals – the View from the Bench. *CrystEngComm* **2016**, *18* (29), 5434–5439.
12. Dubey, R.; Pavan, M. S.; Desiraju, G. R. Structural Landscape of Benzoic Acid: Using Experimental Crystal Structures of Fluorobenzoic Acids as a Probe. *Chem. Commun.* **2012**, *48* (72), 9020–9022.
13. Cheng, H.; Liu, R.; Zhang, R.; Huang, L.; Yuan, Q. Recent Advances in Supramolecular Self-Assembly Derived Materials for High-Performance Supercapacitors. *Nanoscale Adv* **2023**, *5* (9), 2394–2412.
14. Li, Z.; Fan, Q.; Yin, Y. Colloidal Self-Assembly Approaches to Smart Nanostructured Materials. *Chem Rev* **2022**, *122* (5), 4976–5067.
15. Sun, H.; Li, Y.; Yu, S.; Liu, J. Hierarchical Self-Assembly of Proteins Through Rationally Designed Supramolecular Interfaces. *Front Bioeng Biotechnol* **2020**, *8*.
16. Nadi, I.; Bouanis, M.; Nohair, K.; Nyassi, A.; Zarrouk, A.; Jama, C.; Bentiss, F. Elaboration and Corrosion Resistance of Self-Assembled 2,5-Bis(4-Pyridyl)− 1,3,4-Oxadiazole Film on Carbon Steel: Surface Characterisations, Electrochemical Assessments and Surface Pre-Treatment Effect. *Mater Today Commun* **2023**, *35*, 106382.
17. Agarwal, S.; Klocke, M. A.; Pungchai, P. E.; Franco, E. Dynamic Self-Assembly of Compartmentalized DNA Nanotubes. *Nat Commun* **2021**, *12* (1), 3557.
18. Halik, M.; Hirsch, A. The Potential of Molecular Self-Assembled Monolayers in Organic Electronic Devices. *Advanced Materials* **2011**, *23* (22–23), 2689–2695.
19. Chagri, S.; Ng, D. Y. W.; Weil, T. Designing Bioresponsive Nanomaterials for Intracellular Self-Assembly. *Nat Rev Chem* **2022**, *6* (5), 320–338.
20. Zhu, X.; Duan, R.; Chan, S. Y.; Han, L.; Liu, H.; Sun, B. Structural and Photoactive Properties of Self-Assembled Peptide-Based Nanostructures and Their Optical Bioapplication in Food Analysis. *J Adv Res* **2023**, *43*, 27–44.
21. Price, S. L. Predicting Crystal Structures of Organic Compounds. *Chem Soc Rev* **2014**, *43* (7), 2098–2111.

22. Desiraju, G. R. Supramolecular Synthons in Crystal Engineering—A New Organic Synthesis. *Angew. Chem. Int. Ed.* **1995**, *34* (21), 2311–2327.
23. Braga, D.; Desiraju, G. R.; Miller, J. S.; Orpen, A. G.; Price, S. (Sally) L. Innovation in Crystal Engineering. *CrystEngComm* **2002**, *4* (83), 500–509.
24. Corpinot, M. K.; Bučar, D.-K. A Practical Guide to the Design of Molecular Crystals. *Cryst Growth Des* **2019**, *19* (2), 1426–1453.
25. Katz, M. J.; Sakai, K.; Leznoff, D. B. The Use of Aurophilic and Other Metal–Metal Interactions as Crystal Engineering Design Elements to Increase Structural Dimensionality. *Chem Soc Rev* **2008**, *37* (9), 1884–1895.
26. Bachman, R. E.; Andretta, D. F. Metal−Ligand Bonding in Coinage Metal−Phosphine Complexes: The Synthesis and Structure of Some Low-Coordinate Silver(I)−Phosphine Complexes. *Inorg Chem* **1998**, *37* (21), 5657–5663.
27. Tran, R.; Xu, Z.; Radhakrishnan, B.; Winston, D.; Sun, W.; Persson, K. A.; Ong, S. P. Surface Energies of Elemental Crystals. *Sci Data* **2016**, *3* (1), 160080.
28. Pawley, G. S.; Chaplot, S. L. Surface Dynamics of Molecular Crystals. A Calculation for Naphthalene. *physica status solidi (b)* **1980**, *99* (2), 517–529.
29. Zhang, D.-F.; Zhang, H.; Guo, L.; Zheng, K.; Han, X.-D.; Zhang, Z. Delicate Control of Crystallographic Facet-Oriented Cu2O Nanocrystals and the Correlated Adsorption Ability. *J Mater Chem* **2009**, *19* (29), 5220–5225.
30. Bai, S.; Wang, L.; Li, Z.; Xiong, Y. Facet-Engineered Surface and Interface Design of Photocatalytic Materials. *Adv Sci* **2017**, *4* (1), 1600216.
31. Li, R.; Zhang, F.; Wang, D.; Yang, J.; Li, M.; Zhu, J.; Zhou, X.; Han, H.; Li, C. Spatial Separation of Photogenerated Electrons and Holes among {010} and {110} Crystal Facets of BiVO4. *Nat Commun* **2013**, *4* (1), 1432.
32. Nematiaram, T.; Padula, D.; Troisi, A. Bright Frenkel Excitons in Molecular Crystals: A Survey. *Chem Mater* **2021**, *33* (9), 3368–3378.
33. Bondarev, I. V; Berman, O. L.; Kezerashvili, R. Ya.; Lozovik, Y. E. Crystal Phases of Charged Interlayer Excitons in van Der Waals Heterostructures. *Commun Phys* **2021**, *4* (1), 134.
34. Ng, K.; Webster, M.; Carbery, W. P.; Visaveliya, N.; Gaikwad, P.; Jang, S. J.; Kretzschmar, I.; Eisele, D. M. Frenkel Excitons in Heat-Stressed Supramolecular Nanocomposites Enabled by Tunable Cage-like Scaffolding. *Nat Chem* **2020**, *12* (12), 1157–1164.

35. Massicotte, M.; Vialla, F.; Schmidt, P.; Lundeberg, M. B.; Latini, S.; Haastrup, S.; Danovich, M.; Davydovskaya, D.; Watanabe, K.; Taniguchi, T.; Fal'ko, V. I.; Thygesen, K. S.; Pedersen, T. G.; Koppens, F. H. L. Dissociation of Two-Dimensional Excitons in Monolayer WSe2. *Nat Commun* **2018**, *9* (1), 1633.

36. Gierschner, J.; Varghese, S.; Park, S. Y. Organic Single Crystal Lasers: A Materials View. *Adv Opt Mater* **2016**, *4* (3), 348–364.

37. Timpmann, K.; Trinkunas, G.; Olsen, J. D.; Neil Hunter, C.; Freiberg, A. Bandwidth of Excitons in LH2 Bacterial Antenna Chromoproteins. *Chem Phys Lett* **2004**, *398* (4), 384–388.

38. Spano, F. C., Excitons in conjugated oligomer aggregates, films, and crystals. *Annu rev phys chem* **2006,** *57*, 217-43.

39. Alvertis, A. M.; Haber, J. B.; Engel, E. A.; Sharifzadeh, S.; Neaton, J. B. Phonon-Induced Localization of Excitons in Molecular Crystals from First Principles. *Phys Rev Lett* **2023**, *130* (8), 86401.

40. Guedes, I.; Hirano, Y.; Grimsditch, M.; Wakabayashi, N.; Loong, C.-K.; Boatner, L. A., Raman study of phonon modes in ErVO4 single crystals. *J Appl Phys* **2001,** *90* (4), 1843-1846.

41. Luo, Y.; Yang, X.; Feng, T.; Wang, J.; Ruan, X. Vibrational Hierarchy Leads to Dual-Phonon Transport in Low Thermal Conductivity Crystals. *Nat Commun* **2020**, *11* (1), 2554.

42. Craig, D. P.; Dissado, L. A. Exciton-Phonon Coupling in Molecular Crystals: Absorption Band Profiles in the First Singlet System of Anthracene. *Proc R Soc Lond A Math Phys Sci* **1978**, *363* (1713), 153–173.

43. Legenstein, L.; Reicht, L.; Kamencek, T.; Zojer, E. Anisotropic Phonon Bands in H-Bonded Molecular Crystals: The Instructive Case of α-Quinacridone. *ACS Mater Au* **2023**, *3* (4), 371–385.

44. Wang, H.; Li, F.; Gao, B.; Xie, Z.; Liu, S.; Wang, C.; Hu, D.; Shen, F.; Xu, Y.; Shang, H.; Chen, Q.; Ma, Y.; Sun, H. Doped Organic Crystals with High Efficiency, Color-Tunable Emission toward Laser Application. *Cryst Growth Des* **2009**, *9* (11), 4945–4950.

45. Li, G.; Jiang, S.; Liu, A.; Ye, L.; Ke, J.; Liu, C.; Chen, L.; Liu, Y.; Hong, M. Proof of Crystal-Field-Perturbation-Enhanced Luminescence of Lanthanide-Doped Nanocrystals through Interstitial H+ Doping. *Nat Commun* **2023**, *14* (1), 5870.

46. Zhang, A.; Liang, Y.; Zhang, H.; Geng, Z.; Zeng, J. Doping Regulation in Transition Metal Compounds for Electrocatalysis. *Chem Soc Rev* **2021**, *50* (17), 9817–9844.

47. Boles, M. A.; Engel, M.; Talapin, D. V. Self-Assembly of Colloidal Nanocrystals: From Intricate Structures to Functional Materials. *Chem Rev* **2016**, *116* (18), 11220–11289.
48. Murray, C. B.; Norris, D. J.; Bawendi, M. G. Synthesis and Characterization of Nearly Monodisperse CdE (E = Sulfur, Selenium, Tellurium) Semiconductor Nanocrystallites. *J Am Chem Soc* **1993**, *115* (19), 8706–8715.
49. Hanrath, T., Colloidal nanocrystal quantum dot assemblies as artificial solids. *J Vac Sci Technol A* **2012,** *30* (3).
50. Boles, M. A.; Talapin, D. V. Many-Body Effects in Nanocrystal Superlattices: Departure from Sphere Packing Explains Stability of Binary Phases. *J Am Chem Soc* **2015**, *137* (13), 4494–4502.
51. Rupich, S. M.; Shevchenko, E. V; Bodnarchuk, M. I.; Lee, B.; Talapin, D. V. Size-Dependent Multiple Twinning in Nanocrystal Superlattices. *J Am Chem Soc* **2010**, *132* (1), 289–296.
52. Diroll, B. T.; Greybush, N. J.; Kagan, C. R.; Murray, C. B. Smectic Nanorod Superlattices Assembled on Liquid Subphases: Structure, Orientation, Defects, and Optical Polarization. *Chem Mater* **2015**, *27* (8), 2998–3008.
53. Talapin, D. V.; Murray, C. B., PbSe Nanocrystal Solids for n- and p-Channel Thin Film Field-Effect Transistors. *Science* **2005,** *310*, 86.
54. Rupich, S. M.; Shevchenko, E. V.; Bodnarchuk, M. I.; Lee, B.; Talapin, D. V. Size-Dependent Multiple Twinning in Nanocrystal Superlattices. *J. Am. Chem. Soc.* **2010**, *132*, 289–296.
55. Talapin, D. V.; Shevchenko, E. V.; Kornowski, A.; Gaponik, N.; Haase, M.; Rogach, A. L.; Weller, H. A New Approach to Crystallization of CdSe Nanoparticles into Ordered Three-Dimensional Superlattices. *Adv. Mater.* **2001**, *13*, 1868–1871.
56. Paik, T.; Ko, D. K.; Gordon, T. R.; Doan-Nguyen, V.; Murray, C. B. Studies of Liquid Crystalline Self-Assembly of GdF_3 Nanoplates by In-Plane, Out-of-Plane SAXS. *ACS Nano* **2011**, *5*, 8322–8330.
57. Moretti, C.; Goldmann, C.; Imperor-Clerc, M.; Abécassis, B. Gold Nanoparticle Superlattices: Conditions for Long-Range Order, Moiré Patterns, and Binary Phase from a Single Population. *Chem Mater* **2023**, *35* (17), 6637–6650.
58. Hong, G.; Gan, X.; Leonhardt, C.; Zhang, Z.; Seibert, J.; Busch, J. M.; Bräse, S. A Brief History of OLEDs—Emitter Development and Industry Milestones. *Adv Mater* **2021**, *33* (9), 2005630.

59. Tang, C. W.; VanSlyke, S. A., Organic electroluminescent diodes. *Appl Phys Lett* **1987,** *51* (12), 913-915.

60. Kuo, H.-H.; Chen, Y.-T.; Devereux, L. R.; Wu, C.-C.; Fox, M. A.; Kuei, C.-Y.; Chi, Y.; Lee, G.-H. Bis-Tridentate Ir(III) Metal Phosphors for Efficient Deep-Blue Organic Light-Emitting Diodes. *Adv Mater* **2017**, *29* (33), 1702464.

61. Li, K.; Ming Tong, G. S.; Wan, Q.; Cheng, G.; Tong, W.-Y.; Ang, W.-H.; Kwong, W.-L.; Che, C.-M. Highly Phosphorescent Platinum(Ii) Emitters: Photophysics, Materials and Biological Applications. *Chem Sci* **2016**, *7* (3), 1653–1673.

62. Cao, L.; Klimes, K.; Ji, Y.; Fleetham, T.; Li, J. Efficient and Stable Organic Light-Emitting Devices Employing Phosphorescent Molecular Aggregates. *Nat Photon* **2021**, *15* (3), 230–237.

63. Tang, M.-C.; Tsang, D. P.-K.; Wong, Y.-C.; Chan, M.-Y.; Wong, K. M.-C.; Yam, V. W.-W. Bipolar Gold(III) Complexes for Solution-Processable Organic Light-Emitting Devices with a Small Efficiency Roll-Off. *J Am Chem Soc* **2014**, *136* (51), 17861–17868.

64. Chen, J.; Teng, T.; Kang, L.; Chen, X.-L.; Wu, X.-Y.; Yu, R.; Lu, C.-Z. Highly Efficient Thermally Activated Delayed Fluorescence in Dinuclear Ag(I) Complexes with a Bis-Bidentate Tetraphosphane Bridging Ligand. *Inorg Chem* **2016**, *55* (19), 9528–9536.

65. Benito, Q.; Le Goff, X. F.; Nocton, G.; Fargues, A.; Garcia, A.; Berhault, A.; Kahlal, S.; Saillard, J.-Y.; Martineau, C.; Trébosc, J.; Gacoin, T.; Boilot, J.-P.; Perruchas, S. Geometry Flexibility of Copper Iodide Clusters: Variability in Luminescence Thermochromism. *Inorg Chem* **2015**, *54* (9), 4483–4494.

66. Tung, Y.-L.; Lee, S.-W.; Chi, Y.; Chen, L.-S.; Shu, C.-F.; Wu, F.-I.; Carty, A. J.; Chou, P.-T.; Peng, S.-M.; Lee, G.-H., Organic Light-Emitting Diodes based on Charge-Neutral RuII Phosphorescent Emitters. *Adv Mater* **2005,** *17* (8), 1059-1064

67. Liao, J.-L.; Chi, Y.; Yeh, C.-C.; Kao, H.-C.; Chang, C.-H.; Fox, M. A.; Low, P. J.; Lee, G.-H. Near Infrared-Emitting Tris-Bidentate Os(Ii) Phosphors: Control of Excited State Characteristics and Fabrication of OLEDs. *J Mater Chem C Mater* **2015**, *3* (19), 4910–4920.

68. Pandey, R.; Kumar, P.; Singh, A. K.; Shahid, M.; Li, P.; Singh, S. K.; Xu, Q.; Misra, A.; Pandey, D. S. Fluorescent Zinc(II) Complex Exhibiting "On-Off-On" Switching Toward Cu2+ and Ag+ Ions. *Inorg Chem* **2011**, *50* (8), 3189–3197.

69. Gong, Y.; Tan, Y.; Li, H.; Zhang, Y.; Yuan, W.; Zhang, Y.; Sun, J.; Tang, B. Z. Crystallization-Induced Phosphorescence of Benzils at Room Temperature. *Sci China Chem* **2013**, *56* (9), 1183–1186.

70. Wei, J.; Liang, B.; Duan, R.; Cheng, Z.; Li, C.; Zhou, T.; Yi, Y.; Wang, Y. Induction of Strong Long-Lived Room-Temperature Phosphorescence of N-Phenyl-2-Naphthylamine Molecules by Confinement in a Crystalline Dibromobiphenyl Matrix. *Angew. Chem. Int. Ed.* **2016**, *55* (50), 15589–15593.

71. Shen, Q. J.; Wei, H. Q.; Zou, W. S.; Sun, H. L.; Jin, W. J. Cocrystals Assembled by Pyrene and 1,2- or 1,4-Diiodotetrafluorobenzenes and Their Phosphorescent Behaviors Modulated by Local Molecular Environment. *CrystEngComm* **2012**, *14* (3), 1010–1015.

72. Gao, H. Y.; Zhao, X. R.; Wang, H.; Pang, X.; Jin, W. J. Phosphorescent Cocrystals Assembled by 1,4-Diiodotetrafluorobenzene and Fluorene and Its Heterocyclic Analogues Based on C–I···π Halogen Bonding. *Cryst Growth Des* **2012**, *12* (9), 4377–4387.

73. Yoshimura, F.; Yamane, H.; Yamada, T. Synthesis, Crystal Structure, and Luminescence Properties of a White-Light-Emitting Nitride Phosphor, Ca0.99Eu0.01AlSi4N7. *Inorg Chem* **2020**, *59* (1), 367–375.

74. Liu, W.; Zhu, L.; Fang, C. Observation of Sum-Frequency-Generation-Induced Cascaded Four-Wave Mixing Using Two Crossing Femtosecond Laser Pulses in a 0.1 Mm Beta-Barium-Borate Crystal. *Opt Lett* **2012**, *37* (18), 3783–3785.

75. Urban, N. D.; Kafka, K. R. P.; Jang, J.-M.; Hoffman, B. N.; Marshall, K. L.; Emms, R.; Walker, D.; Demos, S. G. Performance Characterization of Freeform Finished Surfaces of Potassium Dihydrogen Phosphate Using Fluid Jet Polishing with a Nonaqueous Slurry. *Sci Rep* **2023**, *13* (1), 6524.

76. Huth, B.; Farmer, G. Laser Action in 9, 10 Diphenylanthracene. *IEEE J Quantum Electron* **1968**, *4* (6), 427.

77. Crossland, E. J. W.; Noel, N.; Sivaram, V.; Leijtens, T.; Alexander-Webber, J. A.; Snaith, H. J. Mesoporous TiO2 Single Crystals Delivering Enhanced Mobility and Optoelectronic Device Performance. *Nature* **2013**, *495* (7440), 215–219.

78. Liu, G.; Zhu, Y.; Gao, H.; Xu, S.; Wen, Z.; Sun, L.; Li, F. Photocatalytic Water Oxidation by Surface Modification of BiVO4 with Heterometallic Polyphthalocyanine. *ACS Catal* **2023**, *13* (13), 8445–8454.

79. Fu, J.; Fan, Z.; Nakabayashi, M.; Ju, H.; Pastukhova, N.; Xiao, Y.; Feng, C.; Shibata, N.; Domen, K.; Li, Y. Interface Engineering of Ta3N5 Thin Film Photoanode for Highly Efficient Photoelectrochemical Water Splitting. *Nat Commun* **2022**, *13* (1), 729.
80. Ma, S. S. K.; Maeda, K.; Domen, K. Modification of TaON with ZrO2 to Improve Photocatalytic Hydrogen Evolution Activity under Visible Light: Influence of Preparation Conditions on Activity. *Catal Sci Technol* **2012**, *2* (4), 818–823.
81. Wang, Y.; Wei, Z.; Zhang, Y.; Chen, Y., Glycerol-Assisted Construction of Long-Life Three-Dimensional Surface-Enhanced Raman Scattering Hot Spot Matrix. *Langmuir* **2019,** *35* (48), 15795-15804.
82. Pramod, P.; Thomas, K. G. Plasmon Coupling in Dimers of Au Nanorods. *Advanced Materials* **2008**, *20* (22), 4300–4305.
83. Udayabhaskararao, T.; Altantzis, T.; Houben, L.; Coronado-Puchau, M.; Langer, J.; Popovitz-Biro, R.; Liz-Marzán, L. M.; Vuković, L.; Král, P.; Bals, S.; Klajn, R., Tunable porous nanoallotropes prepared by post-assembly etching of binary nanoparticle superlattices. *Science* **2017,** *358* (6362), 514-518.
84. Matricardi, C.; Hanske, C.; Garcia-Pomar, J. L.; Langer, J.; Mihi, A.; Liz-Marzán, L. M. Gold Nanoparticle Plasmonic Superlattices as Surface-Enhanced Raman Spectroscopy Substrates. *ACS Nano* **2018**, *12* (8), 8531–8539.
85. Bodelón, G.; Montes-García, V.; López-Puente, V.; Hill, E. H.; Hamon, C.; Sanz-Ortiz, M. N.; Rodal-Cedeira, S.; Costas, C.; Celiksoy, S.; Pérez-Juste, I.; Scarabelli, L.; La Porta, A.; Pérez-Juste, J.; Pastoriza-Santos, I.; Liz-Marzán, L. M. Detection and Imaging of Quorum Sensing in Pseudomonas Aeruginosa Biofilm Communities by Surface-Enhanced Resonance Raman Scattering. *Nat Mater* **2016**, *15* (11), 1203–1211.
86. Qiao, X.; Su, B.; Liu, C.; Song, Q.; Luo, D.; Mo, G.; Wang, T. Selective Surface Enhanced Raman Scattering for Quantitative Detection of Lung Cancer Biomarkers in Superparticle@MOF Structure. *Adv Mater* **2018**, *30* (5), 1702275.
87. Demirel, G.; Gieseking, R. L. M.; Ozdemir, R.; Kahmann, S.; Loi, M. A.; Schatz, G. C.; Facchetti, A.; Usta, H. Molecular Engineering of Organic Semiconductors Enables Noble Metal-Comparable SERS Enhancement and Sensitivity. *Nat Commun* **2019**, *10* (1), 5502.
88. Metaferia, W.; Schulte, K. L.; Simon, J.; Johnston, S.; Ptak, A. J. Gallium Arsenide Solar Cells Grown at Rates Exceeding 300 Mm H−1 by Hydride Vapor Phase Epitaxy. *Nat Commun* **2019**, *10* (1), 3361.
89. Huang, Y.; Duan, X.; Cui, Y.; Lieber, C. M. Gallium Nitride Nanowire Nanodevices. *Nano Lett* **2002**, *2* (2), 101–104.

90. Rüssel, C.; Wisniewski, W. How Can Surface-Crystallized Glass-Ceramics Be Piezoelectric? *Cryst Growth Des* **2021**, *21* (4), 2405–2415.
91. Acosta, M.; Novak, N.; Rojas, V.; Patel, S.; Vaish, R.; Koruza, J.; Rossetti, G. A., Jr.; Rödel, J., BaTiO3-based piezoelectrics: Fundamentals, current status, and perspectives. *Appl Phys Rev* **2017,** *4* (4).
92. Kagan, C. R.; Lifshitz, E.; Sargent, E. H.; Talapin, D. V., Building devices from colloidal quantum dots. *Science* **2016,** *353* (6302), aac5523.
93. Taylor, L. S.; Braun, D. E.; Steed, J. W., Crystals and Crystallization in Drug Delivery Design. *Cryst Growth Des* **2021,** *21* (3), 1375-1377.
94. Taylor, L. S.; Braun, D. E.; Tajber, L.; Steed, J. W., Crystallizing the Role of Solid-State Form in Drug Delivery. *Mol Pharmaceutics* **2022,** *19* (8), 2683-2685.

Chapter 2

Molecular Specificity in the Intense Surface Enhanced Raman Scattering on Copper (II)-8-hydroxyquinoline Microcrystals

Herein we propose and demonstrate that microcrystals of inorganic complexes are suitable platforms for SERS. In particular, they provide molecule-specific enhancement in Raman scattering. We also show that such a microcrystal offers the dual advantage of plasmonic and charge-transfer based enhancement that forms the basis of specificity involving the host crystal and the analyte molecule. For a test case, we have worked on the exceptional SERS activity of π-conjugated copper 8-hydroxyquinolinate (CQ) microcrystals. The UV-Vis diffuse reflectance spectra (DRS) of the solid microcrystalline CQ consisted of a strong and broad peak at 725 nm. This helped in probing the analyte molecules deposited on the crystal surface, using laser excitations at 633 nm and 785 nm. Rhodamine-6G (R6G), rhodamine B (RhB) and copper-(II)-picolinate complex (CuPA) - generated in situ by addition of picolinic acid in the CQ dispersion-, and when deposited on the solid microcrystals, were used as target analytes. Excellent enhancement factors of 28372±1953, 13407±1969 and 12816±900 at 785 nm laser excitation and the values of 3463±110 ,1366±72 and 1447±62 when probed at 633 nm laser were obtained for solution concentration of 25 µM R6G, 25 µM RhB and 250 µM picolinic acid as a precursor of CuPA, respectively.

We have optimized the unit cell structure of CQ crystal using a Gaussian 16 simulation package with cam-B3LYP/gen DFT functional.[1,2] From the optimized structure, electrostatic potential map and possible charge transfer window have been calculated. Further, the electronic structure of CQ crystal has been performed through solid state DFT calculation in Quantum ESPRESSO package.[3] Altogether, the calculations also indicated that CQ is a highly electron-dense metal-like system in which electrons could be involved in photo-induced charge transfer or generate plasmonic field leading to SERS. The positions of HOMO and LUMO of the substrate crystal and the analytes provided opportunity for facile charge transfer and specificity of enhancements.

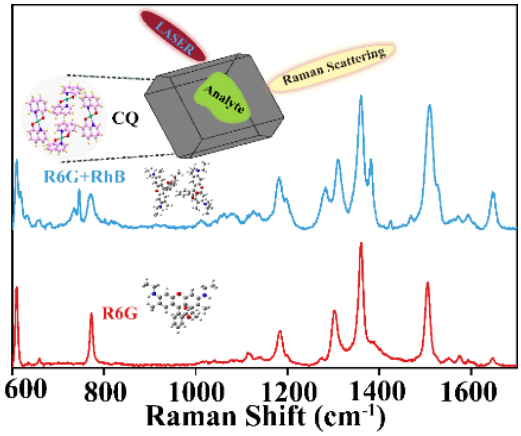

***[*J. Phys. Chem. C* 2023, 127, 10, 5169-5177]- reproduced with permission from the American Chemical Society.**

2.1 Materials and Methods

2.1.1 Materials

Copper-(II)-nitrate trihydrate (241.6 g mol^{-1}), 8-hydroxyquinoline (145.16 g mol^{-1}), rhodamine-6G (R6G) (98%, 479 g mol^{-1}), rhodamine-B (RhB, 479 g mol^{-1}), picolinic acid (99%, 123.11 g mol^{-1}), benzoic acid (BA, 122.12 g mol^{-1}) and methanol (99%) were purchased from Merck. All materials were used without any further purification. Elix grade water from a MilliQ purification system was used for the experiments.

2.1.2 Synthesis of copper-(II)-8-hydroxyquinolate micro-crystal

CQ crystals were prepared using a simple and green synthetic method. At first, 100 mg of copper-(II)-nitrate trihydrate was dissolved in 200 mL water/methanol mixture (1:9 volume ratio), into which 200 mg of HQ was added. Then the reaction mixture was sonicated for 30 min, which was then allowed to settle for 10 min to complete precipitation of the microcrystals. The reaction mixture was centrifuged at 10k rpm for 5 min and the pellet was washed with water twice. The so-obtained microcrystals were stored in 50 mL water/methanol (1:1 v) mixture, which was used for further experiments.

2.1.3 Characterization

Raman spectra were recorded using a Horiba LabRAM HR Evolution microscope Raman instrument attached with 532 nm and 632.8 nm lasers. For Raman measurements with 785 nm excitation wavelength, Horiba Labram HR instrument was used. Baseline subtractions were done in LabSpec 6 software equipped with the Raman instrument. Field emission transmission

electron microscopy (TEM) analyses were done using a JEOL JEM-2100F FETEM instrument (acceleration voltage of 200 kV). A Rigaku TTRAX III diffractometer, running with a CuKα source (λ = 1.54 Å), was used to analyze the powder X-ray diffraction (XRD) pattern of the samples. Also, the UV-Vis diffuse reflectance spectra were recorded using a PerkinElmer Lambda 750 UV-Vis-NIR spectrophotometer. The optical constants n and k of CQ were calculated using an ellipsometer (EP3, Nanofilm, Accurion Scientic Instruments Pvt. Ltd). A JSM-7610F instrument was used for the field emission scanning electron microscopy (FESEM) analysis.

2.1.4 Raman measurement

The SERS behaviours of Copper-(II)-8hydroxyquinolate (CQ) microcrystals were examined using rhodamine 6G (R6G, rhodamine B (RhB) and in-situ generated copper-(II)-picolinate (CuPA) as target molecules at excitation wavelengths of 633 nm and 785 nm. Typically, a stock solution of 5×10^{-2} M R6G or RhB was initially prepared, which was added to the CQ dispersion (in 3:1 methanol/water) such that the final concentration of each dye became 25 μM. In case of CuPA, initially 50 mM stock solution of picolinic acid was prepared; from which 10 μL of the solution was added to the CQ dispersion. The mixture was then evaporated upon which, formation of copper-(II)-picolinate complex over the crystals was detected. For the sample preparation, 20 μL each of the mixtures was drop-cast over a cleaned glass slide and dried at 40 °C for 15 min. Raman spectra were subsequently recorded in a high-resolution confocal Raman spectrometer, Horiba LabRAM HR-Evolution that was equipped with 532 nm and 633 nm lasers and LabRAM HR-800 for 785 nm laser. In case of using 785 nm laser, a 100 ×L objective lens and a laser power of 100 mW were used to collect the Raman spectra, with an acquisition time of 20 s at diffraction grating of 600 gr/mm. For 633 nm laser use, 100 ×L objective lens and a laser power of 0.16 mW were used to record the Raman spectra with acquisition time of 5 s at a diffraction grating of 600 gr/mm. Finally, for control experiments 20 μL of the suspension of 15 mM of R6G, 15 mM of RhB and 20 mM in-situ mixture of copper-(II)-nitrate trihydrate and picolinic acid were drop-cast over cleaned glass slides and dried at 40 °C for 15 min. The Raman test conditions were the same as that described above for all the control samples.

2.1.5 Calculation of the enhancement factor

The EF was calculated according to the formula:

$$EF = (I_{SERS}/N_{SERS})/(I_{bulk}/N_{bulk}) \quad (1)$$

$$N_{SERS} = CVN_AA_{Raman}/A_{Sub} \quad (2)$$

$$N_{bulk} = \rho h A_{Raman} N_A/M \quad (3)$$

Where N_{SERS} and N_{bulk} denote the average numbers of analyte molecules present inside the scattering area of the SERS experiment using CQ and bulk raman measurement and the I_{SERS} and I_{bulk} are the corresponding intensities of Raman scattering at a particular peak position. C represents the concentration of the analyte (when in the liquid mixture) in molarity, V is the drop casted volume of the mixture on the glass slide and N_A is the Avogadro number. A_{Raman} is the Raman scanning laser spot area. 20 µL of the analyte liquid mixtures when evaporated on the glass surface, were deposited as solid into a circles of diameters about 5.5 mm for R6G, 6 mm for RhB and 6.95 mm diameter for CuPA. The effective area of the substrate A_{Sub} was then calculated for the discs of the above can then be obtained. For the bulk, 15 mM R6G (M=479 g/mol, ρ=1.26 g·cm^{-3}), 15 mM RhB (M=479 g/mol, ρ=0.79 g·cm^{-3}) and 20 mM CuPA (M=343.78 g/mol, ρ=1.724 g·cm^{-3}) were evaporated in glass slides similarly.
The confocal depth (h) of the laser beam[4] was 12 µm for 785 nm laser and 3 µm for 633 nm laser and N_{bulk} was calculated by Supplementary equation 3.[5,6]

2.1.6 Theoretical Calculations

The electronic structure calculations were performed using the Quantum ESPRESSO program package. The generalized gradient approximation[7] (GGA) of PBEsol[8] was used for the calculation of the exchange-correlation functional. Kinetic energy cut-off was set to 60 Ry for expansion of wavefunctions in the plane wave basis set. The electronic wave function for charge density and potential were based on a kinetic energy. Initially, the system was relaxed by "vc-relax" calculation. Using the optimized structure density of state and band structure calculations have been performed.

Quantum chemical calculations to analyze and identify the Raman intensities and the frontier molecular orbitals (HOMO and LUMO) energies were carried out with the Gaussian 16 series of programs with DFT as implemented in the computational package. Functionals and basis sets for each molecule are given in Table 2.1 and Table 2.2. Electrostatic potential map in Figure 2.15a has been generated in Avogadro software by post processing the output file generated through Gaussian 16 DFT calculation.

Details of theoretical calculation

Table 2.1 Details for HOMO-LUMO gap calculation using Gaussian 16 simulation code

Molecule	DFT level of theory	Basis set and core potentials
CQ (single unit cell)	CAM-B3LYP[9]/GEN	6-31G(d)[10] for C,N,O,H atoms; LanL2DZ[11] for Cu.
RhB	B3LYP[12,13]	6-311++g(d,p)[14]
CuPA	HSEH1PBE[15]/GEN	6-311++G(d,p) for C,N,O,H atoms; LanL2DZ for Cu.
BA	B3LYP	6-31g(d)

Table 2.2 Details for simulated Raman peak assignment using Gaussian 16 simulation code

Molecule	DFT level of theory	Basis set and core potentials
CQ	B3LYP/GEN	6-31G(d) for C,N,O,H atoms; LanL2DZ for Cu.
CuPA	B3LYP	6-311g(d,p)

2.2 Results and discussion

The UV-Vis diffuse reflectance spectrum of the solid CQ microcrystals at room temperature consisted of four absorption peaks occurring at 390, 470, 625 and 725 nm (Figure 2.1a). However, UV-Vis spectrum of CQ in 9:1(v/v) methanol/water solution, recorded before crystallisation contained two peaks appearing at 390 and 470 nm (Figure 2.1a inset). The peak at 390 nm is due to π to π^* transition in the HQ moiety (Figure 2.2a) and the 470 nm peak is a result of ligand to metal charge transfer (LMCT).[16,17] Hence, 625 nm and 725 nm absorption peaks may be attributed to have originated from crystalline packing. The peak at 625 nm might be due to intermolecular π-π stacking and the broad 725 nm peak is unusual and can be attributed to weak plasmonic band representing high-density free electrons. The generation of

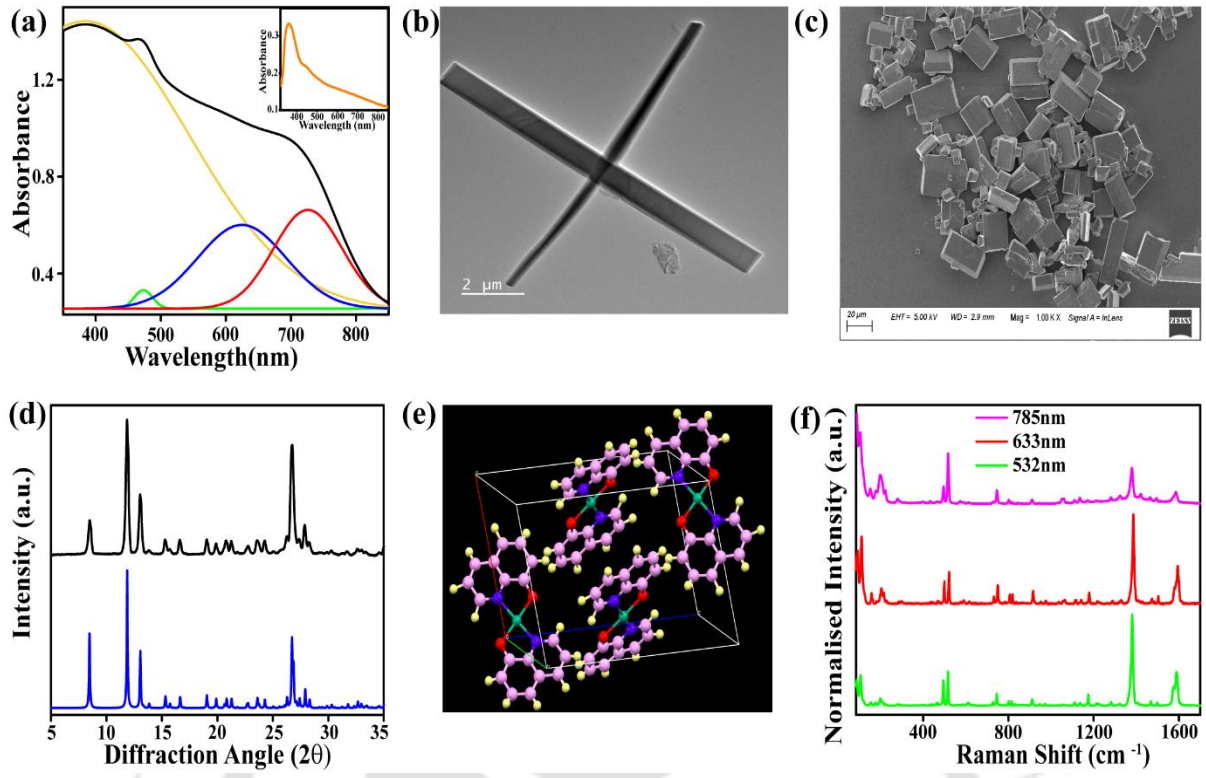

Figure 2.1 Characterization of CQ. (a) UV-Vis DRS spectrum of CQ microcrystals (black line) and deconvoluted UV-Vis spectra of CQ microcrystals. Inset is the UV-Vis spectrum of CQ complex solution. (b) TEM image of CQ microcrystals. (c) FESEM image of CQ microcrystals. (d) Powder XRD pattern of CQ microcrystals. The black line corresponds to the obtained powder pattern and blue line is for the simulated powder XRD pattern. (e) 3D visualisation of unit cell of CQ microcrystal as obtained from single-crystal XRD. (f) Raman spectra of CQ microcrystals at laser excitations mentioned in the legends.

the strong peak in the visible region of the molecular crystalline form indicated strong metallicity and possibly due to the presence of a large number of interconnected π-network between the asymmetric units of the crystals.

CQ's optical constants n and k were measured using variable-angle spectroscopic ellipsometry. Ellipsometry measurements were obtained using a 658 nm laser source and a step size of 0.50 ° to adjust the incidence angle from 50 ° to 55 °. The derived parameters delta (Δ) and psi (ψ) were best suited to the Lorentz

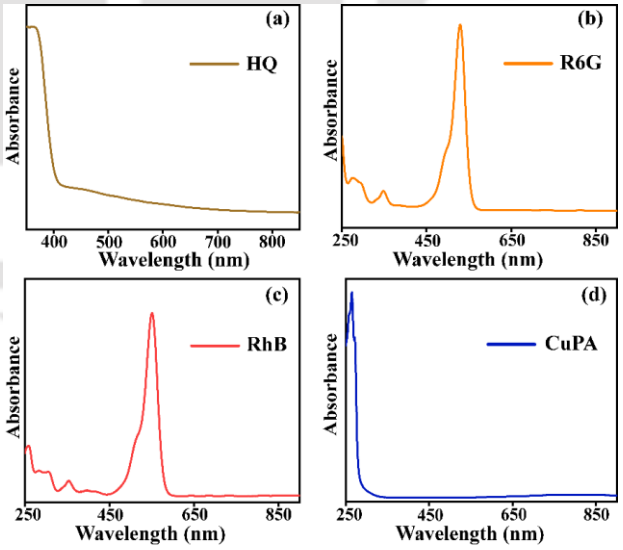

Figure 2.2 (a) UV-Vis diffuse reflectance spectrum (DRS) spectrum of solid 8-hydroxyquinoline. UV-Vis absorption spectra of (b) R6G (c) RhB and (d) CuPA in methanol-water mixture.

dispersion model, with frequency, strength, and damping parameters of 4 eV, 20 eV^2, and 2 eV, respectively (Figure 2.3). The complex refractive index constant for CQ has been calculated using the fitted model in EP4 model software, with n and k values of 1.162 and 0.105 respectively.

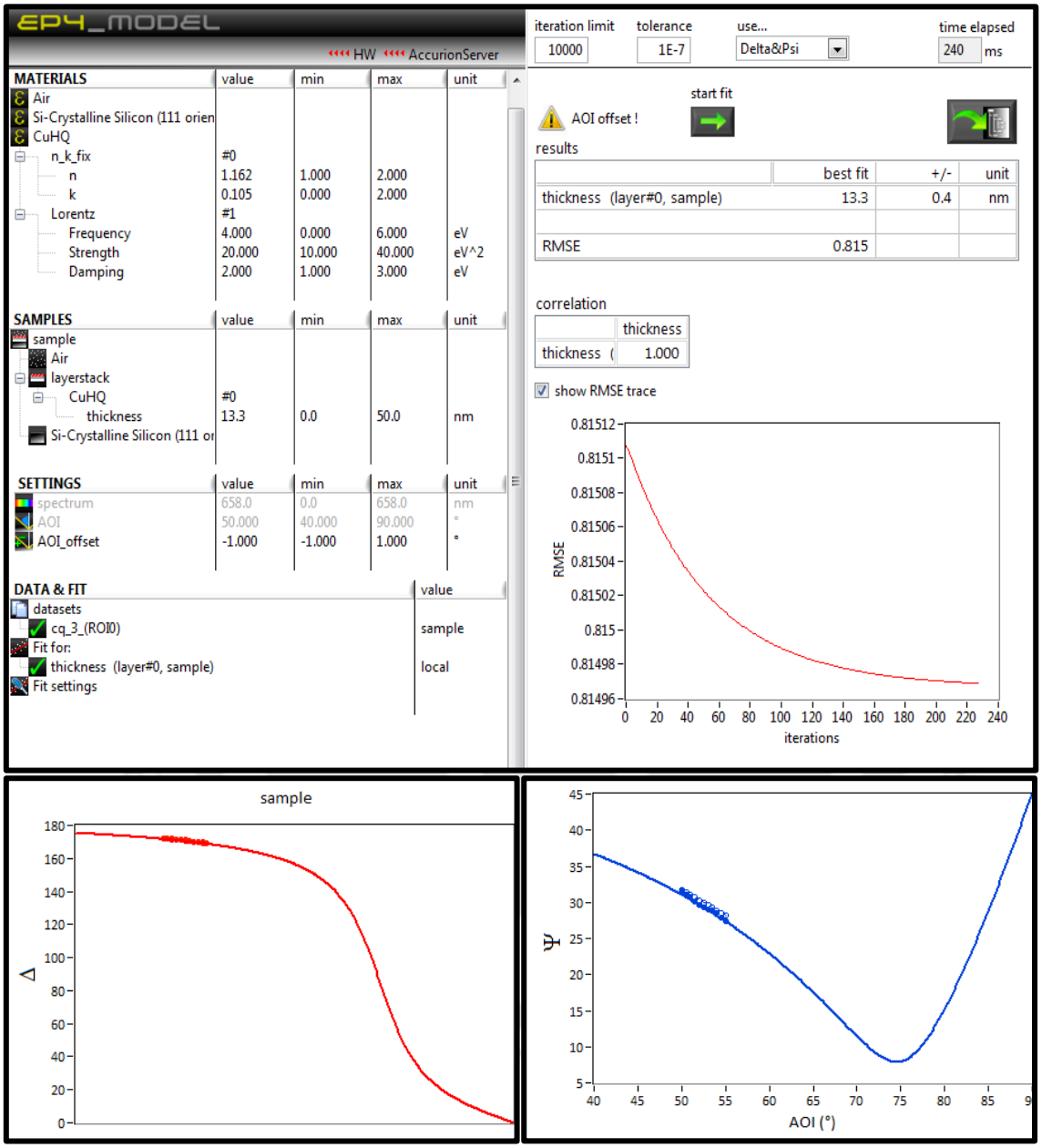

Figure 2.3 Model fitting of raw value of delta (Δ) and psi (ψ) from ellipsometer for CQ thin film in EP4_MODEL software.

It is important mentioning here that 8-hydroxyquinoline (HQ) rapidly crystallizes with Cu^{2+} in the medium forming neutral inner metallic complex with highly efficient intermolecular π-π stacking between HQ ligands. The π- network of HQ ligands in the asymmetric unit provides delocalization of electron throughout the crystal, giving rise to the plasmonic nature of the crystal.[18]

Field emission transmission electron microscopy (FETEM) analysis of the product confirmed the formation of CQ micro crystals (Figure 2.1b). Crystals were mainly of reactangular

shape with size typically in the range of 15 to 30 µm. Discrete rectangular shaped crystals of similar dimensions were also observed in FESEM images (Figure 2.1c).

The structural characterizations of the CQ have been pursued by producing large crystals through slow evaporation of CQ complex solution at room temperature. The single crystal XRD measurement revealed that CQ is a β unique monoclinic crystal with cell dimensions: a = 10.644, b =8.593, c = 15.239; and $\alpha = \gamma = 90^{o}$, $\beta = 102.18°$ (Figure 2.1e), which matched with the literature report.[19] This was further substantiated by powder XRD results of as synthesised crystals, revealing the formation of a well-ordered micro-crystal with exceptional crystallinity (Table 2.3). Simulated powder XRD pattern (obtained using VESTA 3.4.5 analyser)[20] corresponding to the monoclinic CQ structure matched well with the peak positions observed in the measurement (Figure 2.1d).

Table 2.3. hkl values and calculated d spacing values corresponding to the powder XRD peaks of CQ (Figure 2.1d)

Diffraction angle (2θ)	Assigned hkl	Corresponding d-spacing (Å)
8.47	100	10.42
11.87	002	7.44
11.88	011	7.44
13.05	10-2	6.77
15.32	111	5.77
16.65	11-2	5.31
19.06	112	4.65
23.62	121	3.76
26.73	22-1	3.33
27.92	22-2	3.19
29.47	311	3.02

As-synthesized CQ microcrystals were characterized with Raman spectroscopy using 532 nm, 633 nm and 785 nm laser excitations. The main vibrational transitions of the CQ microcrystals consisted of sharp peaks at 1590, 1498, 1468, 1382, 1175, 1137, 1111, 912, 745, 517, 494, 199 and 88 cm^{-1} (Figure 2.1f). Sharp peaks with excellent signal to noise ratios were obtained owing to presence of spatial order and long-range translational symmetry in CQ microcrystals.[21] The observed peaks matched well with those simulated for the complex using a Gaussian 16 package for the asymmetric unit (Table 2.4).

Table 2.4. Raman peak assignments of bis-(8-hydroxyquinolate) copper(II) complex (CQ)

Raman shift (cm^{-1})		
Experimental	**Theoretical**	**Vibration mode**
1589.7	1633.9	$\nu(C=C)_{ring} + \delta(HCC)_{ring}$
1498.1	1518.0	$\nu(C=C)_{ring} + \nu(C=N)_{ring} + \nu(C=O) + \delta(HCC)_{ring}$
1468.2	1473.9	$\delta(HCC)_{ring}$
1381.7	1415.4	$\nu(C=C)_{ring} + \nu(C=N)_{ring} + \delta(HCC)_{ring}$
1175.0	1171.7	$\delta(HCC)_{ring}$
1137.5	1139.7	$\delta(HCC)_{ring} + \delta(CCC)_{ring} + \delta(CNC)_{ring}$
1111.3	1086.9	$\delta(HCC)_{ring} + \delta(CCC)_{ring}$
911.7	927.5	$\nu(Cu-N) + \delta(CCC)_{ring} + \delta(NCC)_{ring}$
745.6	760.9	$\nu(Cu-N) + \nu(Cu-O) + \delta(CCC)_{ring} + \delta(CNC)_{ring}$
517.3	516.6	$\nu(Cu-N) + \nu(Cu-O) + \delta(CCC)_{ring}$
494.4	503.3	$\delta(CCC)_{ring}$
199.6	194.5	$\nu(Cu-O) + \delta(NCuO)$
88.2	92.2	τ(Cu-Ring)

$\nu(C=C)_{ring}$: stretching vibration of C=C of ring; **$\nu(C=N)_{ring}$:** stretching vibration of C=N of ring.; **$\delta(HCC)_{ring}$:** C−H bending of ring; **$\nu(C=O)$:** stretching vibration of C=O; **$\delta(CCC)_{ring}$:** C−C−C bending vibration of ring; **$\delta(CNC)_{ring}$:** C−N−C bending vibration of ring; **$\delta(NCC)_{ring}$:** N−C−C bending vibration of ring; **$\nu(Cu-N)$:** stretching vibration of Cu−N; **$\nu(Cu-O)$:** stretching vibration of Cu−O; **$\delta(NCuO)$:** N−Cu−O bending vibration; **τ(Cu-Ring) :** Cu-Ring twisting.

The crystals were then tested for their efficiency and molecular specificity as sensitive SERS substrate. R6G, RhB and in-situ produced copper-(II)-picolinate complex (CuPA) were chosen as model molecules for measuring the Raman enhancement on the microcrystalline particles. As mentioned in the experimental section, the molecules were mixed in the liquid medium with the dispersions of CQ microcrystals. The mixtures were then drop-cast to make dried samples on glass surface before measurements. Further, Field Emission Scanning Electron Microscopy with Energy Dispersive X-Ray Spectroscopy (FESEM-EDX) mapping for the R6G-CQ Raman sample showed that the percentage of chlorine outside the crystal was in excess as compared to that over the crystal (Figure 2.4). Thus, even though the deposited molecules outside the crystal region were of higher concentrations, the Raman signal of R6G is much higher intensity (Figure 2.10).

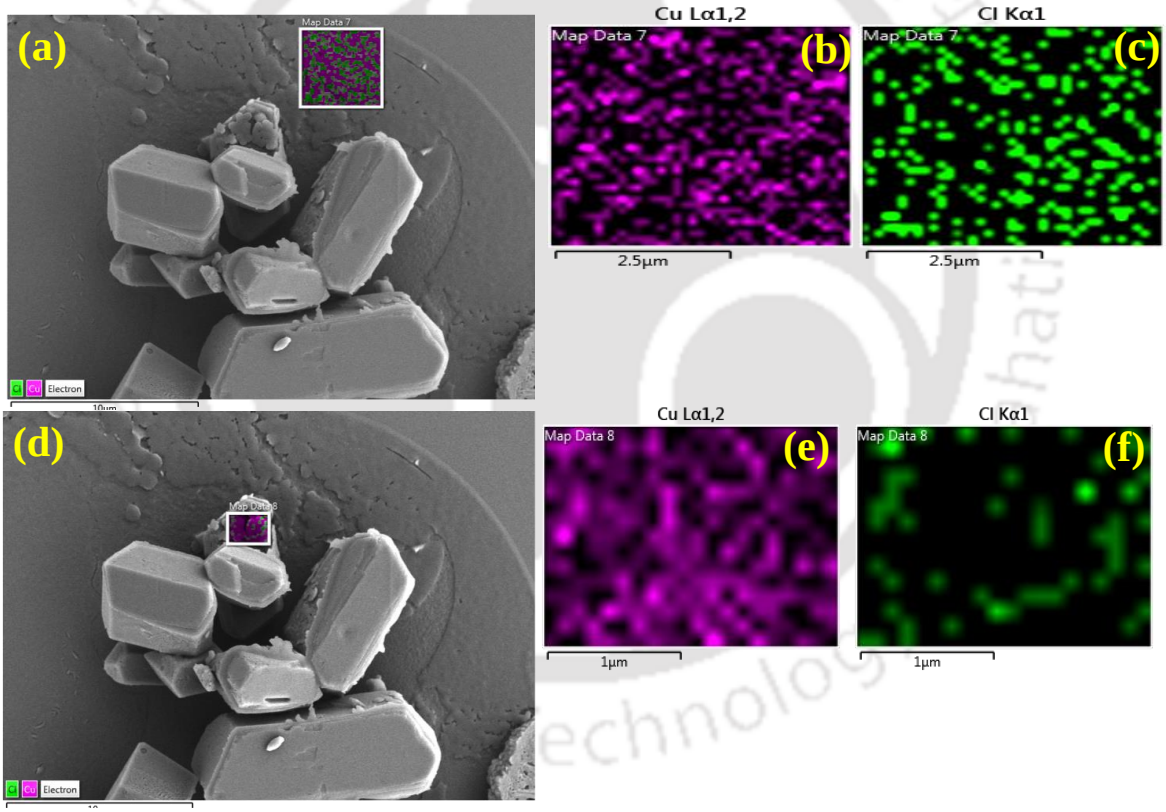

Figure 2.4 Field Emission Scanning Electron Microscopy with Energy Dispersive X-Ray Spectroscopy (FESEM-EDX) mapping results of CQ-R6G sample showing higher density of chloride i.e., due to R6G that was deposited over the crystal. (a) outside the crystal region and (b, c) are percentage of Cu and chlorine respectively. (d) over the crystal region and (e, f) are percentage of Cu and chlorine respectively.

2.2.1 SERS Performance

Figure 2.5a-f displays the SERS spectra of R6G, RhB and CuPA complex over microcrystals when excited with 633 nm and 785 nm laser probes. The choice of these two excitation wavelengths was driven by the UV-Vis absorption peaks (at 625 and 725 nm) owing to π-π stacking and plasmon of microcrystalline CQ substrate. The main vibrational peaks of R6G were recorded at 1648, 1575, 1505, 1360, 1301, 1183, 772, 609 cm^{-1} and in case of RhB the prominent peaks occurred at 1648, 1529, 1504, 1358, 1280, 1077, 735 and 621 cm^{-1} peaks. For the CuPA complex intense vibrational peaks were found at 1632, 1606, 1450, 1345, 1034, 708, 454, 232, 142 and 103 cm^{-1}. Vibrational mode assignments of all the Raman peaks of the analyte molecule deposited over the crystals are presented in the supporting information (Table 2.5, 2.6, 2.7).[22-24] The results with substantial signal to noise improvements - as compared to the control samples - indicated that CQ provided a significantly high SERS enhancement for these probe molecules. The enhancement factor (EF) of each of the prepared analytes was calculated to evaluate the SERS efficiency using 25 μM solution each of R6G and RhB and 250 μM of picolinic acid solution as a precursor of CuPA complex (Table 2.8). The details of calculations are given in the SI.[25,26] It may be mentioned here that a weak peak occurring at 1382 cm^{-1} corresponding to the stretching vibration of quinoline ring ($\nu(C=C)_{ring} + \nu(C=N)_{ring} + \delta(HCC)_{ring}$) of the CQ crystal was present in all the SERS spectra of analytes (Table 2.4). However, being comparatively weak in nature, the peak did not interfere with the SERS measurements of the analytes. The peak further supported the SERS of the analytes on the surface of the CQ microcrystals. The results of higher EFs for all the three molecules under 785 nm laser excitation suggested that to a certain extent the electromagnetic (EM) enhancement due to the plasmon field might have occurred at the longer wavelength. The results also indicated that the plasmonic band of the crystal was closer to the higher wavelength of excitation. Notably, the wavelength-dependent EFs on CQ microcrystals correlated well with their UV-Vis absorption spectrum as measured in diffuse reflectance mode. This is also consistent with the deconvoluted UV-Vis diffuse reflectance spectra of the microcrystals as shown in Figure 1a. In other words, the stronger peak in the absorption spectrum of the crystals at 785 nm in comparison to that 633 nm support higher performance of the microcrystals as SERS substrate at the longer wavelength of excitation.

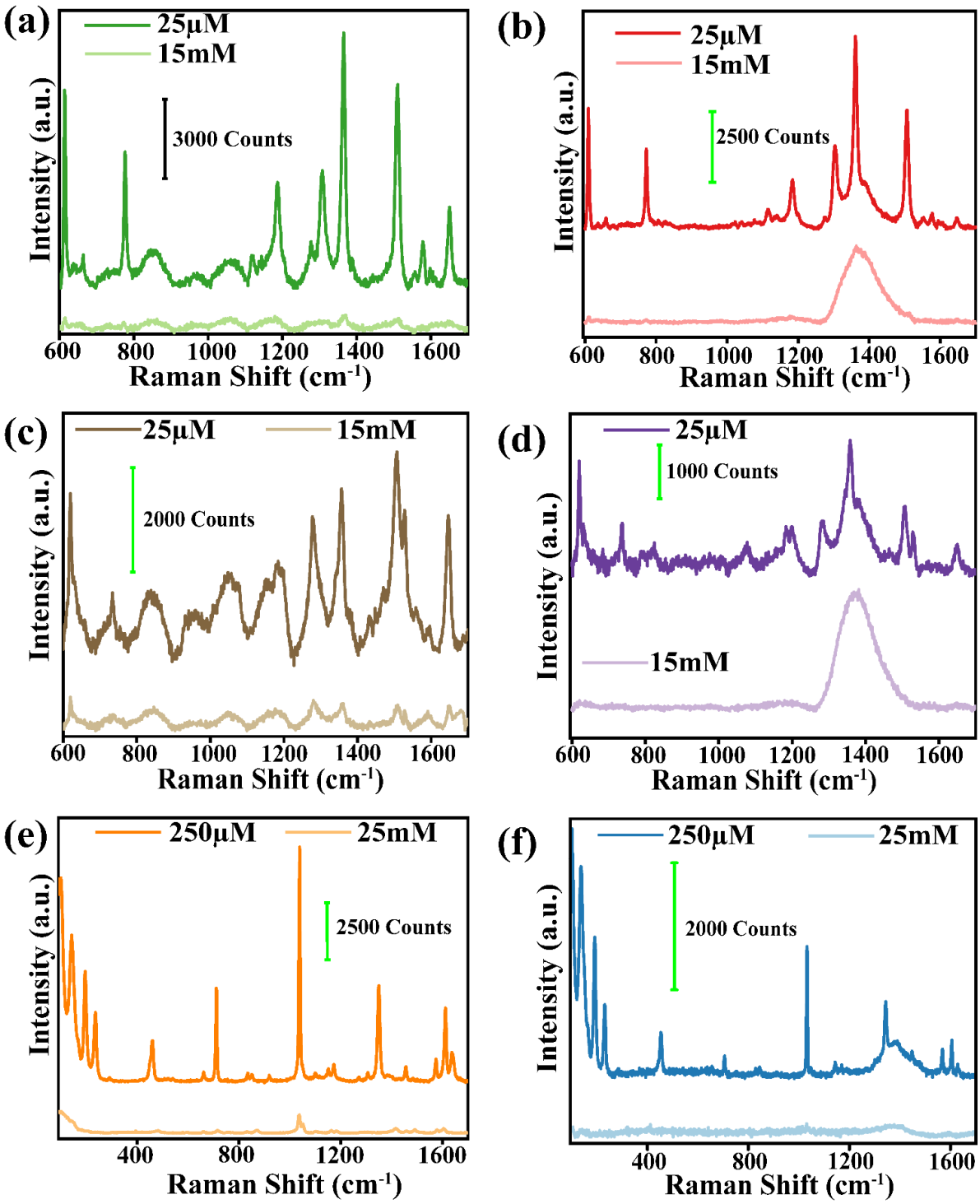

Figure 2.5 SERS performance of R6G, RhB and CuPA over CQ microcrystals. (a), (b) SERS spectrum of R6G on CQ microcrystals and normal Raman spectrum of R6G at laser excitations of 633 nm and 785 nm, respectively. (c), (d) SERS spectrum of RhB on CQ microcrystals and normal Raman spectrum of RhB at laser excitations of 633 nm and 785 nm, respectively. (e), (f) SERS spectrum of CuPA on CQ microcrystals and normal Raman spectrum of CuPA at laser excitations of 633 nm and 785 nm, respectively. Weak peak at 1382 cm^{-1} corresponding to the Stretching vibration of quinoline ring of the crystal is present in all the spectra (Table 2.4).

Table 2.5 Raman peak assignments of copper-(II)-picolinate complex (CuPA)

Raman shift (cm^{-1})		
Experimental	**Theoretical**	**Vibrational mode**
1632	1647.0	$\nu(C=C)_{ring} + \delta(CCC)_{ring} + \delta(CNC)_{ring} + \delta(HCC)_{ring}$
1606	1610.1	$\nu(C=C)_{ring} + \delta(CCC)_{ring} + \delta(CNC)_{ring} + \delta(HCC)_{ring}$
1450	1473.7	$\nu(C=C)_{ring} + \delta(HCC)_{ring}$
1345	1340.5	$\nu(C=C)_{ring} + \nu(C\text{-}C)_{ring} + \nu(C=N)_{ring} + \nu(C=O) + \delta(HCC)_{ring}$
1034	1047.1	$\nu(C=C)_{ring} + \nu(C=N)_{ring} + \nu(Cu-N)$
708	717.8	$\nu(Cu-O) + \nu(C-C) + \delta(CCC)_{ring} + \delta(NCC)_{ring} + \delta(OCO)_{ring}$
454	453.1	$\nu(Cu-N) + \nu(Cu-O)$
232	230.9	$\rho(N-Cu-O)$
142	152.5	$\nu(Cu-N) + \delta(NCuO)$
103	111.2	$\tau(Cu-COO)$
86.7	94.5	$\tau(Cu-Ring)$

$\nu(C=C)_{ring}$: stretching vibration of C=C of ring; **$\nu(C=N)_{ring}$:** stretching vibration of C=N of ring; **$\delta(HCC)_{ring}$:** C−H bending of ring; **$\nu(C=O)$:** stretching vibration of C=O; **$\delta(CCC)_{ring}$:** C−C−C bending vibration of ring; **$\delta(CNC)_{ring}$:** C−N−C bending vibration of ring; **$\delta(NCC)_{ring}$:** N−C−C bending vibration of ring; **$\nu(Cu-N)$:** stretching vibration of Cu−N; **$\nu(Cu-O)$:** stretching vibration of Cu−O; **$\delta(NCuO)$:** N−Cu−O bending vibration; **τ(Cu-Ring) :** Cu-Ring twisting; **$\rho(N-Cu-O)$:** N−Cu−O rocking vibration; **$\tau(Cu-OCO)$:** Cu−OCO twisting vibration; **$\delta(OCO)_{ring}$:** O−C−O bending vibration.

Table 2.6 Raman peak assignments of rhodamine-6G (R6G)[22]

Raman shift (cm^{-1})	**Vibration mode**
1648.5	C−C stretching in xanthene ring
1575.2	C−C stretching in phenyl ring
1505.7	C−C stretching in xanthene ring
1360.5	C−C stretching in xanthene ring
1302.0	Hybrid mode (xanthene/phenyl rings and N−H bending)
1183.9	C−H in-plane bend in xanthene ring
1113.0	C−H in-plane bend in xanthene/phenyl rings
772.5	C−H out-of-plane bending
610.0	C-C-C ring in-plane bending vibration in xanthene/phenyl rings

Table 2.7 Raman peak assignments of rhodamine B (RhB)[23,24]

Raman shift (cm^{-1})	Vibration mode
1648	Aromatic C−C stretching
1529	Aromatic C−H bending
1504	Aromatic C−C stretching
1358	Aromatic C−C stretching
1280	C−C bridge-band stretching
621	Xanthene ring puckering

Table 2.8 Calculated SERS enhancement factors for substrates on copper-(II)-8-hydroxyquinolinate microcrystals.

Analyte	Peak Position (cm^{-1})	Excitation Laser wavelength (nm)	Enhancement Factor (EF)
R6G	610	633	3463±110
R6G	610	785	28372±1953
RhB	621	633	1366±72
RhB	621	785	13407±1969
CuPA	142	633	1447±62
CuPA	142	785	12816±900

Interestingly, when the probe laser wavelength was switched from 633 nm to 785 nm, i.e., away from the absorption peak of R6G, Raman peak intensity of the totally symmetric vibrational mode of R6G at 1649 cm^{-1} decreased due to off resonance condition and the peaks for other vibrations became dominant with better signal to noise ratio (Figure 2.5a,2.5b). Literature report suggests that photo-induced charge transfer following strong absorption of photon at 785 nm - in addition to plasmonic enhancement - might have played a key role in the enhancement of other vibrational modes.[27]

Moreover, for control samples, the presence of absorbance band edge of RhB at 633 nm - in comparison to R6G - might have contributed to the stronger Raman scattering. The above results suggest the importance of the crystalline molecular form giving rise to the additional absorption band at the near infrared region, which resulted in strong enhancement of the Raman activity due to the attainment of both plasmonic and charge transfer conditions.

We were then interested in pursuing the enhancement of Raman signal of one molecule over the other in binary mixtures deposited on the CQ microcrystals. In other words, we investigated the molecular specificity of enhancement over the microcrystals, by comparing the results after depositing solution mixture of two analytes stirred with CQ dispersion. This was performed by sampling equimolar mixtures of R6G/RhB and PA/BA deposited on the surface of the CQ

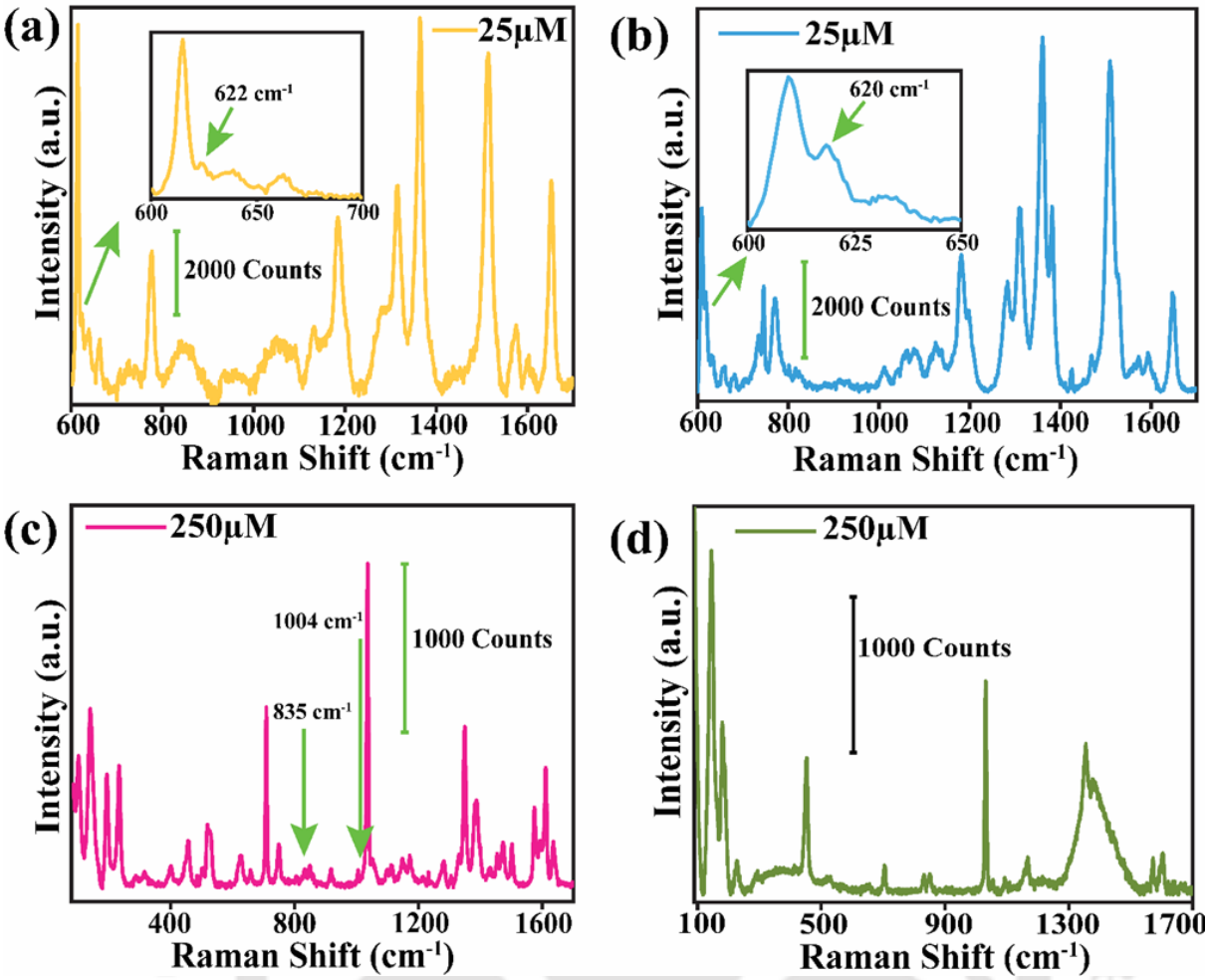

Figure 2.6 Analyte specificity of SERS on CQ microcrystals. (a), (b) SERS spectrum of R6G and RhB mixture on CQ microcrystals at laser excitations of 633 nm and 785 nm, respectively. (c), (d) SERS spectrum of PA and BA mixture on CQ microcrystals at laser excitations of 633 nm and 785 nm, respectively.

microcrystals. As shown in (Figure 2.6 a,b) for the mixture containing RhB and R6G, when excited with the 633 and 785 nm lasers, the SERS signals resembled those of individual molecules on the surface.

The signal intensity ratios appeared to those of individual molecules on the crystal surface. This was pursued by comparing the intensities of the peaks occurring at 611 cm^{-1} and 621 cm^{-1}, corresponding to the bending vibrational modes of the xanthene ring of R6G and RhB, respectively. In the case of PA and BA mixture at 633 nm laser excitation, signals due to CuPA were enhanced possibly owing to photo-induced charge transfer (as discussed later) whereas those due to BA were weak due normal Raman scattering. At 785 nm laser excitation, only scattering signals due to CuPA along with those of the crystal had been detected and no discernible peaks due to BA were observed. (Figure 2.6 c,d). The results mentioned above indicated that molecular enhancement of Raman signals in a mixture retained their individual

characteristics on the surface of the CQ microcrystals. The retention of the characteristic peaks and SERS enhancements of molecules on the surface of a microcrystals in a mixture augur well for identification of chemical moiety in a milieu based on plasmonic enhancement and charger transfer characteristics. The results also indicated the advantage of molecular specificity in the Raman signal enhancement on the SERS substrate.

The signal reproducibility and homogeneity across the substrate especially for solid samples are also important conditions for SERS substrates in routine analytical applications. Generally, Raman experiments with evaporated liquid droplets involve deposition of solid in the form of coffee ring with radius equivalent to that of the pinned droplet.[28] All along the circumference, the concentration of the deposited molecule is assumed to be nearly identical. In order to pursue the repeatability of the SERS signals for R6G, RhB and in-situ CuPA complex, we recorded spectra from 10 different randomly chosen locations on the circumference of the deposited substrate. This was performed at both the laser excitations and the results are shown in Figure 2.7, Figure 2.8 and Figure 2.9. As are clear from the spectra, the results indicated uniform and reproducible SERS signals over the whole circumference, including Raman peak of CQ at 1382 cm^{-1}, which is likely related to homogenous and efficient depositions of the probe molecules.

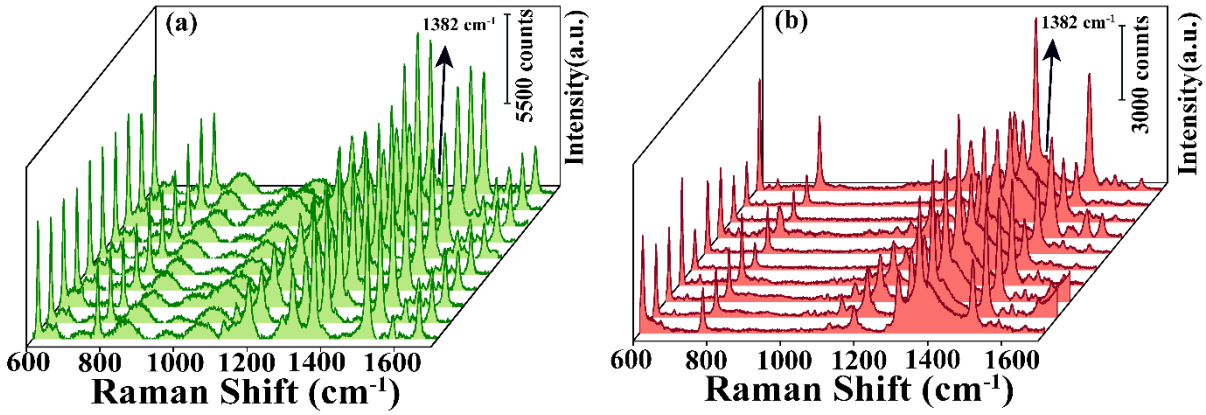

Figure 2.7 SERS spectra for 25 µM R6G (as in the precursor mixture) at laser excitation of (a) 633 nm and (b) 785 nm collected on 10 randomly selected spots of CQ-R6G substrate.

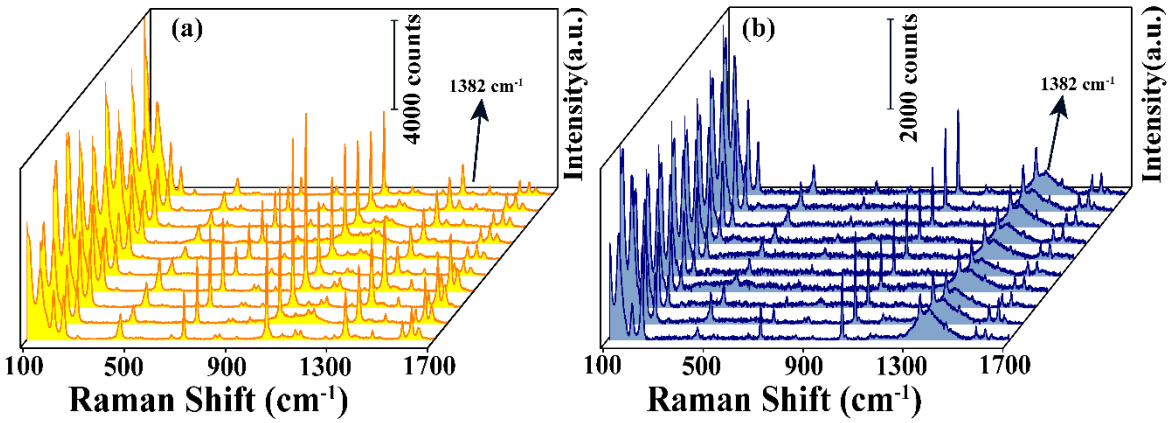

Figure 2.8 SERS spectra for 25 µM RhB (as in the precursor mixture) at laser excitation of (a) 633 nm and (b) 785 nm collected on 10 randomly selected spots of the CQ-RhB substrate.

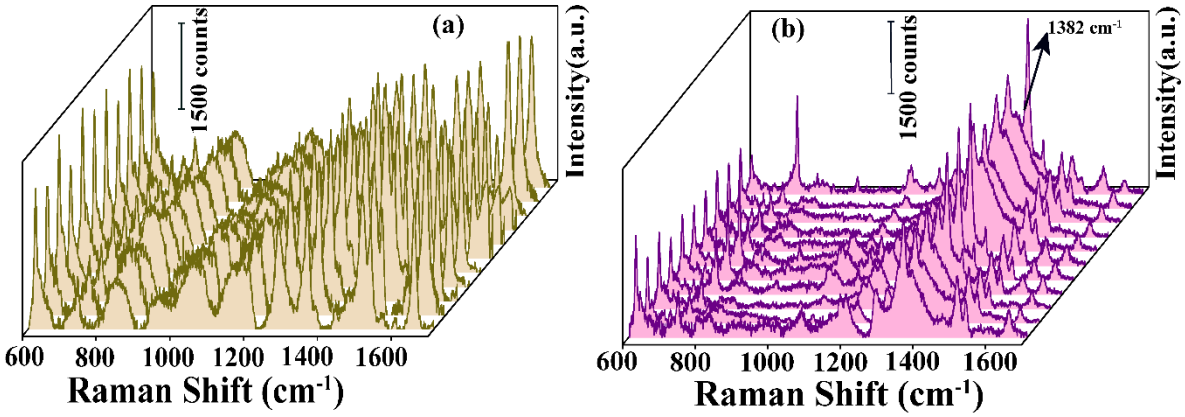

Figure 2.9 SERS spectra for 250 µM CuPA (as in the precursor mixture) at laser excitation of (a) 633 nm and (b) 785 nm collected on 10 randomly selected spots.

In addition, it was observed from Raman mapping of R6G, RhB, CuPA, R6G-RhB, and PA-BA analytes over the CQ substrate that their Raman peaks were highly enhanced compared to the analytes deposited over glass (Figure 2.10, 2.11, 2.12, 2.13 and 2.14 respectively). This implies CQ's efficiency as a SERS substrate and shows the reproducibility and uniformity of the Raman signal along the circumference of the deposited analyte (Figure 2.10-2.14). Thus, solid-state analyses of molecules on the surface of a molecular microcrystal could be considered a robust method for recording molecular-specific SERS.

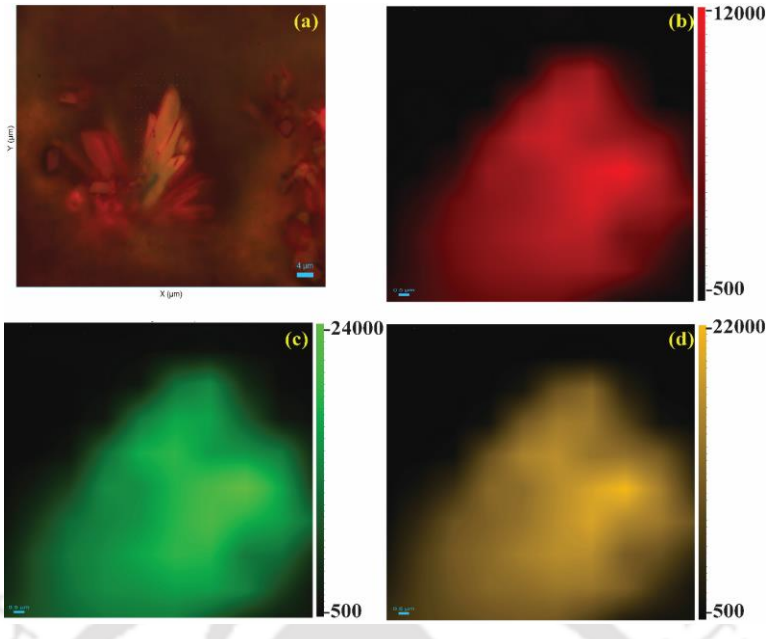

Figure 2.10 Raman intensity mapping of R6G on CQ as SERS substrate. (a) Image of mapping region. (b−d) Intensity profiles of the characteristic Raman peaks of R6G occurring at 611, 1361, and 1505 cm^{-1}, respectively.

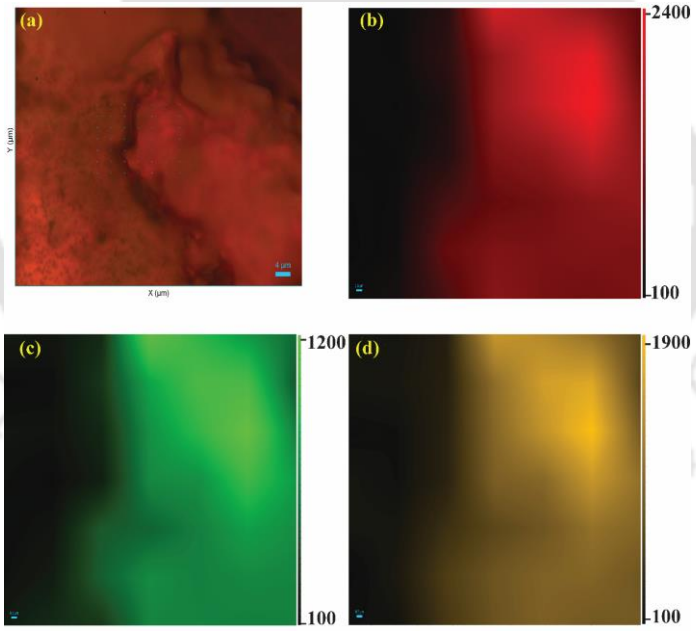

Figure 2.11 Raman intensity mapping of RhB on CQ as SERS substrate. (a) Image of mapping region. (b−d) Intensity profile of the characteristic Raman peaks of RhB occurring at 621, 1184, and 1529 cm^{-1}, respectively.

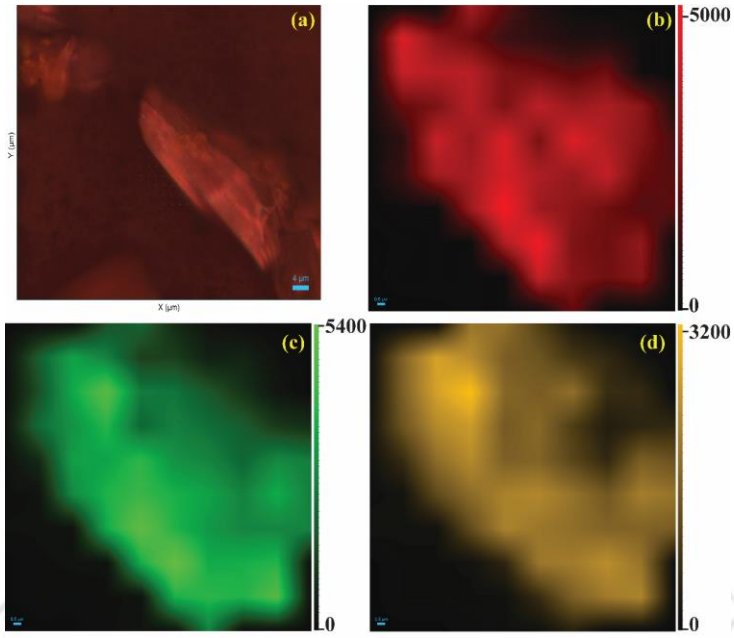

Figure 2.12 Raman intensity mapping of CuPA (in-situ generated) on CQ as SERS substrate. (a) Image of mapping region. (b−d) intensity profile of the Raman peaks at 103, 142, and 1034 cm^{-1}, respectively.

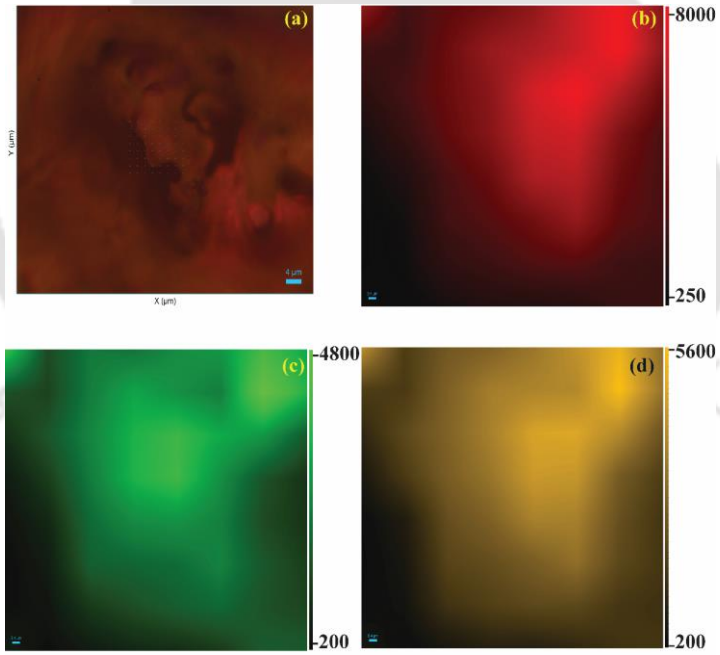

Figure 2.13 Raman intensity mapping of R6G-RhB mixture on CQ as SERS substrate. (a) Image of mapping region. (b−d) intensity profile of the Raman peaks at 611, 623, and 1085 cm^{-1}, respectively.

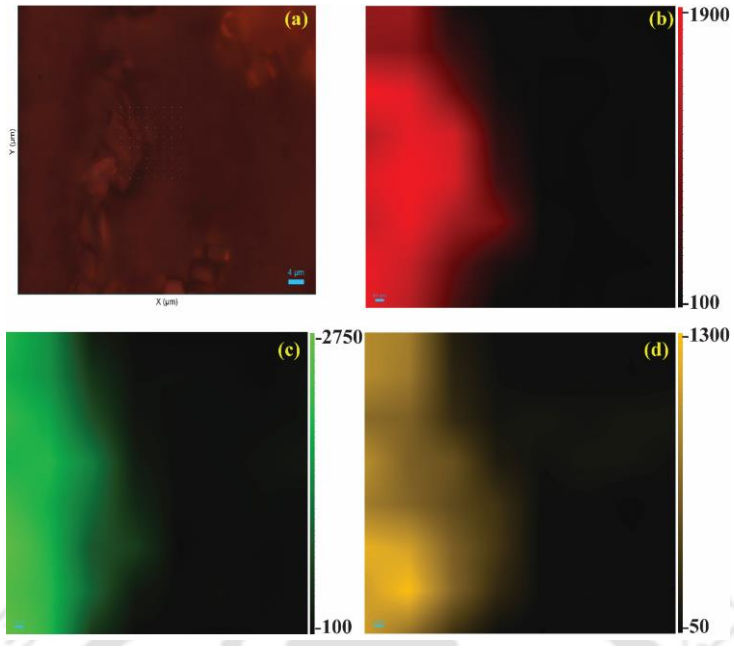

Figure 2.14 PA-BA mixture Raman intensity mapping on CQ as a SERS substrate. (a) Raman mapping region image. (b-d) Raman intensity profile with peaks at 103, 142, and 1034 cm^{-1}, respectively.

Results presented above strongly indicated that the Raman signal enhancement on the surface of the microcrystals could be correlated with the absorption spectrum of the crystals. For example, stronger signals for R6G, CuPA and RhB at 785 nm laser excitation as compared to those at 633 nm indicated that the absorption due to the crystals, in the near infrared region, were primarily responsible for the enhancement. Now, there could be two plausible mechanisms by which the enhancement was achieved. The EM enhancement that might have originated from the delocalized electrons of crystallized molecules giving rise to plasmons or excitons in the presence of radiation. On the other hand, the same delocalized electrons might give rise to facile charge transfer to the analytes in the presence of radiation i.e., the chemical (CHEM) mechanism leading to the strong enhancement in the Raman scattering. Both of the above mechanisms would require strong absorption of radiation in the region of wavelengths exhibiting extraordinary Raman activity.

2.2.2 DFT Calculations and Mechanism of SERS

As discussed earlier, the excellent EF for SERS of molecules observed on the substrate's surface is due to a combination of EM,[29-31] i.e., surface plasmon activation, and CHEM[32-34] pathway in which the probe molecules and the microcrystalline substrates can exchange electrons in both the ground and excited electronic states.

In order to reveal the origin of surface plasmon resonance in the CQ microcrystals and the unusual plasmonic property, we pursued electronic structure calculation of the CQ micro-crystal. Firstly, we have correlated the charge transfer property of CQ with different analytes by optimizing its single unit cell in Gaussian 16 code using cam-B3LYP/gen DFT functional. From the optimized structure, three-dimensional (3D) visualization of the electrostatic potential map showed high density of electrons delocalized throughout the CQ microcrystal (Figure 2.15a) as symbolized by the red colour. Importantly, the energy levels of the LUMO of the crystal's unit cell and the LUMOs of the R6G, RhB and CuPA closely match with each other (Figure 2.15b). This supports a favourable a photo-induced charge transfer in the excited states as R6G, RhB and CuPA are deposited over the crystal.

Secondly, the UV-Vis DRS spectra revealed two notable intra-band transitions inside CQ crystal, which appeared at 625 nm and 725 nm, respectively. In CQ microcrystal, bands A and B correspond to the energy levels of -4.87 eV and -4.59 eV, respectively, from which eV). transitions at 625 nm (1.98 eV) and 725 nm (1.71 eV) could occur to the LUMO of CQ (-2.88 eV). These bands can transport electrons into the LUMO of target molecules when excited by the laser of appropriate wavelength.[35,36]

In the instance of RhB, the energy difference between the A band and the RhB's LUMO (being positioned at -3.23 eV) i.e., 1.64 eV, to some extent matched with laser stimulation at 785 nm (1.58 eV) (Figure 2.15b). Whereas for R6G, the energy gaps between LUMO (-3.4 eV) and both the A and B bands, which are 1.47 eV and 1.2 eV respectively, correlate with 785 nm (energy eV) laser excitation, allowing for easy photo-induced charge transfer to LUMO and hence greater Raman peak amplification. The interaction is largely Coulombic in CuPA, and the energy difference between B band and LUMO (being positioned at -2.7 eV) is 1.68eV, which is close to that of the 785 nm laser excitation. Another factor to consider is the strong dipole-dipole interaction of polar complexes like CuPA, which results in an enhanced electron-transition probability and hence an amplified Raman signal.[37-38] These energy gaps are particularly large for BA and do not correlate with 785 nm laser excitation. The energy mismatch is more significant in the case of 633 nm laser excitation. Even then, the excitation energy is adequate for charge transfer from the A and B bands to the higher LUMO of the target molecule, inducing weak Raman signal amplification. Form the band structure analysis, it can be concluded that efficient charge transfer transitions are taking place at 785 nm laser excitation as compared to 633 nm laser, thus, resulting in better enhancement for 785 nm laser excitation.

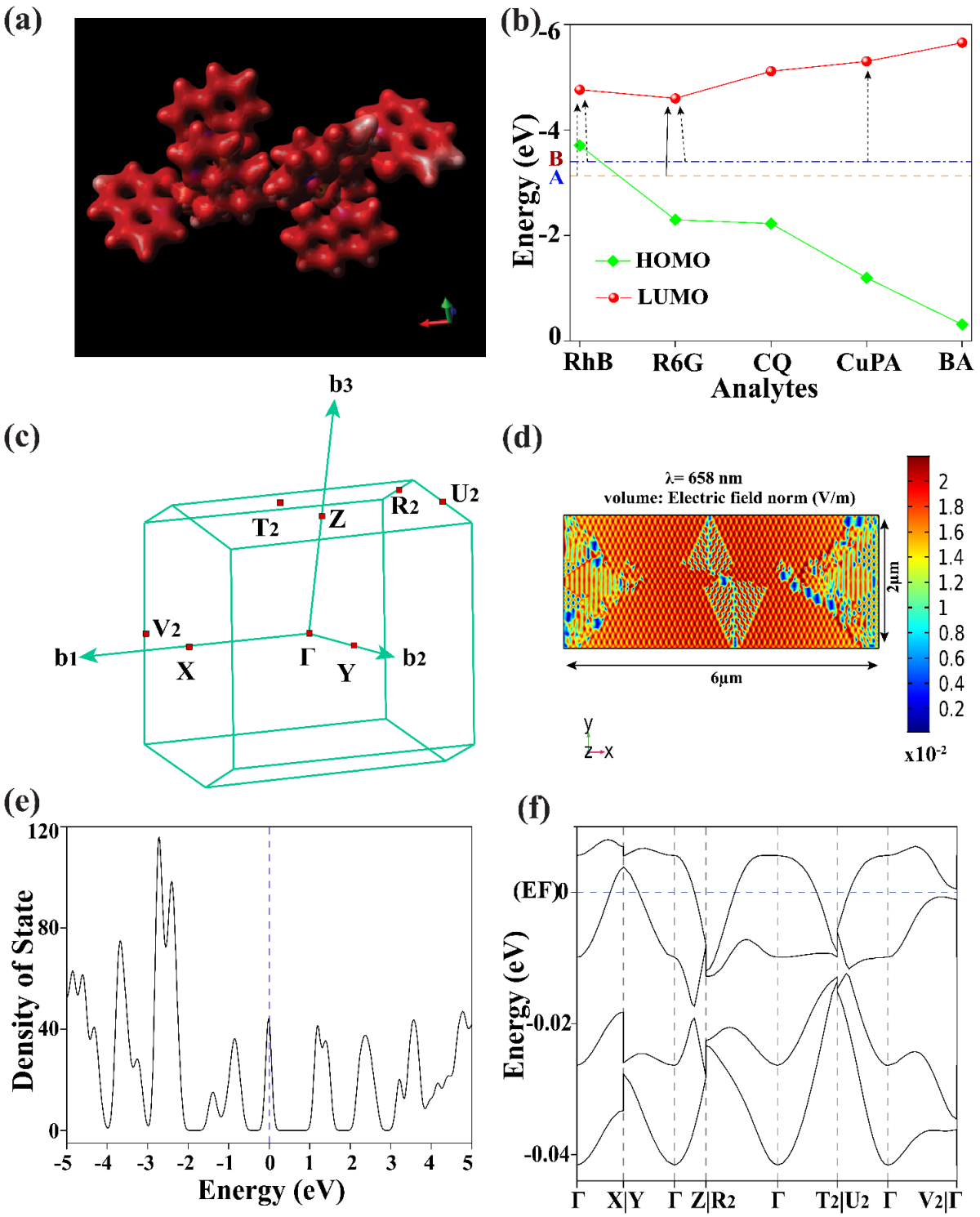

Figure 2.15 (a) Electrostatic potential map (ESP) of CQ unit cell defining highly delocalized electron density throughout the crystal. Red color in the ESP map expound the high electron dense region in the crystal. (b) HOMO-LUMO energy gap diagram of RhB, R6G, CuPA, and BA in comparison with unit cell HOMO-LUMO gap of CQ microcrystal. (c) CQ's first Brillouin zone and K-points with high symmetry. (d) Volume plot of simulated scattered electric field distribution of CQ at 658 nm excitation. (e) Density of states plot of CQ microcrystals. (f) Electronic band structure plot of CQ.

The electromagnetic scattered field distribution in three dimensions of CQ materials in the

presence of 658 nm light excitation has been calculated in COMSOL Multiphysics using the optical constants n and k obtained from ellipsometry. It is noticed that the simulated field of CQ was appropriately dispersed and present all over the crystal surface and thus could provide electromagnetic amplification in the presence of light (Figure 2.15d).[39] As the CQ has moderate absorbance in the excitation wavelength, the impedance boundary condition has been imposed and the incidence beam orientation has been assigned as the z direction to simulated the field.

DFT based calculations of the electronic band structure and density of states, in particular, showed that bulk CQ ought to be metallic in nature. For example, calculations of the electronic band structure revealed that the Fermi energy in CQ is located in a partly filled delocalized band (Figure 2.15e). Additionally, the density of states calculations (Figure 2.15e) indicated that Fermi energy is situated in a widely scattered 0.68 eV (-0.34 to +0.34 eV) band with 40 energy states per electron-volt per unit volume.

The electronic band structure of a substance specifies the spectrum of energy that an electron is restricted or allowed to have. Figure 2.15f depicts the electronic band structures of bulk CQ plotted along the high symmetry sites in the first Brillouin zone. Bands crossing the Fermi level in the Γ−X|Y− Γ, Z|R2− Γ and T2|U2− Γ directions in CQ, indicate the metallic nature of the solids. Importantly, bands cross the Fermi level both in-plane and out-of-plane, implying that the bulk materials will be metallic along the three crystallographic axes. Although band crossing in Γ−V2|Γ direction does not reach beyond the Fermi level having a band gap of 0.0012eV; hence in this direction CQ behaves like an indirect band semiconductor.[40,41] The electronic structures of CQ microcrystals might stem from the delocalization of π-electron throughout the stacked structure. Thus, high metallicity accompanied by such high density of delocalized electrons give rise to surface plasmon resonance in the visible and near infrared regions of electromagnetic spectrum. The calculations indicated the potential of microcrystalline materials with highly delocalized electrons for applications in plasmonics.

2.3 Conclusions

In summary, we have demonstrated that π -conjugated electron rich metallic microcrystals of CQ exhibited extraordinary SERS activity. The appearance of a plasmonic band in UV-Vis DRS spectra of the microcrystals in the NIR region (725 nm) helped probe analyte molecules - being deposited on their surfaces through Raman signal enhancements using 785 nm laser excitations. The CQ microcrystals showed excellent EFs of 28372±1953 for R6G, 13407±1969 for RhB and 12816±900 for CuPA. The SERS property was explained based on a combination

of EM and CHEM enhancements, as interpreted through gas phase and solid state DFT calculations. Systems with distinct plasmonic bands in the visible region of wavelengths, metallic property along all three crystallographic axes and a high degree of photo-induced charge transfer are rare and have great significance in plasmonics. The π-conjugated microcrystals used herein are especially attractive as they are easy to synthesize through environmental-friendly method, cost-effective, and their molecular nature offers a high degree of tunability of physical properties. We have also demonstrated that Raman signals of binary mixtures can have analyte specific enhancements, thus providing opportunity for mole-specific detections. The molecular nature of the substrate not only offers a novel material for SERS but also the repertoire of chemistry for tuning electronic band structures of microcrystals to match those of the intended analytes by adjusting the metal centers and different π-conjugated aromatic rings. This new SERS substrate may add richness to the understanding of chemistry of molecular interactions, catalysis and mass transport.

Reference

1. Frisch, M. J.; Trucks, G. W.; Schlegel, H. B.; Scuseria, G. E.; Robb, M. A.; Cheeseman, J. R.; Scalmani, G.; Barone, V.; Petersson, G. A.; Nakatsuji, H., et al. *Gaussian 16 Rev. C.01*, Wallingford, CT, **2016**.
2. Yanai, T.; Tew, D. P.; Handy, N. C., A new hybrid exchange–correlation functional using the Coulomb-attenuating method (CAM-B3LYP). *Chem. Phys. Lett.* **2004,** *393* (1), 51-57.
3. Giannozzi, P.; Baroni, S.; Bonini, N.; Calandra, M.; Car, R.; Cavazzoni, C.; Ceresoli, D.; Chiarotti, G. L.; Cococcioni, M.; Dabo, I., et al. QUANTUM ESPRESSO: a modular and open-source software project for quantum simulations of materials, *J. Phys.: Condens. Matter* **2009,** *21* (39), 395502.
4. Adar, F.; Lee, E.; Mamedov, S.; Whitley, A., Experimental Evaluation of the Depth Resolution of a Raman Microscope. *Microscopy and Microanalysis* **2010,** *16* (S2), 360-361.
5. Sun, H.; Cong, S.; Zheng, Z.; Wang, Z.; Chen, Z.; Zhao, Z., Metal-Organic Frameworks as Surface Enhanced Raman Scattering Substrates with High Tailorability. *J. Am. Chem. Soc.* **2019,** *141* (2), 870-878.
6. Wang, J.; Yang, Y.; Li, H.; Gao, J.; He, P.; Bian, L.; Dong, F.; He, Y., Stable and tunable plasmon resonance of molybdenum oxide nanosheets from the ultraviolet to the

near-infrared region for ultrasensitive surface-enhanced Raman analysis. *Chem. Sci.* **2019,** *10* (25), 6330-6335.

7. Perdew, J. P.; Yue, W., Accurate and simple density functional for the electronic exchange energy: Generalized gradient approximation. *Phys. Rev. B, Condens Matter.* **1986,** *33* (12), 8800-8802.
8. Perdew, J. P.; Ruzsinszky, A.; Csonka, G. I.; Vydrov, O. A.; Scuseria, G. E.; Constantin, L. A.; Zhou, X.; Burke, K., Restoring the density-gradient expansion for exchange in solids and surfaces. *Phys. Rev. lett.* **2008,** *100* (13), 136406.
9. Yanai, T.; Tew, D. P.; Handy, N. C., A new hybrid exchange–correlation functional using the Coulomb-attenuating method (CAM-B3LYP). *Chem. Phys. Lett.* **2004,** *393* (1), 51-57.
10. Rassolov, V. A.; Ratner, M. A.; Pople, J. A.; Redfern, P. C.; Curtiss, L. A., 6-31G* basis set for third-row atoms. *J. Comput. Chem.* **2001,** *22* (9), 976-984.
11. Roy, L. E.; Hay, P. J.; Martin, R. L., Revised Basis Sets for the LANL Effective Core Potentials. *J. Chem. Theory Comput* **2008,** *4* (7), 1029-1031.
12. Becke, A. D., A new mixing of Hartree–Fock and local density-functional theories. *J. Chem. Phys.* **1993,** *98* (2), 1372-1377.
13. Lee, C.; Yang, W.; Parr, R. G., Development of the Colle-Salvetti correlation-energy formula into a functional of the electron density. *Phys. Rev. B, Condens Matter* **1988,** *37* (2), 785-789.
14. Blaudeau, J.-P.; McGrath, M. P.; Curtiss, L. A.; Radom, L., Extension of Gaussian-2 (G2) theory to molecules containing third-row atoms K and Ca. *J. Chem. Phys.* **1997,** *107* (13), 5016-5021.
15. Heyd, J.; Scuseria, G. E.; Ernzerhof, M., Erratum: "Hybrid functionals based on a screened Coulomb potential". *J. Chem. Phys.* **2006,** *124* (21), 219906.
16. Yusuf, T. L.; Oladipo, S. D.; Zamisa, S.; Kumalo, H. M.; Lawal, I. A.; Lawal, M. M.; Mabuba, N., Design of New Schiff-Base Copper(II) Complexes: Synthesis, Crystal Structures, DFT Study, and Binding Potency toward Cytochrome P450 3A4. *ACS Omega* **2021,** *6* (21), 13704-13718.
17. Siqueira, J. D.; de Pellegrin, S. F.; Dos Santos, S. S.; Iglesias, B. A.; Piquini, P. C.; Arantes, L. P.; Soares, F. A.; Chaves, O. A.; Neves, A.; Back, D. F., SOD activity of new copper II complexes with ligands derived from pyridoxal and toxicity in Caenorhabditis elegans. *J. Inorg Biochem* **2020,** *204*, 110950.

18. Monzon, L. M. A.; Burke, F.; Coey, J. M. D., Optical, Magnetic, Electrochemical, and Electrical Properties of 8-Hydroxyquinoline-Based Complexes with Al3+, Cr3+, Mn2+, Co2+, Ni2+, Cu2+, and Zn2+. *J. Phys. Chem. C* **2011,** *115* (18), 9182-9192.
19. Palenik, G., The structure of coordination compounds. II. The crystal and molecular structure of the [beta] form of anhydrous copper 8-hydroxyquinolinate. *Acta Crystallographica* **1964,** *17* (6), 687-695.
20. Momma, K.; Izumi, F., VESTA 3 for three-dimensional visualization of crystal, volumetric and morphology data. *J. Appl. Cryst.* **2011,** *44* (6), 1272-1276.
21. Tuschel, D., Why are the Raman spectra of crystalline and amorphous solids different? **2017,** *32*, 26-33.
22. Zhong, F.; Wu, Z.; Guo, J.; Jia, D., Porous Silicon Photonic Crystals Coated with Ag Nanoparticles as Efficient Substrates for Detecting Trace Explosives Using SERS. *Nanomaterials (Basel)* **2018,** *8* (11).
23. Lin, S.; Hasi, W.-L.-J.; Lin, X.; Han, S.-q.-g.-w.; Lou, X.-T.; Yang, F.; Lin, D.-Y.; Lu, Z.-W., Rapid and sensitive SERS method for determination of Rhodamine B in chili powder with paper-based substrates. *Anal. Methods* **2015,** *7* (12), 5289-5294.
24. Zhang, J.; Li, X.; Sun, X.; Li, Y., Surface Enhanced Raman Scattering Effects of Silver Colloids with Different Shapes. *J. Phys. Chem. B* **2005,** *109* (25), 12544-12548.
25. Wang, J.; Yang, Y.; Li, H.; Gao, J.; He, P.; Bian, L.; Dong, F.; He, Y., Stable and tunable plasmon resonance of molybdenum oxide nanosheets from the ultraviolet to the near-infrared region for ultrasensitive surface-enhanced Raman analysis. *Chem. Sci.* **2019,** *10* (25), 6330-6335.
26. Adar, F.; Lee, E.; Mamedov, S.; Whitley, A., Experimental Evaluation of the Depth Resolution of a Raman Microscope. *Microscopy and Microanalysis* **2010,** *16* (S2), 360-361.
27. Watanabe, H.; Hayazawa, N.; Inouye, Y.; Kawata, S., DFT Vibrational Calculations of Rhodamine 6G Adsorbed on Silver: Analysis of Tip-Enhanced Raman Spectroscopy. *J. Phys. Chem. B* **2005,** *109* (11), 5012-5020.
28. Wang, W.; Yin, Y.; Tan, Z.; Liu, J., Coffee-ring effect-based simultaneous SERS substrate fabrication and analyte enrichment for trace analysis. *Nanoscale* **2014,** *6* (16), 9588-9593.
29. Ausman, L. K.; Schatz, G. C., On the importance of incorporating dipole reradiation in the modeling of surface enhanced Raman scattering from spheres. *J Chem Phys* **2009,** *131* (8), 084708.

30. Chulhai, D. V.; Chen, X.; Jensen, L., Simulating Ensemble-Averaged Surface-Enhanced Raman Scattering. *J. Phys. Chem. C* **2016,** *120* (37), 20833-20842.
31. Ansar, S. M.; Li, X.; Zou, S.; Zhang, D., Quantitative Comparison of Raman Activities, SERS Activities, and SERS Enhancement Factors of Organothiols: Implication to Chemical Enhancement. *J Phys. Chem. Lett.* **2012,** *3*, 560-565.
32. Morton, S. M.; Jensen, L., Understanding the Molecule−Surface Chemical Coupling in SERS. *J. Am. Chem. Soc* **2009,** *131* (11), 4090-4098.
33. Valley, N.; Greeneltch, N.; Van Duyne, R. P.; Schatz, G. C., A Look at the Origin and Magnitude of the Chemical Contribution to the Enhancement Mechanism of Surface-Enhanced Raman Spectroscopy (SERS): Theory and Experiment. *J. Phys. Chem. Lett.* **2013,** *4* (16), 2599-2604.
34. Birke, R. L.; Lombardi, J. R.; Saidi, W. A.; Norman, P., Surface-Enhanced Raman Scattering Due to Charge-Transfer Resonances: A Time-Dependent Density Functional Theory Study of Ag13-4-Mercaptopyridine. *J. Phys. Chem. C* **2016,** *120* (37), 20721-20735.
35. Lombardi, J. R.; Birke, R. L., Theory of Surface-Enhanced Raman Scattering in Semiconductors. *J. Phys. Chem. C* **2014,** *118* (20), 11120-11130.
36. Hilty, F. W.; Kuhlman, A. K.; Pauly, F.; Zayak, A. T., Raman Scattering from a Molecule–Semiconductor Interface Tuned by an Electric Field: Density Functional Theory Approach. *J. Phys. Chem. C* **2015,** *119* (40), 23113-23118.
37. Otto, A., The 'chemical' (electronic) contribution to surface-enhanced Raman scattering. *J. Raman Spectrosc.* **2005,** *36* (6-7), 497-509.
38. Baik, S. Y.; Cho, Y. J.; Lim, Y. R.; Im, H. S.; Jang, D. M.; Myung, Y.; Park, J.; Kang, H. S., Charge-Selective Surface-Enhanced Raman Scattering Using Silver and Gold Nanoparticles Deposited on Silicon–Carbon Core–Shell Nanowires. *ACS Nano* **2012,** *6* (3), 2459-2470.
39. Zhou, Q.; Hu, J.; Liang, C.; Chen, X.; Liu, D.; Ma, J., Study on electric field distribution in cylindrical metal silo containing charged polyethylene powder. *Powder Technology* **2019,** *353*, 145-155.
40. Dou, J. H.; Sun, L.; Ge, Y.; Li, W.; Hendon, C. H.; Li, J.; Gul, S.; Yano, J.; Stach, E. A.; Dinca, M., Signature of Metallic Behavior in the Metal-Organic Frameworks M3(hexaiminobenzene)2 (M = Ni, Cu). *J. Am. Chem. Soc.* **2017,** *139* (39), 13608-13611.
41. Cheng, H.; Wen, M.; Ma, X.; Kuwahara, Y.; Mori, K.; Dai, Y.; Huang, B.; Yamashita, H., Hydrogen Doped Metal Oxide Semiconductors with Exceptional and Tunable

Localized Surface Plasmon Resonances. *Journal of the American Chemical Society* **2016,** *138* (29), 9316-9324.

Chapter 3

Molecular Cooperativity in the Intense Raman Scattering on the Surface of an Organic Molecular Microcrystal

Herein we suggest and demonstrate that microcrystals of small organic molecular crystals are novel platforms for SERS. In particular, they offer molecule-specificity and co-operativity in Raman scattering. The Raman enhancement in the organic crystal was observed mainly due to photo induced charge transfer and selective chemical interaction. For a test case, we have studied the extraordinary SERS behavior of π-conjugated TA microcrystals. The UV-vis diffuse reflectance spectra (DRS) of the solid microcrystalline TA consisted of a strong and broad peak starting from 400 to 850 nm with a maximum close to 800 nm. This helped in probing the analyte molecules deposited on the crystal surface, using laser excitations at 785 nm. The EF of TA crystals was observed to have been as high as (>10^6), which is equivalent to the EFs of coinage metals with no "hot spots" and recently discovered semiconductors. Further, we observed molecular cooperativity in the signal enhancement or reduction when two molecules such as rhodamine 6G (R6G) and rhodamine B (RhB), R6G and eosin (EY) or RhB and EY were simultaneously deposited on the crystal surfaces. The density functional theory (DFT) based electronic structure of the crystals, the ultraviolet photoelectron spectroscopy study, and the concept of hybrid orbitals through noncovalent interactions in the combined system give insight into the molecule-specific intense SERS performance. A quantum mechanics-based noncovalent interaction reduced density gradient (NCI-RDG) approach was used to determine

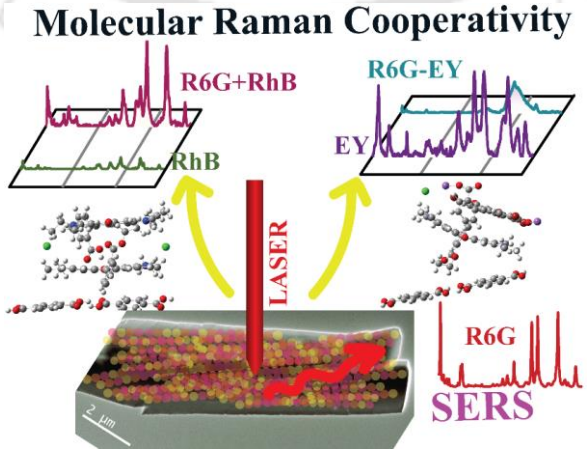

[*Adv. Optical Mater.* 2024, 12, 2301776]- reproduced with permission from *John Wiley and Sons.

the types of weak interactions causing the cooperativity in the case of a binary mixture of dyes.[1] Our findings reflect a significant exploratory development in organic SERS and help initiate the molecular design of more delicate versatile SERS substrates and also showed molecular specificity and cooperativity in non-covalent interactions for organic SERS substrate.

3.1 Materials and Methods

3.1.1 Materials

Terephthalic acid (98%, 166.13 g mol^{-1}), rhodamine-6G (R6G) (98%, 479 g mol^{-1}), rhodamine-B (RhB), (≥ 95%, 479 g mol^{-1}), eosin yellowish (EY),(≥ 85%, 691.85 g mol^{-1}), picric acid (PA),(moistened with water, ≥ 98%, 229.1 g mol^{-1}) and methanol (99%) were bought from Merck. Without additional purification, all materials were utilized. The experiments were performed with Elix grade water obtained from a MilliQ filtration system.

3.1.2 Terephthalic acid micro-crystal

Micro-crystalline TA was purchased from Sigma-Aldrich (CAS No. 100-21-0) and was utilized as supplied.

3.1.3 Characterization

Raman spectra were collected with a Horiba LabRAM HR-800 microscope Raman system equipped with 785 nm laser. Baseline corrections were carried out using LabSpec 6 software available with the Raman instrument. A JEOL JEM-2100F FETEM apparatus (acceleration voltage of 200 kV) was used to perform field emission transmission electron microscopy (TEM). The samples' powder X-ray diffraction (XRD) patterns were examined using a Rigaku TTRAX III diffractometer with a CuK source (λ = 1.54 Å). A PerkinElmer Lambda 750 UV-Vis-NIR spectrometer helped measure the UV-Vis diffuse reflectance spectrum. The field emission scanning electron microscopy (FESEM) study was performed using Gemini 300 equipment. PHI 5000 Versa Probe III, ULVAC-PHI, Inc was employed for ultraviolet photoelectron spectroscopy (UPS) studies. All the UPS data used here were taken under -5 V bias.

3.1.4 Raman measurement

The SERS characteristics on TA microcrystals were examined using rhodamine 6G (R6G), rhodamine B (RhB) and eosin yellowish (EY) as analyte molecules at excitation wavelengths of 785 nm. Typically, a stock solution either of 5×10^{-2} M R6G, RhB and EY was initially

prepared, which was added to the TA dispersion (in 2:1 methanol/water) such that the final concentration of dye became 25 µM for R6G as well as RHB and 50 µM for EY. The mixture was then sonicated for 30 min and stirred at dark for 2 hr. For the sample preparation, 20 µL each of the mixtures was drop-cast over a cleaned glass slide and dried at 40 °C for 15 min. Raman spectra were subsequently recorded in a high-resolution confocal Raman spectrometer, Horiba LabRAM HR-800, that was equipped with 785 nm laser. For 785 nm laser, 100 ×L objective lens and a laser power of 100 mW were used to collect the Raman spectra, with an acquisition time of 20 s at diffraction grating of 600 gr/mm. For TA-PA and Bulk PA samples 50 ×L objective lens was employed. Finally, for control experiments 20 µL of the suspension of 15 mM of R6G, 15 mM of RhB and 15 mM of EY, were drop-cast over cleaned glass slides and dried at 40 °C for 15 min. The Raman test conditions were the same as that described above for all the control samples. In 633nm laser excitation, 100 ×L objective lens and 0.01% for R6G, 0.1% for RhB, R6G-RhB mixture and 25% for EY of 18 mW laser power were used to collect the Raman spectra at diffraction grating of 600 gr/mm.

For cooperative SERS study equimolar mixture of dyes (R6G-RHB, R6G-EY and RhB-EY) were added to TA dispersion having individual dyes concentration of 25 µM.

3.1.5 Calculation of the enhancement factor (EF)

The EF was calculated according to the formula[2]

$$EF = (I_{SERS}/N_{SERS})/(I_{bulk}/N_{bulk}) \quad (1)$$

$$N_{SERS} = CVN_A A_{Raman}/A_{Sub} \quad (2)$$

$$N_{bulk} = \rho h A_{Raman} N_A/M \quad (3)$$

Where N_{SERS} and N_{bulk} denote the average numbers of analyte molecules present inside the scattering area of the SERS experiments for TA and bulk (area) Raman measurement and the I_{SERS} and I_{bulk} are the corresponding intensities of Raman scattering at a particular peak position. C represents the concentration of the analyte (when in the liquid mixture) in molarity, V is the drop cast volume of the mixture on the glass slide and N_A is the Avogadro number. A_{Raman} is the Raman scanning laser spot area. 20 µL of the analyte liquid mixtures when evaporated on the glass surface, were deposited as solid circular discs of diameter about 7.66 mm for R6G, 8 mm for RhB, 7.4 mm diameter for EY and 6.6 mm diameter for PA. The effective area of the substrate A_{Sub} was then calculated for the circler disc of the above can then be obtained. For the bulk, 15 mM R6G (Mol. Wt. =479 g/mol, ρ=1.26 g·cm^{-3}), 15 mM RhB

(Mol. Wt. =479 g/mol, ρ=0.79 g·cm^{-3}), 15 mM EY (Mol. Wt. =691.85 g/mol, ρ= 1.018 g·cm^{-3}) and 1mM PA (Mol. Wt. = 229.1g/mol, ρ= 1.76 g·cm^{-3}) were evaporated in glass slides similarly.

The confocal depth (h) of the laser beam was 12 µm for 785 nm laser.[3] N_{bulk} was calculated by Supporting equation 3 (as above).[4,5]

In quantitative assignment of cooperativity study for TA-R6G-RhB system, ratio of a particular peak for samples prepared as individual and mixture was taken into account, as the concentration was kept identical in both the cases. For all the binary mixture the liquid concentration of an individual dye was kept at 25µM.

3.1.6 Theoretical Calculations

The Quantum ESPRESSO programme suite was used to calculate the electronic structure.[6] The exchange-correlation function was calculated using PBEsol's generalized gradient approach (GGA).[7,8] The kinetic energy cut-off had been adjusted to 60 Ry for wavefunction evolution in the plane wave basis set. The charge density and potential electronic wave functions depended on kinetic energy. The system was first optimized using the "vc-relax" algorithm. The density of state computations have been done using the relaxed geometry.

Quantum chemical computations were performed using the Gaussian 16 series of programmes by using DFT to assess and determine the Raman signals and molecular orbital energies.[9] Tables S1 and S2 show functionals, and basis sets executed for every system. Crystal and all the hybrid structures were generated following which time-dependent density functional theory (TD-DFT) and noncovalent interaction reduced density gradient (NCI-RDG) calculations were carried out. Avogadro software was used to construct an electrostatic potential mapping by subsequent processing of the resultant file obtained by Gaussian 16 DFT computations.[10]

A quantum mechanics-based noncovalent interaction reduced density gradient (NCI-RDG) method was employed to quantify the weak interactions dictating the cooperativity in the SERS spectra of a binary mixture of dyes over the TA microcrystals. The structures of the host-crystal and dye complexes were quantum-mechanically optimized in the gas phase using DFT and they were then employed for further investigation. This study yields a scatter map (colour-filled iso-surface chart) using an iso-surface value of 0.7 and a preset colour range of 0.035 and 0.020. Here, the Multiwfn algorithm was utilised for analysis,[11,12] and the Visual Molecular Dynamics (VMD) package was used to analyse and visualise the simulated paths.[13]

3.1.7 Details of theoretical calculation

Table 3.1 Details of Structure optimisation using Gaussian 16 simulation code

Molecule	DFT level of theory	Basis set and core potentials
TA (12 molecule)	HSEH1PBE[14]	6-311++G(d,p)[15]
TA-R6G	M062X[16]	6-311G(d,p)
TA-RhB	M062X	6-311G(d,p)
TA-EY	M062X	6-311G(d,p)
TA-R6G-RHB	B3LYP[17,18]	6-31G(d,p)[19]
TA-R6G-EY	B3LYP	6-31G(d,p)

Table 3.2 Details for simulated Raman peak assignment using Gaussian 16 simulation code

Molecule	DFT level of theory	Basis set and core potentials
TA (2 molecule)	B3LYP	6-31++G(d,p)
PA	B3LYP	6-311++G(d,p)

3.2 Result and Discussion

All the experiments reported here were performed with the as-purchased TA microcrystals. The UV-vis spectrum of TA in DMF consisted of a peak appearing at 280 nm (Figure 3.1a).[20] That would mean a molecular HOMO-LUMO energy gap of 4.07 eV (tauc plot, Figure 3.12) . The TEM image of as obtained TA showed distinct rectangular-shaped microparticles with diameters of 20-30 μm (Figure 3.2a). FESEM images also revealed discrete rectangular-shaped particles of comparable dimensions (Figure 3.1b). Further, powder XRD pattern of the TA comprised multiple sharp peaks, demonstrating a well-ordered structure with high crystallinity (Figure 3.1c). The single crystal XRD measurement of recrystallised TA showed that it is a triclinic crystal with cell parameters: a = 3.77930, b = 6.47910, and c = 7.40400; and α = 82.9420°, β = 81.0060°, and γ = 88.9820° (Figure 3.2b), which matched the previous report.[21] TA crystals are known to have two polymorphic structures with triclinic unit cells, and space group P(-1). In both the forms, molecules are connected through hydrogen-bonded carboxyl

dimers into infinite chains. These chains form layers of two-dimensional structure through van der Waals and hydrogen bonding (C-H...O) interactions.[22]

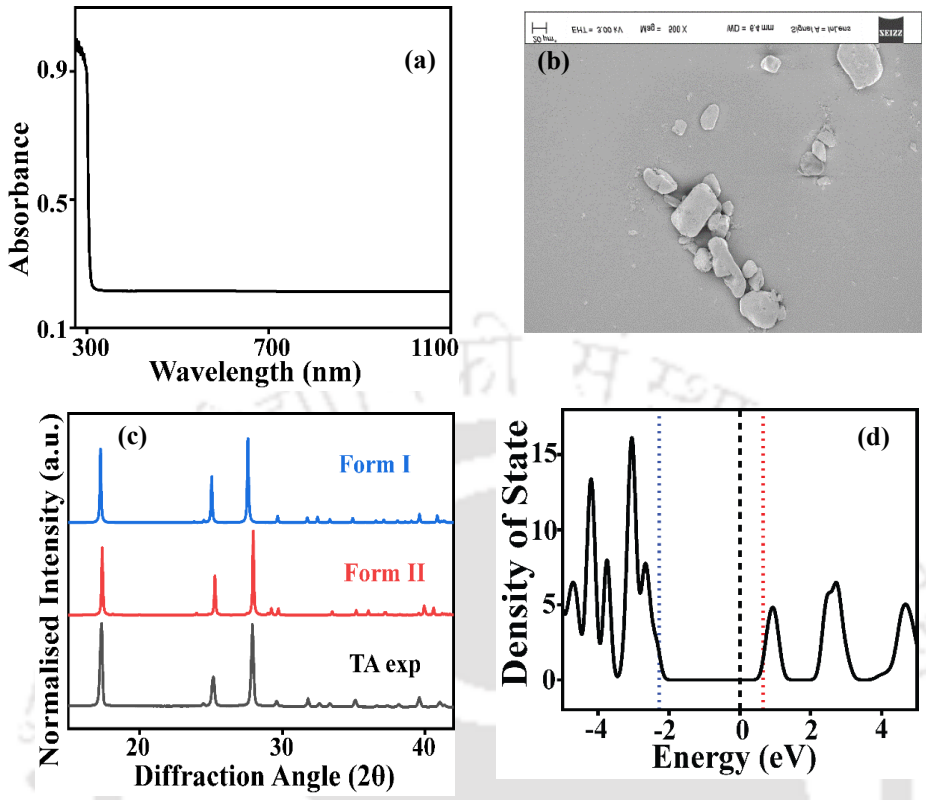

Figure. 3.1 (a) Absorbance spectra of TA in DMF (b) FESEM image of TA microcrystals (c) Powder-XRD of TA in comparison to the simulated patterns with Form-I and Form-II of the crystal. (d) Density of state plot for TA crystals.

The carbon to oxygen distances between the two layers are 3.79 and 3.42 ^{0}A in forms I and II, respectively. Based on the single crystal x-ray diffraction and powder XRD, it can be concluded that Form I is dominant here (Figure 3.1c, Table 3.3). Thus, the samples that we have used for further studies here were of TA microcrystals. The UV-vis diffuse reflectance spectrum of the solid TA microcrystals at room temperature comprised of a broad absorption starting from 400 nm with a maximum at around 800 nm (Figure 3.2c), which is far lower in energy than its molecular HOMO-LUMO energy gap. These low energy transitions can be attributed to the inter-band states that originated upon crystallization of the molecule. Solid-state DFT calculations of TA crystals, show a high energy fermi level, and the gap between the fermi level and the LUMO is 0.69 eV (Figure 3.1d). Further, lower energy inter-band states possibly originating from the chains of 2D carboxyl dimers having extensive H-bonding and van-der-walls networks help facilitate charge transfer that is useful for pursuing SERS, using the microcrystal as the substrate.

Table 3.3 hkl values and computed d spacing values calculated from the powder-XRD peaks of the as-purchased TA microcrystals (Figure 3.1c).

Diffraction angle (2θ)	Assigned hkl	Corresponding d-spacing (Å)
17.3	011	5.13
24.48	002	3.62
25.2	101	3.55
27.9	01-2	3.23
29.61	10-2	3.0
31.8	02-1	2.81
32.6	11-1	2.75
33.3	112	2.68
35.1	022	2.56
39.6	02-2	2.27
41.04	103	2.19

The significant changes in both the reflectance and absorbance spectra suggests that the optical gap was substantially narrowed by charge-transfer transition states similar to systems like TiO_2,[23] graphene,[24] organic crystals like benzil and benzophenone,[25] and other organic semiconductors.[26]

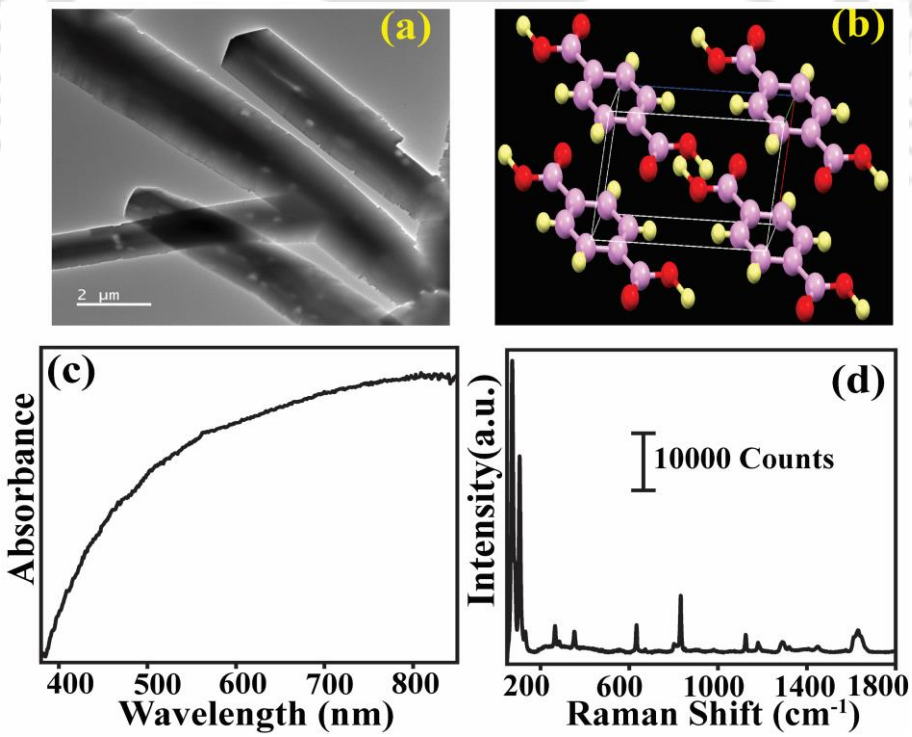

Figure 3.2 Characterization of TA microcrystals. (a) TEM image of TA microcrystals. (b) 3D-visualization of TA's Form I unit cell as obtained from single crystal XRD. (c) UV-Vis DRS spectrum of TA microcrystals. (d) Raman spectrum of TA microcrystals at a laser excitation of 785 nm.

The TA microcrystals were further studied with Raman spectroscopy using 785 nm laser excitation. The prominent vibrational transitions consisted of sharp peaks at 1632, 832, 632, 128, 104 and 70 cm^{-1} (Figure 3.2d). Notably, the most intense peak at 70 cm^{-1} is due to combined twisting vibration of ring and -COOH group and the peak at 832 cm^{-1} can be referred to as due to the combination of the ring (C-C-C and C-H) and -COOH group bending vibration (Table 3.4).[27] On the other hand, when TA crystals were dissolved in DMF solvent and then drop-cast on solid substrate, the Raman signal intensity was observed to have been weak. At the same time, the number of Raman peaks was also reduced (Figure 3.3), which suggested crystallization induced Raman signal enhancement (as observed above). The results indicated that the spatial arrangements of functional groups and long-range translational symmetry in TA microcrystals resulted in collective vibration, which had produced noticeable peaks with high signal-to-noise ratio. Furthermore, the inter-band states inside the crystals can absorb 785 nm laser light and create excitons, leading to the resonance Raman condition and thus, increasing the Raman scattering cross-section. The recorded peaks aligned well with the simulated ones for the compound that was performed using a Gaussian 16 code for carboxyl dimer (Table 3.4).

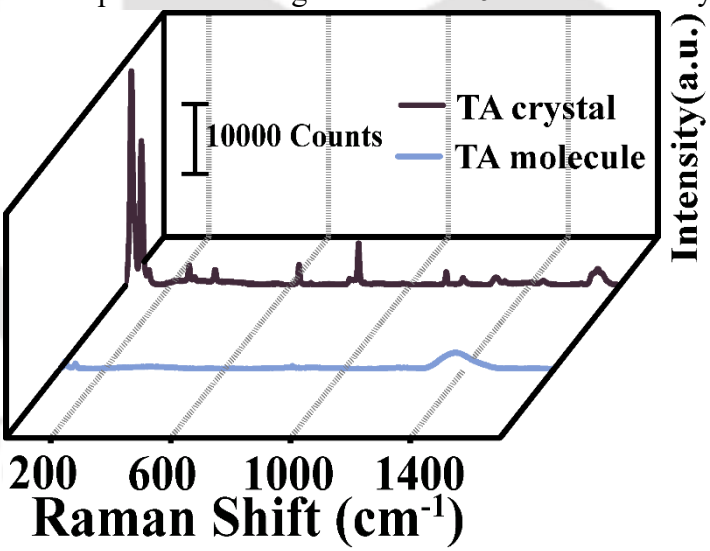

Figure 3.3 Raman spectra of TA deposited as a molecule from a DMF solution and microcrystals from a dispersion in water.

In other words, the experimental Raman peaks matched well with the simulated ones when we take two terephthalic acid molecule instead of single molecule during computational analysis.

The crystals were then examined for their capability and molecular specificity as efficient SERS substrates. R6G, RhB, EY and PA were chosen as analytes for determining the Raman enhancement over the microcrystals. As stated in the experimental section, the analyte molecules were mixed in a liquid medium with TA microcrystal dispersion under vigorous stirring condition, in order to co-deposit them on the microscope slides. Thus, 20 μL the mixtures were drop-cast on the

slides and the liquid was allowed to dry in the air prior to measurements. Furthermore, mapping for the TA-R6G Raman sample using FESEM-EDS revealed that the proportion of chlorine deposited outside the crystal was significantly higher than that over the crystal (Figure 3.4).

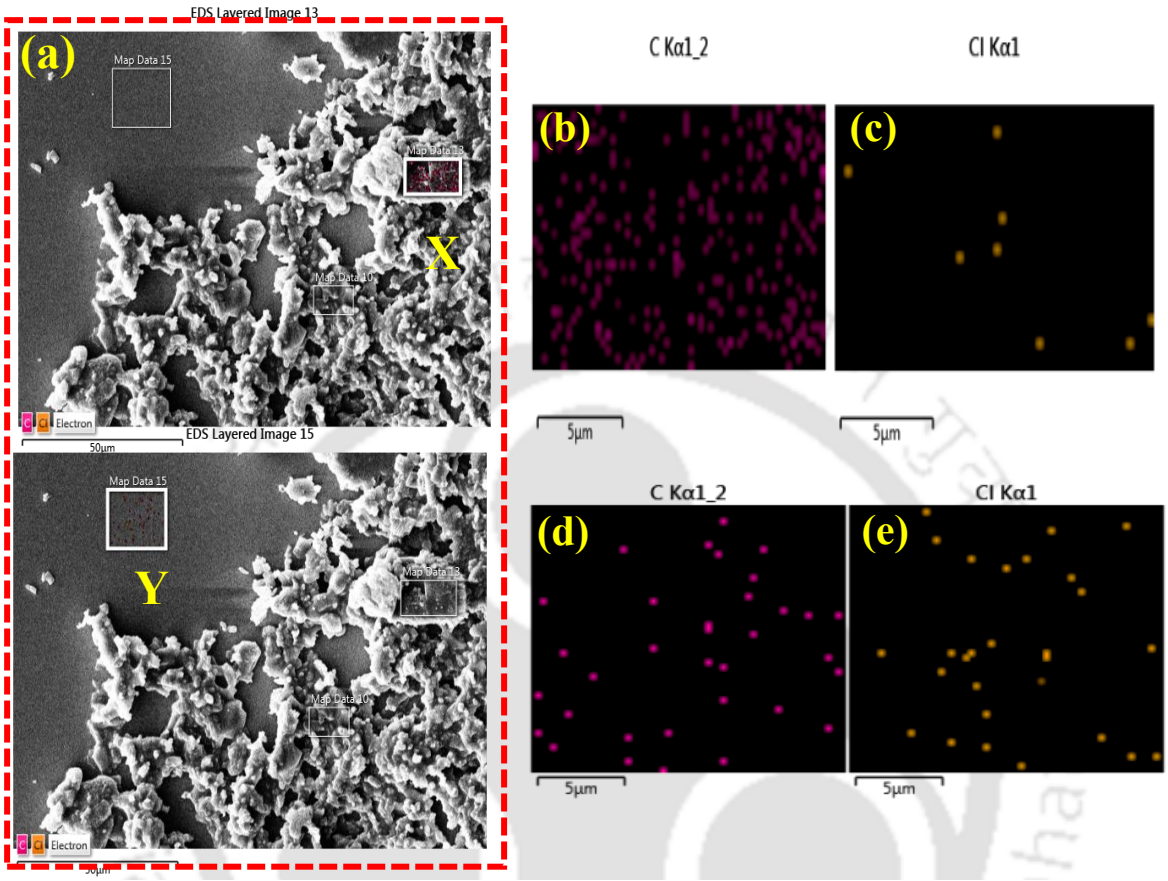

Figure. 3.4 FESEM-EDX mapping findings of a TA-R6G sample demonstrating chloride density, i.e., due to R6G deposited over the crystal. (a) FESEM image of the deposited TA microcrystals. The image areas for mapping through EDX are identified by the boxes. Box X represents mapping area over the crystals and Y represents mapping area outside the crystal region. (b, c) EDX mapping of the carbon and chlorine percentages, respectively, on the TA crystal sample in (a) over area X. (d,e) EDX mapping of the carbon and chlorine percentages, respectively, recorded in the region outside the deposited crystals in (a) for the region marked as Y.

This indicated that the analyte molecules were deposited more in the area outside the crystals as compared to the depositions upon them. However, the Raman signals due to R6G were clearly more intense over the crystals as compared to the same for the deposited on the glass slide (Figure 3.25).

3.2.1 SERS Performance

Figure 3.5a-d shows the SERS spectra of R6G, RhB, EY and PA analytes over microcrystals when excited with 785 nm laser probes. The selection of excitation wavelengths was dictated by the UV-vis absorption peak (at 800 nm) owing to inter-band transitions of microcrystalline TA substrates. The prominent Raman peaks of R6G were noticed at 1656, 1575, 1519, 1363, 1317, 1183, 1129, 1093, 779, and 611 cm^{-1}. In the case of RhB, the main vibrational signals

Table 3.4 Raman peak assignments of TA microcrystals. The calculated values were based on using gaussian 16 simulation code.

Raman shift (cm^{-1})		
Experimental	**Theoretical**	**Vibration mode**
1632	1688	$\delta(COH)+\nu(C\text{-}O)+\nu(C=C)_{ring}$
1613	1661	$\nu(C=C)_{ring}$
1450	1497	$\delta(OH)+\nu(C=O)+\nu(C=C)_{ring}$
1288	1322	$\rho(CH)_{ring} + \delta(HOC)$
1180	1192	$\delta(COH)+\nu(C\text{-}C) +\delta(HCC)_{ring}$
1124	1156	$\delta(HCC)_{ring} + \nu(C\text{-}O)$
832	830	$\delta(CCH)_{ring} +\delta(CCC)_{ring} + \delta(COO)+\delta(COH)$
632	644	$\delta(CCC)_{ring}$
350	327	$\nu(C=C)_{ring}$
264	273	δ(COO)in plane
128	113	δ(COO) out of plane
104	76	τ(ring C-H)+ δ(COO)
70	43	τ(ring + COOH)

$\nu(C=C)_{ring}$: stretching vibration of C=C of ring; **$\delta(HCC)_{ring}$:** C−H bending of ring; **$\nu(C=O)$:** stretching vibration of C=O; **$\delta(CCC)_{ring}$:** C−C−C bending vibration of ring;; **δ(COO) :** C-O-O bending vibration; **ν(C−O) :** stretching vibration of C−O; **τ(Ring) :** Ring twisting.

were recorded at 1648, 1529, 1506, 1358, 1280, 1197, 1077, 735 and 621 cm^{-1}. For EY, strong vibrational Raman signals were originated at 1626, 1576, 1509, 1349, 1285, 1182, 964, 833, 715, 641 and 634 cm^{-1}. The key vibrational signals in the case of PA were observed at 1343, 1277, 1177, 1089, 941 and 830 cm^{-1}. Raman signal assessments of all of the probe molecules deposited over the crystals are represented in Table 3.5, 3.6, 3.7 and 3.8. [28-34] The results, which showed considerable signal-to-noise increases

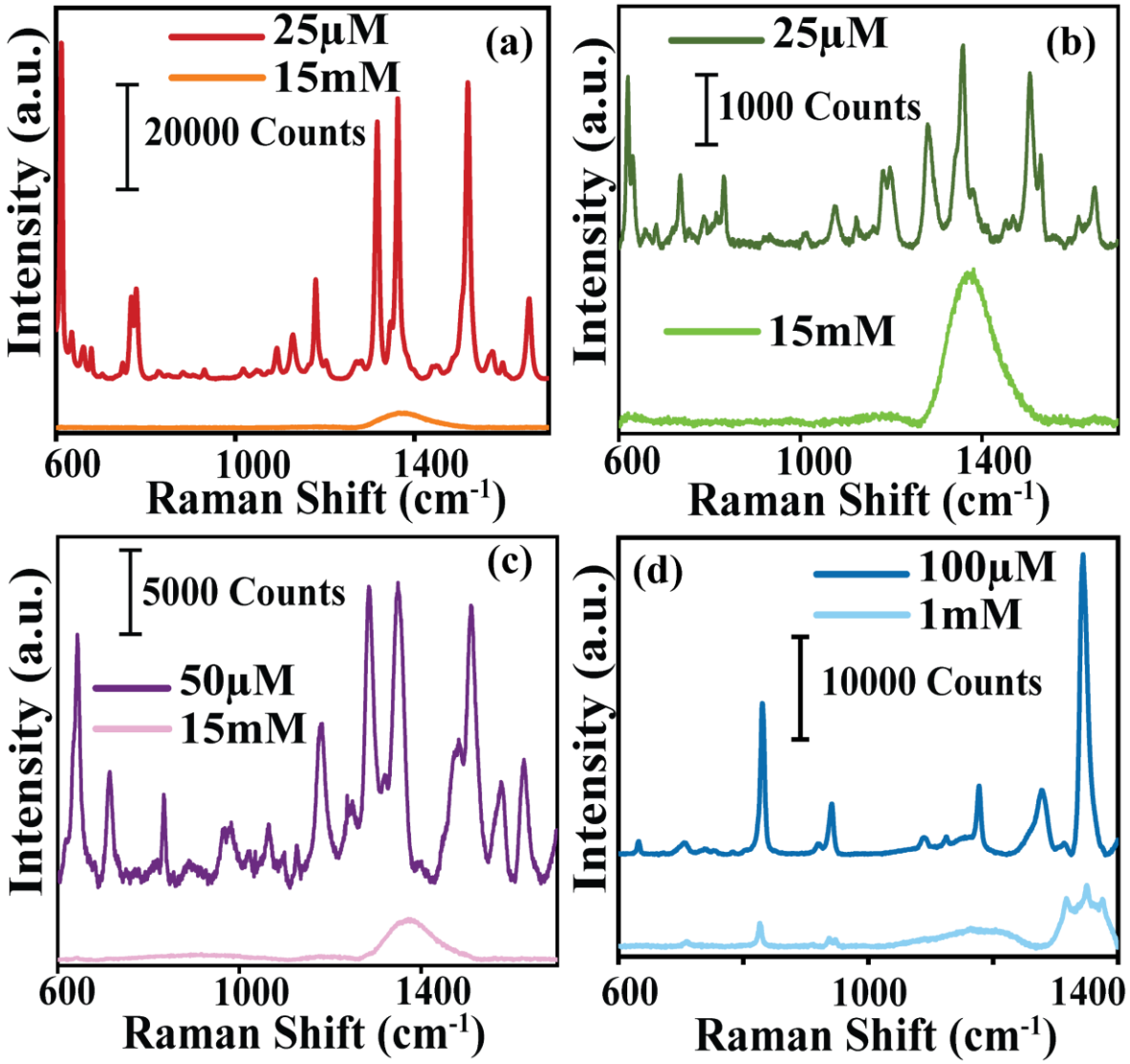

Figure 3.5 SERS spectrum of R6G, RhB and EY on TA microcrystals. (a) SERS signals of R6G on TA microcrystals and normal Raman signals of R6G (on glass substrate) at a laser excitation of 785 nm. (b) RhB SERS signals on TA microcrystals and RhB normal Raman signals (on glass substrate) at 785 nm laser excitation. (c) SERS signals of EY on TA microcrystals and normal Raman vibrations of EY (on glass substrate) at a laser excitation of 785 nm. (d) SERS signals of PA on TA microcrystals and normal Raman signals of PA (on glass substrate) at a laser excitation of 785 nm.

when compared with the control samples, indicated that the surfaces of TA micro-crystals improved greatly the signals due to SERS for these molecules. Further, 25 µM solution each of

R6G and RhB, 50 μM of EY analytes and 100 μM of PA were taken along with TA to estimate the enhancement factor (EF) and correlate SERS efficiencies for the molecules on the substrate surfaces (Table 3.9). [35,36]

Table 3.5 Raman peak assignments of rhodamine-6G (R6G).[29,30]

Raman shift (cm^{-1})	Vibration mode
1656	xanthene ring Stretching
1575	C−C stretching in phenyl ring
1519	XR stretching, C−N stretching, N−H bending
1363	methyl wagging
1317	Hybrid mode (xanthene breathing/ twisting of phenyl rings and NHC2H5 group)
1183	in plane XR deformation + C−H in-plane bend in xanthene ring
1129	C−H in-plane bending in xanthene/phenyl rings
1093	C−H in-plane bend in xanthene/phenyl rings
779	C−H out-of-plane bending
611	XR puckering + bending of phenyl ring

Table 3.6 Raman peak assignments of rhodamine B (RhB).[31,32]

Raman shift (cm^{-1})	Vibration mode
1648	Aromatic C−C stretching
1529	XR stretching
1506	Aromatic C−C stretching
1358	Aromatic C−C stretching
1280	C−C bridge-band stretching + methyl wagging
1197	C-H bending
1077	Methyl rocking
621	Xanthene ring puckering

As indicated in the table 3.9, the EF of R6G was measured to be the highest with a value on the order of ~1.5×10^6, followed by that of EY with a value of ~7×10^4, and for RhB being on the order of ~3×10^4 and finally that of PA being on the order of ~1.3×10^4. Importantly, the results indicated that the efficiency of SERS by the TA microcrystals could be comparable to inorganic semiconductors as reported recently. Further, we observed that the SERS signal strength of R6G, RhB, EY decreased with concentration and that the detection limits for R6G, RhB, and EY solution concentrations were found to be as low as 0.5 μM, 1 μM and 1 μM, respectively (Figure 3.6). At lower concentrations of the dyes, the signals due to the TA crystals

more prominent, corroborating that the signal enhancement occurred solely from the crystal's surface. Furthermore, as the TA microcrystals have significant absorbance near 633 nm, Raman signals of analyte dyes deposited over the crystals were recorded under this excitation. The results showed strong background signals during Raman measurement in the case of R6G and RhB due to substantial absorbance band edge of these dyes at 633nm laser excitation (Figure 3.7, 3.8). The interfering background interference was lower for EY (having significantly low absorbance band edge at 633 nm), and TA-EY combination showed prominent Raman enhancement of EY signals at this laser irradiation (Figure 3.9).

Table 3.7 Raman peak assignments of eosin yellowish (EY).[33]

Raman shift (cm^{-1})	**Vibration mode**
1626	xanthene ring C−C stretches
1576	Benzene ring stretch
1509	xanthene (perp) and Benzene ring C−C stretches
1349	Aromatic C−C stretching
1285	xanthene and Benzene ring C−C stretching
1182	xanthene and Benzene ring stretching and symmetric CO2 stretch
964	xanthene and Benzene ring stretching
715	xanthene out of plane ring deformation
641	xanthene breathing + Benzene breathing

Table 3.8 Raman peak assignments of picric acid (PA).[34]

Raman shift (cm^{-1})	**Vibration mode**
1343	NO_2 symmetric stretching
1277	C−N stretching + (C-H + O-H in-plane bending)
1177	Ring C-C-C in plane bending
1089	Ring C-H bending
941	Ring C-H out of plane bending
830	C-N stretching + NO_2 Bending

Table 3.9. Calculated SERS enhancement factors (EFs) for the referred analytes on terephthalic acid (TA) microcrystals.

Analyte	Raman Peak Position (cm^{-1})	Excitation Laser wavelength (nm)	Enhancement Factor (EF)
R6G	610	785	$(1.50 \pm 0.02) \times 10^6$
RhB	621	785	$(3.23 \pm 0.18) \times 10^4$
EY	644	785	$(7.17 \pm 0.29) \times 10^4$
PA	830	785	$(1.37 \pm 0.03) \times 10^4$

It should be noted here that weak but significant peaks at 632 ($\delta(CCC)_{ring}$) and 832 ($\delta(CCH)_{ring}$ +$\delta(CCC)_{ring}$ + $\delta(COO)$+$\delta(COH)$) cm^{-1}, corresponding to the TA microcrystals have been prevalent in all SERS spectra (Table 3.4). However, since these peaks were relatively weak, they did not affect the analytes' SERS readings. On the other hand, the peaks support the strong enhancements of SERS of analyte molecules on the microcrystal surfaces. The results also indicated that the EFs were dependent on the nature of the molecule on the substrate (TA

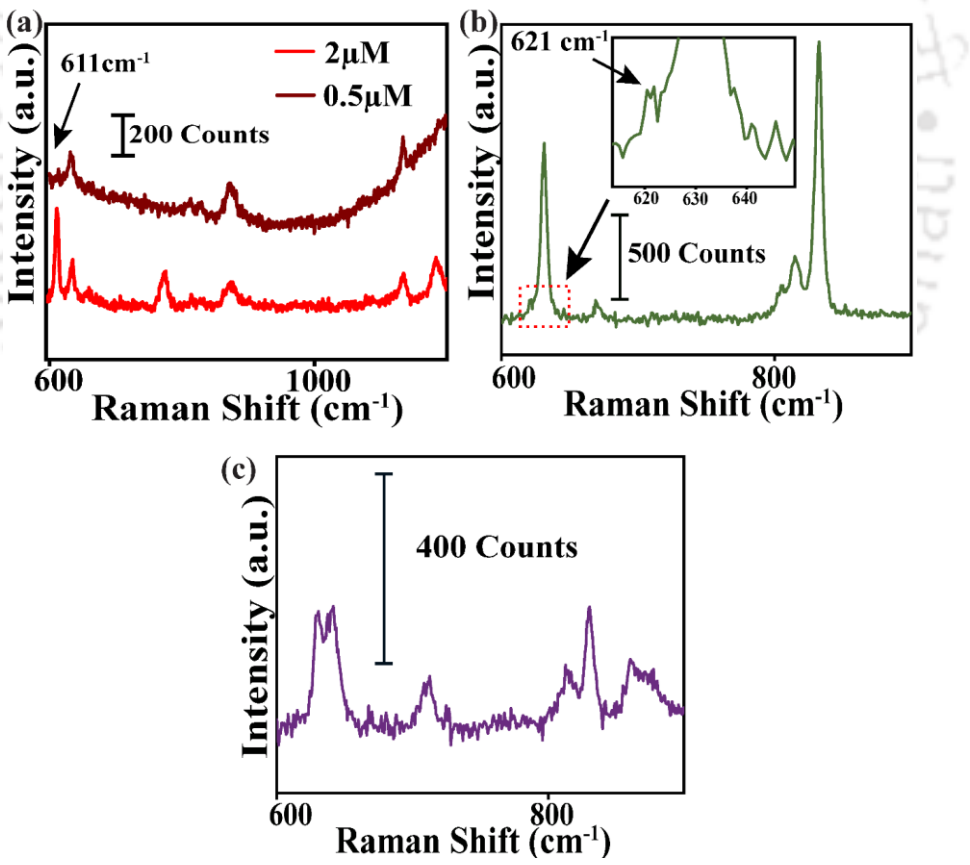

Figure 3.6 SERS spectra of (a) R6G at 2μM (red) and 0.5 μM (brown) (b) RhB at 1μM (c) EY at 1μM liquid concentrations recorded after being co-deposited with the TA microcrystals.

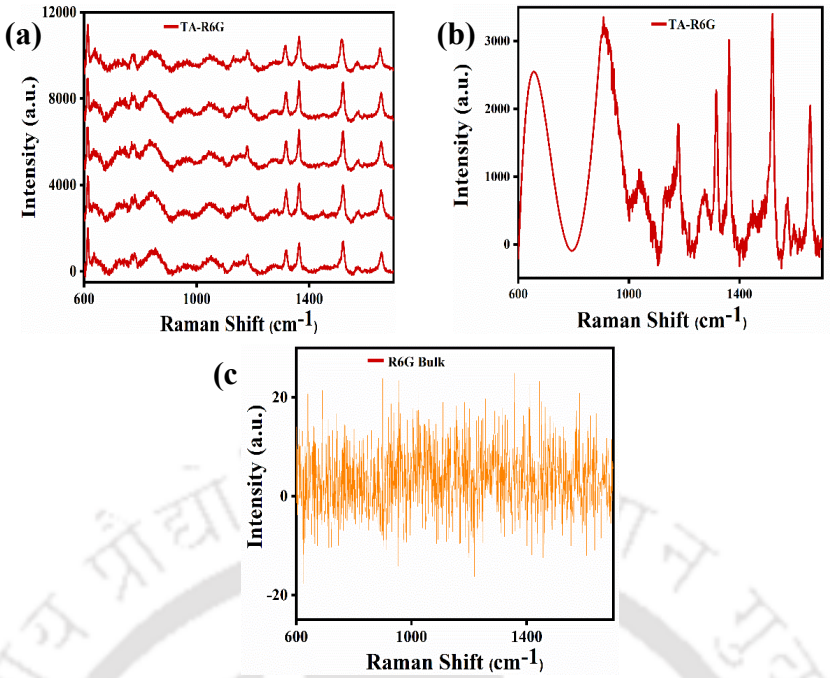

Figure 3.7 SERS spectra of 25 µM R6G on TA microcrystals at (a) 0.01% and (b) 0.1% laser power under 633nm laser excitation. (c) Normal Raman signals of R6G (on glass substrate) at 0.01% laser power under 633 nm laser irradiation.

microcrystals) surfaces. The specificity of enhancement could be due to molecular interactions between the analyte molecules and the TA molecules present on the surface. Thus, specific interactions between the molecular bonds of R6G, RhB or EY and those of TA molecules, which were also based on their orientations on the substrate surfaces played significant roles

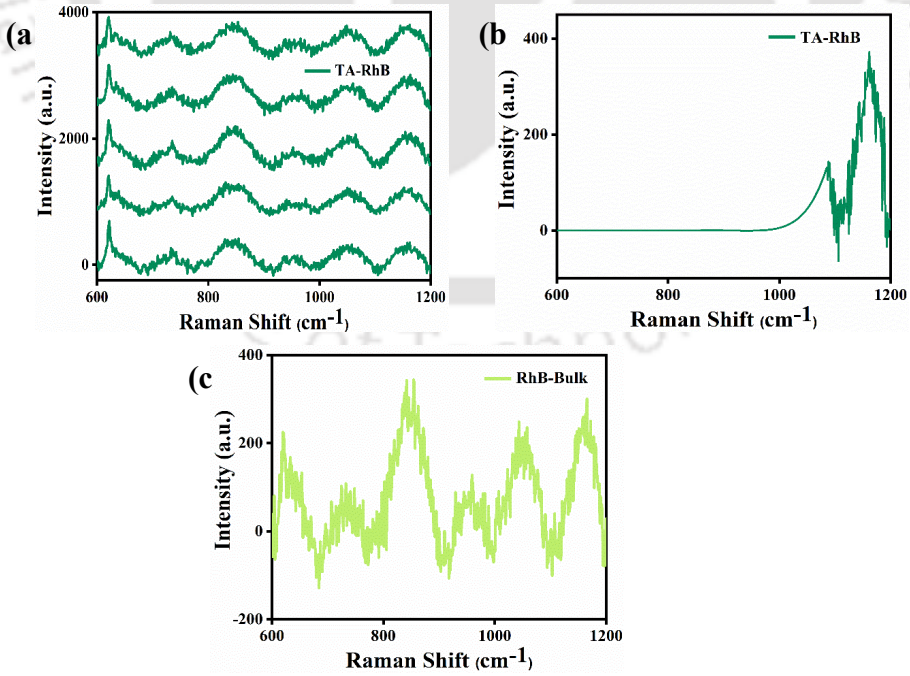

Figure 3.8 SERS spectra of 25 µM RhB on TA microcrystals at (a) 0.1% and (b) 1% laser power under 633nm laser excitation. (c) Normal Raman spectra of RhB (on glass substrate) at 0.1% laser power under 633 nm laser irradiation.

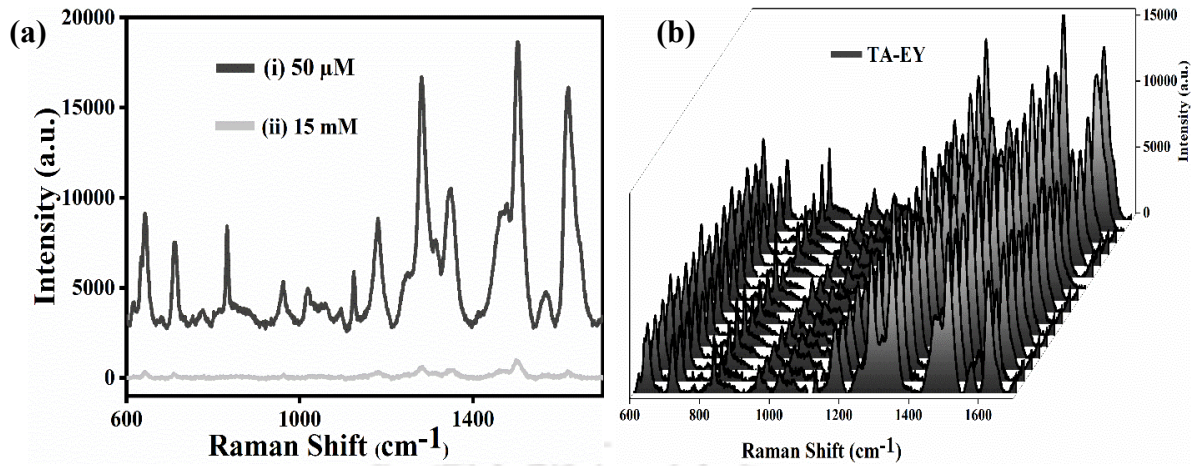

Figure 3.9 (a) SERS signals of (i) EY on TA microcrystals and (ii) normal Raman signals of EY (on glass substrate) at a laser excitation of 633 nm. (b) SERS spectra for 50 µM EY (as in the initial mixture) acquired on 16 randomly chosen locations of the TA-EY substrate under laser excitation of 633 nm.

in the enhancements of the Raman signals. In addition, HOMO-LUMO energy difference of each analyte molecule as compared to the band-gap and inter-band states of the TA microcrystals might have played pivotal roles in the extent of enhancements of the signals. The charge transfer between the analyte molecules and the substrate crystals might have been an important factor in the enhancements of Raman signal intensity on the organic crystal surfaces.

3.2.2 Mechanism of SERS

In general, SERS of molecules on the surface of the substrate may occur either through EM,[37-39] i.e., surface plasmon stimulation or, the CM route,[40,41] where the probe molecules and the microcrystalline substrates can transfer electrons in the ground as well as excited electronic state(s). Sometimes, a combination of the two mechanisms may lead to better SERS enhancement.[42] As a result of the low density of free electrons in the conduction band, organic crystals typically have an insignificant plasmon resonance.[43]Hence, the EM mechanism is not expected to drive Raman enhancement over TA microcrystals. However, exciton resonances, which are generally unimportant in metal SERS but are essential in crystal charge transport, will affect the SERS spectrum. The proximity of an exciton resonance can boost the strength of the Raman signal as charge-transfer transitions between the molecule and the SERS substrate can occur via the exciton resonance. The most intense SERS enhancement is observed for transitions terminating at the crystal's band edges (conduction and valence bands). As a result, charge-transfer from the analyte molecule's HOMO to the crystal's conduction band edge or from the valence band edge of the crystal to the LUMO of the molecule is possible. The UV-

vis DRS results indicated strong inter-band transitions in TA microcrystals ranging from 400 to 850 nm (and possibly beyond), with a peak of 800 nm.

Importantly, we probed the SERS efficiency with the laser at 785 nm, at which TA microcrystals absorb well; however, the probe molecules do not have significance absorbance at the wavelength. Thus, the SERS efficiency due to the microcrystals could be quantified. Further, when probed with the 785 nm laser wavelength, these electronic inter-band states in crystals can participate in exciton generation, which can be coupled with the charge transfer process between crystal and analytes.[44] The energy gap for charge transfer transition between crystals valence band and dye's LUMO needs to be in range of external laser excitation. The photo-induced charge transfer occurring between the crystal's valence band maximum and the probe molecules' LUMO might well contribute significantly to the Raman enhancement through CM.

The work function and valence band maximum of the TA microcrystals, and the HOMO energy levels of R6G, RhB, and EY dyes in the solid state were measured using ultraviolet photoelectron spectroscopy (UPS), in order to evaluate the significant charge transfer transitions. The results revealed the valence band maximum of TA microcrystals, and HOMO energy levels of R6G, RhB, and EY to have been -7.33, -8, -7.6, and -7.9 eV, respectively, with respect to the vacuum level (Figure 3.10, 3.11, Table 3.10). The optical band gap as measured from the tauc plot revealed the relative positions of the conduction band minimum of TA crystals and LUMO energy levels of the related probe molecules (Figure 3.12).

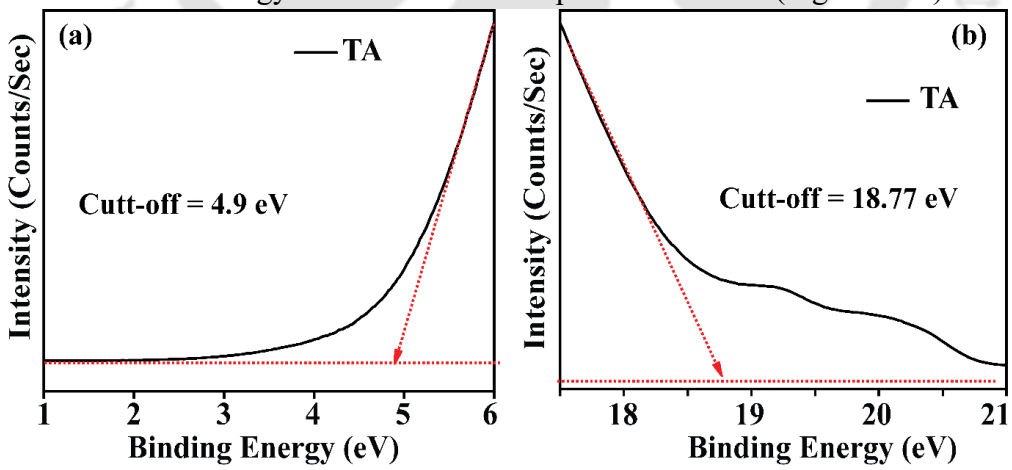

Figure 3.10 (a,c,e) Low-BE slope and (b,d,f,) high-BE slope of the UPS spectra of TA, R6G-RhB equimolar mixture, R6G-EY equimolar mixture, respectively.

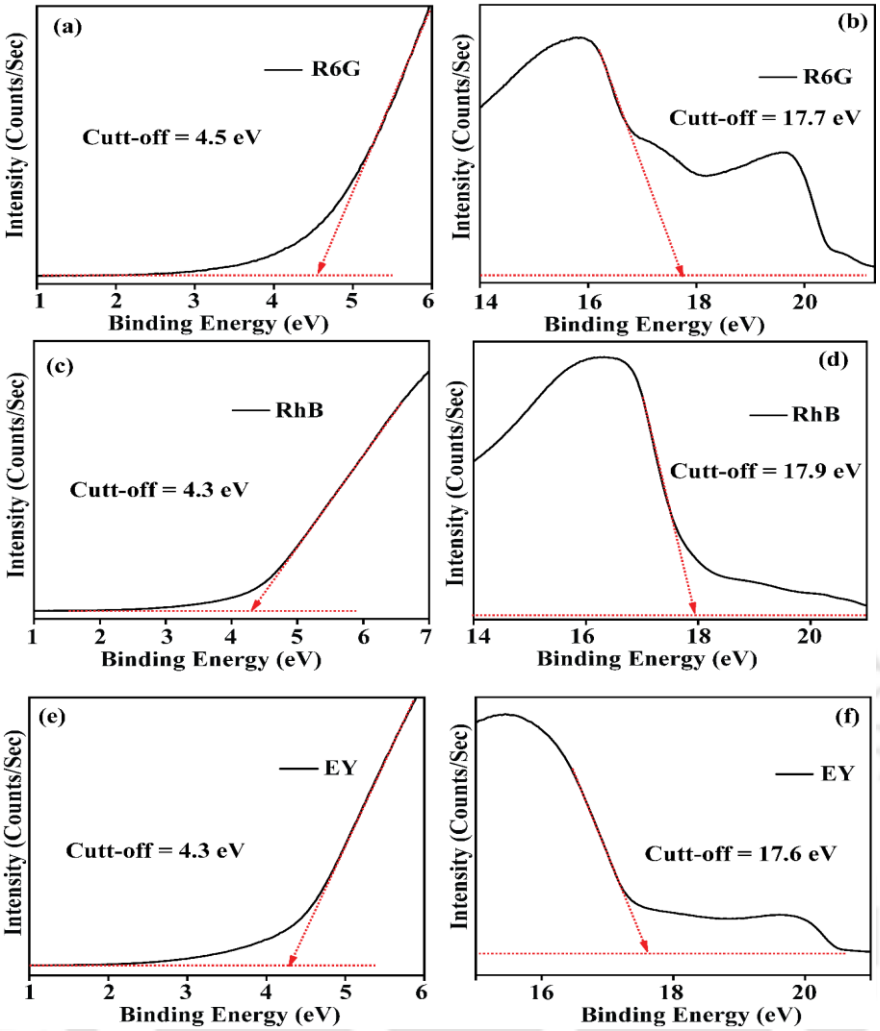

Figure 3.11 (a,c,e) Low-BE slope and (b,d,f,) high-BE slope of the UPS spectra of R6G, RhB, and EY respectively

Table 3.10 Results of UPS analyses of crystals and probe dye molecules.

Compounds	High-Binding energy cut off	work function	low-energy tail	Valence band maxima/HOMO	optical band gap	conduction band minimum
TA	18.77	-2.43	4.9	-7.33	4.07	-3.26
R6G	17.7	-3.5	4.5	-8	2.26	-5.74
RhB	17.9	-3.3	4.3	-7.6	2.18	-5.42
EY	17.6	-3.6	4.3	-7.9	2.3	-5.6

The optical band gaps for TA crystals was measured to be 4.07 eV and the HOMO-LUMO energy differences in R6G, RhB, and EY were found to have been 2.26, 2.18, and 2.3 eV, respectively (Figure 3.10 and 3.11). The corresponding conduction band minimum of TA

microcrystals was measured to be -3.26 eV and the LUMO energy for analyte dyes (as above) were -5.74, -5.42, and -5.6 eV respectively (Table 3.10). According to the UPS analysis, the difference between TA's valance band maximum and LUMO of R6G, RhB and EY were 1.59, 1.91, and 1.73 eV, respectively (Figure 3.13a), which are close to the excitation wavelength energy of 1.58 eV (λ_{ex}=785 nm). However, the gap aligns well with the LUMO levels of R6G and EY, providing significant charge transfer probability along with coupled exciton resonance, resulting in outstanding Raman enhancement. However, the gap is slightly larger for RhB, and consequently resulting in moderate Raman enhancement.

Understanding of another aspect of SERS enhancement over the TA microcrystals can be attained through the concept of hybrid orbital generated due to the overlap of the surface molecular orbitals of TA and the dye molecule.[45] In other words, new energy states might be generated following the overlap of the molecular orbitals of the dye and the surface molecules of the crystal. Also, large CT resonance enhancement requires good spatial overlap between the crystal and dye frontier molecular orbitals. The electrostatic potential map of TA microcrystals showed that the surface molecular orbitals primarily constitute electron-rich (red zone) regions, with a few blue spots corresponding to electron-deficient regions (Figure 3.13b).

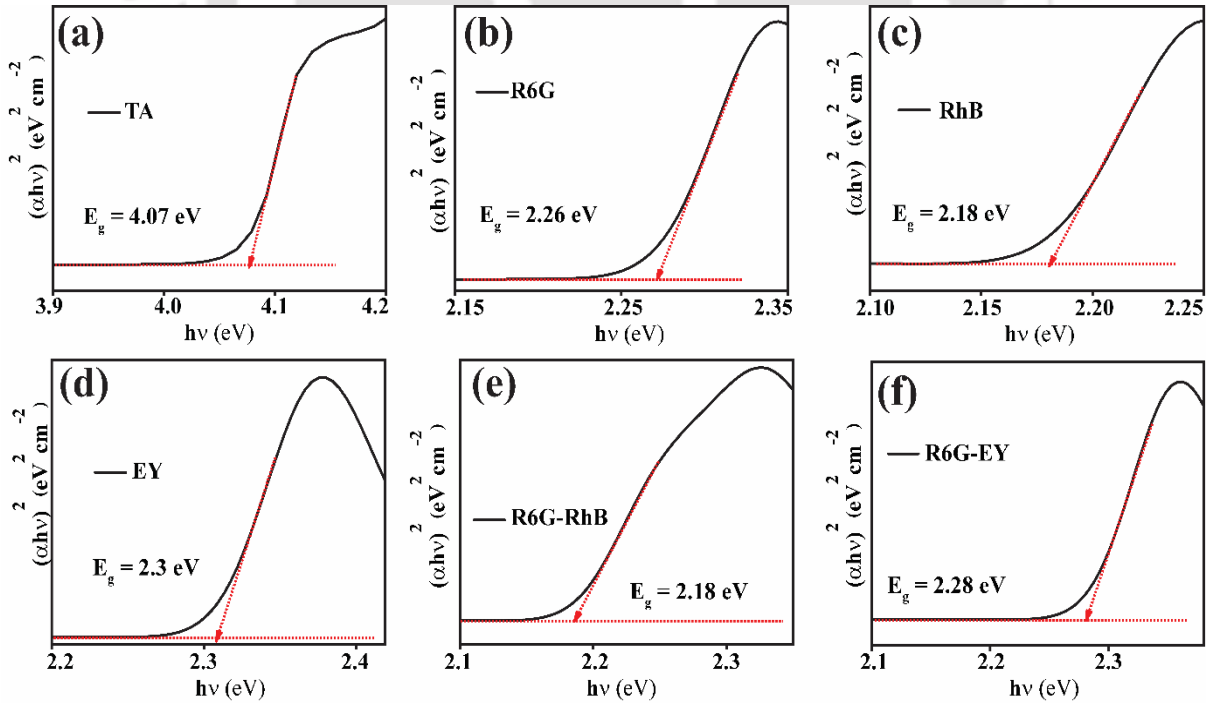

Figure. 3.12 Tauc plot of $(\alpha h\nu)^2$ versus $h\nu$ for (a) TA (b) R6G (c) RhB (d) EY (e) R6G-RHB equimolar mixture (f) R6G-EY equimolar mixture respectively.

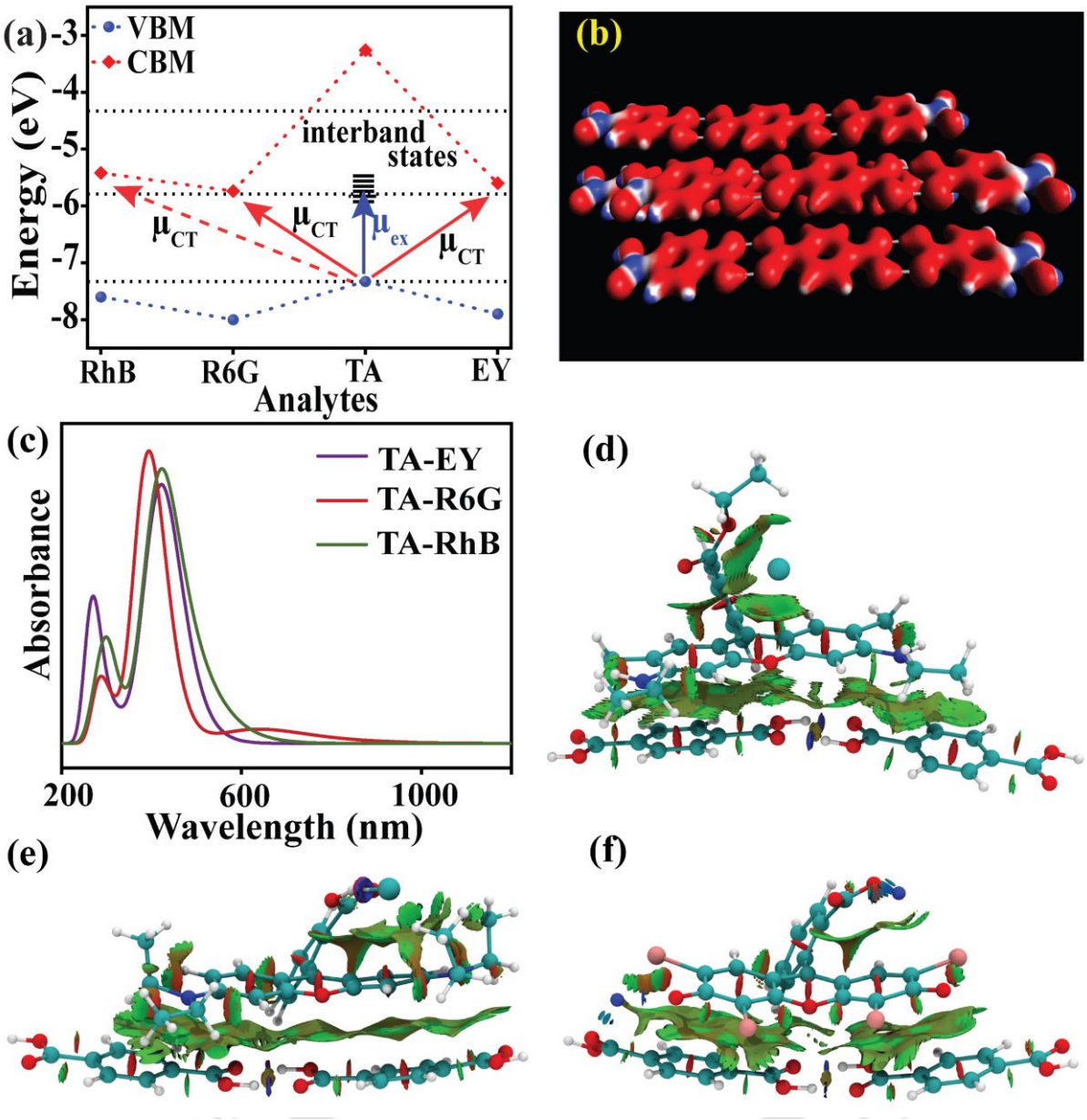

Figure 3.13 Mechanism of SERS for TA microcrystals. (a) Diagram of HOMO-LUMO energy gaps with respect to vacuum of R6G, RhB and EY in comparison with valence and conduction band edges of TA microcrystal obtained from UPS analyses. (b) Simulated electrostatic potential map (ESP) of TA microcrystals. Red color in the ESP map illustrates the high electron dense region in the crystal and blue color defines electron deficit region. (c) Overall orbital interactions between dye and TA crystals quantified through theoretical absorbance data of TA-R6G, TA-RhB and TA-EY hybrid systems obtained from TD-DFT calculations of the optimized structures. Note: TA-R6G hybrid system has significant absorbance near 785nm laser excitation. Diagrams displaying non-covalent interactions (NCI) of the (d) TA-R6G, (e) TA-RhB and (f) TA-EY systems as represented by the quantum-based color-filled RDG iso-surface approach.

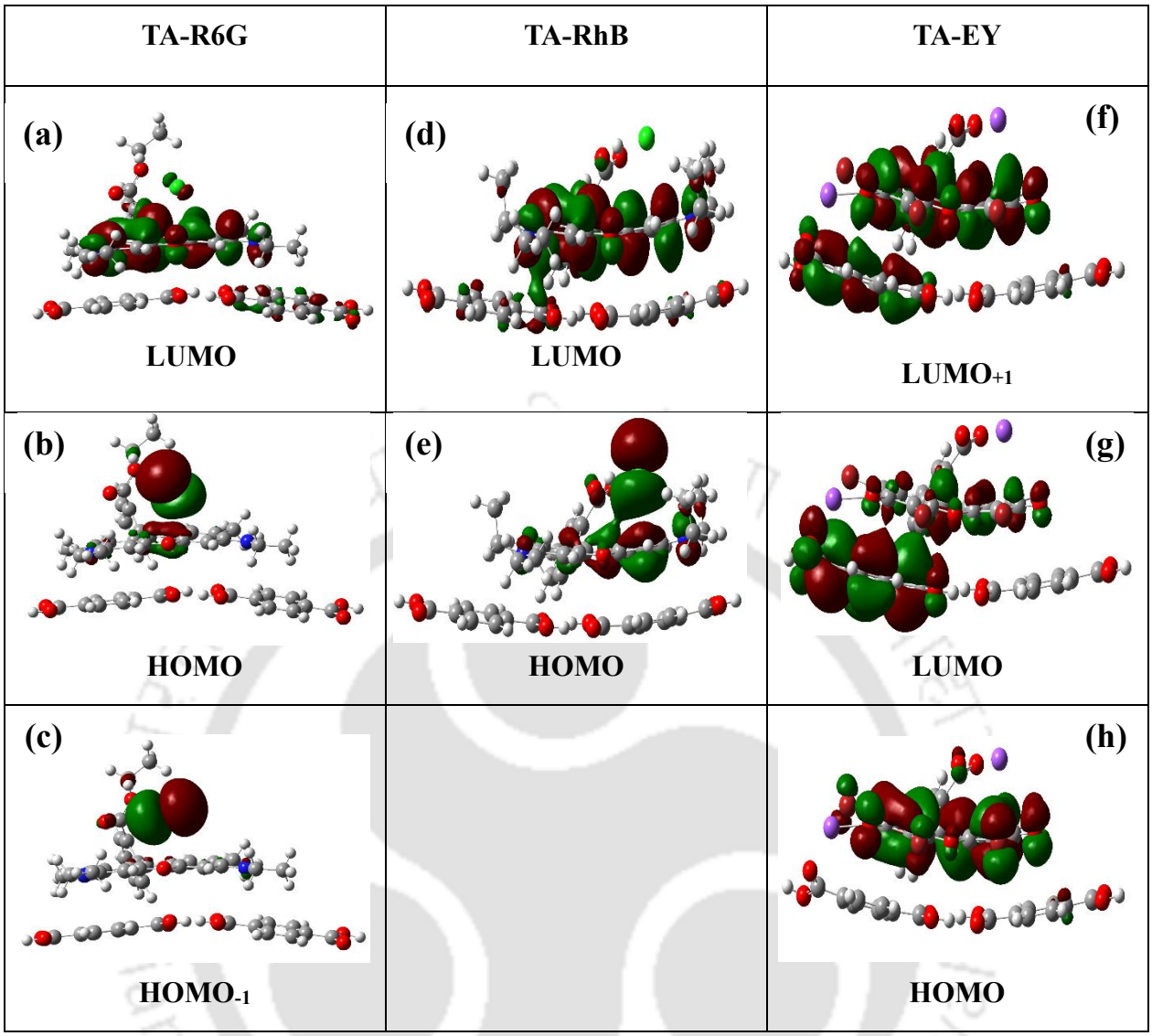

Figure. 3.14 Pictorial representation of frontier orbitals of TA-R6G, TA-RhB, TA-EY systems obtained from theoretical calculations.

Thus, electron transfer from the surface TA molecules to analyte dye molecules and vice versa may occur in the presence of incident light of wavelength matching the excitation energy. Thus, the presence of hybrid orbitals, involving the substrate and the analyte molecules would facilitate significant orbital interaction in the event of a hybrid integrated system. The Raman scattering cross section may increase or decrease significantly depending on the interactions between the orbitals. Further, the infinite 2d network of π-orbitals present in the TA microcrystals may favour both energy and stereochemistry-based interactions between the orbitals. In hybrid molecular system, TD-DFT calculations showed that a lower energy transition had been generated owing to significant interactions between the participating

molecular orbitals (Figure 3.13c). The theoretical absorption spectrum (Figure 3.13b) of TA-R6G hybrid system showed a peak at 675.7 nm that appeared due to HOMO/LUMO and $HOMO_{-1}$/LUMO transitions of the coupled molecular system (Figure 3.14a-c). This transition when excited with 785 nm laser can significantly alter the Raman polarizability tensor that results in large signal enhancement for the coupled system (Figure 3.13b red spectra). In case of TA-RhB system, the lowest energy transition occurs at 507.2 nm involving HOMO/LUMO transition (Figure 3.14d,e) and for TA-EY system it occurs at 427.2 nm owing to HOMO/LUMO and HOMO/$LUMO_{+1}$ transitions (Figure 3.14f-h). At external 785 nm laser excitation, the above transitions had no meaningful contribution and hence moderate SERS enhancement for RhB and EY. Figures 3.13d-f show the optimized model of the dye's orientation over the crystal surface along with the weak nonbonded covalent interactions, leading to the orbitals' overlap for TA-R6G, TA-RhB, and TA-EY systems, respectively.

The noncovalent interaction (NCI) plots shown in Figure 3.13d-f are based on a reduced density gradient (RDG), which indicates electron density change. It elucidates the intensity and type of noncovalent interactions like hydrogen bonding, π-π stacking, van der Waals interactions, and halogen bonding.[46,47] The NCI plot can give indirect information about the nature of noncovalent interactions involving hybridized orbitals. The electron density is shown by a colour scale in an NCI plot, with steric repulsion in red, attractive van der Waals in green, and hydrogen bonding in blue. The results indicated that there are significant noncovalent interactions between TA and dyes in all three systems. This facilitates charge transfer in both directions, resulting in improved SERS.

3.2.3 Cooperative SERS

We were further interested in pursuing molecular cooperativity in the Raman signal when two analyte molecules were simultaneously deposited over the TA microcrystals. In other words, when one of the two analyte molecules were placed on top of the other as deposited over the TA microcrystal surfaces, do the molecules enhance or reduce the Raman signal intensities of each other? Further, how do the signals compare when molecules are deposited on top of each other but on an inert substrate (such as glass) instead of TA microcrystals? (Figure 3.16) This was accomplished by taking samples of equimolar mixtures of R6G-RhB and R6G-EY and then evaporated on a glass slide in the presence of TA microcrystal dispersion in 2:1 methanol-water mixture. This was followed by recording of the Raman spectra of the evaporated solids (Figure 3.15a,b). As demonstrated in (Figure 3.15a), when the RhB and R6G

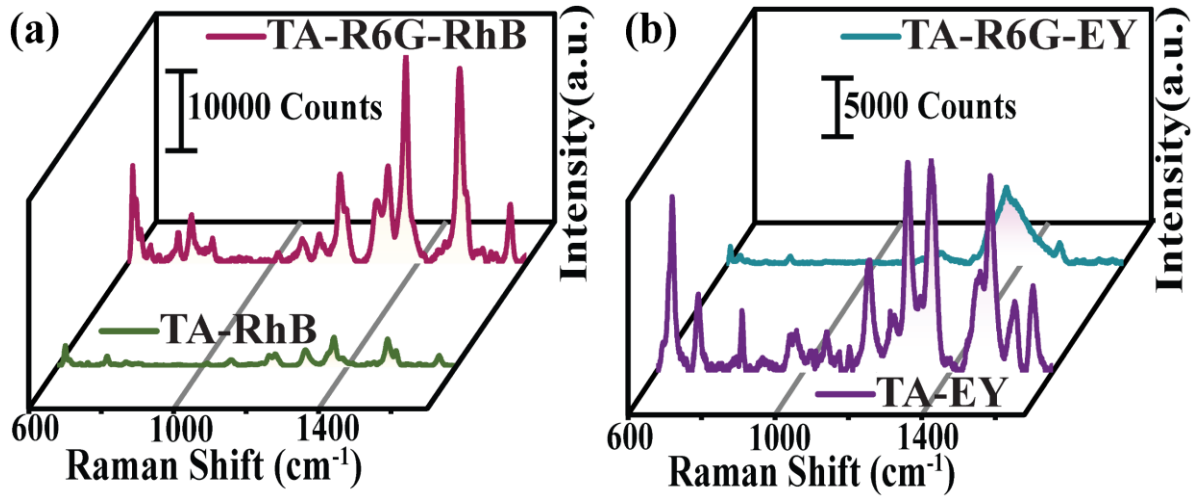

Figure 3.15 Cooperative SERS on TA microcrystals. (a) SERS spectrum of R6G and RhB binary mixture on TA microcrystals at laser excitation of 785 nm (red spectrum) and SERS spectra of only RhB (in green) over TA microcrystals. (b) SERS spectrum of R6G and EY mixture (in cyan) on TA microcrystals and SERS spectrum of only EY (in violet) over TA microcrystals at 785 nm laser excitation.

combination was irradiated with 785 nm laser, the SERS signals of RhB were greatly amplified, whereas those due to R6G were significantly diminished. On the other hand, Raman signals from the evaporated solid of an equimolar mixture of R6G and RhB on glass without crystals did not generate such a distinction (Figure 3.16). Raman spectrum of the mixture showed independent peaks due to both the dyes. In addition, there were the presence of overlapping broad peaks of the molecules together. In the combined system there were thirteen strong Raman peaks located at 613, 622, 776, 1080, 1129, 1185, 1203, 1287, 1317, 1367, 1516, 1534 and 1656 cm^{-1}, respectively (Figure 3.15a). The intensity of peaks appearing in the mixture differed from the intensity of their individual peaks on the crystal surface. For example, 611

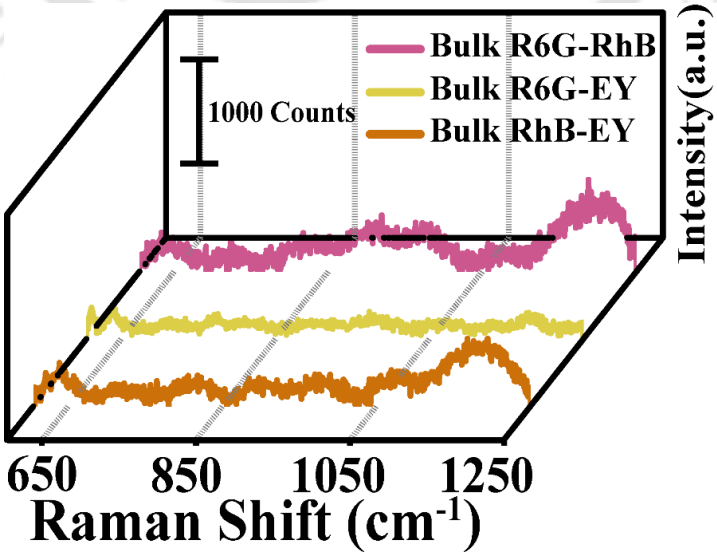

Figure 3.16 Raman spectra of binary mixture of dyes at 785nm laser excitation.

cm^{-1} (XR puckering + bending of phenyl ring), and 1317 cm^{-1} (hybrid mode due to xanthene breathing/ twisting of phenyl rings and NHC_2H_5 group) peaks of R6G were reduced by a factor of 3.5, 2.8 respectively, whereas 620 cm^{-1} (XR puckering), 1288 cm^{-1} (methyl wagging) and 1537 cm^{-1} (XR stretching) vibrational modes of RhB were enhanced approximately by a factor of 4.7, 6.5 and 8.9 from their individual SERS signals over TA microcrystals, respectively (Table 3.11). From the vibrational analysis of the binary mixture it can be concluded that Raman signal intensity due to the R6G xanthene ring out of plane and phenyl ring vibrations were highly quenched whereas those due to RhB's xanthene ring vibrations were greatly enhanced. The results reported here hint towards molecular cooperativity in the Raman signal intensities when the analyte molecules were placed on the surface of the TA microcrystals.[48] In other words, it is plausible that R6G and RhB molecules when evaporated together on the microcrystal surfaces there was a particular alignment of the molecules that resulted in the Raman signal enhancement of one while there was the same was diminished for the other. At 633 nm laser excitation, Raman spectra of R6G-RhB equimolar mixture over TA microcrystals showed similar trend (Figure 3.17). The results showed that in the mixture RhB signal is enhanced compared to individual RhB signals over TA microcrystals at identical experimental conditions. However, in mixture, the signals due to R6G were reduced significantly from their individual SERS signals. This can be attributed to RhB having a higher absorbance coefficient than R6G at 633 nm, whereas at 785 nm laser excitation, such interference is missing, giving better SERS cooperativity.

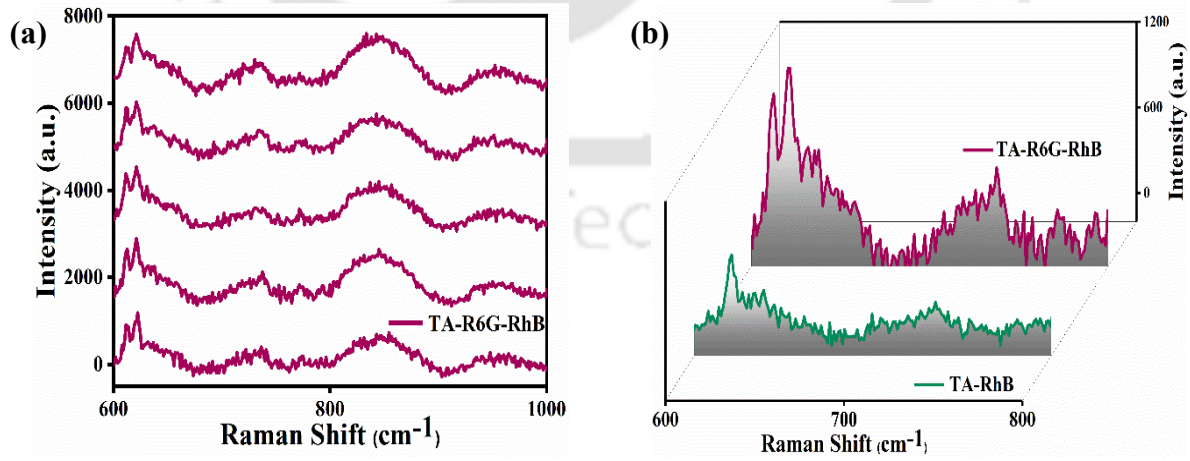

Figure 3.17. (a) SERS spectra of an equimolar binary mixture of R6G and RhB on TA microcrystals at 0.1% laser power recorded at five different spots under 633nm laser excitation. (b) SERS spectrum of R6G and RhB binary mixture on TA microcrystals at laser excitation of 633 nm (red spectrum) and SERS spectra of only RhB (in green) over TA microcrystals recorded at identical experimental setup.

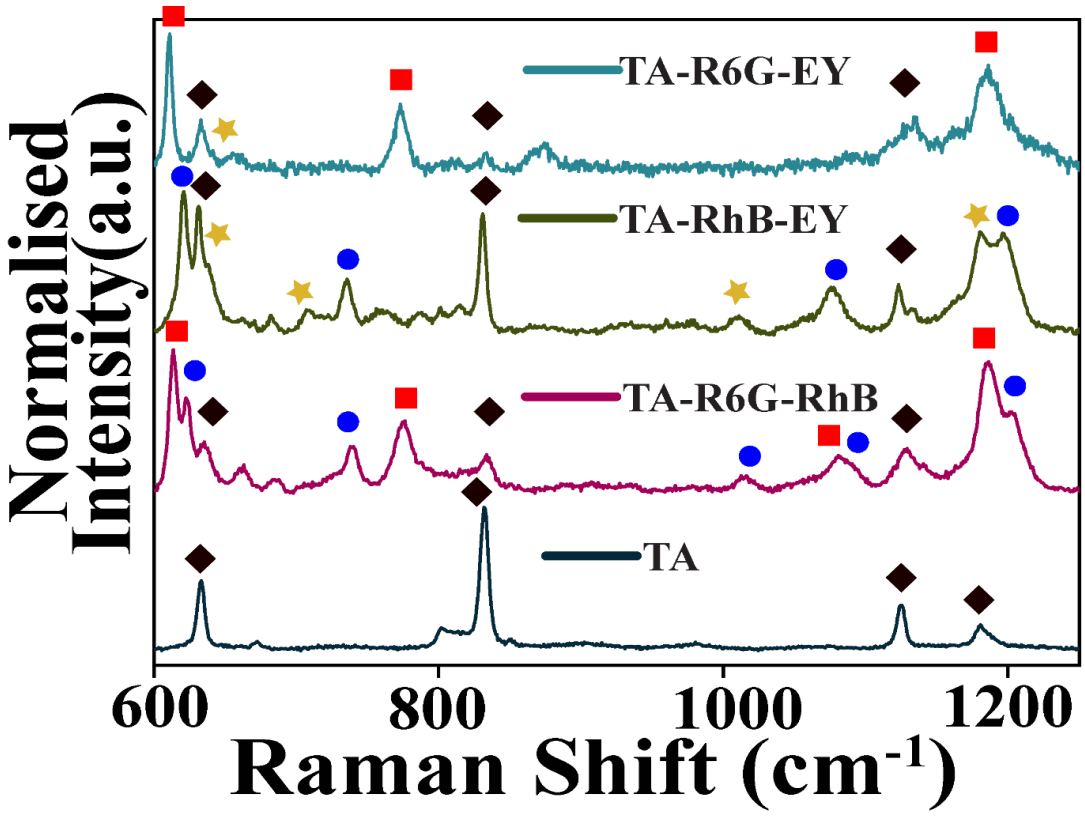

Figure 3.18 SERS spectra of binary mixture of dyes over TA microcrystals along with Raman spectra of TA crystal. SERS peaks associated with TA crystals, R6G, RhB and EY were designated with ◆ ■ ● ★ symbols respectively.

The results for the R6G and EY equimolar combination are particularly fascinating since the separate dyes have significant Raman amplification over the TA micro-crystals. Still, their mixture has significantly decreased Raman signals, resulting in a flat Raman spectrum. A few weak Raman signals were observed, mostly due to the crystal and R6G. Interestingly, when deposited as a binary mixture with R6G on TA microcrystals, the EY Raman signals had nearly disappeared (Figure 3.15b). The enhancement and lowering of the Raman signal intensities for the combination of dyes on the TA microcrystal surfaces demonstrate that interactive molecular systems when placed on a molecular (organic) substrate with delocalized π electrons may provide a new way of identification of molecules and their interactions through their vibrational Raman spectra. In addition to this, we have also pursued Raman spectra for equimolar mixture of RhB and EY over the TA microcrystals. In this case, RhB signals remained almost identical to those of molecules when deposited singularly on the crystals. However, EY signals were reduced approximately to 40% from their individual SERS signals over TA crystals (Figure 3.19). The results indicated weak interactions between these dyes when co-deposited on the crystal surfaces, resulting in lack of cooperativity. In order for a better appreciation of the

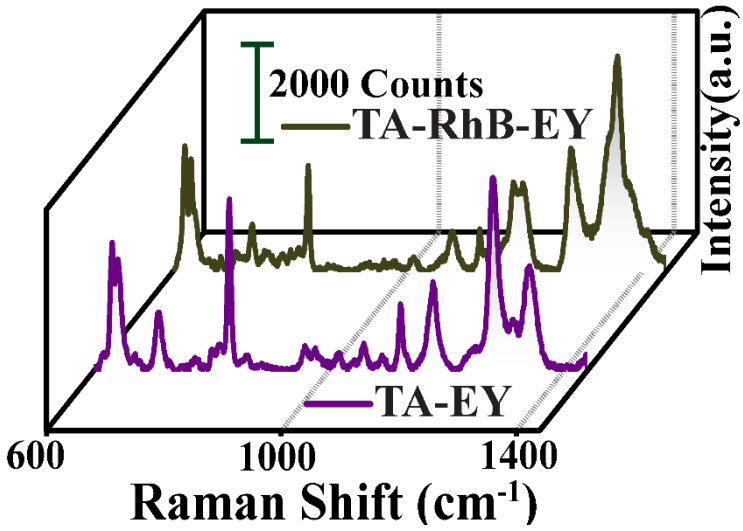

Figure 3.19 SERS spectrum of RhB and EY binary mixture (TA-RhB-EY, in dark green) on TA microcrystals at laser excitations of 785 nm and SERS spectra of only EY(TA-EY, in indigo) over TA microcrystals.

differences in cooperativity, Raman spectra for all three binary mixtures of dyes are presented in Figure 3.18.

To account for the cooperative Raman enhancement as well as diminishment for the binary mixtures of dyes over the TA crystal surface, we have calculated the HOMO and LUMO energies using UPS experiment for equimolar mixture of dyes when evaporated as solids(Figure 3.20). The energy gap between TA's valence band maximum and the LUMO of R6G+RhB mixture is decreased by 0.38 eV compared to RhB and matched well (1.53 eV) with the external laser excitation (785 nm) (Figure 3.21a). The energy gap between TA's valence band maximum and the LUMO of the R6G-EY equimolar mixture is increased by 0.54 eV compared to R6G, and the energy gap falls off-resonance (2.13 eV) with the external laser excitation (785 nm =1.6 eV) as well as TA's exciton resonance, thus, producing significantly quenched Raman spectra (Table 3.12).

DFT calculations for the hybrid system comprising a model of mixture of dyes stacked over the crystal surface revealed more details about the cooperative nature of the SERS enhancement. TD-DFT calculation for TA-R6G-RhB system showed that a new excited has been generated at energy equivalent to 755 nm light, which has a significant absorbance coefficient near the experimental laser stimulation (Figure 3.21b). The newly generated excited state can resonate with external laser excitation and give enormous Raman enhancement. HOMO-LUMO of this hybrid system (also contribute in 755 nm excited state) shows electronic

Table 3.11 SERS assessment of TA-R6G-RhB system.

Peak position (cm^{-1})	Intensity change	mode	factor	Assignment
613	quenched	R6G	3.5	C−C ring in-plane bending in xanthene/phenyl rings
622	enhanced	RhB	4.7	XR puckering
776	quenched	R6G	2	C−H out-of-plane bending
1080	enhanced	RhB	6	methyl rocking
1129	quenched	R6G	1.54	C−H in-plane bending in xanthene/phenyl rings
1185	quenched	R6G	1.17	C−H in-plane bending in xanthene ring
1203	enhanced	R6G+RhB	2.76	hybrid mode (xanthene/phenyl rings) + RhB C−H bending
1287	enhanced	R6G+RhB	6.5	C−C bridge-band stretching RhB methyl wagging
1317	quenched	R6G	2.81	hybrid mode (xanthene/phenyl rings and NHC2H5 group)
1367	quenched	R6G	1.47	C−C stretching in xanthene ring
1516	quenched	combination	1.66	C−C stretching in xanthene ring/Aromatic C−C stretching
1534	enhanced	RhB	8.87	Aromatic C−H bending /XR stretching
1656	quenched	R6G	1.50	C−C stretching in xanthene ring

Table 3.12. Results of UPS analyses of crystals and probe dye molecules.

Compounds	High-Binding energy cut off	work function	low-energy tail	Valence band maxima/HOMO	optical band gap	conduction band minimum
TA	18.77	-2.43	4.9	-7.33	4.07	-3.26
R6G+RhB	18.12	-3.08	4.9	-7.98	2.18	-5.8
R6G+EY	18.39	-2.81	4.67	-7.48	2.28	-5.2

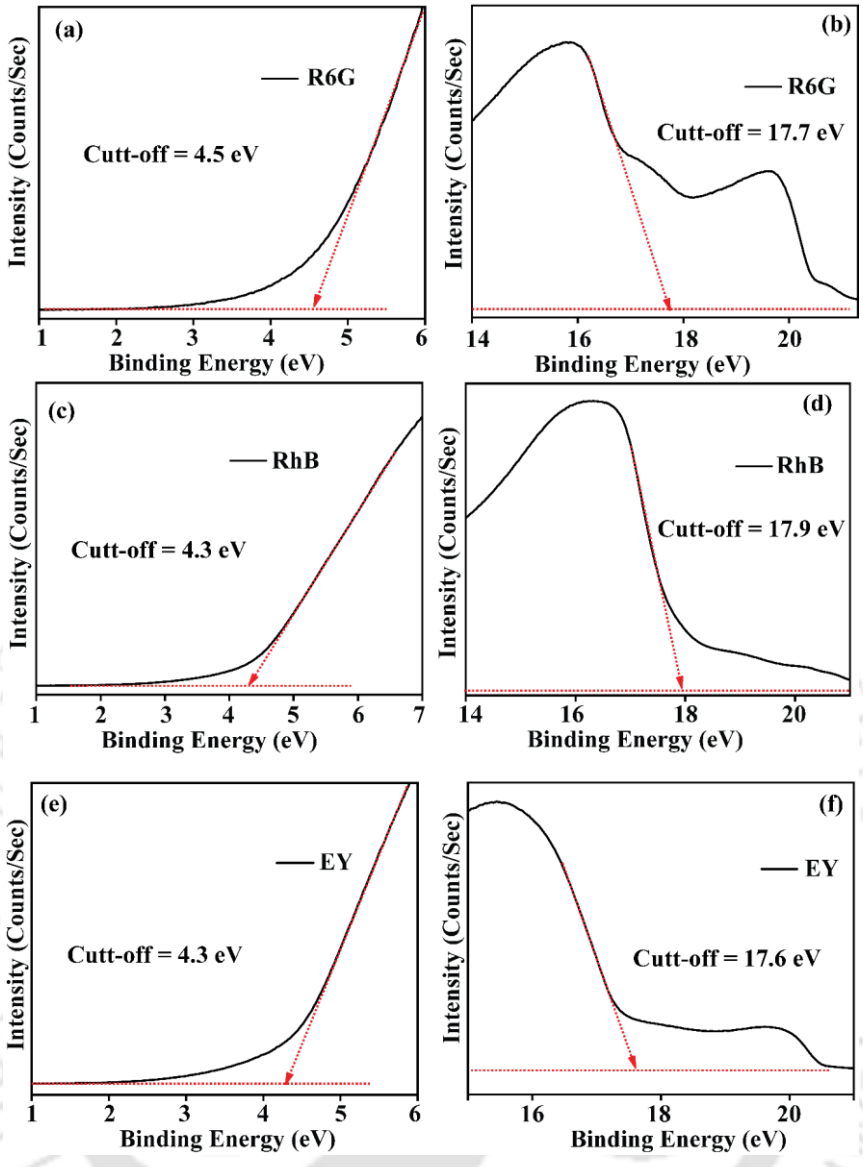

Figure 3.20 (a,c,e) Low-BE slope and (b,d,f,) high-BE slope of the UPS spectra of R6G, RhB, and EY respectively.

excitation form the R6G's xanthene ring orbitals to the fully delocalized orbital of RhB (Figure 3.21c,d). Phenyl ring and the NHC_2H_5 group do not participate in this excitation and resulting in significant damping of the Raman vibrational excitation involving these groups. On the other hand, involvement of xanthene ring vibration (primarily) of RhB resulted in enhanced Raman signals with dominating signals due to the same. For the TA-R6G-EY hybrid system, TD-DFT calculations showed lack of an excited state near the external laser excitation wavelength (Figure 3.21b cyan spectra).

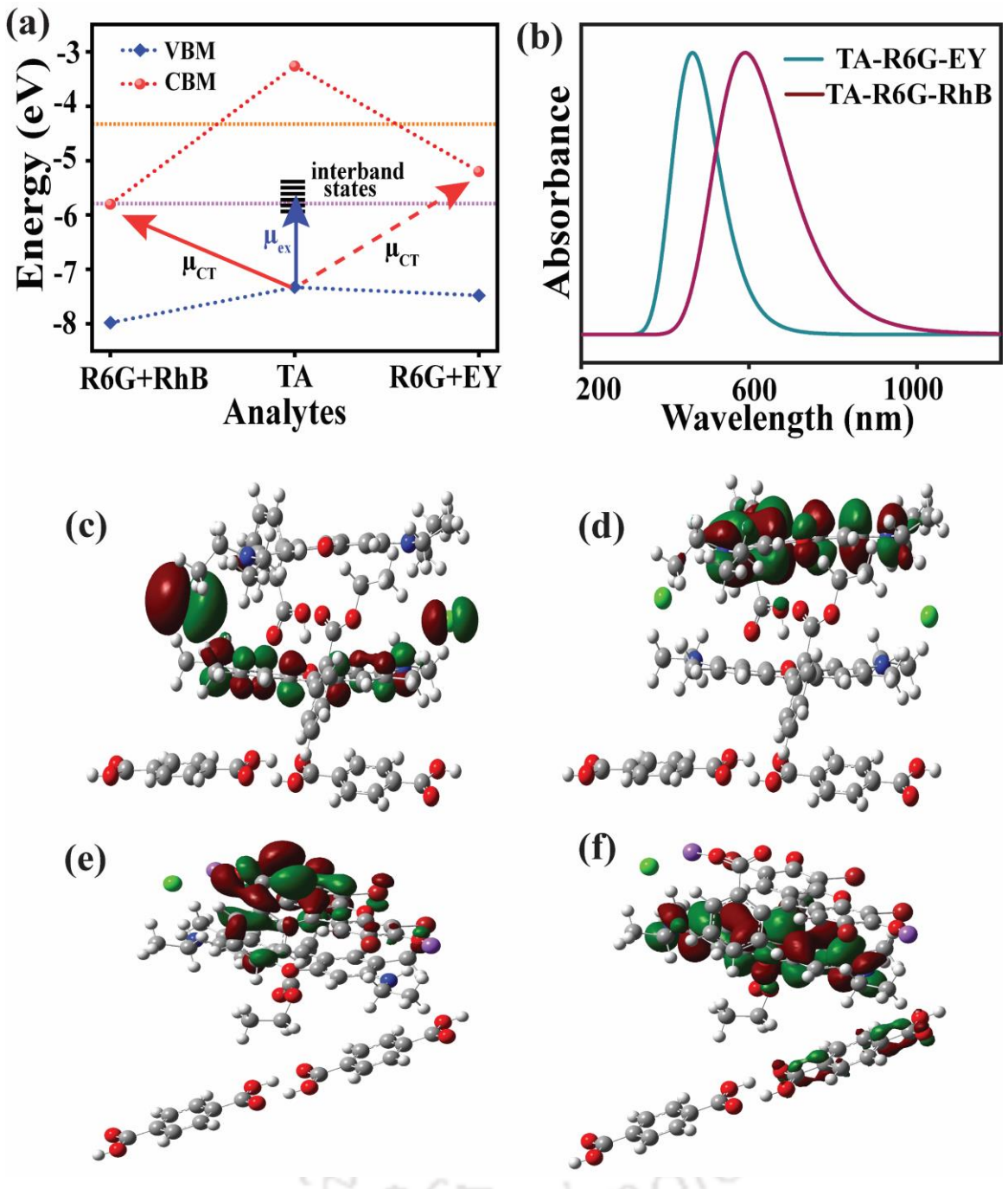

Figure 3.21 Under standing of molecular cooperativity in terms of charge transfer transitions and hybrid orbitals. (a) Diagram of HOMO-LUMO energy gaps with respect to vacuum of R6G+RhB and R6G+EY in comparison with valence and conduction band edges of TA microcrystal obtained from UPS analyses. (b) Theoretical normalized absorbance spectra of TA-R6G-RhB (brown) and TA-R6G-EY (red) hybrid systems. (c, d) HOMO and LUMO (respectively) of TA-R6G-RhB hybrid system generated through DFT calculations. (e,f) HOMO and LUMO (respectively) of TA-R6G-EY hybrid system generated through DFT calculations.

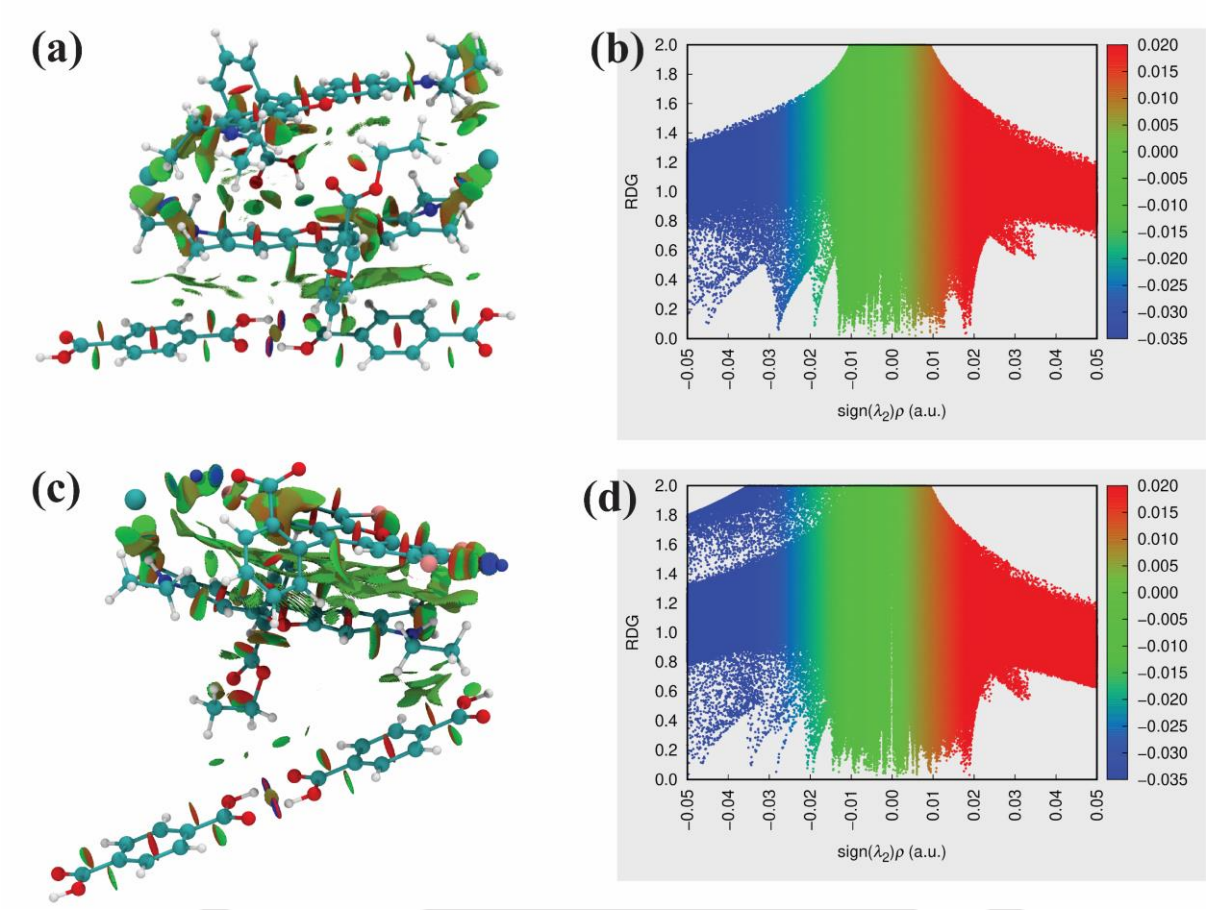

Figure 3.22 Cooperativity assessment in terms of non-covalent interactions. (a,b) Diagrams displaying non-covalent interactions (NCI) of the TA-R6G-RhB system as represented by the quantum-based color-filled RDG iso-surface approach. (c,d) Diagrams displaying non-covalent interactions (NCI) of the TA-R6G-EY system as represented by the quantum-based color-filled RDG iso-surface approach.

The energy mismatch of the excited state (as also supported by the UPS analysis) with the external laser excitation might be the reason for the highly quenched Raman spectra (Figure 3.21b). Further, the frontier molecular orbital analysis of TA-R6G-EY system showed that HOMO is delocalized over EY molecule and LUMO is delocalized over R6G molecule. It was evident from the optimized structure of the TA-R6G-EY system that the interactions between R6G and EY are so dominant that the interaction between TA and R6G becomes less significant, resulting in severely quenched Raman spectra. (Figure 3.21e, f).

We were then interested in gauging the weak interactions that cause the positive and negative Raman scattering cooperativity in the two-molecule systems as deposited on the TA microcrystals. For this, we used a quantum mechanics-based noncovalent interaction reduced density gradient (NCI-RDG) approach (details in theoretical calculation section). The results indicated the important roles steric repulsion, nonbonded hydrophobic and hydrogen bonding

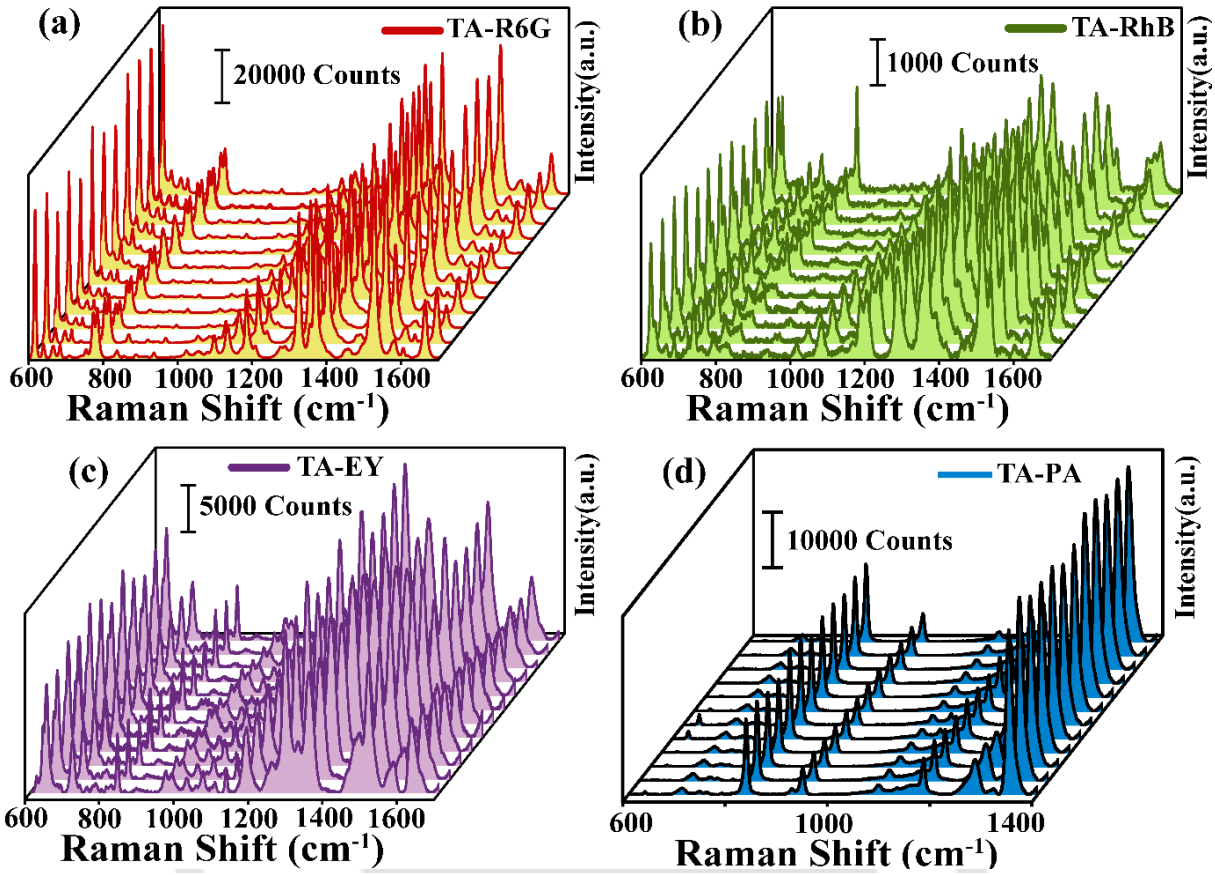

Figure 3.23 SERS spectra for (a) 25 µM R6G (b) 25 µM RhB (c) 50 µM EY and (d) 100 µM PA (as in the initial mixture) acquired on 12 randomly chosen locations of the TA-R6G, TA-RhB, TA-EY, TA-PA substrate respectively under laser excitation of 785 nm.

interactions. In the case of TA-R6G-RhB system, the van der Waals interaction between R6G and TA crystal is stronger than the nonbonded interactions between R6G and RhB (Figure 3.22a, b). These intermolecular interactions are moderate and involve the localized molecular bonds. As a result, cooperative Raman enhancement occurs. In the TA-R6G-EY system, the interaction between R6G and EY is more pronounced than between R6G and the crystal (Figure 3.22c, d). This sort of nonbonded interactions may also originate from the electrostatic interactions as R6G is a cationic dye and EY is an anionic dye.[49,50] Thus, when combined, ionic interactions reduce their contact with TA microcrystal and results in flat Raman spectra. It also lends credence to TA's important role in the Raman amplification of the superimposed dye molecule.

The above experimental results as substantiated by computational calculations indicated that n-type π-conjugated organic crystals of small molecule having significant inter-band transitions can perform well as a potential molecule-specific cooperative SERS platform through chemical enhancement mechanism. The cooperativity is based on the directional non-covalent

interaction producing hybrid orbitals and energy-gap guided transitions matching with the incoming laser light energy.

3.3 Reproducibility

SERS spectral reproducibility and uniformity across the material, particularly for thin film samples, are crucial for regular analytical investigations. Raman measurements with dried liquid droplets typically comprise the accumulation of a solid in the form of a coffee ring with a radius equal to that of the wedged droplet. The accumulation of the deposited compound is presumed to be nearly identical along the circumference.[51] To investigate the consistency of the SERS signals for R6G, RhB, EY, and PA, we recorded Raman spectra from 12 arbitrarily selected areas around the rim of the deposited substrates (Figure 3.23). In case of binary mixture, reproducibility and uniformity has also been tested by collecting Raman spectra form different spots (Figure 3.24). As the spectra demonstrate, (Figure 3.23, 3.24), the results showed consistent and repeatable SERS signals around the entire circumference, along with a Raman peak of TA microcrystal at 632 and 832 cm^{-1} (Figure 3.18), which is probably indicative

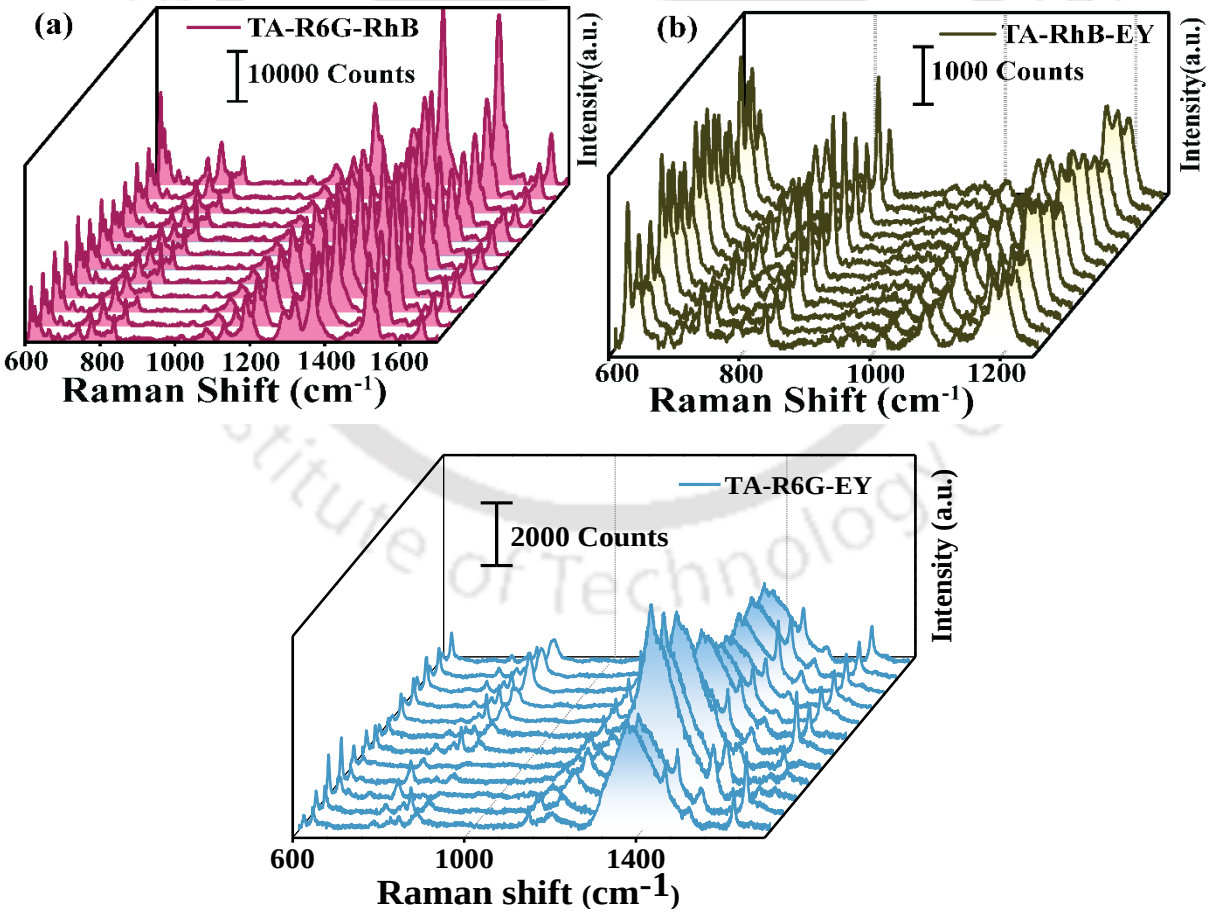

Figure 3.24 SERS spectrum of (a) R6G and RhB (b) RhB and EY (c) R6G-EY binary mixture on TA microcrystals acquired on 12 randomly chosen locations at laser excitations of 785 nm.

of the homogeneous probe molecule deposition. Furthermore, Raman mapping of R6G, RhB, EY, PA, R6G-RhB, R6G-EY and RhB-EY (Figure 3.25-3.31) analytes over the crystals showed uniform deposition of probe molecules over the crystals with consistent Raman signals. This demonstrates TA's competence as a SERS substrate and the repeatability and homogeneity of the Raman spectrum around the circumference of the deposited target molecules. Therefore, solid-state assessments of binary molecules on the surface of a molecular microcrystals could be regarded as a reliable technique for capturing molecular-specific SERS on the circumference of the deposited substrate.

3.4 Conclusion

In conclusion, we have shown that π-conjugated electron-rich TA microcrystals displayed exceptional SERS property. The emergence of a prominent absorbance band in the UV-Vis DRS spectra of the microcrystals in the NIR region (800 nm) assisted in investigating probe molecules being placed on their surfaces by Raman signal enhancement utilising 785 nm laser excitations. The TA microcrystals displayed good EFs of 1.5×10^6, 3.2×10^4, 7.17×10^4 , $\sim1.3\times10^4$ for R6G, RhB, EY, and PA, respectively. Importantly, the microcrystals showed cooperative Raman amplification or reduction in the cases of binary mixtures of dyes based on their noncovalent interactions. The results indicated the potential of the TA microcrystals or similar organic molecule-based microcrystals for Raman cooperativity hitherto unreported.

These findings provide helpful information for the future construction of metal-free semiconductor-based SERS platforms and represent a significant advancement in applying SERS to bio- and chemical sensing. Chemical impurity doping or charge infusion (such as using gate bias) might modify band positions and infuse free charge carriers into organic semiconductor devices, potentially producing localized surface plasmons. This might be beneficial in furthering the SERS EFs of organic semiconducting substrates. Altogether π-conjugated skeletons of organic semiconductors provide a superb foundation for practically limitless structural modifications, their chemical architectures might be specially tuned to enhance charge transfer to a specific analyte molecule.

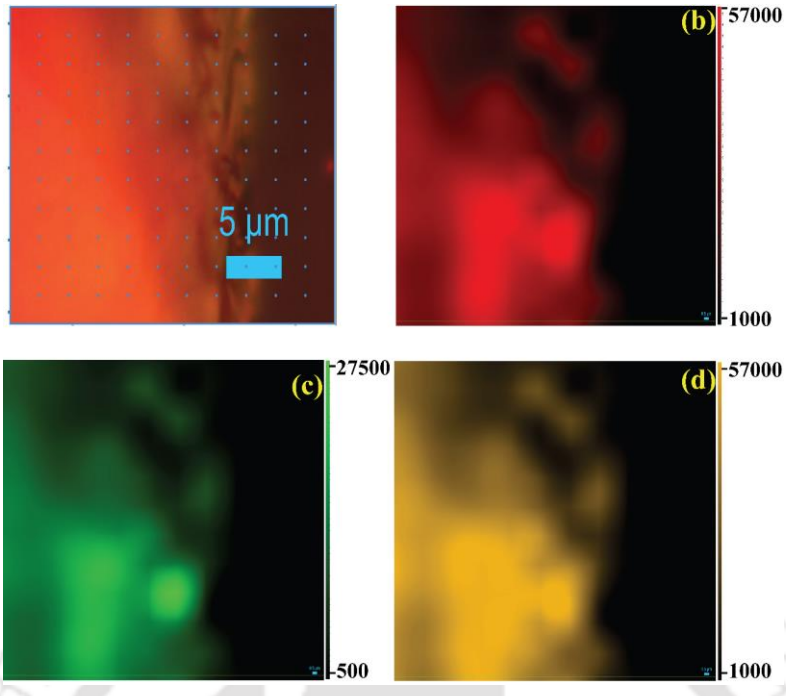

Figure. 3.25 Raman intensity mapping of R6G on TA as SERS substrate(TA-R6G). (a) Image of mapping region. (b−d) Intensity profiles of the characteristic Raman peaks of R6G occurring at 611, 1183, and 1519 cm^{-1}, respectively.

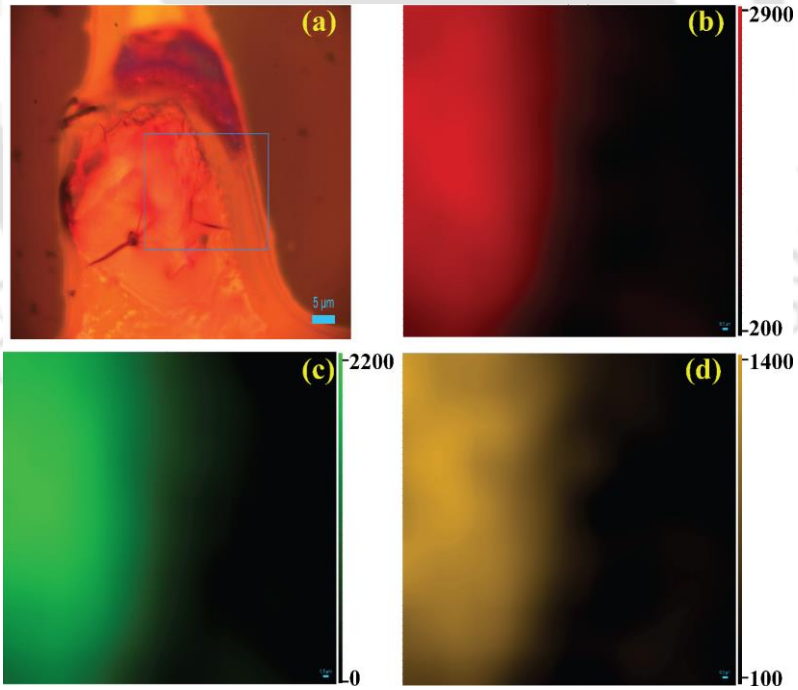

Figure 3.26 Raman intensity mapping of RhB on TA as SERS substrate (TA-RhB). (a) Image of the mapping region. (b−d) Intensity profile of the characteristic Raman peaks of RhB occurring at 621, 735, and 1280 cm^{-1}, respectively.

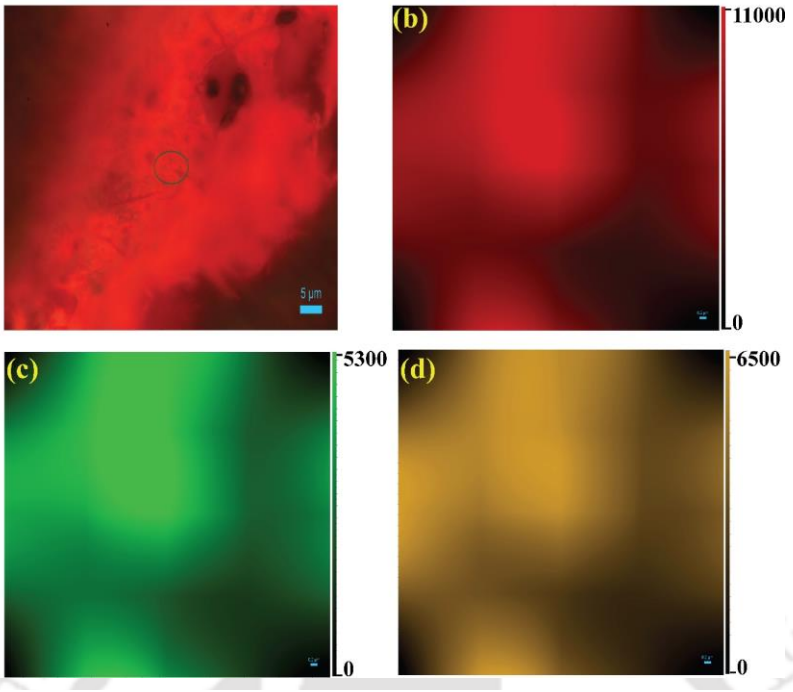

Figure 3.27 Raman intensity mapping of EY on TA as SERS substrate (TA-EY). (a) Image of the mapping region. (b–d) intensity profile of the Raman peaks at 644, 715, and 1182 cm^{-1}, respectively.

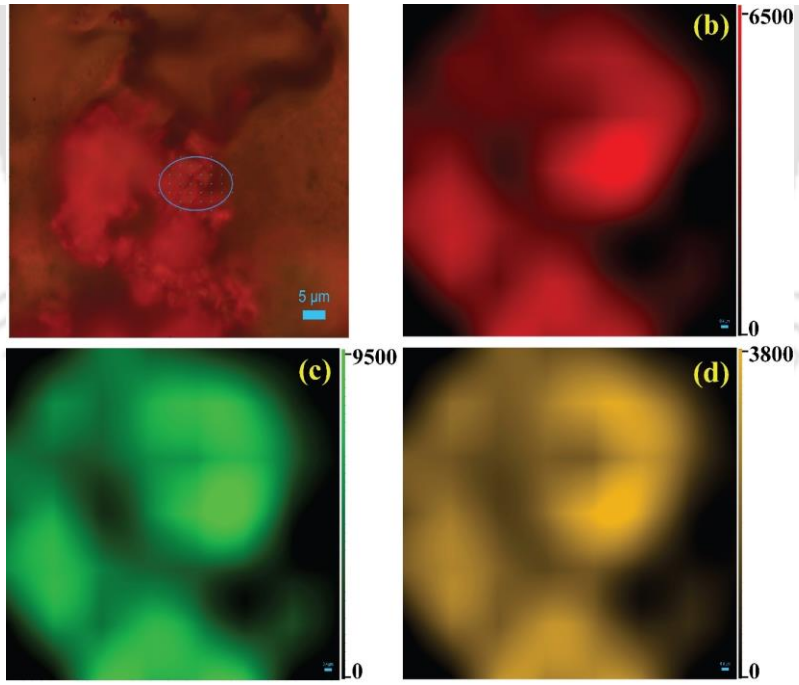

Figure 3.28 SERS intensity mapping of an R6G-RhB combination on a TA substrate (TA-R6G-Rhb). (a) Image of the mapping region. (b-d) Raman intensity profile with peaks at 623-634, 833, and 1129 cm^{-1}, respectively.

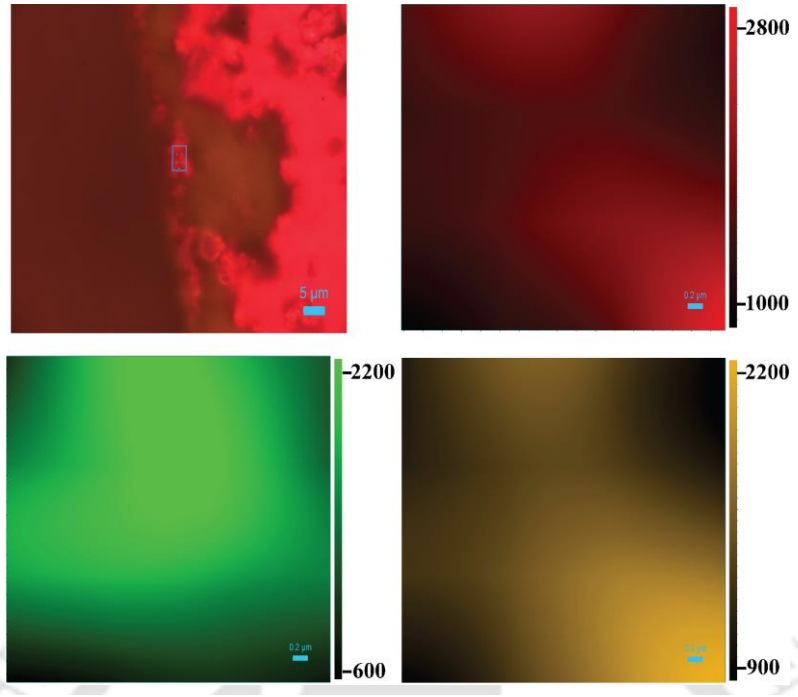

Figure 3.29 SERS intensity mapping of an RhB-EY combination on a TA substrate (TA-RhB-EY). (a) Image of the mapping region. (b-d) Raman intensity profile with peaks at 621, 833, and 1182-95 cm^{-1}, respectively.

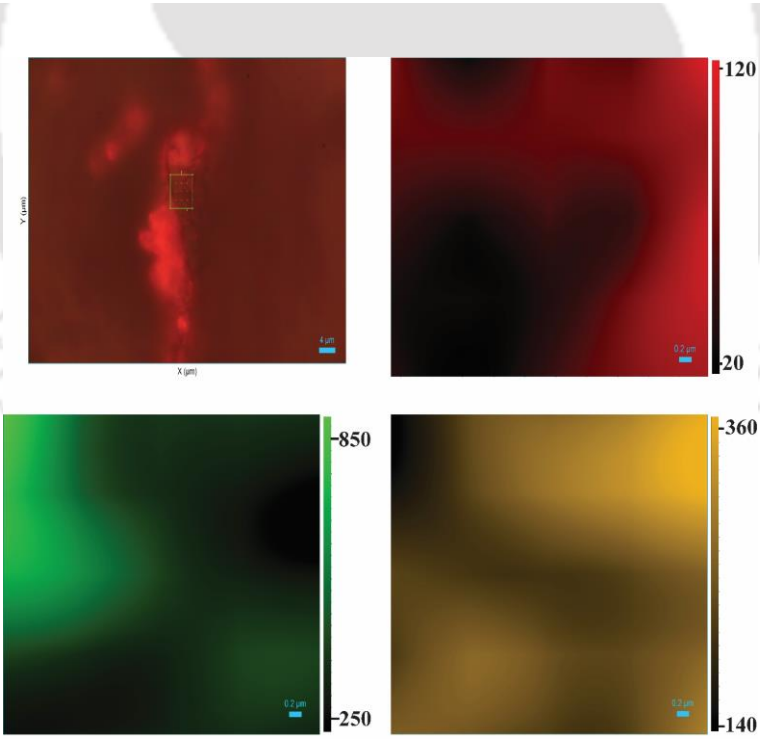

Figure 3.30 Raman intensity mapping of an R6G-EY combination on a TA as a SERS substrate (TA-R6G-EY). (a) Image of the mapping region. (b-d) Raman intensity profile with peaks at 611, 833, and 1134 cm^{-1}, respectively.

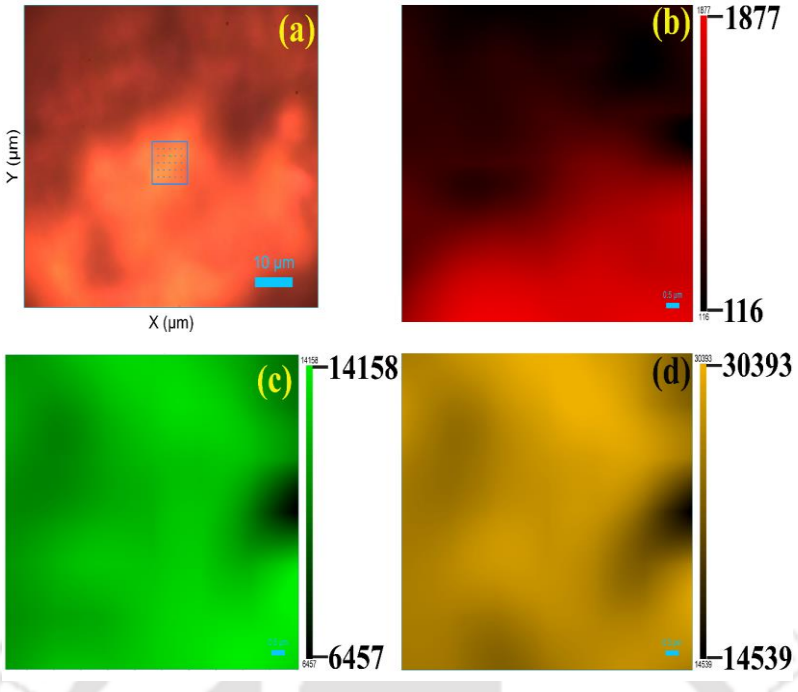

Figure 3.31 Raman intensity mapping of PA on TA as SERS substrate (TA-PA). (a) Image of the mapping region. (b–d) Intensity profile of the characteristic Raman peaks of PA occurring at 633, 830, and 1344 cm^{-1}, respectively.

Reference

1. Paul, R.; Mitra, A.; Paul, S., A computational approach on the stereoselective binding of peptides from aqueous medium with endo-functionalized molecular tubes. *Phys. Chem. Chem. Phys.* **2021,** *23* (39), 22703-22717.
2. Bhakat, A.; Paul, S.; Chattopadhyay, A., Molecular Specificity in the Intense Surface-Enhanced Raman Scattering on Copper(II) 8-Hydroxyquinoline Microcrystals. *The J. Phys. Chem. C* **2023,** *127* (10), 5169-5177.
3. Adar, F.; Lee, E.; Mamedov, S.; Whitley, A., Experimental Evaluation of the Depth Resolution of a Raman Microscope. *Microscopy and Microanalysis* **2010,** *16* (S2), 360-361.
4. Sun, H.; Cong, S.; Zheng, Z.; Wang, Z.; Chen, Z.; Zhao, Z., Metal-Organic Frameworks as Surface Enhanced Raman Scattering Substrates with High Tailorability. *J. Am. Chem. Soc.* **2019,** *141* (2), 870-878.
5. Wang, J.; Yang, Y.; Li, H.; Gao, J.; He, P.; Bian, L.; Dong, F.; He, Y., Stable and tunable plasmon resonance of molybdenum oxide nanosheets from the ultraviolet to the near-infrared region for ultrasensitive surface-enhanced Raman analysis. *Chem. Sci.* **2019,** *10* (25), 6330-6335.

6. Giannozzi, P.; Baroni, S.; Bonini, N.; Calandra, M.; Car, R.; Cavazzoni, C.; Ceresoli, D.; Chiarotti, G. L.; Cococcioni, M.; Dabo, I., et al. QUANTUM ESPRESSO: a modular and open-source software project for quantum simulations of materials, *J. Phys.: Condens. Matter* **2009,** *21* (39), 395502.
7. Perdew, J. P.; Yue, W., Accurate and simple density functional for the electronic exchange energy: Generalized gradient approximation. *Phys. Rev. B, Condens Matter.* **1986,** *33* (12), 8800-8802.
8. Perdew, J. P.; Ruzsinszky, A.; Csonka, G. I.; Vydrov, O. A.; Scuseria, G. E.; Constantin, L. A.; Zhou, X.; Burke, K., Restoring the density-gradient expansion for exchange in solids and surfaces. *Phys. Rev. lett.* **2008,** *100* (13), 136406.
9. Frisch, M. J.; Trucks, G. W.; Schlegel, H. B.; Scuseria, G. E.; Robb, M. A.; Cheeseman, J. R.; Scalmani, G.; Barone, V.; Petersson, G. A.; Nakatsuji, H., et al. *Gaussian 16 Rev. C.01*, Wallingford, CT, **2016**.
10. Hanwell, M. D.; Curtis, D. E.; Lonie, D. C.; Vandermeersch, T.; Zurek, E.; Hutchison, G. R., Avogadro: an advanced semantic chemical editor, visualization, and analysis platform. *J. Cheminform.* **2012,** *4* (1), 17.
11. Johnson, E. R.; Keinan, S.; Mori-Sánchez, P.; Contreras-García, J.; Cohen, A. J.; Yang, W., Revealing Noncovalent Interactions. *J. Am. Chem. Soc.* **2010,** *132* (18), 6498-6506.
12. Lu, T.; Chen, F., Multiwfn: A multifunctional wavefunction analyzer. *J. Comput. Chem.* **2012,** *33* (5), 580-592.
13. Humphrey, W.; Dalke, A.; Schulten, K., VMD: Visual molecular dynamics. *J. Mol. Graphics* **1996,** *14* (1), 33-38.
14. Heyd, J.; Scuseria, G. E.; Ernzerhof, M., Erratum: "Hybrid functionals based on a screened Coulomb potential". *J. Chem. Phys.* **2006,** *124* (21), 219906.
15. Blaudeau, J.-P.; McGrath, M. P.; Curtiss, L. A.; Radom, L., Extension of Gaussian-2 (G2) theory to molecules containing third-row atoms K and Ca. *J. Chem. Phys.* **1997,** *107* (13), 5016-5021.
16. Zhao, Y.; Truhlar, D. G. The M06 suite of density functionals for main group thermochemistry, thermochemical kinetics, noncovalent interactions, excited states, and transition elements: two new functionals and systematic testing of four M06-class functionals and 12 other functionals. *Theor. Chem. Acc.* **2008**, 120, 215−241.
17. Becke, A. D., A new mixing of Hartree–Fock and local density-functional theories. *J. Chem. Phys.* **1993,** *98* (2), 1372-1377.

18. Lee, C.; Yang, W.; Parr, R. G., Development of the Colle-Salvetti correlation-energy formula into a functional of the electron density. *Phys. Rev. B: Condens. Matter* **1988,** *37* (2), 785-789.

19. Rassolov, V. A.; Ratner, M. A.; Pople, J. A.; Redfern, P. C.; Curtiss, L. A., 6-31G* basis set for third-row atoms. *J. Comput. Chem.* **2001,** *22* (9), 976-984.

20. Berman, N.; Ruof, C.; Howard, H., Ultraviolet Absorption Spectra of Benzencarboxylic Acids. *Anal. Chem.* **1951,** *23* (12), 1882-1883.

21. Davey, R. J.; Maginn, S.; Andrews, S. J.; Black, S. N.; Buckley, A. M.; Cottier, D.; Dempsey, P.; Plowman, R.; Rout, J. E.; Stanley, D. R.; Taylor, A. J. M. C.; Crystals, L., Morphology and Polymorphism of Terephthalic Acid. *J. CHEM. SOC. FARADAY TRANS.,* **1994,** *242*, 79-90.

22. Karothu, D. P.; Weston, J.; Desta, I. T.; Naumov, P., Shape-Memory and Self-Healing Effects in Mechanosalient Molecular Crystals. *J. Am. Chem. Soc.* **2016,** *138* (40), 13298-13306.

23. Chen, X.; Liu, L.; Yu, P. Y.; Mao, S. S., Increasing Solar Absorption for Photocatalysis with Black Hydrogenated Titanium Dioxide Nanocrystals. *Science* **2011,** *331* (6018), 746-750.

24. Morris, J.; Yoshihara, K. J. M. P. , **1978**, *36*, 993-1003.

25. Zarrabi, N.; Sandberg, O. J.; Meredith, P.; Armin, A., Subgap Absorption in Organic Semiconductors. *J. Phys. Chem. Lett.* **2023**, *14*, 3174-3185.

26. Ma, H.; Peng, Q.; An, Z.; Huang, W.; Shuai, Z., Efficient and Long-Lived Room-Temperature Organic Phosphorescence: Theoretical Descriptors for Molecular Designs. *J. Am. Chem. Soc.* **2019**, *141*, 1010-1015.

27. Pritchina, E. A.; Kolesov, B. A., Raman spectra of terephthalic acid crystals in the temperature range 5K–300K. *Spectrochim. Acta, Part A* **2018,** *202*, 319-323.

28. Yong, M.; Wei, H.; Xiu-neng, S.; Chuan-kui, W., Density Functional Theory Study on Raman Spectra of Rhodamine Molecules in Different Forms. *Chin. J. Chem. Phys.* **2014,** *27* (3), 291-296.

29. Zhong, F.; Wu, Z.; Guo, J.; Jia, D., Porous Silicon Photonic Crystals Coated with Ag Nanoparticles as Efficient Substrates for Detecting Trace Explosives Using SERS. *Nanomaterials (Basel)* **2018,** *8* (11).

30. Watanabe, H.; Hayazawa, N.; Inouye, Y.; Kawata, S., DFT Vibrational Calculations of Rhodamine 6G Adsorbed on Silver: Analysis of Tip-Enhanced Raman Spectroscopy. *The J. Phys. Chem. B* **2005,** *109* (11), 5012-5020.

31. Lin, S.; Hasi, W.-L.-J.; Lin, X.; Han, S.-q.-g.-w.; Lou, X.-T.; Yang, F.; Lin, D.-Y.; Lu, Z.-W., Rapid and sensitive SERS method for determination of Rhodamine B in chili powder with paper-based substrates. *Anal. Methods* **2015,** *7* (12), 5289-5294.

32. Zhang, J.; Li, X.; Sun, X.; Li, Y., Surface Enhanced Raman Scattering Effects of Silver Colloids with Different Shapes. *J. Phys. Chem. B* **2005,** *109* (25), 12544-12548.

33. Greeneltch, N. G.; Davis, A. S.; Valley, N. A.; Casadio, F.; Schatz, G. C.; Van Duyne, R. P.; Shah, N. C., Near-Infrared Surface-Enhanced Raman Spectroscopy (NIR-SERS) for the Identification of Eosin Y: Theoretical Calculations and Evaluation of Two Different Nanoplasmonic Substrates. *The J. Phys. Chem. A* **2012,** *116* (48), 11863-11869.

34. Byram, C.; Moram, S. S. B.; Soma, V. R., SERS based detection of multiple analytes from dye/explosive mixtures using picosecond laser fabricated gold nanoparticles and nanostructures. *Analyst* **2019,** *144* (7), 2327-2336.

35. Adar, F.; Lee, E.; Mamedov, S.; Whitley, A., Experimental Evaluation of the Depth Resolution of a Raman Microscope. *Microscopy and Microanalysis* **2010,** *16* (S2), 360-361.

36. Wang, J.; Yang, Y.; Li, H.; Gao, J.; He, P.; Bian, L.; Dong, F.; He, Y., Stable and tunable plasmon resonance of molybdenum oxide nanosheets from the ultraviolet to the near-infrared region for ultrasensitive surface-enhanced Raman analysis. *Chem. Sci.* **2019,** *10* (25), 6330-6335.

37. Morton, S. M.; Jensen, L., Understanding the Molecule−Surface Chemical Coupling in SERS. *J. Am. Chem. Soc.* **2009,** *131* (11), 4090-4098.

38. Valley, N.; Greeneltch, N.; Van Duyne, R. P.; Schatz, G. C., A Look at the Origin and Magnitude of the Chemical Contribution to the Enhancement Mechanism of Surface-Enhanced Raman Spectroscopy (SERS): Theory and Experiment. *J. Phys. Chem. Lett.* **2013,** *4* (16), 2599-2604.

39. Birke, R. L.; Lombardi, J. R.; Saidi, W. A.; Norman, P., Surface-Enhanced Raman Scattering Due to Charge-Transfer Resonances: A Time-Dependent Density Functional Theory Study of Ag13-4-Mercaptopyridine. *J. Phys. Chem. C* **2016,** *120* (37), 20721-20735.

40. Schlücker, S., Surface-Enhanced Raman Spectroscopy: Concepts and Chemical Applications. *Angew. Chem. Int. Ed.* **2014,** *53* (19), 4756-4795.

41. Otto, A., The 'chemical' (electronic) contribution to surface-enhanced Raman scattering. *J. Raman Spectrosc.* **2005,** *36* (6-7), 497-509.
42. Zhou, X.; Zhao, X.; Gu, S.; Gao, K.; Xie, F.; Wang, X.; Tang, Z., A novel sensitive ACNTs–MoO2 SERS substrate boosted by synergistic enhancement effect. *Phys. Chem. Chem. Phys.* **2021,** *23* (36), 20645-20653.
43. Demirel, G.; Usta, H.; Yilmaz, M.; Celik, M.; Alidagi, H. A.; Buyukserin, F., Surface-enhanced Raman spectroscopy (SERS): an adventure from plasmonic metals to organic semiconductors as SERS platforms. *J. Mat. Chem. C* **2018,** *6* (20), 5314-5335.
44. Lombardi, J. R.; Birke, R. L., Theory of Surface-Enhanced Raman Scattering in Semiconductors. *J. Phys. Chem. C* **2014,** *118* (20), 11120-11130.
45. Morton, S. M.; Jensen, L., Understanding the Molecule−Surface Chemical Coupling in SERS. *J. Am. Chem. Soc.* **2009,** *131* (11), 4090-4098.
46. Ding, K.; Yin, S.; Li, Z.; Jiang, S.; Yang, Y.; Zhou, W.; Zhang, Y.; Huang, B., Observing Noncovalent Interactions in Experimental Electron Density for Macromolecular Systems: A Novel Perspective for Protein–Ligand Interaction Research. *J. Chem. Inf. Model.* **2022,** *62* (7), 1734-1743.
47. Contreras-García, J.; Yang, W.; Johnson, E. R., Analysis of Hydrogen-Bond Interaction Potentials from the Electron Density: Integration of Noncovalent Interaction Regions. *J. Phys. Chem. A* **2011,** *115* (45), 12983-12990.
48. Ercolani, G., Assessment of Cooperativity in Self-Assembly. *J. Am. Chem. Soc.* **2003,** *125* (51), 16097-16103.
49. Stefancu, A.; Iancu, S. D.; Leopold, N., Selective Single Molecule SERRS of Cationic and Anionic Dyes by Cl– and Mg2+ Adions: An Old New Idea. *J. Phys. Chem. C* **2021,** *125* (23), 12802-12810.
50. Gopinathan, R.; Bhowal, A.; Garlapati, C., Adsorption Studies of Some Anionic Dyes Adsorbed by Chitosan and New Four-Parameter Adsorption Isotherm Model. *J. Chem. Eng. Data* **2019,** *64* (6), 2320-2328.
51. Wang, W.; Yin, Y.; Tan, Z.; Liu, J., Coffee-ring effect-based simultaneous SERS substrate fabrication and analyte enrichment for trace analysis. *Nanoscale* **2014,** *6* (16), 9588-9593.

Chapter 4

Room Temperature Persistent Phosphorescence of Aggregated Gold Nanoclusters under Molecular crystal confinements

Herein, we have demonstrated that the aggregation of water-dispersible AuNCs doped inside an organic crystal induced reversible fluorescence to phosphorescence switching with excitation tuneable emission at room temperature. In addition, if the host crystal has an emissive state, there can be an energy transfer from the long-lived singlet or triplet state of the crystal to the singlet or triplet state of the aggregated NCs. For a test case, we have doped histidine-stabilized AuNCs (HIS-AuNCs) inside histidine crystals (HIS-AuNCs-HIS) and isophthalic acid crystals (HIS-AuNCs-IPA), respectively, and glutathione-stabilized AuNCs (GSH-AuNCs) inside histidine crystals (GSH-AuNCs-HIS). The doped crystals showed solvent-processable phosphorescence. Upon dissolution of the crystal with appropriate solvent, phosphorescence vanished and a weak delayed fluorescence was observed. In case of HIS-AuNCs-HIS and HIS-AuNCs-IPA composite crystals the phosphorescence lifetime was in milliseconds whereas that for GSH-AuNCs-HIS was in microseconds. In addition, for His-AuNCs-IPA doped crystals, there is energy transfer from the singlet sate of the IPA crystal to the guest AuNCs singlet state along with the triplet-triplet energy transfer between the same. The possible energy states and interactions involved in agglomerated NCs was accounted for through DFT calculations. The molecular docking approach was employed to understand the possible interactions and bonding between the host crystals and the guest NCs that led to origination of phosphorescence. These findings provide an easy route for solvent-processable

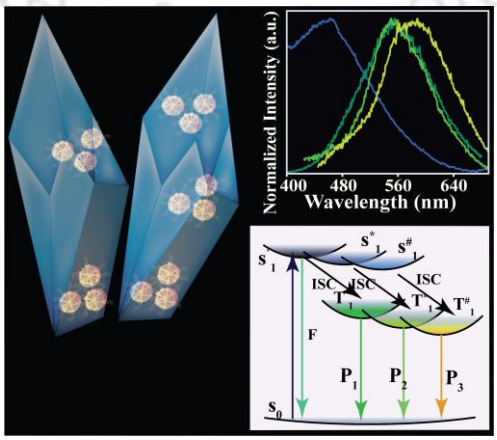

Scheme 4.1 Brief graphical representation of the work demonstrated in chapter 4.

fluorescence to phosphorescence switching at room temperature and provide significant insight on the tunability of PL property of dopant i.e., metal nanoclusters, depending on the surrounding crystalline environment and compactness of the confinement.

4.1 Experimental Section

4.1.1 Materials

L-histidine (≥99%, 155.15 g mol^{-1}), isophthalic acid (99%, 166.13 g mol^{-1}), L-glutathione reduced(≥98%, 307.32), tetrachloroauric acid solution $HAuCl_4$ and methanol (99%, 60.10 g mol^{-1}) and were purchased from Sigma-Aldrich India. All materials were used without any further purification. Elix grade water from a MilliQ purification system was used for the experiments.

4.1.2 Synthesis of HIS-AuNCs

L-histidine stabilised AuNCs (HIS-AuNCs) were prepared by following a previously reported method with slight modification.[1,2] At first, 0.3 millimole (164.6 mg) of L-histidine was dissolved in 3 mL of water. After that, 1 mL of 10 mM $HAuCl_4$ water solution was added to the histidine solution under stirring condition. The reaction was allowed to stir for 2.5 h at room temperature and the reaction mixture was stored at 4 ºC in dark and used for further experiments.

4.1.3 Synthesis of GSH-AuNCs

L-glutathine reduced stabilised AuNCs were prepared by following a previously reported method with slight modification.[3] At first, 0.015 millimole (164.6 mg) of L-glutathione was dissolved in 3 mL of water. After that, 1 mL of 10 mM $HAuCl_4$ water solution was added to the histidine solution under stirring condition at 70 ºC. The reaction was allowed to stir for 24 h at 70 ºC and the reaction mixture was stored at 4 ºC in dark and used for further experiments.

4.1.4 Synthesis of HIS-AuNCs-HIS doped crystals

First 0.5 mM L-histidine was dissolved in 10 mL of water in a 250 mL beaker. One whole reaction batch of HIS-AuNCs reaction mixture (4 mL) was added to it and mixed well. The solution was set to dry over a hot plat at 40 ºC for complete solvent evaporation. When the reaction mixture was completely evaporated the as prepered crystals were then taken in centrifudge tube with (1:9) water/methanol mix solvent and centrifudged twice at 15 k for 10 min. The purified as synthesised crystals were stored in methanol at 4 ºC.

4.1.5 Synthesis of GSH-AuNCs-HIS doped crystals

First 0.5 mM L-histidine was dissolved in 10 mL of water in a beaker. One whole reaction batch of GSH-AuNCs reaction mixture (4 mL) was added to it and mixed well. The total

solution was set to dry over a hot plat at 40 ºC for complete solvent evaporation. When the reaction mixture was completely evaporated the as prepered crystals were then taken in centrifudge tube with (1:9) water/methanol mix solvent and centrifudged twice at 15 k for 10 min. The purified as synthesised crystals were stored in methanol at 4 ºC.

4.1.6 Synthesis of HIS-AuNCs-IPA doped crystals

First 0.5 mM isophthalic was dissolved in 32 mL of methanol/water (3:1) mix solvent in a beaker. Two batch of HIS-AuNCs reaction mixture (8 mL) was added to it and mixed well. The total solution was set to dry over a hot plat at 40 ºC for solvent evaporation. When the reaction mixture was 90% evaporated the as prepered crystals were then taken in centrifudge tube in water and centrifudged twice at 15 k for 10 min. The purified as synthesised crystals were stored in methanol at 4 ºC.

4.1.7 Theoretical calculation

The GAUSSIAN 16 code optimized the modelled AuNC and its aggregated dimer, followed by time-dependent density functional theory (TD-DFT) calculations.[4] The M06-2X functional and Gen basis-set was used for the optimization using density functional theory (DFT) studies.[5] LanL2DZ[6] pseudopotential was applied for Au atoms and 6-311++G(d,p)[7] basis set for C, N, O and H atoms. TD-DFT computations were carried out in the gas phase. Docking studies were employed for HIS-AuNC with histidine and IPA crystal separately in AutoDockTools version 1.5.7.[8]

4.1.8 Characterization

Field emission transmission electron microscopy (TEM) analyses were done using a JEOL JEM-2100F FETEM instrument (acceleration voltage of 200 kV). A Rigaku TTRAX III diffractometer, running with a CuKα source (λ = 1.54 Å), was used to analyze the powder X-ray diffractin (XRD) pattern of the samples. UV−vis and fluorescence spectroscopy were performed using a Perkin Elmer Lambda 365+ spectrophotometer and Horiba Fluoromax-4 spectrofluorometer, respectively. Phosphorescence emission, excitation were measured in Horiba Fluoromax-4 spectrofluorometer. Phosphorescnece lifetime was measured in Horiba Fluoromax-4 and edinburgh FLS-1000 instrument. Time-resolved photoluminescence (TRPL) spectroscopy was done with Edinburgh Life-Spec-II spectrofluorometer. Fluorescence microscopy images were captured in OLYMPUS BX51 instrument in blue light excitation.

4.1.9 Average lifetime (τ_{av}), radiative (K_r) and non-radiative (K_{nr}) recombination rate constant calculation

Average lifetime values (τ_{av}) were calculated using equation 5.2. Further, calculations of radiative decay rate constant (K_r) and non-radiative decay rate constant (K_{nr}) were performed using equation 5.3 and equation 5.4.

$$\tau_{av} = \frac{\sum_i \alpha_i \tau_i^2}{\sum_i \alpha_i \tau_i} \quad 5.2$$

$$K_r = \frac{\varphi_D}{\tau_{av}} \quad 5.3$$

$$K_{nr} = \frac{1-\varphi_D}{\tau_{av}} \quad 5.4$$

Here, φ_D refers to the measured quantum yield value. Also, α_i and τ_i correspond to pre-exponential factor and decay time of the *i*-th component, respectively.

Table 4.1 The fluorescence lifetime decay parameters of HIS-AuNCs and GSH-AuNCs at room temperature and corresponding abosolute PLQY

Samples	λ^2	1st component (α_1) (%)	1st component Lifetime (τ_1) (ns)	2nd component (α_2) (%)	2nd component lifetime (τ_2) (ns)	3rd component (α_1) (%)	3rd component Lifetime (τ_1) (ns)	Average lifetime (τav) (ns)	PLQY (%)
GSH-AuNCs	1.1	6.11	0.014	93.89	12.8	-	-	12.8±0.5	0.58 ±0.04
His-AuNCs	1.05	36.9	0.92	56.5	3.66	6.6	0.009	3.26±0.2	0.7± 0.05 %
HIS-AuNCs -IPA λ_{ex}292-λ_{em} 360nm	1.08	16.5	0.011	83.5	2.70	-	-	2.70±0.18	-
IPA λ_{ex}292-λ_{em} 360 nm	1.09	8.6	0.008	91.4	3.041	-	-	3.04±0.14	-

Table 4.2 The phosphoresence lifetime decay parameter of doped crystal system at room temperature with abosolute PLQY

Samples	λ^2	α_1 (%)	τ_1 (ms)	α_2 (%)	τ_2 (ms)	α_3 (%)	τ_3 (ms)	τav (ms)	PLQY (%)
GSH-AuNCs-HIS	0.99	89.4	0.016	10.1	0.045	0.56	0.39	0.06±0.004	25±0.6%
HIS-AuNCs-HIS	1.3	63.4	0.652	30.2	4.231	6.4	18.185	9.38±0.8	0.78±0.06%
HIS-AuNCs-IPA λ_{ex}360- λ_{em} 550 nm	0.99	45	0.083	32	0.959	23	6.312	5.24±0.3	1.15±0.08%
HIS-AuNCs-IPA λ_{ex}420- λ_{em} 590 nm	0.99	46	0.227	38	1.202	16	6.277	4.47±0.25	-
HIS-AuNCs-IPA λ_{ex}295- λ_{em} 500 nm	0.92	71	0.306	18.5	2.761	10.5	31.447	26.2±1.5	-
IPA λ_{ex}295- λ_{em} 500 nm	0.93	71	4.941	29	40.783	-	-	32.6±1.1	-

4.2 Result and Discussion

HIS-AuNCs and GSH-AuNCs were synthesized by reducing $HAuCl_4$ solution with L-histidine and glutathione ligands in water, respectively.[1] The UV-vis absorbance spectrum of HIS-AuNCs consisted of a strong peak at 340 nm (Figure 4.2a). Under UV light (365 nm), the dispersion displayed a bright blue-green luminescence. HIS-AuNCs showed excitation

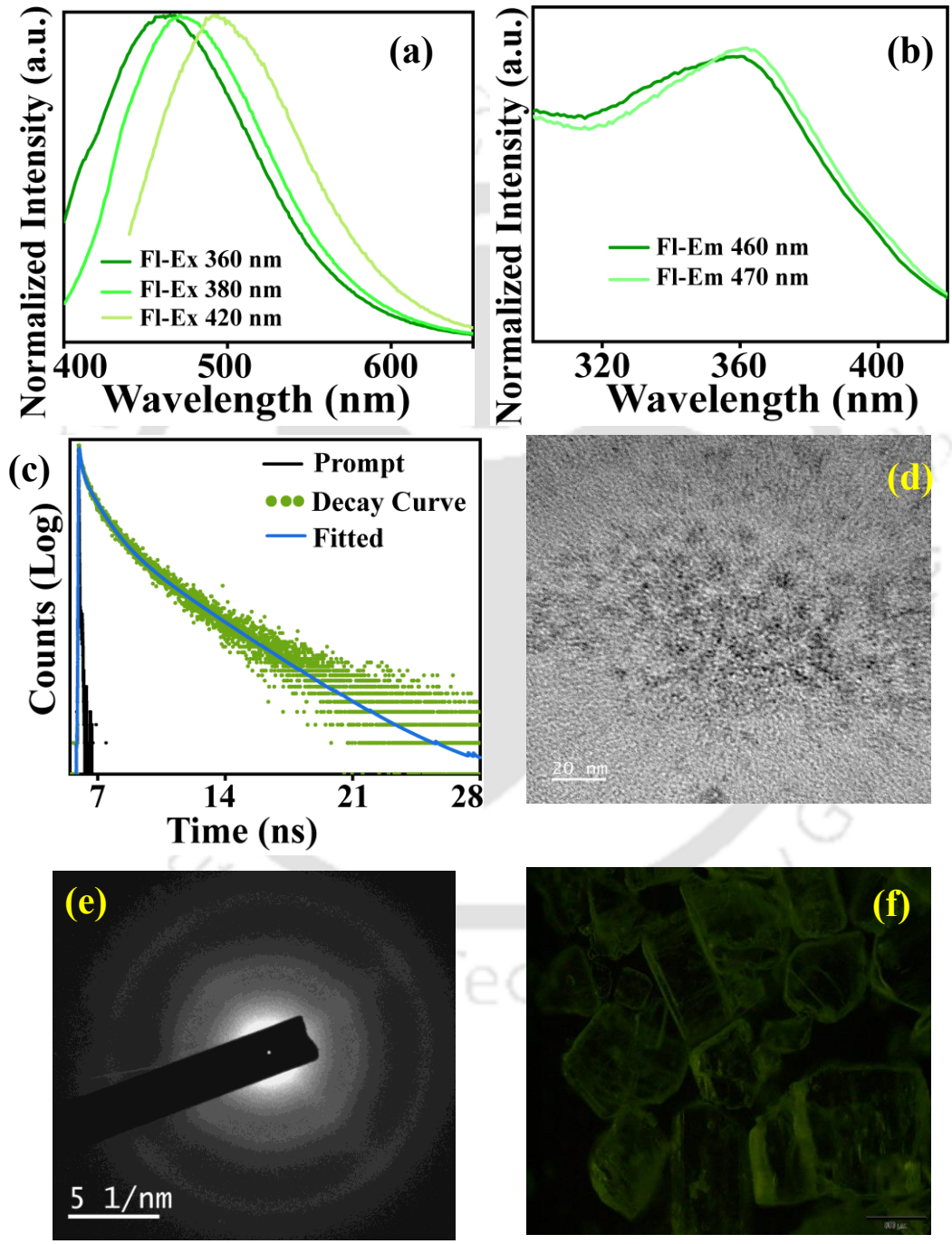

Figure 4.1 (a) Fluorescnece emission spectra of HIS-AuNCs at 360, 380 and 420 nm excitation. (b) Fluorescence excitation spectra for 460, 470 nm emission. (c) TRPL spectra of HIS-AuNCs at 360 nm excitation and 460 nm emission. (d,e) FETEM and SAED image of HIS-AuNCs. (f) fluorescence microscope image of L-histidine crystals.

dependent emission characteristics. The fluorescence emission spectra of HIS-AuNCs revealed peak maxima at 465, 475, and 495 nm at excitation wavelengths of 360, 380, and 420 nm, respectively (Figure 4.1a). The fluorescence excitation spectra of HIS-AuNCs were likewise tuneable, with peak maxima at 360 and 365 nm for 460 and 470 nm emission (Figure 4.2a). However the maximum emission was observed at 465 nm and corresponding excitation was 360 nm. In an aqueous medium, the absolute PL quantum yield (QY) of HIS-AuNCs was measured to be 0.7±0.05 %. At the 470 nm (peak) emission wavelength, the average fluorescence decay lifetime of the clusters was found to be 3.26±0.2 ns (Figure 4.1c, Table 4.1). The formation of NCs with diameter on the order of 1.1±0.15 nm was revealed by the FETEM analysis (Figure 4.1d). Notably, the lattice spacing values of 0.20 nm observed in the selected area diffraction (SAED) pattern corresponded to the lattice d-spacing values for 200 planes in FCC AuNCs (Figure 4.1e).[9] Tuneable emission for AuNCs is due to the varied proportion of clusters generated during the synthesis method. This wavelength tuneable emission of AuNCs is directly connected to the number of histidine molecules instead of the Au kernel. Peripheral binding groups may affect fluorescence based on charge transfer from the molecules to the Au core, and molecules with electron-rich groups (e.g., CO_2H, NH_2), like histidine, can heavily increase fluorescence quantum yield, and the more exterior ligands, the more redshift of the His-AuNCs emission profile.[10] In other words, the number of capping groups linked to the shell-gold atoms determines the relaxation of core-gold to shell-gold via various interim shell-gold energy states.[11]

The NCs were then used to dope His crystals in water medium by evaporation of the solvent containing mixture of dispersed NCs along with His molecules at 40 $^{\circ}$C. The doped crystals were then centrifuged, rinsed with a methanol/water (9/1) mixture and dispersed in methanol by thorough sonication. The so-synthesized doped crystals had a strong absorbance peak at 280 nm due to histidine crystals, along with absorbance due to the NCs at 340 nm and a broad peak at 420 nm, which was accounted for by the formation of the HIS-AuNCs aggregates inside the crystal (Figure 4.3a). The steady state emission spectra of HIS-AuNCs-HIS doped crystals showed excitation tuneable emission with peak maxima at 465, 480, 495 nm for 360, 390 and 420 nm excitation which are similar to the pristine HIS-AuNCs (Figure 4.3b). The steady state excitation spectra of HIS-AuNCs-HIS doped crystals had peak maxima at 365 and 370 nm for 460 and 500 nm emission (Figure 4.3c). The time-resolved emission spectra of His-AuNCs-His doped crystals with 50 µS delay showed a broad spectrum from 450 to 680 nm, progressively shifting towards higher wavelengths as the excitation wavelength was moved from 360 to 420 nm (Figure 4.2b). These ultralong delayed emissions were at longer

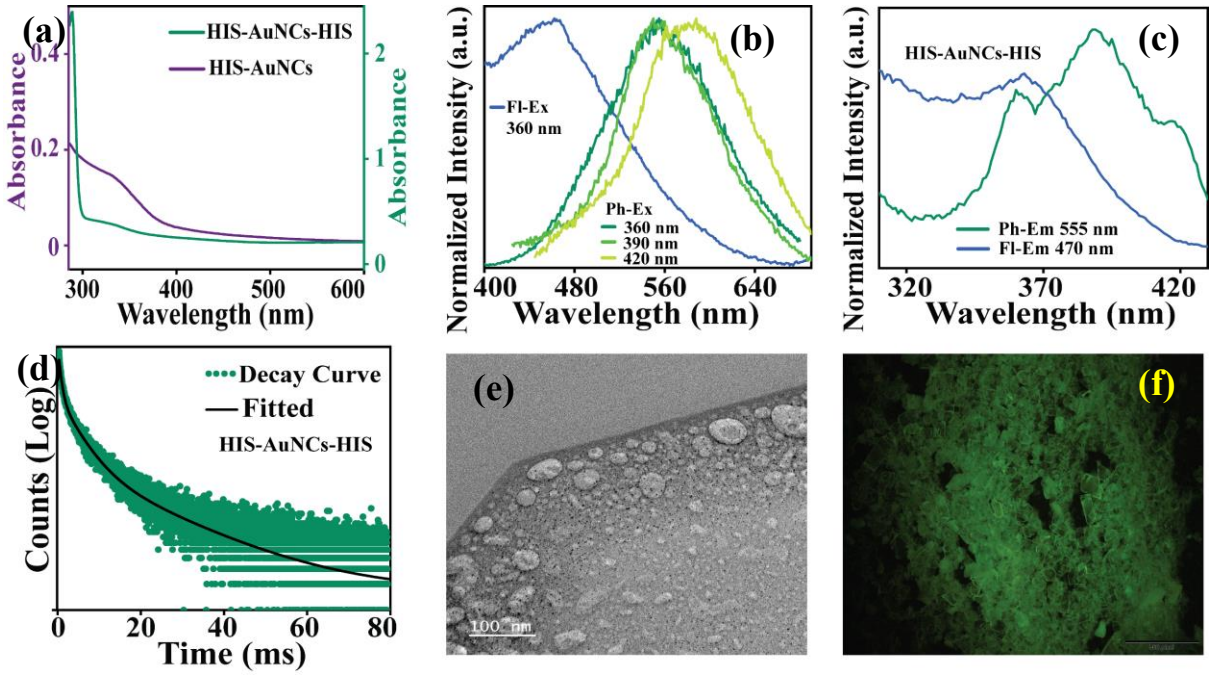

Figure 4.2 (a) UV-vis absorbance spectra of HIS-AuNCs (violet) and HIS-AuNCs-HIS doped crystals (green). (b) Fluorescence emission at 360 nm excitation and the time resolved emission spectra of HIS-AuNCs-HIS crystals at 360, 390 and 420 nm excitation. (c) Steady state fluorescence excitation (λem=470 nm, blue) and phosphorescence excitation spectra of HIS-AuNCs-HIS doped crystals (λem=555 nm, green). (d) Phosphorescence lifetime decay spectra of HIS-AuNCs-HIS composite crystal corresponding (λex=360 and λem=555 nm) (e) FETEM image and (f) Fluorescence microscopy image of HIS-AuNCs-HIS doped crystals.

wavelength and far away from their steady-state PL spectra, and hence may be interpreted as triplet-singlet state emission resulting in phosphorescence in ambient conditions. The time-resolved excitation measurements, with a delay period of 50 μs, revealed three notable excitations region concentrated at 360, 390 and 420 nm for the 555 nm emissive state for the doped crystals (Figure 4.2c). According to the phosphorescence excitation spectra, there were mainly three singlet state that take part in the inter system crossing process that has been originated from the rigid structure of the aggregated AuNCs inside the histidine crystal environment. To understand further about the excited triplet states we have performed phosphorescence excitation spectra for three different emission at 530, 550 and 640 nm (Figure 4.3d). The results indicate that for 530 nm emission, 360 nm was dominant excitation where as for 640 nm emission, 420 nm was dominant excitation and in-between 550 nm emission 390 nm excitation was dominant excitation. These results suggest that these three triplet states were broad and energetically overlapped with each other but uncorrelated i.e., they had different singlet-states origins which were generated from the different levels of agglomeration.[12] Thus, the emission wavelength was dependent on independent emissive state with differing excited

states. The host crystal played an important role of providing rigidity, which restricted the structure to relax through a common triplet emissive state although they were energetically close.[13] The average lifetime associated with 555 nm emission (λex = 360 nm) for HIS-AuNCs-HIS system was calculated to be 9.38±0.8 ms, as determined by modelling the decay curve with a triexponential function (Figure 4.2d). Table 4.2 shows each component's lifetime value

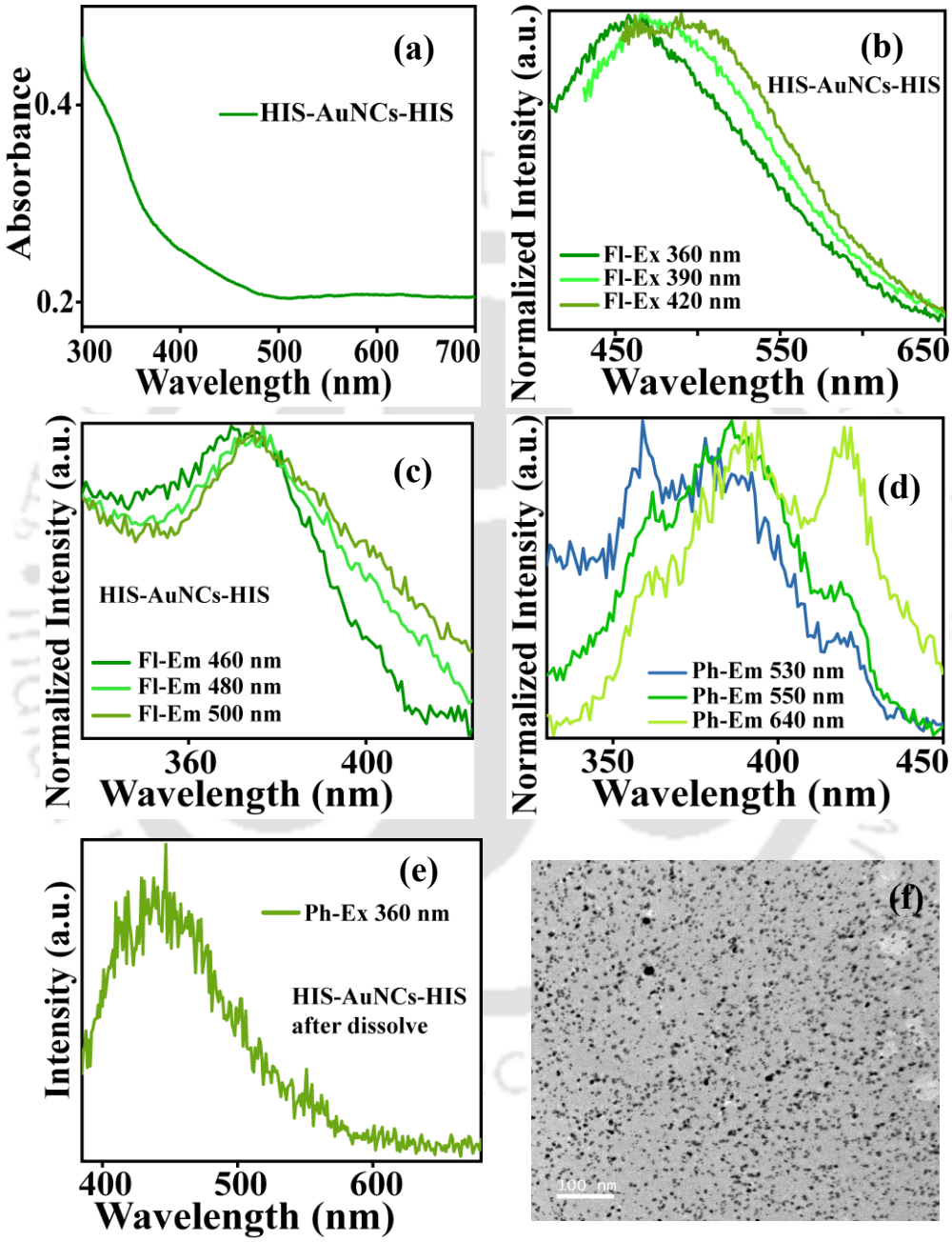

Figure 4.3 (a) Magnified Absorbance spectra of HIS-AuNCs-HIS. (b)Fluorescnece emission spectra of HIS-AuNCs-HIS at 360, 380 and 420 nm excitation. (c) Fluorescence excitation spectra of HIS-AuNCs-HIS at 460, 480 and 500 nm emission. (d) Phosphorescence excitation spectra of HIS-AuNCs-HIS at 530, 550 and 640 nm emission. (e) Phosphorescence emission spectra of HIS-AuNCs-HIS doped crystals at 360 nm after dissolving the crystals in water and (f) corresponding FETEM image.

and accompanying weight percentage. The NCs inside the histidine crystals had a PL decay component of 18.18 ms with a weight of 6.4%. There were also two considerably rapid decay components with lifetimes of 4.23 ms and 652 μs. Analysis of FETEM images of the hybrid system revealed that the presence of agglomerated NCs within histidine crystals with average diameter of 3.3±1 nm, which was much larger than the HIS-AuNCs present in the dispersion (Figure 4.2e). The phosphorescence of the aggregated AuNCs, and the excitation-tuneable emission of HIS-AuNCs-HIS doped crystals might be due to the distinct triplet emissive states originating from the compact structure of agglomerated NCs inside the histidine crystals depending on the excitation wavelength. As a result, the fluorescence-to-phosphorescence (F-P) transition occurred at room temperature in the aggregated AuNCs under histidine crystal confinement. Such a switch is also known in the self-assembly of NCs by blended solutions.[14,15] As far as our knowledge goes, the HIS-AuNCs-HIS crystals reported here have the longest phosphorescence lifetime for any known AuNC self-assembly.[16] The appearance of phosphorescence is also ascribed to the aurophilic Au(I)···Au(I) interactions, compact rigid structure formation and improved ligand to metal charge transfer (LMCT) due to the agglomeration and strong ligand field provided by the electron rich crystals.[17] At 360 nm excitation wavelength, the absolute PL QY of HIS-AuNCs and HIS-AuNCs-HIS crystallized assemblies were 0.7±0.05% and 0.78±0.06%, respectively. Fluorescence microscopy images recording green emission also support the emissive characteristics of the NCs inside the crystals (Figure 4.2f). Interestingly, when the HIS-AuNCs-HIS crystals were dissolved in water, the phosphorescence was lost (Figure 4.3e), resulting in faint, delayed fluorescence caused by formation of larger aggregate of the NCs in the dispersion medium observed from the FETEM analysis (Figure 4.3f).

Further, we were interested in energy transfer processes between the host crystals and the aggregated AuNCs. We had crystallized IPA with HIS-AuNCs in methanol/water mixture at 40 °C. The doped crystals were then washed with water following centrifugation. This was followed by their dispersion in water. The optical characteristics of the synthesized His-AuNCs-IPA doped crystals revealed a dominant absorbance peak at 295 nm due to IPA crystals and a broad peak ranging from 310 to 400 nm appeared due to the aggregated AuNCs (Figure 4.5a). The steady-state PL spectrum of the His-AuNCs-IPA doped crystals at 295 nm excitation (at crystal excitation) revealed three emission peak at 360, 470 and 500 nm out of which 360 nm emission was from host IPA crystals and other two had originated from the aggregation of

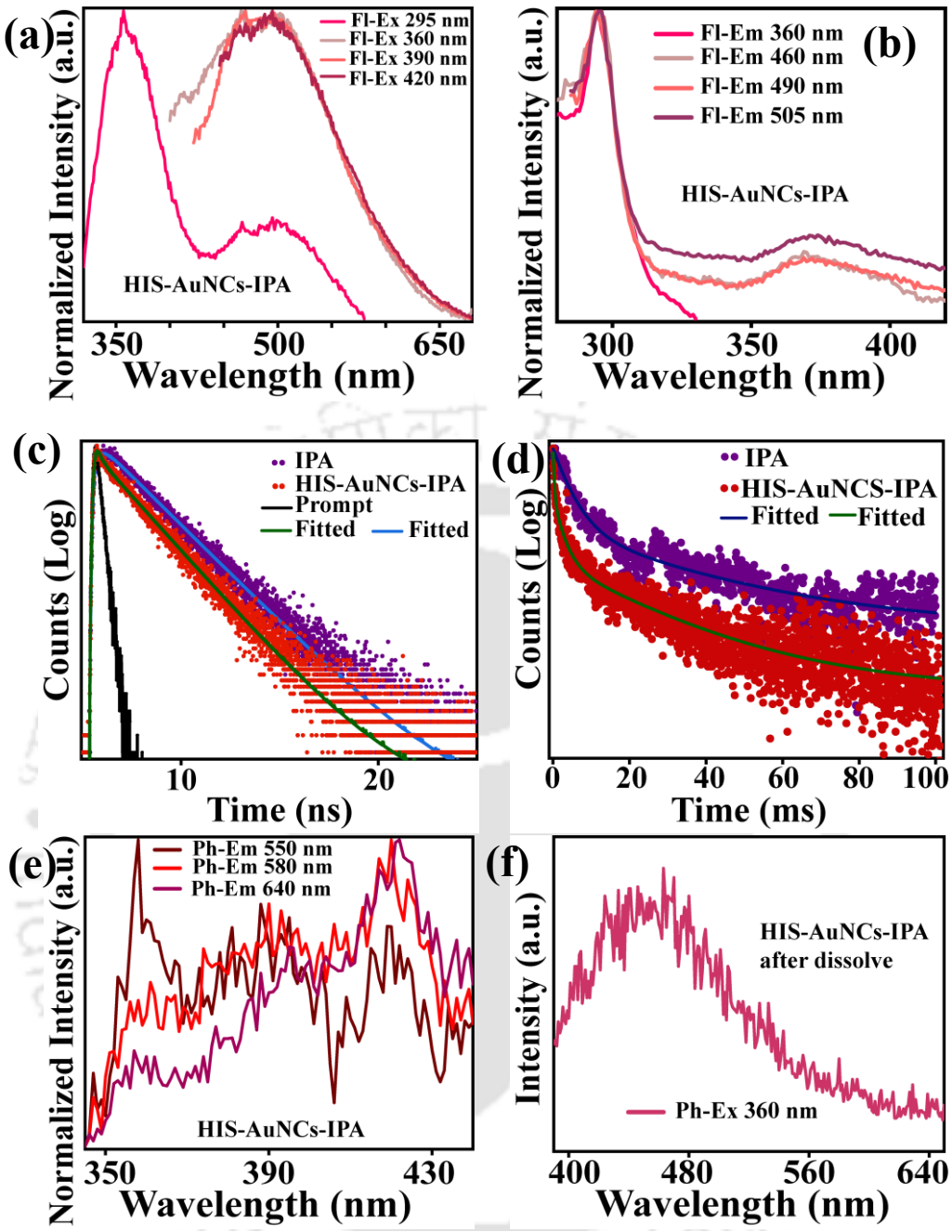

Figure 4.4 (a) Fluorescnece emission spectra of HIS-AuNCs-IPA doped crystals at 295, 360, 390 and 420 nm excitation. (c) fluorescence excitation spectra of HIS-AuNCs-IPA crystals for 360,460,490 and 505nm emission. (d) TRPL spectra of pristine IPA and HIS-AuNCs-IPA crystal corresponding (λex=295 and λem=360 nm) (e) phosphorescence lifetime decay spectra of pristine IPA and HIS-AuNCs-IPA doped crystals corresponding (λex=295 and λem=500 nm) (e) Phosphorescence excitation spectra of HIS-AuNCs-HIS at 530, 550 and 640 nm emission. (f) time resolved emission spectra of HIS-AuNCs-HIS doped crystals at 360 nm after dissolving the crystals in methanol.

AuNCs under IPA crystal environment (Figure 4.4a).[18] The steady-state PL spectrum of the His-AuNCs-IPA doped crystals at 360 nm excitation (at AuNCs excitation) have two peaks 470 and 500 nm similar to the 295 nm emission owing to aggregated cluster. Interestingly, the

wavelength dependent emission characteristics like in HIS-AuNCs or HIS-AuNC-HIS that was absent here may be due to the different crystal environment. (Figure 4.4a,b). The steady-state excitation spectrum of the doped crystals consisted primarily of two peaks at 295 nm and 370 nm (Figure 4.4b). Interestingly, 295 nm excitation leads to both crystal and AuNCs fluorescence emission and fluorescence excitation spectra also support that 500 nm fluorescence emission of HIS-AuNCs-IPA doped crystals has significant contribution from 295 nm excitation. The above experimental results suggest that there is a energy transfer from the crystal S_1 state to the S_1 state of the aggregated AuNCs in HIS-AuNCs-IPA doped crystals. Time-resolved photoluminescence (TRPL) spectroscopy showed decrease in average lifetime following doping for 360 nm fluorescence emission that also support the energy transfer phenomenon between crystal and AuNCs (Figure 4.4c, Table 4.1).[19] The time resolved emission spectra of pristine IPA crystals exhibited mainly two emission peaks at 360 and 500 nm at 300 nm excitation, with the 360 nm peak being due to delayed fluorescence and the other being phosphorescence (Figure 4.5b).[20] The PL properties of the HIS-AuNCs-IPA crystals were altered considerably from the NCs or the crystals after crystals were doped with the NCs. The phosphorescence emission spectrum of HIS-AuNCs-IPA crystals had wavelength dependent emission characteristics like HIS-AuNCs-HIS crystals i.e., phosphorescence emission gradually red shifted with excitation wavelength when moving toward longer wavelength (Figure 4.5b). This supported a similar type of aggregation and excitation like previous case, inside the IPA crystals. For example at 300 nm phosphorescence excitation of the doped crystals, 360 nm delayed fluorescence peak of the host IPA crystal was absent, at the same time 500 nm peak of the host crystal was present along with a broad phosphorescence emission of the aggregated AuNCs confined within IPA crystal at nearly 550 nm which gradually shifted towards longer wavelength as move towards lower energy excitation at room temperature (Figure 4.5b). In the Phosphorescence emission spectra of HIS-AuNCs-IPA crystals when the excitation wavelength was changed from 360 to 420 nm, the main emission

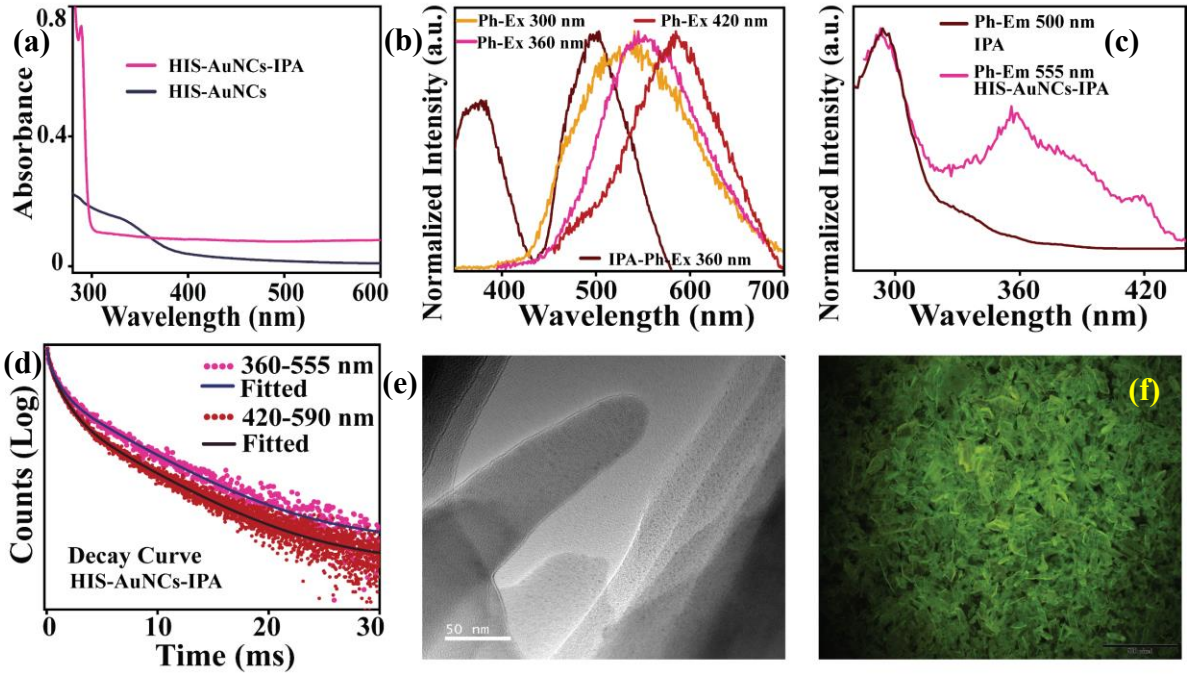

Figure 4.5 (a) UV-vis absorbance spectra of HIS-AuNCs (black green) and HIS-AuNCs-IPA doped crystals (pink). (b phosphorescence emission spectra of HIS-AuNCs-IPA doepd crystals at 300, 360 and 420 nm excitation and IPA crystals at 300 nm excitation. (c) phosphorescence excitation spectra of HIS-AuNCs-IPA system(λem=555 nm) and IPA crystals (λem=500 nm). (d) Phosphorescence lifetime decay spectra of HIS-AuNCs-IPA composite crystal corresponding (λex=360 and λem=550 nm and λex=420 and λem=590 nm) (e) FETEM image and (f) Fluorescence microscopy image of HIS-AuNCs-IPA composite crystals.

center showed a significant bathochromic shift from 555 to 585 nm like HIS-AuNCs-HIS crystals under ambient conditions (Figure 4.5b). The pure IPA crystals had a single phosphorescence excitation peak at 295 nm for the 500 nm triplet emissive state (Figure 4.5c).[18] The phosphorescence excitation spectra recorded with a 50 μs delay of HIS-AuNCs-IPA system revealed four excitation peaks at 295, 360, 390 and 420 nm for the 555 nm emission (Figure 4.5c) which support that there was an energy transfer from the crystals triplet state to the host aggregated AuNCs triplet state for 555 nm emission. To understand further about the excited triplet states we had performed phosphorescence excitation spectra of HIS-AuNCs-IPA crystals for three different emission at 530, 580 and 640 nm wavelength (Figure 4.4e). These results were in correlation with the previous HIS-AuNCs-HIS crystals which suggest that these three triplet states were broad and energetically overlapped with each other but uncorrelated i.e., they had different singlet-states origins which were generated from the excitation of different component of the aggregated AuNCs under crystal confinement (Details in section 4.3). Thus, the emission wavelength was dependent on independent emissive state with differing excited states. Interestingly, the 360 nm delayed fluorescence peak of IPA was

absent, in the doped crystals, indicating energy transfer from the triplet state of IPA corresponding to 360 nm emissive state to the triplet energy state of aggregated AuNCs in the doped system, which will ultimately relax through a broad 540 nm triplet emission (Figure 4.5b). We performed time-resolved phosphorescence lifetime delay experiments of HIS-AuNCs-IPA crystals for the 555 and 590 nm emission to probe the excited state kinetics (Figure 4.5d). The decay curves were fitted with tri-exponential equations. The decay curve of HIS-AuNCs-IPA crystals revealed that the 555 nm emissive state had the highest lifespan component of 6.31 ms with a 23% weight, while the 588 nm emissive state had the most extended lifetime component of 6.27 ms with a 16% weight (Table 4.2). The average lifetime of all three components was 5.24±0.3 ms and 4.47±0.25 ms for the excited states corresponding to 555 and 588 nm excitation, respectively. Table 4.2 shows the individual component lifetime values with their accompanying magnitudes. The phosphorescence decay experiment of HIS-AuNCs-IPA crystals for 500 nm emission (where the host pristine crystal had phosphorescence emission) revealed that it had a longer tail component of 30 ms which is reduced from its pristine crystal counterpart of 40 ms support that crystal triplet states took part in energy transfer process when doped (Figure 4.4d, Table 4.2).[21] Furthermore, longer wavelength triplet emissive state (588 nm) has a shorter lifetime than that of 555 nm, possibly due to lower stability of the longer wavelength emitting triplet state. The FETEM image analysis of the hybrid system indicated that the average aggregated NC diameter inside the IPA crystals was 2.8±1 nm, much larger than the individual AuNCs in the dispersion (Figure 4.5e). As a result, when NCs aggregated into rigid structure inside crystals, ISC process became more prominent and new radiative triplet emission pathways had been introduced. At 360 nm excitation, the absolute PL QY recorded for His-AuNCs-IPA crystallized assemblies was 1.15±0.8%, slightly higher than His-AuNCs due to the reduction of non-radiative routes via aggregated rigidification and interactions between crystals emissive and clusters emissive states. Fluorescence microscopy images also support the emissive character of NCs inside IPA crystals (Figure 4.5f). When the aggregated His-AuNCs doped IPA crystals were dissolved in methanol, the composite system lost their phosphorescent characteristics, resulting in faint, delayed fluorescence from weakly interacting aggregated states in the dispersion, which is in line with observations with the previous HIS-AuNCs_HIS system (Figure 4.4f).

Finally, we pursued the idea further in GSH-AuNCs-HIS crystals. GSH-AuNCs in water appeared as yellow suspension with a spectacular orange glow when exposed to UV light.[3] The excitation and emission maxima of the produced nanoclusters were about 365 nm and 605 nm,

respectively in water (Figure 4.6a,b), which corresponded well with the previous reports. Fluorescence lifetime decay for GSH-AuNCs was measured to be 12.8±0.5 ns for 605 nm emission (Figure 4.6c, Table 4.1). The average particle diameter of 1.5±0.2 nm as calculated from FETEM imaging analysis (Figure 4.6d), with a measured lattice spacing of 0.24 nm (from selected area electron diffraction (SAED) analysis) matched, with the lattice spacing of the face centred cubic (111) gold (Figure 4.6d inset).[3] The UV-vis absorption spectrum of GSH-AuNCs (Figure 4.7a, black line) indicated the presence of a weak peak at 395 nm with a background absorbance that went beyond 500 nm (Figure 4.7a). The absence of the surface plasmon resonance peak at 520 nm, which is typical of Au nanoparticles, further demonstrated the effective synthesis of GHS-AuNCs.

The GSH-AuNCs were then used for doping HIS crystals in water medium through complete solvent evaporation. The as-obtained evaporated crystals were washed by methanol/water (9/1) mixture followed by centrifugation and dispersion in methanol. UV-vis absorption spectrum of the GSH-AuNCs-HIS crystals consisted of an absorption band at 405 nm, slightly red-shifted from that of the GSH-AuNC (Figure 4.7a, orange spectra). The change in the peak position can be attributed to the aggregation of the NCs inside the histidine crystals

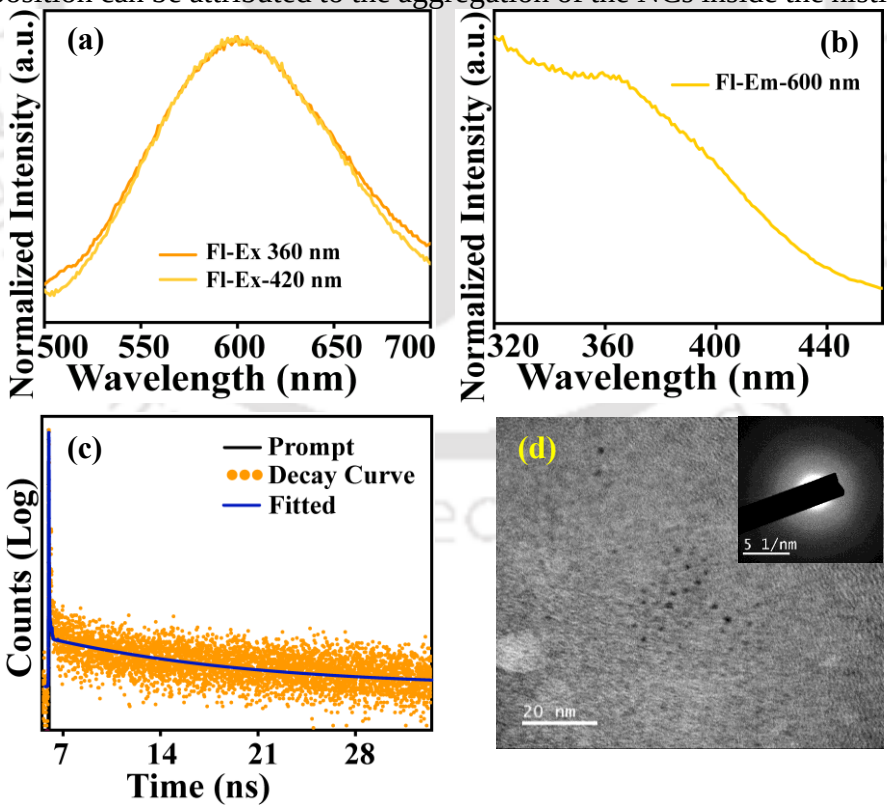

Figure 4.6 (a) Fluorescnece emission spectra of GSH-AuNCs at 360 and 420 nm excitation. (b) Fluorescence excitation spectra for 600 nm emission. (c) Fluorescence lifetime decay spectra of GSH-AuNCs at 360 nm excitation and 600 nm emission. (d,e) FETEM image of GSH-AuNCs.

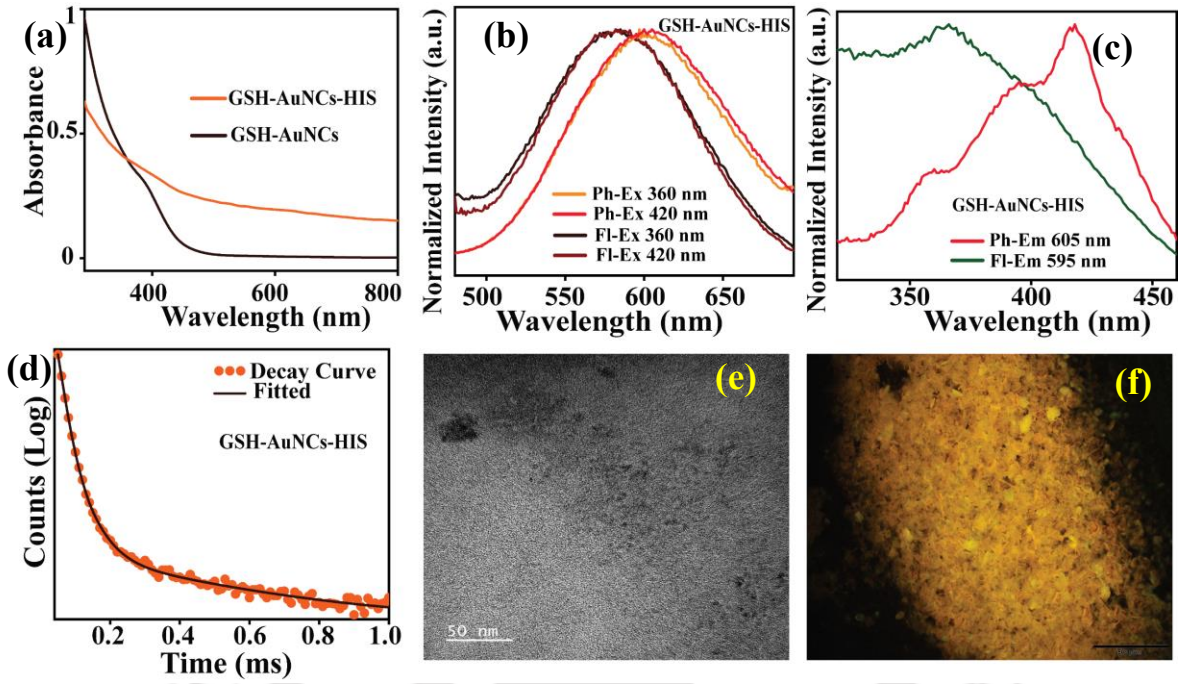

Figure 4.7 (a) UV-vis absorbance spectra of GSH-AuNCs (black spectra) and GSH-AuNCs-HIS doped crystals (orange spectra). (b) fluorescence emission and time resolved emission spectra with 50 µs decay period of GSH-AuNCs-HIS system at 360 and 420 nm excitation. (c) fluorescence excitation (λem=595 nm) and time resolved excitation spectra with 50 µs decay period of GSH-AuNCs-HIS doped crystals (λem=605 nm). (d) phosphorescence lifetime decay spectra of GSH-AuNCs-HIS doped crystal corresponding (λex=360 and λem=610 nm) (e,f) Fluorescence microscopy image and FETEM image of GSH-AuNCs-HIS doped crystals respectively.

(Figure 4.7a). The FETEM image of the doped crystals showed the presence of aggregated clusters with average diameter of 4.5±1 nm (Figure 4.7e). The aggregated clusters inside the crystals exhibited stead- state fluorescence emission with a peak at 595 nm (λex = 360 nm) in methanol (Figure 4.7b, black spectra). However, the phosphorescence spectrum recorded with 50 µs delay of the GSH-AuNCs-His system consisted of a new excitation-independent radiative emission at 605 nm (i.e., ~10 nm red shifted form steady state emission) upon 360 nm excitation (when dispersed in methanol; Figure 4.7b, red and orange spectra). Hence, following crystallization, distinct luminescence properties were observed as a new radiative pathway has been induced in the time-resolved emission spectra. The phosphorescence excitation spectrum, recorded with 50 µs delay (Figure 4.7c), also revealed that the doped crystals had three major excitations at 360, 390, 420 nm (λex = 605 nm), respectively; whereas steady-state fluorescence excitation spectrum had a single peak around 360 nm (Figure 4.7b, green spectra). To understand further about the excited triplet states we have performed phosphorescence excitation spectra of HIS-AuNCs-IPA crystals for three different emission at 550, 605 and 660 wavelength (Figure 4.8a). Interestingly, this time for all three phosphorescence emission

wavelength the excitation spectra looks identical. These results unlike previous doped crystals, suggest that these three triplet states were broad and overlapped with each other and coupled i.e., they had different singlet-states origins which were generated from the excitation of different component of the aggregated AuNCs under crystal confinement but relax through a common lower energy triplet radiative pathway.[22] Three peaks in the phosphorescence excitation spectrum may be ascribed to three new triplet energy states that had been generated and successfully participated in the ISC process for the confined, rigid, aggregated GSH-AuNCs doped HIS crystals, which eventually relaxed by a single lower energy triplet emissive state. These results can be accounted for by the compactness of the rigidity inside crystal environment, as GSH is a tripeptide based ligand and is much longer then L-histidine, compactness will be less for GSH-based aggregation and the triplet excited states were coupled and recombine through a common single radiative pathway.

The absolute PLQY of the GSH-AuNCs and the GSH-AuNCs-His crystals were measured to be 0.58±0.04 and 25±0.6%, respectively, at 360 nm excitation wavelength (Table 4.1 and 4.2). The enhancement of PL QY could be attributed to the aggregation of the clusters inside the crystal. The results showed that rigid aggregated NC doping in molecular crystals could facilitate singlet to triplet crossover in the excited state and provided an alternate phosphorescence radiative channel, resulting in greater QY. The average phosphorescence lifetime decay parameter corresponding to 605 nm emissive state for GSH-AuNCs-HIS system was found to be 60±4 μs as derived by fitting the decay graph with a triexponential function (Figure 4.7d). Table 4.2 shows the lifetimes of different components corresponding to the above emissions. The most extended decay component was 390 μs with a weight value of 1%, and the shortest segment was 16 μs (Figure 4.7d).

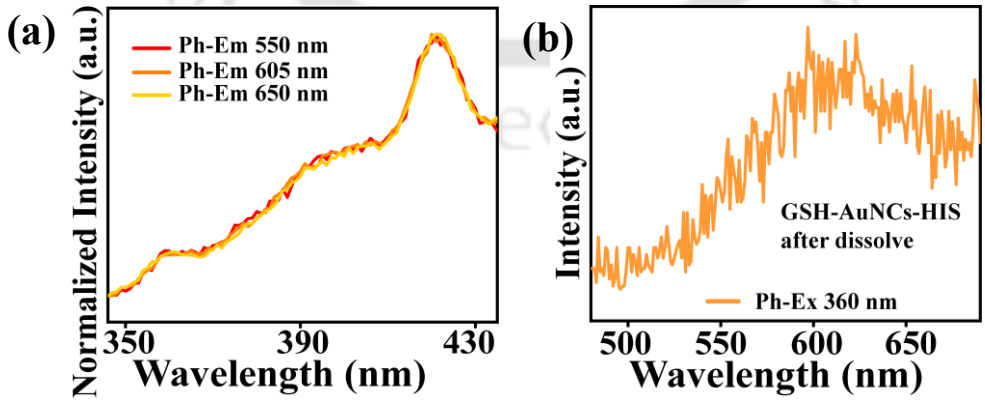

Figure 4.8 (e) Phosphorescence excitation spectra of GSH-AuNCs-HIS at 550, 605 and 660 nm emission. (f) time resolved emission spectra of GSH-AuNCs-HIS doped crystals at 360 nm after dissolving the crystals in methanol.

As observed on the previous cases, we can generalize that confining AuNCs inside suitable molecular crystals in aggregated forms may lead to room temperature phosphorescence. One intriguing finding is that when NC aggregated crystals were dissolved in an aqueous medium through sonication, their phosphorescence disappeared, and only mild delayed fluorescence was observed, emphasising the importance of the crystal environment in facilitating phosphorescence emission in GSH-AuNCs (Figure 4.8b). The FETEM and fluorescence microscopy images revealed the integration of aggregated NCs inside the crystals while remaining emissive in that form (Figure 4.7e,f).

Powder-XRD measurement of the doped crystals (Figure 4.9a,b) showed that peaks were broadened and appeared shifted from those in the undoped crystals, which implied the efficient doping of AuNCs inside the molecular crystals.[23] The AuNC doped crystals comprised multiple sharp peaks (Figure 4.9a,b) like the undoped crystals, demonstrating the formation of structure with high crystallinity that also supported that the AuNCs did not distort the structure of pure molecular crystals. Powder XRD analysis of the pure crystals demonstrated that HIS crystals had monoclinic P21 unit cell with cell parameters cell parameter a= 5.172 Å, b= 7.384 Å, c= 9.474 Å, β=97.162º and IPA had monoclinic P21/c unit cell with Cell parameters a= 3,758 Å, b= 16.364 Å, c=11.703 Å, β=90.3º.[24,25]

The above experimental results suggest that room temperature phosphorescence emission in water dispersible fluorescent AuNCs can be achieved through their incorporation in molecular crystals as aggregated dopants. Importantly, the switching of fluorescence in aqueous dispersion and phosphorescence in crystal is reversible, making them amenable to solvent processible device fabrication. Furthermore, if the triplet and singlet energy states of the crystal and that of the confined aggregated AuNCs are in close proximity, there is a

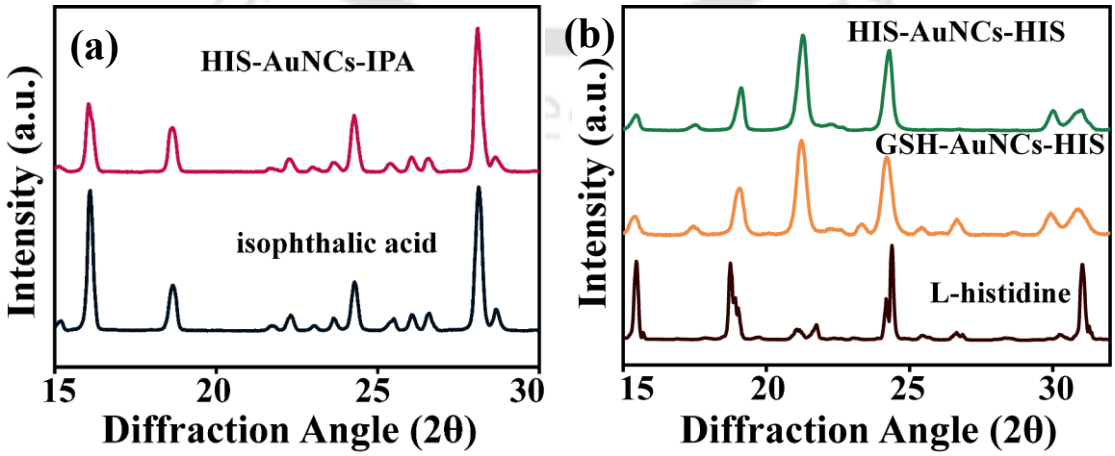

Figure 4.9 (a,b) Powder XRD pattern of AuNCs doped and pristine L-histidine and IPA crystals.

possibility of energy transfer from the crystal to NCs through the interacting triplet as well as singlet energy states. Again, the number of phosphorescence emissive states for doped crystals can also be changed based on the rigid structure's compactness. For example, in the case of a highly compact, rigid structure, multiple triplet emissions were recorded, but in the case of a less compact, rigid structure, one triplet emission was noticed.

4.3 Mechanism of Phosphorescence

The PL of AuNCs could be primarily explained by two mechanisms. Firstly, there is the quantum confinement effect in the metal kernel, producing discrete molecule-like energy states. The emission mainly comprises of HOMO-LUMO transitions accompanied by intraband (sp−sp) and interband (sp−d) relaxations. Secondly, the second the ligand-to-metal charge transfer (LMCT) or ligand-to-metal−metal charge transfer (LMMCT: that highlights the gold–gold interactions in pure or aggregated form) caused by the charge transfer from electron rich ligand centre to the Au atom through surface interactions. Furthermore, when LMCT or LMMCT type radiative relaxation occurs from the triplet state of the metal center, the emission lifetime can be prolonged.[26-28]

We suggest the following mechanism (Figure 4.10e) to depict the excited state behaviors in the AuNC doped molecular crystals based on the experimental data. The NCs were aggregated inside the crystal in all three cases due to crystal confinement and the hydrogen bonding and N-H/C-H..π interactions between surface ligands. The induction of phosphorescence into the AuNCs dopants can be explained by two phenomena. Firstly, the molecular crystals rigidified the aggregated AuNCs into compact structures that helped enhance the inter-cluster aurophilic interactions facilitating efficient intersystem crossing via spin-orbit coupling to the triplet state. Secondly, the electron rich atoms in the molecular crystal can interact with the surface ligands of the AuNCs through van der Waals forces (including hydrogen bonding) and can boost the LMCT or LMMCT transitions, favouring inter-system crossing and stabilizing the triplet emissive states.[29] A model DFT computation of AuNCs was performed to account for the orbitals involved in the HOMO-LUMO transition, utilizing one or two AuNC units. These were the small replica of AuNCs made of four Au atoms and four histidine ligands (Figure 4.10c,d and 4.11). The DFT calculation revealed that for single-unit AuNC the HOMO is mainly situated over two histidine ligand and the LUMO is mainly dispersed over Au kernel, supporting the LMCT type transitions involved in excited state dynamics (Figure 4.11a,b).

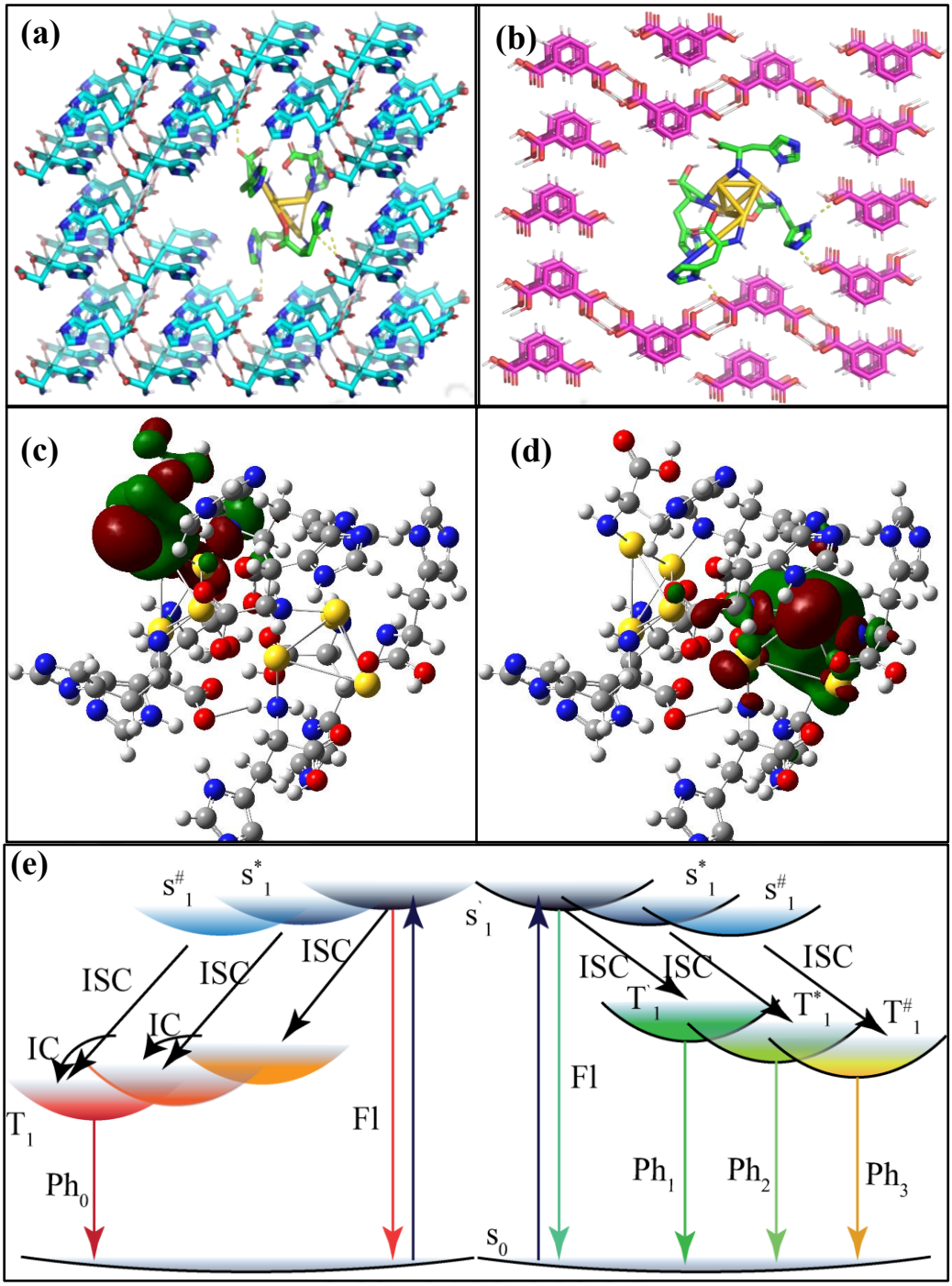

Figure 4.10 Molecular docking study of HIS-AuNCs inside (a) L-histidine (b) IPA crystal. Based on DFT calculation (c) HOMO and (d) LUMO orbital's pictorial representation of HIS-AuNCs aggregation.(e) Schematic illustration of the Phosphorescence mechanism.

Aggregated cluster replica employing two AuNC units revealed that the HOMO is located over histidine ligand and the LUMO is situated mainly over Au kernel of adjacent AuNC, allowing extensive orbital interactions between aggregated AuNCs (Figure 4.10c,d). The TD-DFT calculation also showed that the aggregated AuNCs had two higher energy triplet states at 479 (2.58eV) and 502 nm (2.47eV), whereas single AuNC unit had one higher energy triplet state at 496 nm (2.49 eV) consistent with our experimental observations (Figure 4.11c). These

orbitals involved in lowest and second lowest triplet transitions of aggregated HIS-AuNCs in ground state support different components of aggregation may be responsible for multiple lower energy emission channels if the structure were rigid. Furthermore, the molecular docking analysis was conducted aggregated to account for the potential interactions in the AuNCs doped crystal system. Docking studies were employed for HIS-AuNC with histidine and IPA crystal separately to determine possible interactions leading to molecular anchoring. The results demonstrated that there were four potential hydrogen bonding interactions between HIS-AuNC and histidine crystal, and three between HIS-AuNC and IPA crystal in the lowest energy docked conformer (Figure 4.10a,b).

Mechanistically, upon UV light excitation, the crystal doped NCs occupied the excited singlet states, which underwent efficient intersystem crossing to the triplet states. All doped crystals' phosphorescent excitation spectra had primarily three peaks. However, HIS-AuNCs-HIS and HIS-AuNCs-IPA doped crystal's triplet states were broad and overlapped with each other but uncorrelated i.e., they had different singlet-states origins which were generated from the excitation of different component of the aggregated AuNCs under crystal confinement. Thus, the emission wavelength was dependent on independent emissive state with differing excited states. Furthermore, for HIS-AuNCs-GSH doped crystals, these three triplet states were

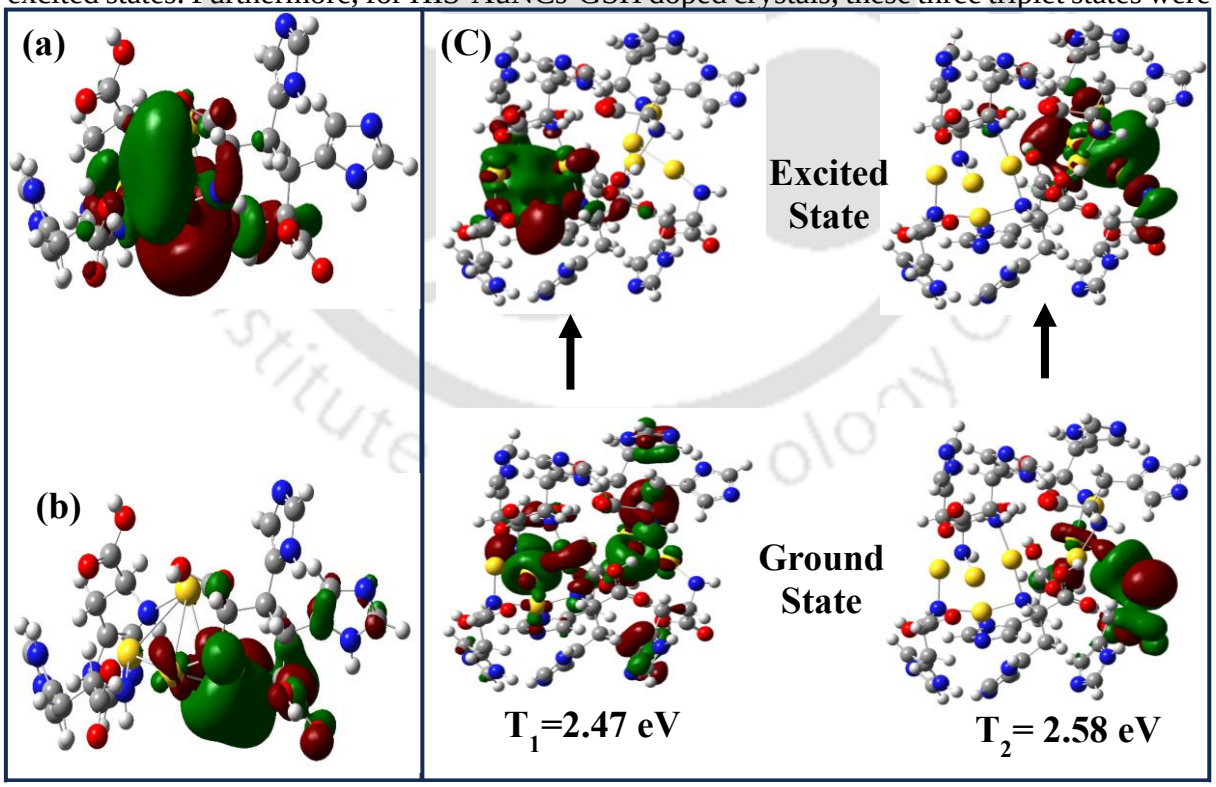

Figure 4.11 Based on DFT calculation (a) LUMO and (b) HOMO orbital's pictorial representation of single HIS-AuNC. (c) Transition orbitals for the lowest and second lowest triplet transitions of aggregated HIS-AuNCs in ground state showed multiple components of aggregation were involved in different type transition.

broad and overlapped with each other and were coupled i.e., they had different singlet-states origins which were generated from the excitation of different component of the aggregated AuNCs under crystal confinement but relax through a common triplet radiative pathway. Electrons in these higher-lying triplet states relaxed to low-lying triplet levels based on the aggregated NC structures' compactness and which eventually reached the ground states by different radiative phosphorescent transitions.[30] Furthermore, by restricting non-radiative routes, the rigidified structure primarily boosted the luminescence QY.[31] For large surface ligands (as in the GSH-AuNCs case), the rigidification in terms of compactness for aggregated AuNCs will be less and the higher-lying triplets were coupled, would relax to the lower-lying triplet state, resulting in a single phosphorescence peak. For small surface ligands (as in the HIS-AuNCs case) i.e., in a highly compact rigid structure, the high-lying triplets state were uncorrelated and relax though different wavelength radiative emission depending on the excitation. The higher-lying coupled triplet states in less rigidified structures, undergo vibrational relaxation to single lower energy triplet state and recombine through phosphorescence. For more rigidified structures the higher-lying triplet states were uncorrelated underwent vibrational relaxation to different lower energy triplet state depending on the source singlet state and recombine through wavelength tuneable phosphorescence emissions similar to the phenomenon observed for multicomponent emissive polymers. In case of HIS-AuNCs-IPA doped crystals, crystal's singlet and triplet states were involved in energy transfer process to the corresponding singlet and triplet states of doped aggregated AuNCs.

The generalised Jablonski diagram can be represented by categorising it as more rigid or less rigid structural situations.[32] For more rigid structure, depending on the excitation wavelength, crystal confined aggregated AuNCs occupied a distinct singlet state from which it underwent intersystem crossing to the corresponding high-laying triplet state and vibrationally relaxed to the low-laying triplet state and recombine to S_0 through phosphorescence emission ($S_1^{`} \rightarrow T_1^{`}$). As the structure was rigid, different wavelength excitation leads to independent distinct singlet states, which were not correlated and similar type ISC happened to different triplet states and we observed a excitation dependent phosphorescence emission (similar process but different channel, i.e., $S_1^{*} \rightarrow T_1^{*}$ or $S_1^{\#} \rightarrow T_1^{\#}$). Thus, a single AuNCs aggregate behaved like a multicomponent luminophore for more compact structure inside a crystal (Ph_1, Ph_2, Ph_3 and so on) (Figure 4.10e). In less rigid structures, the triplets states were coupled and the lowest-energy triplet state (T_1) gets filled by internal conversion (IC) and relaxes to the ground singlet state (S_0), resulting in single phosphorescence (Ph_0) emission (Figure 4.10e).

4.4 Conclusion

In conclusion, we have provided a easy generalized route colour tuneable solvent-processable persistent fluorescence to phosphorescence switching at room temperature by doping inside a molecular crystals and provide significant insight on the tunability of PL property of dopant i.e., aggregated metal nanoclusters, depending on the surrounding crystalline environment and compactness of the confinement. Importantly, the switching between fluorescence in aqueous dispersion and phosphorescence in crystal was reversible, making them amenable to solvent processible device fabrication. Furthermore, if the triplet and singlet energy states of the crystal and those of the confined aggregated AuNCs are in close proximity, there is a possibility of energy transfer from the crystal to NCs through the interacting triplet as well as singlet energy states. Again, the number of phosphorescence emissive states for doped crystals can also be changed based on the rigid structure's compactness. For example, in the case of a highly compact, rigid structure, multiple triplet emissions were recorded, but in the case of a less compact, rigid structure, single triplet emission was noticed. The phosphorescence decay time can be 9.4 ms for molecular crystal doped aggregated AuNCs, and the PLQY can be up to 25%. This discovery not only opens up new avenues for designing and preparing colour-tuneable persistent gold nanocluster-based luminescent materials but also provides a roadmap for creating materials for multilayer information encryption, multicolour display, and biological applications.

Reference

1. Zhang, Y.; Hu, Q.; Paau, M. C.; Xie, S.; Gao, P.; Chan, W.; Choi, M. M. F. Probing Histidine-Stabilized Gold Nanoclusters Product by High-Performance Liquid Chromatography and Mass Spectrometry. *The Journal of Physical Chemistry C* **2013**, *117* (36), 18697–18708.
2. Yang, X.; Shi, M.; Zhou, R.; Chen, X.; Chen, H. Blending of HAuCl4 and Histidine in Aqueous Solution: A Simple Approach to the Au10 Cluster. *Nanoscale* **2011**, *3* (6), 2596–2601.
3. Luo, Z.; Yuan, X.; Yu, Y.; Zhang, Q.; Leong, D. T.; Lee, J. Y.; Xie, J. From Aggregation-Induced Emission of Au(I)–Thiolate Complexes to Ultrabright Au(0)@Au(I)–Thiolate Core–Shell Nanoclusters. *J Am Chem Soc* **2012**, *134* (40), 16662–16670.
4. Frisch, M. J.; Trucks, G. W.; Schlegel, H. B.; Scuseria, G. E.; Robb, M. A.; Cheeseman, J. R.; Scalmani, G.; Barone, V.; Petersson, G. A.; Nakatsuji, H., et al. *Gaussian 16 Rev. C.01*, Wallingford, CT, **2016**.

5. Zhao, Y.; Truhlar, D. G. The M06 suite of density functionals for main group thermochemistry, thermochemical kinetics, noncovalent interactions, excited states, and transition elements: two new functionals and systematic testing of four M06-class functionals and 12 other functionals. *Theor. Chem. Acc.* **2008**, 120, 215−241.
6. Roy, L. E.; Hay, P. J.; Martin, R. L., Revised Basis Sets for the LANL Effective Core Potentials. *J. Chem. Theory Comput* **2008,** *4* (7), 1029-1031.
7. Blaudeau, J.-P.; McGrath, M. P.; Curtiss, L. A.; Radom, L., Extension of Gaussian-2 (G2) theory to molecules containing third-row atoms K and Ca. *J. Chem. Phys.* **1997,** *107* (13), 5016-5021.
8. Sanner, M. F., Python: a programming language for software integration and development. *Journal of molecular graphics & modelling* **1999,** *17* (1), 57-61.
9. Reyes-Gasga, J.; Tehuacanero-Nuñez, S.; Montejano-Carrizales, J. M.; Gao, X.; Jose-Yacaman, M. Analysis of the Contrast in Icosahedral Gold Nanoparticles. *Top Catal* **2007**, *46* (1), 23–30. https://doi.org/10.1007/s11244-007-0311-y.
10. Wu, Z.; Jin, R. On the Ligand's Role in the Fluorescence of Gold Nanoclusters. *Nano Lett* **2010**, *10* (7), 2568–2573.
11. Yang, T. Q.; Peng, B.; Shan, B. Q.; Zong, Y. X.; Jiang, J. G.; Wu, P.; Zhang, K., Origin of the Photoluminescence of Metal Nanoclusters: From Metal-Centered Emission to Ligand-Centered Emission. *Nanomaterials (Basel)* **2020,** *10* (2).
12. Gu, L.; Wu, H.; Ma, H.; Ye, W.; Jia, W.; Wang, H.; Chen, H.; Zhang, N.; Wang, D.; Qian, C.; An, Z.; Huang, W.; Zhao, Y. Color-Tunable Ultralong Organic Room Temperature Phosphorescence from a Multicomponent Copolymer. *Nat Commun* **2020**, *11* (1), 944. https://doi.org/10.1038/s41467-020-14792-1.
13. Zhu, H.; Badía-Domínguez, I.; Shi, B.; Li, Q.; Wei, P.; Xing, H.; Ruiz Delgado, M. C.; Huang, F. Cyclization-Promoted Ultralong Low-Temperature Phosphorescence via Boosting Intersystem Crossing. *J Am Chem Soc* **2021**, *143* (4), 2164–2169.
14. Sugiuchi, M.; Maeba, J.; Okubo, N.; Iwamura, M.; Nozaki, K.; Konishi, K. Aggregation-Induced Fluorescence-to-Phosphorescence Switching of Molecular Gold Clusters. *J Am Chem Soc* **2017**, *139* (49), 17731–17734.
15. Yang, T.; Dai, S.; Yang, S.; Chen, L.; Liu, P.; Dong, K.; Zhou, J.; Chen, Y.; Pan, H.; Zhang, S.; Chen, J.; Zhang, K.; Wu, P.; Xu, J. Interfacial Clustering-Triggered Fluorescence–Phosphorescence Dual Solvoluminescence of Metal Nanoclusters. *J Phys Chem Lett* **2017**, *8* (17), 3980–3985.

16. Shen, J.; Xiao, Q.; Sun, P.; Feng, J.; Xin, X.; Yu, Y.; Qi, W. Self-Assembled Chiral Phosphorescent Microflowers from Au Nanoclusters with Dual-Mode PH Sensing and Information Encryption. *ACS Nano* **2021**, *15* (3), 4947–4955.
17. Wu, Z.; Du, Y.; Liu, J.; Yao, Q.; Chen, T.; Cao, Y.; Zhang, H.; Xie, J. Aurophilic Interactions in the Self-Assembly of Gold Nanoclusters into Nanoribbons with Enhanced Luminescence. *Angewandte Chemie International Edition* **2019**, *58* (24), 8139–8144.
18. Kuno, S.; Akeno, H.; Ohtani, H.; Yuasa, H. Visible Room-Temperature Phosphorescence of Pure Organic Crystals via a Radical-Ion-Pair Mechanism. *Physical Chemistry Chemical Physics* **2015**, *17* (24), 15989–15995.
19. Edhborg, F.; Küçüköz, B.; Gray, V.; Albinsson, B. Singlet Energy Transfer in Anthracene–Porphyrin Complexes: Mechanism, Geometry, and Implications for Intramolecular Photon Upconversion. *J Phys Chem B* **2019**, *123* (46), 9934–9943.
20. Zhao, T.; Busko, D.; Richards, B. S.; Howard, I. A., Limitation of room temperature phosphorescence efficiency in metal organic frameworks due to triplet-triplet annihilation. **2022,** *10*.
21. Li, M.; Sun, M.-J.; Yang, J.; Huo, D.; Lv, J.; Shi, D.; Zhong, Y.-W.; Wan, Y. Triplet–Triplet Energy Transfer inside the Single Organic Nanocrystal Revealed by Microscopic Time Resolved Spectroscopy. *The Journal of Physical Chemistry C* **2022**, *126* (27), 11033–11041.
22. Salas Redondo, C.; Kleine, P.; Roszeitis, K.; Achenbach, T.; Kroll, M.; Thomschke, M.; Reineke, S. Interplay of Fluorescence and Phosphorescence in Organic Biluminescent Emitters. *The Journal of Physical Chemistry C* **2017**, *121* (27), 14946–14953.
23. Shah, W. H.; Alam, A.; Javed, H.; Rashid, K.; Ali, A.; Ali, L.; Safeen, A.; Ali, M. R.; Imran, N.; Sohail, M.; Chambashi, G., Tuning of the band gap and dielectric loss factor by Mn doping of Zn1-xMnxO nanoparticles. *Sci Rep* **2023,** *13* (1), 8646.
24. Madden, J. J.; McGandy, E. L.; Seeman, N. C.; Harding, M. M.; Hoy, A., The crystal structure of the monoclinic form of l-histidine. *Acta Crystal. B* **1972,** *28* (8), 2382-2389.
25. Derissen, J. L. The Crystal Structure of Isophthalic Acid. *Acta Crystal. B* **1974**, *30* (11), 2764–2765.
26. Stamplecoskie, K. G.; Chen, Y.-S.; Kamat, P. V. Excited-State Behavior of Luminescent Glutathione-Protected Gold Clusters. *The Journal of Physical Chemistry C* **2014**, *118* (2), 1370–1376.

27. Stamplecoskie, K. G.; Kamat, P. V. Size-Dependent Excited State Behavior of Glutathione-Capped Gold Clusters and Their Light-Harvesting Capacity. *J Am Chem Soc* **2014**, *136* (31), 11093–11099.
28. Zhu, M.; Aikens, C. M.; Hollander, F. J.; Schatz, G. C.; Jin, R. Correlating the Crystal Structure of A Thiol-Protected Au25 Cluster and Optical Properties. *J Am Chem Soc* **2008**, *130* (18), 5883–5885.
29. Sharma, S.; Das, S.; Kaushik, K.; Yadav, A.; Patra, A.; Nandi, C. K. Unveiling the Long-Lived Emission of Copper Nanoclusters Embedded in a Protein Scaffold. *J Phys Chem Lett* **2023**, *14* (40), 8979–8987.
30. Yang, J.; Fang, M.; Li, Z. Stimulus-Responsive Room Temperature Phosphorescence Materials: Internal Mechanism, Design Strategy, and Potential Application. *Acc Mater Res* **2021**, *2* (8), 644–654.
31. Clabau, F.; Rocquefelte, X.; Le Mercier, T.; Deniard, P.; Jobic, S.; Whangbo, M.-H. Formulation of Phosphorescence Mechanisms in Inorganic Solids Based on a New Model of Defect Conglomeration. *Chemistry of Materials* **2006**, *18* (14), 3212–3220.
32. Baryshnikov, G.; Minaev, B.; Ågren, H. Theory and Calculation of the Phosphorescence Phenomenon. *Chem Rev* **2017**, *117* (9), 6500–6537.

Chapter 5

Complexation-based Super Crystalline Assembly of Zinc Oxide Quantum Dots for Sensitive Carbon Dioxide Gas Sensing

Herein, we report a facile method to assemble ZnO quantum dots (Qdots) into three-dimensional superstructures via surface complexation between zinc ions and phosphate. Results suggest that such programmed assembly was initiated by control growth of triclinic zinc phosphate tetrahydrate ($Zn_3(PO4)_2$, $4H_2O$) structures over the Qdot surface. Addition of phosphate to ZnO Qdot dispersion not only led to growth of such parahopeite structures but also resulted in crystalline assembly of the Qdots in the colloidal medium. The crystalline nature of the assembly was investigated by using spectroscopic and microscopic characterization techniques. The inter-Qdot distance was found to be 0.53 nm in the assembled superstructure. The assembled Qdots exhibited physical properties markedly different from the Qdots themselves. In general, the method described here has the potential to generate new ideas in the structural engineering of nanoscale assemblies, key to fabricating devices with rich functionalities. Finally, the so-generated ZnO Qdot-phosphate crystalline assembly was successfully applied to devise a gas sensor, which showed great sensitivity and selectivity towards CO_2 gas at room temperature.

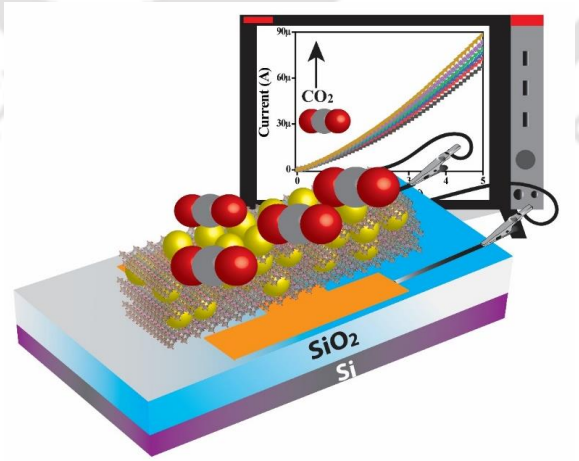

***[*J. Phys. Chem. C* 2021, 125, 22, 12316-12323]- reproduced with permission from the American Chemical Society.**

5.1 Experimental Section

5.1.1Materials

Zinc acetate dihydrate (98%, 219.49 g mol^{-1}), disodium hydrogen phosphate (Merck), 2-propanol (99%, 60.10 g mol^{-1}) and KOH (56.11 g mol^{-1}) were purchased from Merck. All materials were used without any further purification. Elix grade water from a MilliQ purification system was used for the experiments.

5.1.2 Synthesis of Qdots

ZnO Qdots were prepared by following a previously reported method with slight modification.[1,2] At first, 0.75 millimole (164.6 mg) of zinc acetate dihydrate was dispersed well in 15 mL of 2-propanol through sonication for 5 min. After that, 5 mL of 0.3 M (16.8 mg/mL) KOH solution in 2- propanol was added drop-wise for 7 min to the reaction mixture under stirring condition. The reaction was allowed to continue for 12 min at 40 ^{o}C until the clear reaction mixture became turbid. Subsequently, the medium was centrifuged at 12 000 rpm for 15 min. The resultant pallet, as-obtained following centrifugation, was collected carefully and washed well with ethanol solution twice to remove the unreacted residuals. The pellet was re-dispersed in 2- propanol, which was used for further experiments.

5.1.3 Synthesis of phosphate decorated ZnO Qdot assembly

In order to prepare phosphate decorated ZnO Qdot crystalline assembly (termed as ZnO Qdot-phosphate), 3.5 mL of 0.2 M disodium hydrogen phosphate (Na_2HPO_4) aqueous solution was added dropwise to the as-prepared ZnO Qdot reaction mixture (in 2- propanol) and was allowed to stir for 10 min. Subsequently, the resultant medium was cetrifuged at 12 000 rpm for 15 min. As-obtained pallet was washed twice and re-dispersed in water. After that, the solution was centrifuged for two times at 2 000 rpm (3 min each). Next, The supernatant part was collected carefully and subjected to centriguge for 12 000 rpm (15 min). The as-obtained pallet was finally dried at 55 ^{o}C overnight to get powder sample.

5.1.4 Characterization

Field emission transmission electron microscopy (TEM) analyses were done using a JEOL JEM-2100F FETEM instrument (acceleration voltage of 200 kV). A Rigaku TTRAX III diffractometer, running with a CuKα source (λ = 1.54 Å), was used to analyze the powder X-ray diffractin (XRD) pattern of the samples. X-ray photoelectron spectroscopy (XPS) analyses were performed using a PHI 5000 Versa Probe II, FEI Inc. instrument. Fourier transform

infrared (FTIR) spectra were aquired by using a PerkinElmer spectrometer. Also, UV−vis and fluorescence spectroscopy were performed using a Perkin Elmer Lambda 35 spectrophotometer and Horiba Fluoromax-4 spectrofluorometer, respectively. Time-resolved photoluminescence (TRPL) spectroscopy was done with Edinburgh Life-Spec-II spectrofluorometer. A JSM-7610F instrument was used for the field emission scanning electron microscopy (FESEM) anlysis. An Oxford Cypher S microscope was used for atomic force microscope (AFM) imaging.

5.1.5 Fabrication of device

SiO_2/Si substrate was first cleaned with 2- propanol, acetone, and piranha solution separately followed by rinsing with deionized (DI) water in each step. The substrate was then dried well in the presence of nitrogen gas (N_2). A primer hexamethyldisilazane (HMDS) was used for spin coating the cleaned substrate and was annealed at 125 ^oC for 10 min. Soon afterwards, S1813 (a positive photoresist) was spincoated and soft-baked at 125 ^oC for 3 min.

Next, a two-terminal electrode with a length of 5 µm and width of 10 µm was drawn using CleWin software; then the substrate was patterned using direct laser beam lithography [Make: KLOE, Model-Dilase-250] by maintaining appropriate velocity and modulation. After that, the substrate was dipped into a developer solution for 1 min and hard-baked at 125 ^oC. Finally, aluminum (100 nm thick) was deposited over the patterned substrate using a thermal evaporation system [Make: HHV Auto 500]. For the lift-off process, the aluminum deposited substrate was immersed in acetone, followed by washing with DI water.

Crystalline ZnO assembly or only ZnO Qdot based gas sensing device was fabricated by using a simple drop-casting method. At first, 2 µL of the sensing material was deposited over electrodes and annealed at 100 ^oC for 10 min; this process was repeated twice to reinforce the material uniformly between the electrodes. The drop-cast material had a diameter of approximately 2 to 3 mm over electrodes and average thickness of 831 nm.

5.1.6 Electrical characteristics of sensors

For electrical characterization, the fabricated sensor was placed inside a controlled environment chamber (CEC, Gen Renew India), and the contact pads were connected to a source meter by using low-noise triaxial cables (Keithley 4200A-SCS, U.S.A.) via crocodile clips. The CEC system consists of three mass flow controllers (MFCs) [Make: Alicat Scientific] with different flow rates to control carrier and analyte gas. In the CEC set up (Figure 5.1), the test gas in/outflow for the sensing chamber affected the sensor response and recovery

time.[3,4] The sensing chamber had 6 L volume in the sensing setup, and analyte gas was passed at 5 standard liters per minute (SLPM) until it reached the atmospheric pressure (760 Torr). For evacuation of the chamber, 25 SLPM pump was connected, which pumped down until it reached soft vacuum (200 Torr); hence, the sensor reported fast recovery compared to the response time. The chamber consisted of a pressure regulator by using which the pressure was regulated during the in/outflow of the test gas. Alicat's Flow Vision MX^{TM} gas-blending software in the computer regulated the gas mixing as per the preferred percentage and pressure. The MFCs output was connected to the sensing chamber through an in-line mixing unit. A high purity N_2 gas was used as a carrier, and for CO_2, CO, and NO_2 gases, a calibrated gas cylinder with 5000 ppm, 100 ppm, and 100 ppm pre-mixed in N_2 was respectively used.

The sensing chamber was evacuated prior to sensing, followed by N_2 purge; the aforementioned pump and purge cycle was performed three times to avoid contamination. The base resistance for both the ZnO Qdot-phosphate assembly and ZnO Qdot sensors were taken in the N_2 ambient at room temperature and atmospheric pressure. After that, the sensors' *I-V* characteristics and response to analyte gases were examined by sweeping voltage from 0 to +5 V and under different gas concentrations.

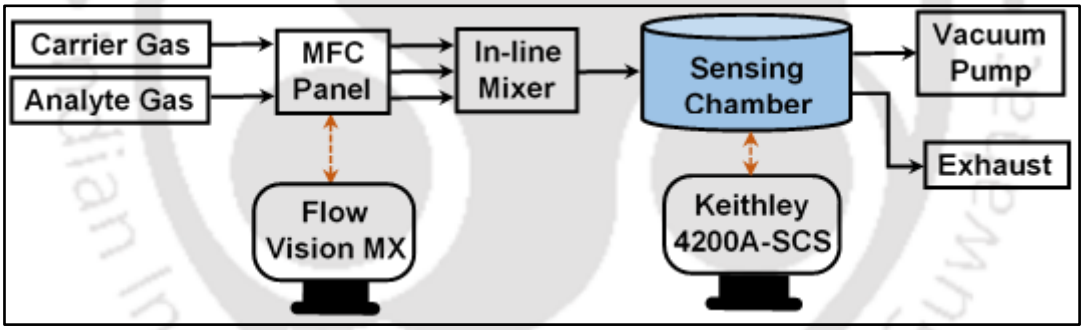

Figure 5.1 Schematic diagram of the controlled environment chamber (CEC) sensing setup.

5.1.7 Volatile organic compound (VOC) detection

An airtight chamber was used to analyze the ZnO Qdot-phosphate senor response towards different volatile organic compounds (VOCs). The sensor was tested against each VOC with 100 ppm concentration, formulated using the ideal gas equation. The measurement was made after 20 s of injection of the corresponding VOC into the chamber, and it was continuously observed for the response for 3 min. Soon after the observation, VOC content was removed using Kimwipe and N_2 flux, then an ample amount of time gap (approximately 3-5 min) was maintained for the sensor before starting with another VOC.

5.1.8 Quantum Yield Measurement

Quantum yield (QY) was calculated with respect to quinine sulphate in 0.1M H_2SO_4 as the reference using the following equation.

$$Q_S = Q_R \times \frac{I_S}{I_R} \times \frac{A_R}{A_S} \times \frac{\eta_S^2}{\eta_R^2} \quad 5.1$$

Here, Q_S= quantum yield of the sample; Q_R = quantum yield of the reference; I_S = area under the PL curve of the sample; I_R = area under the PL curve of reference; A_R = absorbance of reference; A_S = absorbance of the sample; η_S = refractive index of the sample solution; η_R = refractive index of reference.

Refractive index of water = 1.33 and QY of quinine sulphate = 0.54.

Absorbance of quinine sulphate (A_R) = 0.1. Area under the emission curve (I_R) = 2.88×10^8 (a.u.).

5.1.9 Average lifetime (τ_{av}), radiative (K_r) and non-radiative (K_{nr}) recombination rate constant calculation

Average lifetime values (τ_{av}) were calculated using equation 5.2. Further, calculations of radiative decay rate constant (K_r) and non-radiative decay rate constant (K_{nr}) were performed using equation 5.3 and equation 5.4.

$$\tau_{av} = \frac{\sum_i \alpha_i \tau_i^2}{\sum_i \alpha_i \tau_i} \quad 5.2$$

$$K_r = \frac{\varphi_D}{\tau_{av}} \quad 5.3$$

$$K_{nr} = \frac{1-\varphi_D}{\tau_{av}} \quad 5.4$$

Here, φ_D refers to the measured quantum yield value. Also, α_i and τ_i correspond to pre-exponential factor and decay time of the *i*-th component, respectively.

Table 5.1 Calculated parameters, as-obtained from time-resolved photoluminescence study, of ZnO Qdots and ZnO Qdot-phosphate.

Samples	λ^2	First component (α_1) (%)	First component lifetime (τ_1) (ns)	Second component (α_2) (%)	Second component lifetime (τ_2) (ns)
ZnO Qdots	1.0	4.73	6.29	95.26	55.7
ZnO Qdot-phosphate assembly	1.01	5.89	2.07	94.1	34.1

Table 5.2 Measured quantum yield values, average lifetime and corresponding radiative and non-radiative decay rate constants of the as-synthesized ZnO Qdots and ZnO Qdot-phosphate.

Samples	Quantum yield (φ_D) (%)	Average lifetime (τ_{av}) (ns)	Radiative decay rate constant (K_r) (s^{-1})	Non radiative decay rate constant (K_{nr}) (s^{-1})
ZnO Qdots	1.36 [a]	55.49 [c]	2.45×10^5 [e]	1.77×10^7 [g]
ZnO Qdot-phosphate assembly	1.76 [b]	34.03 [d]	5.17×10^5 [f]	2.88×10^7 [h]

[a] ± 0.02 %, [b] ± 0.16 %, [c] ± 3.9 ns, [d] ±1.5 ns, [e] ± 0.18× 10^5 s^{-1}, [f] 0.24 × 10^5 s^{-1}, [g] 0.14 × 10^7 s^{-1}, [h] 0.14 × 10^7 s^{-1}.

5.1.10 Limit of detection calculation

Limit of detection (LOD) for CO_2 detection was calculated according to the following formula.[5,6]

$$LOD = \frac{3\sigma}{K} \qquad 5.5$$

Here, σ corresponds to standard deviation in measured response % and K denotes the gradient of response (%) vs. concentration plot. As calculated, standard deviation i.e., σ for ZnO Qdot-phosphate assembly film was found to be 0.703 %. Gradient of response (%) vs. concentration plot was found to be 0.367 % per ppm of CO_2. Introducing the obtained values in the above equation, the calculated value of LOD was found to be 5.7 ppm.

5.2 Results and discussion

TEM analysis of the product of the phosphate-treatred ZnO Qdot (ZnO Qdot-phosphate) (Figure 5.2a, 5.2j, 5.2k) exhibited the formation of assembly of particles with diameters typically in the range of 5.0 nm to 9.0 nm. Notably, the diameter of the constituents (i.e., 7.0±2

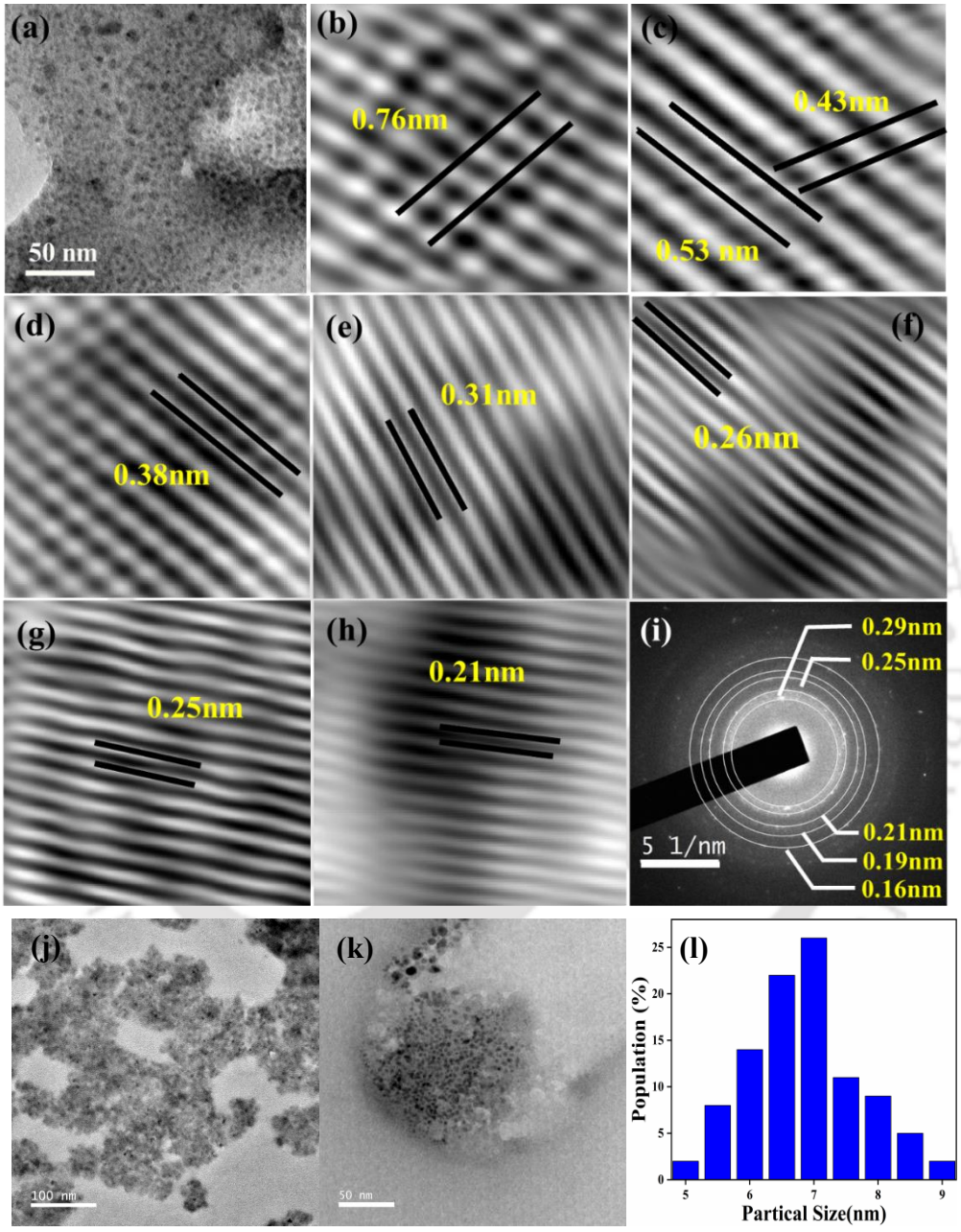

Figure 5.2 (a) TEM image of the ZnO Qdot-phosphate assembly. Lattice spacing values were found to be (b) 0.76, (c) 0.53, 0.43, (d) 0.38, (e) 0.31, (f) 0.26, (g) 0.25 and (h) 0.21 nm as calculated from the high-resolution TEM images and corresponding IFFT patterns. (i) SAED pattern observed for the assembled nanostructure. (j-k) Additional TEM image of the ZnO Qdot-phosphate assembly obtained from different places. (l) Size distribution plot of the constituent particles in the assembled system. Distribution was calculated from several TEM images (with 100 particles).

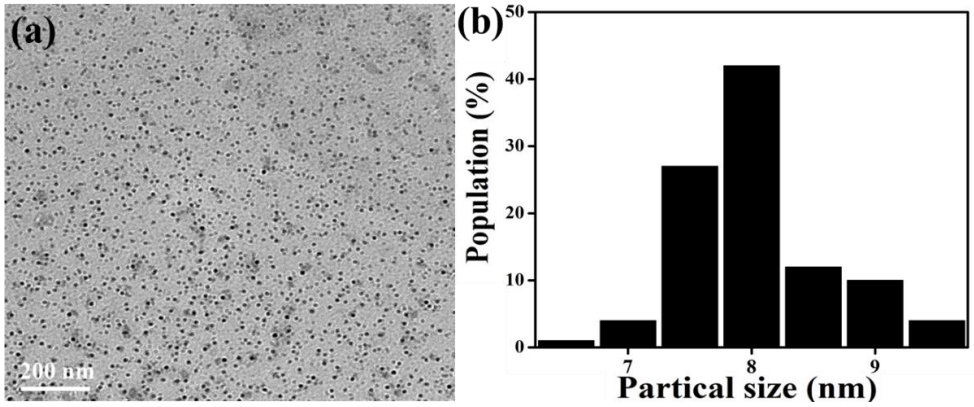

Figure 5.3 (a) TEM images of the ZnO Qdots. (b) Size distribution plot of the particles. Distribution was calculated from several TEM images (with 100 particles).

nm) in the assembly was comparable to the diameter of the as-prepared ZnO Qdots (8.0±1.5 nm; Figure 5.3a,b). The images indicated possible assembly of ZnO mediated by phosphate where zinc ions may bind with phosphate via oxygen. High-resolution transmission electron microscopy (high-resolution TEM) and selected-area electron diffraction (SAED) analyses of the assembled system confirmed their polycrystalline nature, which was also different from the untreated ZnO crystallinity. High-resolution TEM images (Figure 5.2b-h) and corresponding inverse fast Fourier transform (IFFT) patterns indicated presence of several distinct fringes with calculated lattice spacing values of 0.76, 0.53, 0.43, 0.38, 0.31, 0.26, 0.25 and 0.21 nm. Importantly, lattice spacing values of 0.26, 0.25 and 0.21 nm matched well with d-spacing values obtained during the SAED pattern analysis (Figure 5.2i).

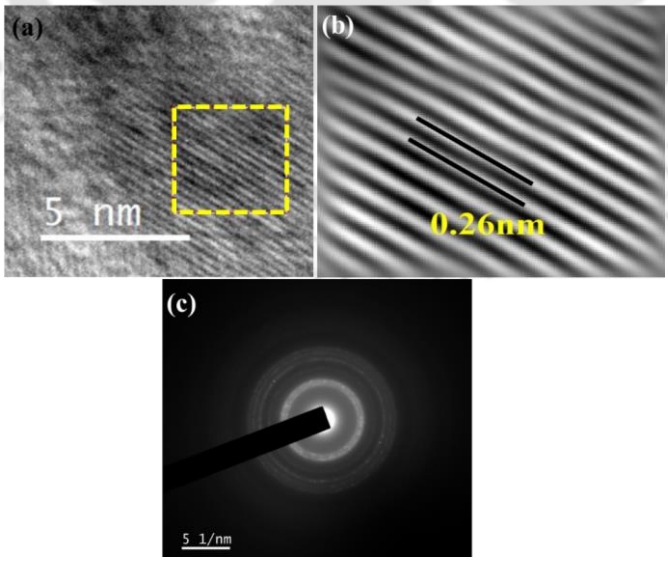

Figure 5.4 (a) High-resolution TEM of ZnO Qdots. (b) Corresponding IFFT pattern. (c) SAED of ZnO Qdots.

It is known that ZnO Qdots consist of wurtzite structure, which is also confirmed from the observed lattice spacing of 0.26 nm (Figure 5.4) during high-resolution TEM analysis in the present study. Indeed, 0.26 nm lattice spacing was also present in the ZnO Qdot-phosphate assembly. However, generation of new lattice planes, coexisting with the ZnO crystal planes further supported the formation of phosphate mediated assembly in Qdots.

The Powder XRD pattern, as represented in Figure 5.5c, substantiated the presence of wurtzite structure in ZnO Qdots with a = b = 3.2Å, C= 5.2Å and $\alpha = \beta = 90^{o}$, $\gamma = 120^{o}$ lattice parameters (JCPDS No. 36-1451).[7] However, the powder XRD pattern of ZnO Qdot-phosphate assembly comprised of multiple new sharp peaks (Figure 5.5a), demonstrating the formation of well-ordered new nanostructure with high crystallinity. The diffraction pattern of the Qdot assembly consisted of intense sharp peaks at *2*θ values of 11.6, 16.5, 20.2, 23.3, 28.7, 31.7, 33.4, 35.4, 37.4, and 39.3° along with other peaks between 41.1° and 77.6°. Appearance of the new peaks in the diffraction pattern indicated interaction between the ZnO Qdots and added

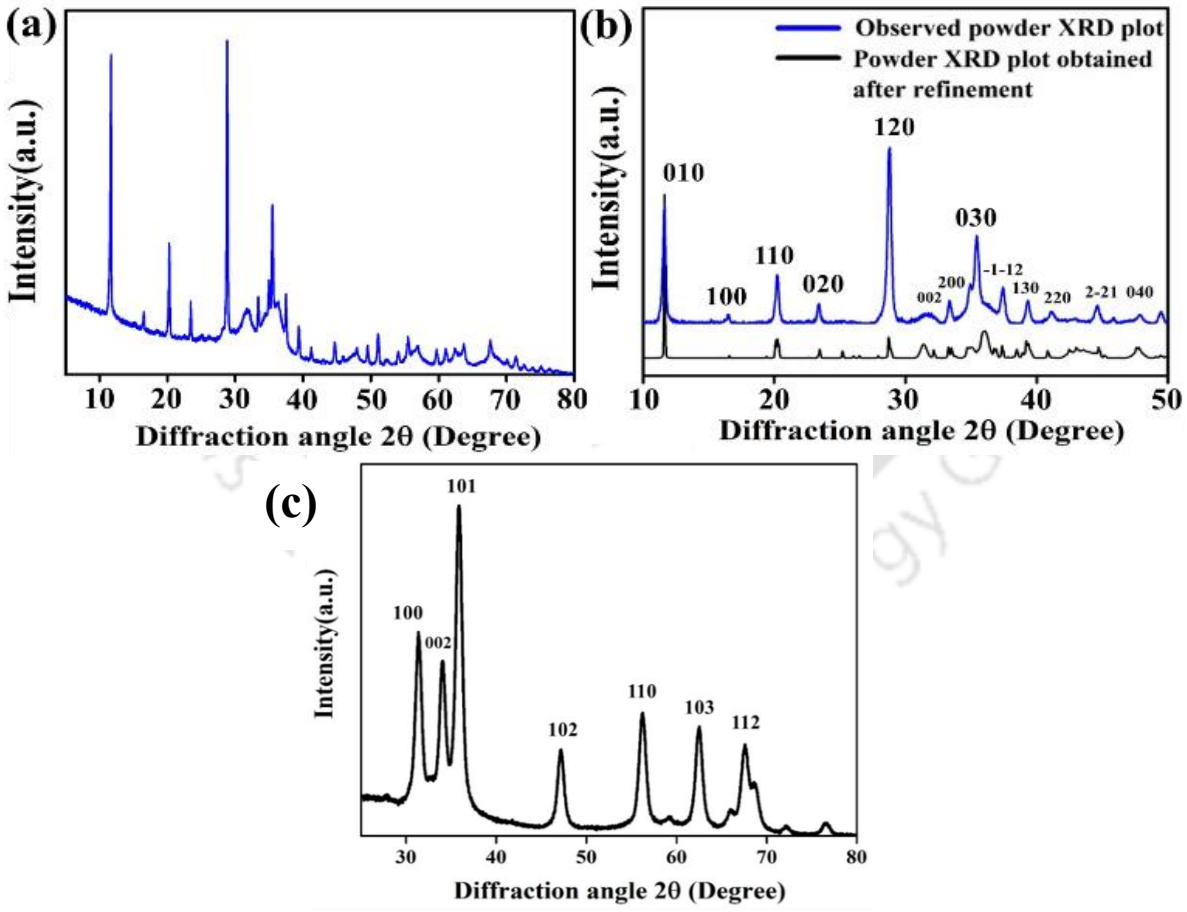

Figure 5.5 (a) Powder XRD pattern of ZnO Qdot-phosphate assembly. (b) Theoritical refinement of the powder XRD pattern of ZnO Qdot-phosphate assembly. The blue line corresponds to the obtained powder pattern and black line is for the calculated LeBail fit. (c) Powder XRD pattern of ZnO Qdots

phosphate resulting in assembly of Qdots. After that, we performed analyses of the obtained powder pattern (in Figure 5.5a) by using Fullprof suite of utilities via LeBail method (Figure 5.5b). The crystal structure of the as-synthesized assembled system mathched with the best chi-square value that had a triclinic unit cell of zinc phosphate tetrahydrate ($Zn_3(PO4)_2$, $4H_2O$) with unit cell parameters of a = 5.3503 Å, b = 7.6102 Å, c = 5.5744 Å, and $\alpha = 92.09^o$, $\beta = 92.06^o$, $\gamma = 89.59^o$ (along with the P-1 space group symmetry). Following refinement the obtained d-spacing values of 0.76, 0.53, 0.43, 0.38, 0.31, 0.25 and 0.21 nm (refer to Table 5.3) matched well with values obtained from high-resolution TEM and SAED analyses of the Qdot assebly (as mentioned in Figure 5.2). Based on all of the aforementioned information, we surmise that addition of disodium hydrogen phosphate into ZnO Qdots led to spontaneous growth of zinc phosphate tetrahydrate triclinic structure on the Qdot surface, which further assisted in the

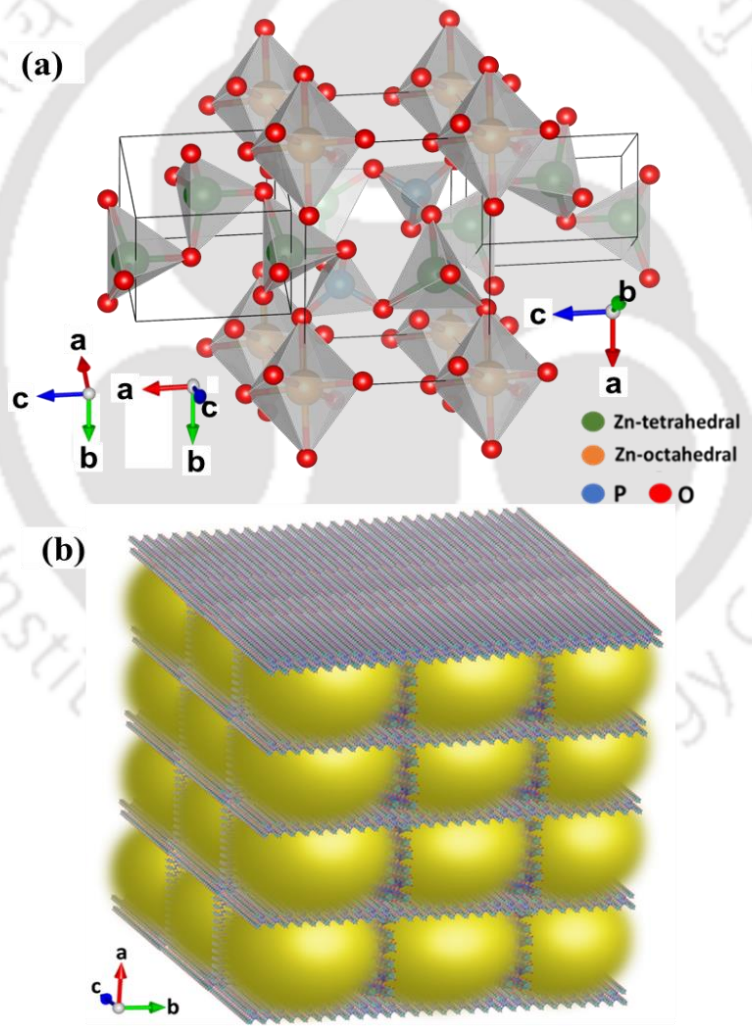

Figure 5.6 (a) Preferred orietation of ZnO wurtzite coupled with zinc phosphate triclinic arrangement in the assembled superstructure. (b) A schematic 3D visual corresponding to phosphate-mediated Qdot assembly.

formation of surface complexation mediated crystalline and self-assembled Qdot superstructures. In the assembled structure surface zinc ions from Qdots were bonded with added phosphate *via* Zn-O-P linkage. Thus, multiple wurtzite structured ZnO Qdots were organized with the triclinic zinc phosphate structure to result in a supercrystalline assembly. Possible arrangement of the surface zinc ions and added phosphate during complexation is represented in Figure 5.6a along with a 3D arrangement corresponding to the assembly in Figure 5.6b. It is important to note that the distance of 0.53 nm matches with the distance between the two neighboring ZnO wurtzite crystals structures, connected via the phosphate linkage. According to theoritical refinement the lattice spacing of 0.53 nm corresponds to peak at 16.5° in the obtained powder pattern due to 100 plane (refer to Table 5.3). Thus, 0.53 nm lattice spacing represents the inter Qdot distance, which originated from the assembly of dots (Figure 5.7).

Table 5.3 hkl values and theoritically calculated d spacing values correponding to the powder XRD diffraction peaks of ZnO Qdot-phosphate assembly.

Diffraction angle (2θ)	**Assigned *hkl***	**Corresponding d-spacing (Å)**
11.62	010	7.60
16.56	100	5.34
20.23	110	4.38
23.37	020	3.80
28.70	120	3.10
33.49	200	2.67
35.37	030	2.53
37.35	-1-12	2.40
39.21	130	2.29
41.12	220	2.19
44.71	2-21	2.02
47.8	040	1.90

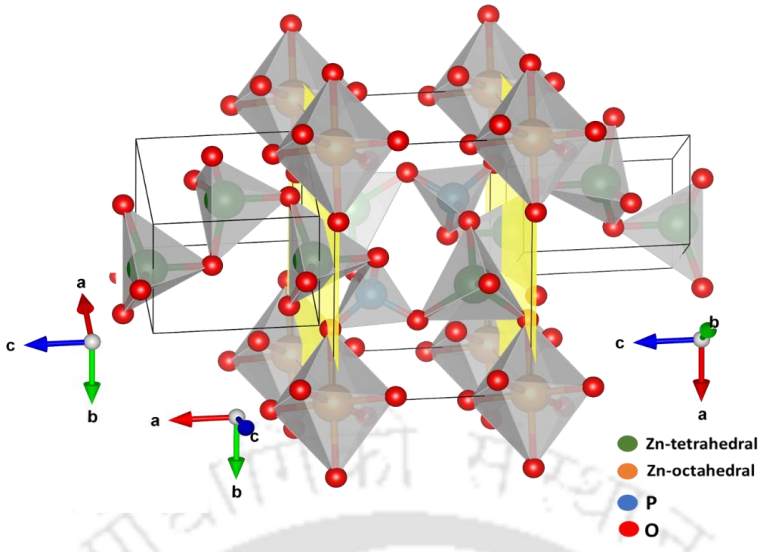

Figure 5.7. Identified 100 plane corresponding to distance between wurtzite crystal structures. According to the results the distance between two planes (yellow colored; 100) is 0.53 nm. A VESTA 3.5.2 analyzer was used for the structure generation.

Interaction between surface zinc and added phophate due to assembly was further characterized by using spectroscopic techniques. X-ray photoelectron spectroscopy (XPS) analysis of the Qdot assembly (Figure 5.8) exhibited two major sharp peaks at 1043.2 and 1020 eV corresponding to Zn $2p_{1/2}$ and Zn $2p_{3/2}$, respectively.[8] Similar peaks were observed for ZnO

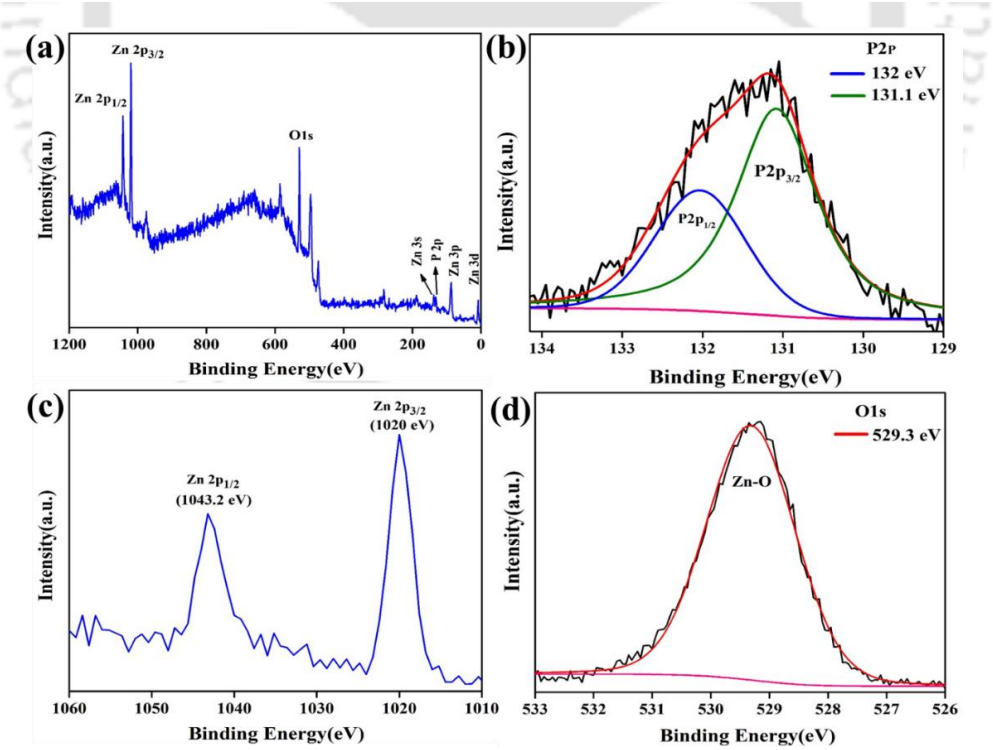

Figure 5.8. (a) XPS plot of Qdot assembly consisting of peaks due to phosphorus. (b) Deconvoluted plot for P2p peak. Enlarged plots for Zn $2p_{1/2}$ and Zn $2p_{3/2}$ peaks, observed at 1043.2 and 1020 eV respectively. (d) XPS peak for O1s signal, appearing at 529.3 eV in ZnO Qdot-phosphate assembly.

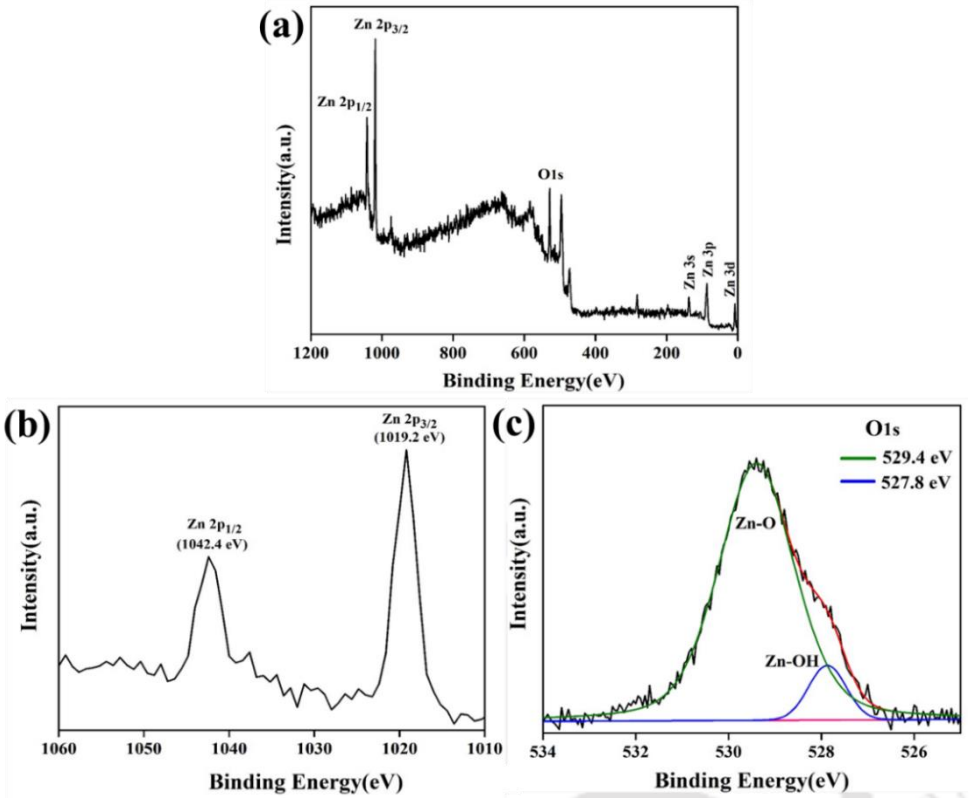

Figure 5.9. (a-c) XPS results for ZnO Qdots indicating presence of zinc along with oxygen in the structure.

Qdot XPS plot as well, at 1042.4 and 1019.2 eV, respectively (Figure 5.9).[8] However, another intense peak was observed at 132 eV in ZnO Qdot-phosphate assembly XPS plot due to P_{2p} (which was perticularly absent in ZnO XPS plot in Figure 5.9a), confirming successful incorporation of phosphorus into the structure.[9] Other major peaks appering in XPS analysis plots of both the ZnO Qdot-phosphate assembly and ZnO Qdots were identified and are represented in Figure 5.8 and 5.9, respectively. Presence of phosphates with ZnO Qdots and

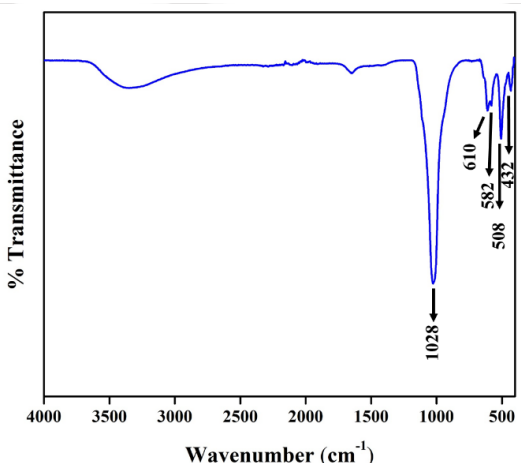

Figure 5.10 FTIR spectrum of the as-prepared ZnO Qdot-phosphate assembly. Here, the characteristic sharp peak appearing at 1028 cm^{-1} corresponds to P-O stretching in phosphates. Peak appearing at 610 cm^{-1} indicates Zn-OH bond vibration. Additional peaks observed at 582 508 and 432 cm^{-1} correspond to translational modes of Zn-O bonds.[10,11]

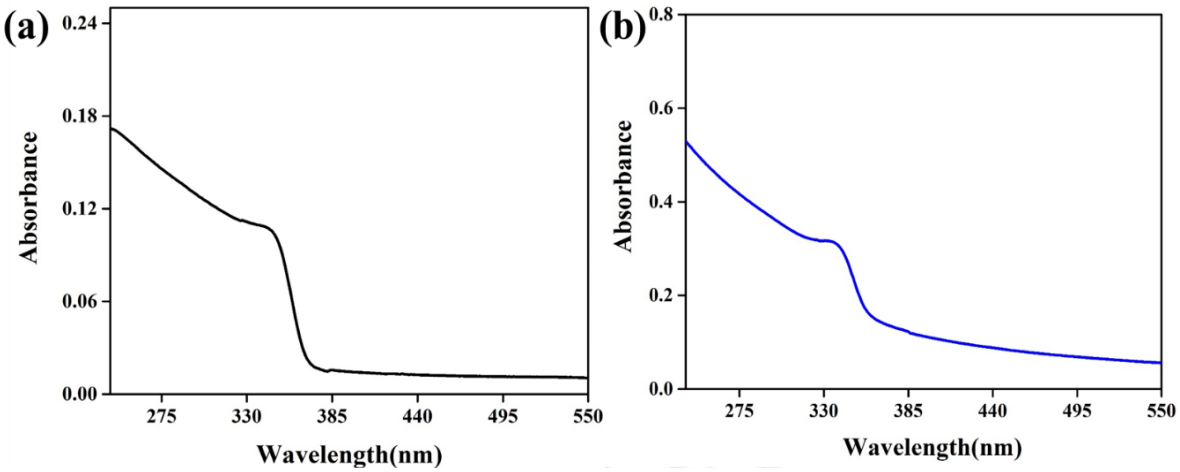

Figure 5.11 UV-vis absorption spectra of (a) ZnO Qdots and (b) ZnO Qdot-phosphate assembly.

their interactions were further confirmed by Fourier transformed infrared (FTIR) spectroscopy, presented in Figure 5.10. Sharp peak could be observed at 1028 cm^{-1} corresponding to P-O stretching in phosphates thus supportig the presence of phosphate in the assembled structure.[12]

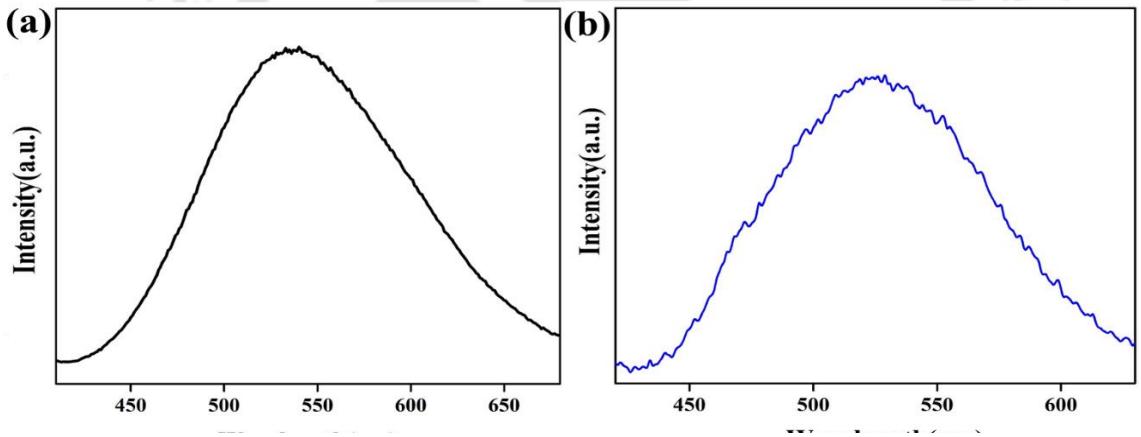

Figure 5.12 Emission spectra of (a) ZnO Qdots and (b) ZnO Qdot-phosphate assembly. The excitation wavelength was set at 350 nm and 340 nm respectively.

Figure 5.11a, 5.12a represents UV-vis and emission characteristics of the as-prepared ZnO Qdots that consist of an absorption band at 345 nm and emission maximum centered at 540 nm (corresponding λ_{ex} = 350 nm). However, following complexation, the absorption band and emission maximum blue-shifted to 335 nm and 525 nm (λ_{ex} = 340 nm), respectively (Figure 5.11b, 5.12b). Excitation spectra of both the ZnO Qdots and the assembly were recorded, corresponding to λ_{em} of 540 and 525 nm, respectively, and are presented in Figure 5.13 as well. They also match with the absorption maximum of the respective species. The photoluminescence quantum yield (PL QY) of ZnO Qdot and ZnO Qdot-phosphate assembly were measured to be 1.36 and 1.76 % respectively at 340 nm excitation wavelength.

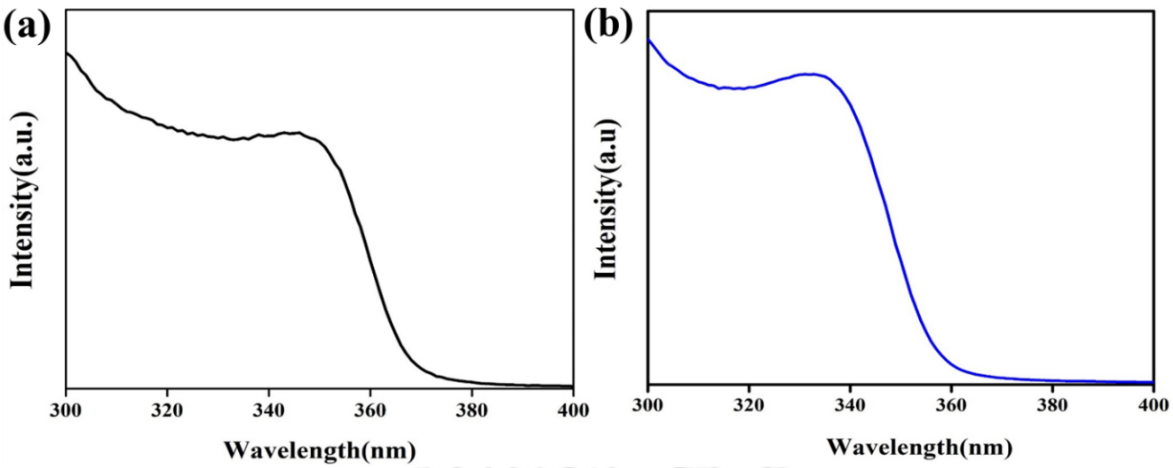

Figure 5.13 Excitation spectra of (a) ZnO Qdots and (b) ZnO Qdot-phosphate. The emission maxima were set at 540 and 525 nm wavelengths for ZnO Qdots and ZnO Qdot-phosphate, respectively.

Time-resolved photoluminescence (TRPL) spectroscopy showed decrease in average lifetime following the formation of crystalline assembly (Figure 5.14). As mentioned in Table 5.1 and 5.2, the average PL lifetime for ZnO Qdot was found to be 55.49 ns wher as the same for ZnO Qdot-phosphate assebly was measured to be 34.03 ns. Corresponding radiative (K_r) and non-radiative decay rate constants (K_{nr}) for both the systems are included in Table 5.2 as well. Results indiacte that surface complexation mediated assebly in Qdots assisted in excitonic recombination through radiative pathway, leading to higher QY.

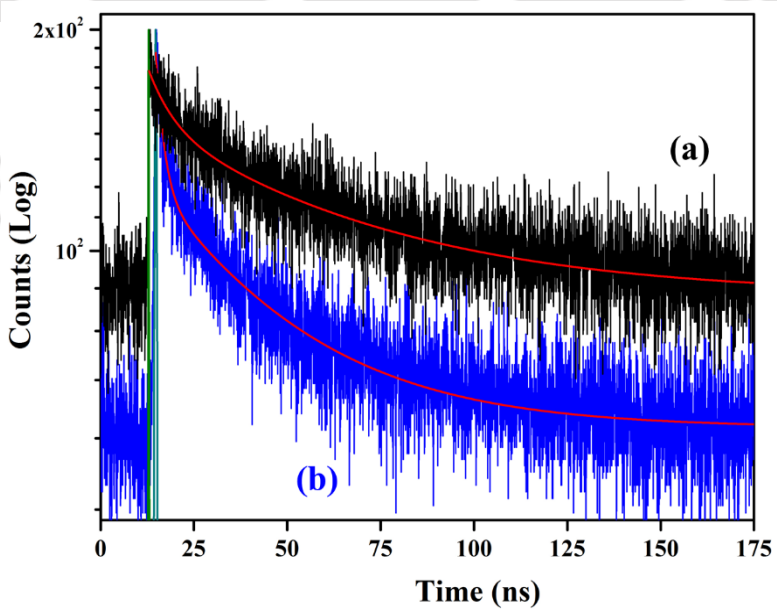

Figure 5.14 Time resolved photoluminescence (TRPL) spectra of (a) ZnO Qdots and (b) ZnO Qdot-phosphate assembly. The excitation wavelengths were set at 375 nm and 336 nm respectively.

Gas sensing characteristics of crystalline ZnO Qdot-phosphate assembly was studied at room temperature by using a device fabricated over SiO_2/Si substrate. Details are mentioned in the experimental section. Figure 5.15a,b and 5.16a,b represent the optical image of the device and surface morphology of ZnO Qdot-phosphate substrate over the device, respectively. From the AFM image analysis average thickness ($d_{av.}$) of the Qdot assembly film was found to be 831 nm (Figure 5.15c). The electrical conductance of ZnO Qdot-phosphate based sensing device was measured by sweeping the voltage source from 0 to + 5 V with 0.1 V steps. Corresponding changes in currents were recorded in absence of analyte gas (Figure 5.15d), under the N_2 environment (carrier gas here). A complete Schematic diagram of the controlled environment chamber (CEC) sensing setup is presented in Figure 5.1. Details of the measurement procedure have been mentioned in the experimental section. As indicated by the *I–V* characteristic plot (Figure 5.15d), an increase in the supplied voltage to ZnO Qdot-phosphate sensor film produced a Schottky diode behavior characteristic, with low barrier height. Further as-prepared ZnO Qdot-phosphate sensor device was exposed under various CO_2

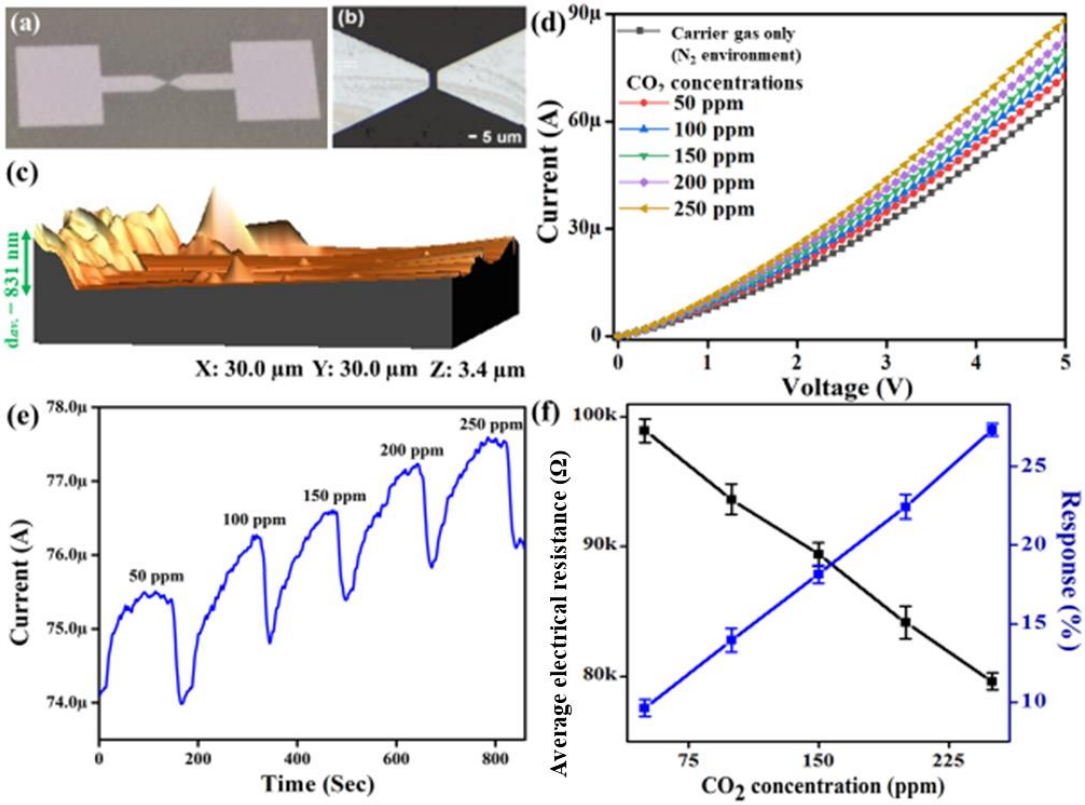

Figure 5.15 (a) Microscopic image of the two-terminal electrode. (b) Enlarged view of the channel. (c) Representative AFM image corresponding to parallel view of sensor film. Average film thickness ($d_{av.}$) was 831 nm. (d) *I–V* characteristic plots of ZnO Qdot-phosphate sensor film in the presence of varying concentrations of CO_2 gas. (e) Transient response plot of the assembly film. (f) Average electrical resistance change with CO_2 concentration and sensor response plot of ZnO Qdot-phosphate assembly based CO_2 sensor film.

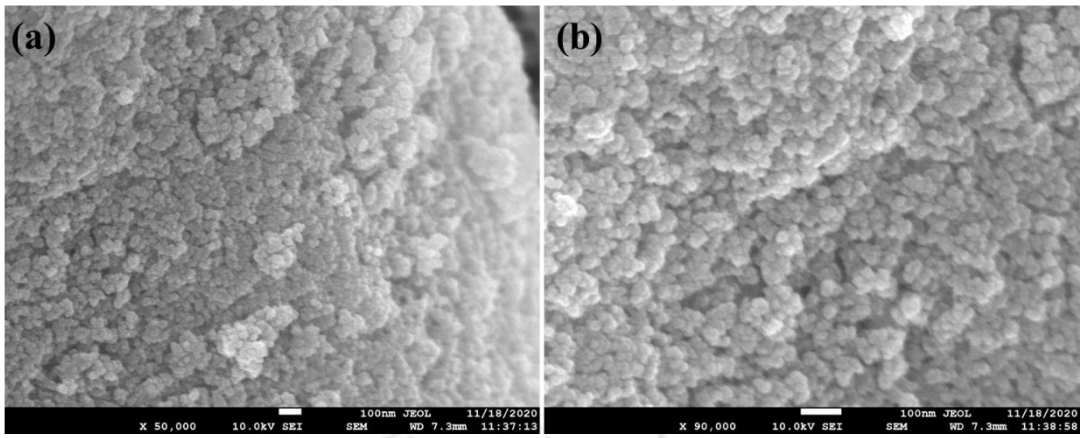

Figure 5.16 FESEM image corresponding to ZnO Qdot-phosphate sensor film recorded at two different places.

analyte concentrations. Interestingly, as shown in Figure 5.15d, with increasing the CO_2 concentrations, the *I–V* characteristic plot became steeper, suggesting higher conductance of the composite film at higher concentrations of CO_2 gas. Eventually, the result showed a systematic increase in film conductance with increase in the CO_2 concentration. Figure 5.15e shows recovery characteristics of ZnO Qdot-phosphate sensor film at different concentrations (50-250 ppm) of CO_2 at room temperature with bias of +5 V. The representative transient plot in Figure 5.15e indicated that the ZnO Qdot-phosphate sensor was reversible towards CO_2 sensing, where the reponse time was measured to be 35-40 sec and recovery time was 20-25 sec. Evidently, a proportional increase in the real time response (*R*) was observed (Figure 5.15f). Here, the response % was calculated based on the following equation.

$$R = \frac{|R_g - R_0|}{R_0} \times 100\ \% \qquad (5.6)$$

Where R_0 and R_g are the channel resistance before and after CO_2 exposure, respectively. Figure 5.17a represents *I–V* response for the less crystalline and un-assembled ZnO sensor film where CO_2 concentration was varied between 50 and 250 ppm. Unlike the Qdot assembly sensor film, a negligible response in the *I–V* plot was observed for ZnO Qdot sensor film. Corresponding real time response vs CO_2 concentration plot has been represented in Figure 5.17b. We surmise that ZnO Qdot-phosphate sensor consisted of a higher degree of crystallinity than ZnO Qdots. Such crystalline networks assisted in superior electron mobility throughout the structure resulting in improved conductance.

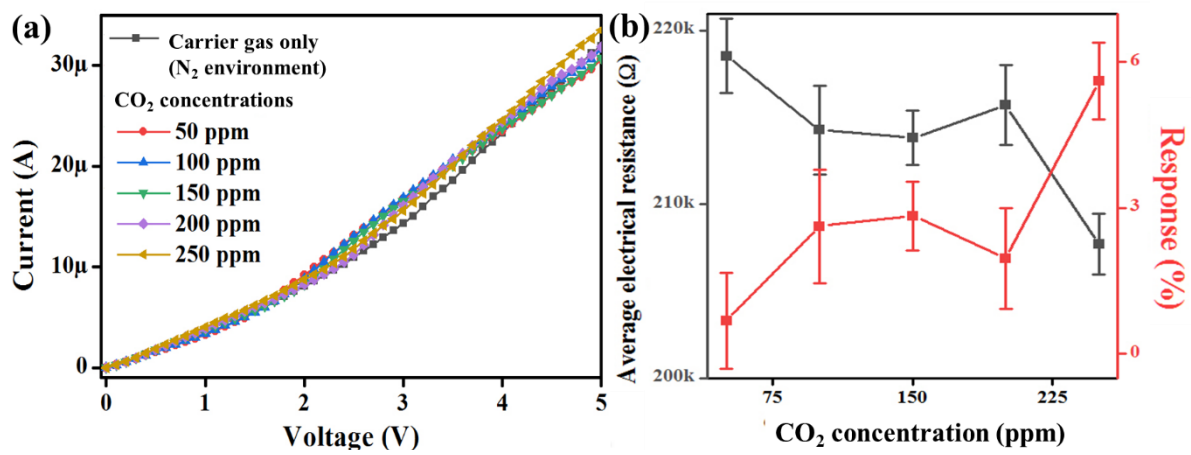

Figure 5.17 (a, b) CO_2 response by ZnO Qdot sensor film. Similar to ZnO Qdot-phosphate assembly, the conductance of ZnO Qdot device was measured by sweeping the voltage source from 0 to + 5 V with 0.1 V steps. *I-V* plot of ZnO Qdots film has Schottky diode behavior characteristic, with low barrier height. Further, the ZnO Qdots sensor device was exposed to different CO_2 analyte concentrations. Here, the response was aberrant against ZnO Qdot-phosphate assembly. The response towards CO_2 concentrations at bias points was varying irregularly .

Literature reports suggest that phosphates and their composites act as potential CO_2 absorbents at ambient conditions.[13-16] In the present study, with the help of free phosphates, the crystalline assembly system captured maximum amount of CO_2 gas from atmosphere. Thus, higher sensitivity towards CO_2 can be attributed to ordered geometry, high conductance and finally, the free phosphates capturing CO_2 gas effectively. On the other hand, in case of the ZnO Qdot sensor film, inherent conductance was found to be low and there were no free phosphate groups present for effective CO_2 capture. Furthermore, mechanism corrsponding to the enhanced sensitivity of ZnO Qdot-phosphate sensor film towards CO_2 can be explained based on the oxygen vacancy principle. As per the principle, metal oxide surface consists of oxygen vacancies, determining the chemiresistance behavior. Since, these vacancies are electron donors, ZnO acts as an n-type semiconductor. The sensor resistivity and therefore the gas sensing performances exclusively depend upon the adsorbed CO_2 concentrations. At first, CO_2 reacts with doubly ionized oxygen vacancy ($V_O^{\bullet\bullet}$) to form $CO_2^{\bullet\bullet}$ and neutral oxygen vacancies ($V_O^{\times}$). After that, $V_O^{\times}$ ionizes to release electron to the conduction band of the semiconductor. Thus, exposure to CO_2 leads to higher free carrier density in the composite, resulting in increased conductivity and lowering of the average electrical resistance (as are evident from Figure 5.15d and 5.15f as well). The process can be described as following equations.[17-19]

$$CO_2 + V_O^{\bullet\bullet} \Leftrightarrow CO_2^{\bullet\bullet} + V_O^{\times} \quad (5.7)$$

$$V_O^{\times} \Leftrightarrow V_O^{\bullet} + e' \quad (5.8)$$

$$V_O^{\bullet} \Leftrightarrow V_O^{\bullet\bullet} + e' \quad (5.9)$$

The sensor response was verified in soft vacuum (200 Torr), N_2 (760 Torr) and ambient air conditions (760 Torr) as well. Responses in soft vacuum and N_2 environment were nearly identical, whereas 39.7% response was calculated under the ambient air (Figure 5.18). Indeed, the sensor response was in line with our obtained results, as shown in Figure 5.15. The increase in response in the air may be attributed to CO_2 concentration (ranging between 300-400 ppm under ambient conditions) and relative humidity.

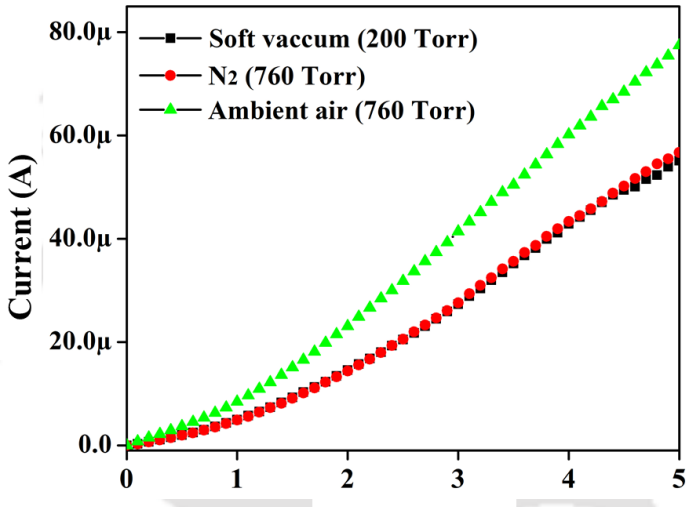

Figure 5.18 ZnO Qdot-phosphate sensor response under the soft vacuum (200 Torr), N_2 (760 Torr) and ambient air conditions (760 Torr).

As shown in Figure 5.19, the sensing performance of the Qdot assembly was much higher toward CO_2 gas (by about an order of magnitude) as compared to other gaseous analytes such

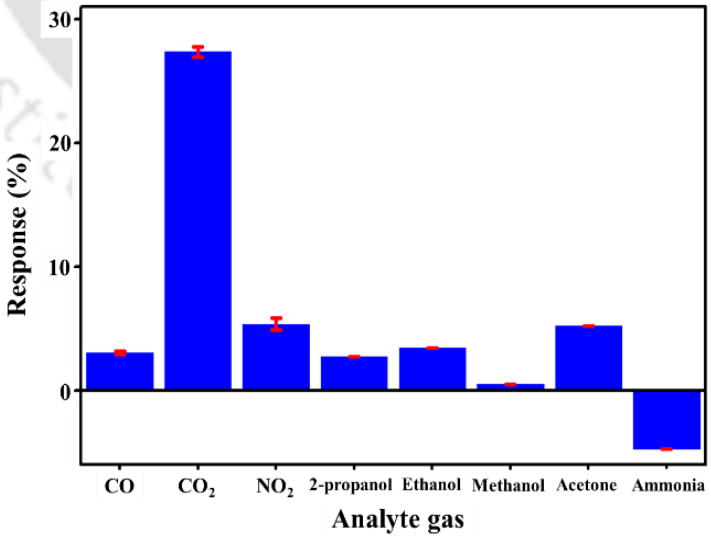

Figure 5.19 Response of the ZnO Qdot-phosphate assembly based sensor film towards several gaseous analytes. Here, CO_2 gas concentration was 250 ppm. The concentration of interfering analyte (CO, NO_2, 2-propanol, ethanol, methanol, acetone and ammonia) was 100 ppm.

as CO, NO_2, and common volatile organic compounds (VOCs) such as 2-propanol, ethanol, methanol, acetone, thus demonstrating selectivity for the detection of CO_2 gas. Since the as-prepared ZnO Qdot-phosphate sensor film showed sufficient change in *I-V* characteristics between 50 and 250 ppm, we further lowered CO_2 concentrations for obtaining the limit of detection (LOD). Corresponding plots have been represented in Figure 5.20a and 5.20b. LOD for CO_2 was calculated to be 5.7 ppm. It is important to note that the lower limit of CO_2 ranges between 300 and 400 ppm in the terrestrial air.[20] Thus, the present device fabricated with highly crystalline Qdot assembly film can be considered to have sufficient sensitivity and selectivity towards CO_2 gas above 5.7 ppm concentration.

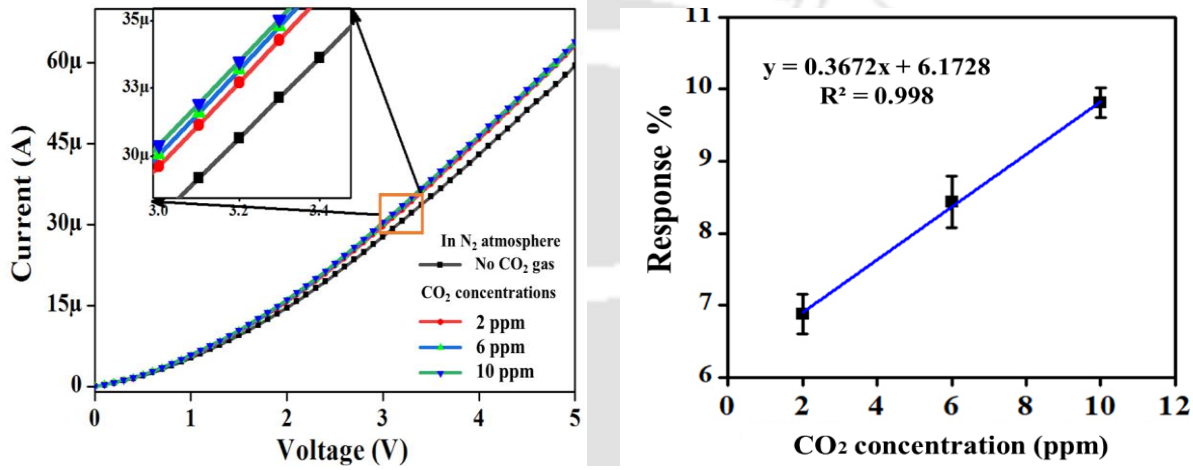

Figure 5.20 (a) Current vs voltage diagram for ZnO Qdot-phosphate sensor film in the presence of CO_2 concentrations ranging between 2 and 10 ppm. (b) Sensor response curve of the ZnO Qdot-phosphate sensor film in the presence of different concentrations of CO_2 gas.

5.3 Conclusion

In conclusion, we have demonstrated a simple strategy to form crystalline assembly in colloidal ZnO Qdots that also provided a new platform for efficient CO_2 sensing at room temperature. Such assembly of ZnO Qdots not only generated high crystallinity but also induced favourable electron transportations, which was successfully utilized for selective and sensitive gas sensing performance. Such crystalline assembly maximized charge carrier density, conductivity of the substrate and therefore demonstrating high sensitivity (LOD 5.7 ppm) towards CO_2 gas under room temperature conditions. The programmed super crystalline assembly made of ZnO Qdots can be considered as remarkable and the idea and the knowledge presented here have the kernel to create new advanced materials with great potential for applications, based on organizations of nanoscale particles into higher dimensions.

Reference

1. Roy, S.; Pramanik, S.; Bhandari, S.; Chattopadhyay, A. Surface Complexed ZnO Quantum Dot for White Light Emission with Controllable Chromaticity and Color Temperature. *Langmuir* **2017**, *33*, 14627–14633.
2. Wong, E.; Hoertz, P.; Liang, C.; Shi, B.; Meyer, G.; Searson, P. Influence of Organic Capping Ligands on the Growth Kinetics of ZnO Nanoparticles. *Langmuir* **2001,** *17*, 8362-8367.
3. Annanouch, F.-E.; Bouchet, G.; Perrier, P.; Morati, N.; Reynard-Carette, C.; Aguir, K.; Bendahan, M. How the Chamber Design Can Affect Gas Sensor Responses. *Proceedings* **2018**, *2*, 820.
4. Lopez, L., Copa, V., Hayasaka, T. Faustino-Lopez, M. A.; Wu, Y.; Liu, H.; Liu, Y.; Estacio, E.; Somintac, A.; Lin, L.; Salvador, A. Influence of Chamber Design on the Gas Sensing Performance of Graphene Field-effect-transistor. *SN Appl. Sci.* **2020**, 2, 1185.
5. Huang, J.; Wang, L.; Shi, C.; Dai, Y.; Gua, C.; Liu, J. Selective Detection of Picric Acid Using Functionalized Reduced Graphene Oxide Sensor Device. *Sens. Actuators, B* **2014**, *196*, 567-573.
6. Ang, C.; Tan, S.; Wu, S.; Qu, Q.; Wong, M.; Luo, Z.; Li, P.; Selvan, S.; Zhao, Y. A Dual Responsive "Turn-On" Fluorophore for Orthogonal Selective Sensing of Biological Thiols and Hydrogen Peroxide. *J. Mater. Chem. C* **2016**,*4*, 2761-2774.
7. Choi, S.; Kim, E.; Park, J.; An, K.; Lee, N.; Kim, S.; Hyeon, T. Large-Scale Synthesis of Hexagonal Pyramid-Shaped ZnO Nanocrystals from Thermolysis of Zn-Oleate Complex. *J. Phys. Chem. B* **2005**, *109*, 14792-14794.
8. Zhang, Z.; Shao, C.; Li, X.; Wang, C.; Zhang, M.; Liu, Y. Electrospun Nanofibers of P-Type NiO/ n-Type ZnO Heterojunctions with Enhanced Photocatalytic Activity. *ACS Appl. Mater. Interfaces* **2010**, *2* (10), 2915–2923.
9. Kim, S. O.; Manthiram, A. The Facile Synthesis and Enhanced Sodium-Storage Performance of a Chemically Bonded CuP_2/C Hybrid Anode. *Chem. Commun.* **2016**, *52*, 4337–4340.
10. Qin, N.; Xiang, Q.; Zhao, H.; Zhang, J.; Xu, J. Evolution of ZnO Microstructures from Hexagonal Disk to Prismoid, Prism and Pyramid and Their Crystal Facet-dependent Gas Sensing Properties. *CrystEngComm* **2014**, *16*, 7062–7073.

11. Mahapure, S.; Palei, P.; Nikam, L.; Panmand, R.; Ambekar, J.; Apte; S.; Kale, B. Novel Nanocrystalline Zinc Silver Antimonate ($ZnAg_3SbO_4$): An Efficient & Ecofriendly Visible Light Photocatalyst with Enhanced Hydrogen Generation. *J. Mater. Chem. A* **2013**, *1*, 12835–12840.
12. Wang, C.; Sun, D.; Zhuo, K.; Zhang, H.; Wang, J. Simple and Green Synthesis of Nitrogen-, Sulfur-, and Phosphorus-Co-Doped Carbon Dots with Tunable Luminescence Properties and Sensing Application. *RSC Adv.* **2014**, *4*, 54060–54065.
13. Mondal, M. ; Singh, J. ; Khatri, D. Equilibrium CO_2 Capture in Aqueous Blend of Trisodium Phosphate and Piperazine. *J. Chem. Eng. Data* **2014**, *59*, 1175 -1180.
14. Pereira, L.; Oliveira, M.; Dias, A.; Llovell, F.; Vega, L.; Carvalho, P.; Coutinho, J. High Pressure Separation of Greenhouse Gases from Air with1-ethyl-3-methylimidazolium methyl-phosphonate. *Int. J. Greenhouse Gas Control* **2013**, *19*, 299-309.
15. Balsora, H.; Mondal, M. Solubility of CO_2 in an Aqueous Blend of Diethanolamine and Trisodium Phosphate. *J. Chem. Eng. Data* **2011**, *56*, 4691- 4695.
16. Nowicki, D.; Skakle, J.; Gibson, I. Nano-Scale Hydroxyapatite Compositions for the Utilization of CO_2 Recovered Using Post-Combustion Carbon Capture. *J. Mater. Chem. A* **2018**,*6*, 5367-5377.
17. Kanaparthi, S.; Singh, S. G. Chemiresistive Sensor Based on Zinc Oxide Nanoflakes for CO_2 Detection. *ACS Appl. Nano Mater.* **2019**, *2*, 700–706.
18. Gurlo, A.; Riedel, R. In Situ and Operando Spectroscopy for Assessing Mechanisms of Gas Sensing. *Angew. Chemie - Int. Ed.* **2007**, *46*, 3826–3848.
19. Xiong, Y.; Xue, Q.; Ling, C.; Lu, W.; Ding, D.; Zhu, L.; Li, X. Effective CO_2 Detection Based on LaOCl-Doped SnO_2 Nanofibers: Insight into the Role of Oxygen in Carrier Gas. *Sensors Actuators, B Chem.* **2017**, *241*, 725–734.
20. Sanz-Pérez, E. S.; Murdock, C. R.; Didas, S. A.; Jones, C. W. Direct Capture of CO_2 from Ambient Air. *Chem. Rev.* **2016**, *116*, 11840−11876.

Chapter 6

Summary and Future Prospects

6.1 Summary

The present thesis represents the synthesis and potential application of molecular crystals at various dimensional-scales crystallization-induced assembly of nanomaterials.

1. We revealed that the surface of molecular crystals may serve as an appropriate SERS platform. The surface functionality of molecular crystals can participate in non-covalent interactions with the deposited analyte molecules, allowing for efficient photoinduced charge transfer. We have also shown that inorganic molecular crystals can exhibit metallic characteristics and cause surface plasmons. These molecular crystals have the potential to be employed as SERS substrate due to their excellent photochemical stability, simplicity of synthesis, outstanding environmental stability, biocompatibility, and target molecule selectivity.
2. Instead of inorganic crystals or metal nanoparticles, metal-free small organic molecular microcrystals such as terephthalic acid can exhibit considerable SERS properties similar to coinage metals with no "hot spots" and recently identified inorganic semiconductors. It delivers both molecule-specific and cooperative Raman scattering. The electronic structure of the crystals based on density functional theory (DFT) revealed photo-induced charge transfer transitions, and the concept of hybrid orbitals formed by non-covalent interactions between analyte and crystal surface in the hybrid system that provided insights into the cooperative, molecule-specific intense SERS performance.
3. Doping inside molecular crystals can be used as a easy generalized route colour tuneable solvent-processable persistent fluorescence to phosphorescence switching at room temperature. They provide significant insight on the tunability of PL property of dopant i.e., aggregated metal nanoclusters, depending on the surrounding crystalline environment and compactness of the confinement.
4. The surface complexation process between zinc ions and phosphate can be utilised to construct colloidal zinc oxide (ZnO) quantum dots (Qdots) assembly into three-dimensional crystalline superstructures. Crystalline assembly was initiated by adding

an aqueous solution of disodium hydrogen phosphate to the in situ ZnO reaction mixture. This resulted in the controlled development of zinc phosphate tetrahydrate structures across the Qdot surface, leading to assembly formation. Crystalline networks in the ZnO Qdot-phosphate nano-sensor film contributed to improved electron mobility throughout the structure, that was effectively used for selective and sensitive electrochemical gas sensing performance.

Overall, crystalline molecule and nanoparticle assemblages have enormous potential to transform the area of nanoscience and technology. Their unique features open up exciting prospects in SERS, cutting-edge luminous materials, and the development of functionalized and miniaturized electrochemical devices.

6.2 Future outlook

The present thesis will aid in the future growth of molecular crystal-based SERS devices and represent a significant advancement in the potential application of SERS for bio- and pollutant detection. Chemical doping or electrical charge infusion may cause band edges to shift and free charge carriers to be injected into molecular crystals, possibly resulting in localised surface plasmons. The substrate's molecular structure not only provides a novel material for SERS but also a chemical repertoire for modifying the electronic band structures of microcrystals to match those of the targeted analytes by altering the metal centres and various aromatic analogues. This novel SERS substrate may enrich the knowledge of molecular interplays, catalysis, and mass transport chemistry. Tuning of NCs property as a dopant inside molecular crystals shed light on the approaches that can induce tuneable phosphorescence properties on simple metal NCs through ordered packing structures by manipulating the surrounding environment and electronic confinements. These new improved optical and physiochemical materials have applications in imaging, multicolour displays, LED, persistent energy storage and discharge, data encryption, and other solid-state devices. The ordered assembly of nanomaterials not only produced high crystallinity but also induced advantageous electron transports, which were effectively used for selective and accurate sensing performance. The programmed super crystalline assembly constructed of nanomaterials is extraordinary, and the idea and information offered here have the foundation to produce new sophisticated materials with tremendous application potential, based on the organisation of nanoscale materials into hierarchical ordered structure.

In addition, as part of the future perspective, I have added experimental data illustrating the synthesis of moiré superlattice of non-van der Waals and van der Waals 2D crystals from corresponding bulk crystals.

The field of crystal engineering producing innovative molecular crystals designs especially at the nanoscale two-dimensions and method of designing thereof, providing new paradigm of optical, magnetic, electronic or catalytic properties of such molecules. We have demonstrated a generalized one-step method for synthesizing moiré superlattices from covalent molecular crystals, ionic crystals and metal complex crystals which comprises the steps of finely grounding bulk crystals, and sonicating the grounded crystals in ultrasonic bath at moderate temperature in presence of a solvent system to obtain a dispersion of moiré superlattices of the molecules in the solvent system. Such approach can be applicable to vast range of crystals in synthesizing moiré superlattices form versatile precursors.

In brief, heat assisted liquid phase ultrasonic exfoliation tears the crystals in 2D-sheets along the direction where the attractive interactions are minimal, or the produced 2D-sheets can achieve more thermodynamically stable structures. In case of 2D-sheet, hexagonal lattice is typically the most stable conformer. After exfoliation, the solvent-sheet interaction has to reconcile the inter-sheet attraction forces. In an appropriate solvent and temperature, these sheets can rearrange themselves to form more thermodynamically stable twisted superlattice structure (Figure 6.1).

Here, we have synthesised moiré superlattices of simple organic molecules, ionic salts and metal complexes crystals that includes- sodium chloride (NaCl), potassium chloride (KCl), ammonium iron (III)-sulphate, hexahydrate ($NH_4Fe(III)(SO_4)_2.6H_2O$), ammonium iron (II)-sulphate, hexahydrate ($(NH_4)_2Fe(II)(SO_4)_2.6H_2O$), ammonium manganese (II)-sulphate, hexahydrate ($(NH_4)_2Mn(II)(SO_4)_2.6H_2O$) and ammonium zinc (II)-sulphate, hexahydrate ($(NH_4)_2Zn(II)(SO_4)_2.6H_2O$), diaqua-8-hydroxyquinolinyl-5-sulfonato zinc(II) (ZQS. $2H_2O$), tris(acetylacetonato)iron(III) ($Fe(acac)_3$), and L-tryptophan. Brief experimental results of as synthesized moiré superlattice have been demonstrated here comprising ionic crystals (sodium chloride, NaCl, Figure 6.2), one metal complex (diaqua-8-hydroxyquinolinyl-5-sulfonato zinc(II), ZQS. $2H_2O$, Figure 6.3) and a organic crystal (L-tryptophan, Figure 6.4). The details have been represented in Appendix 1.

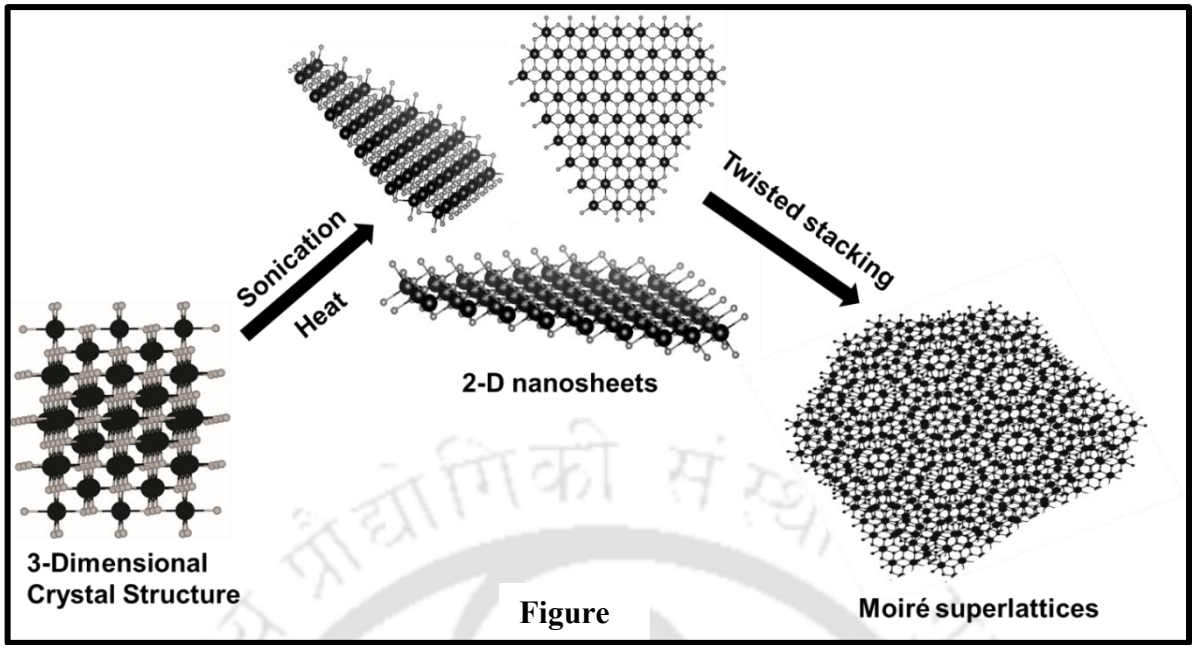

Figure 6.1 Schematic representation of the invented protocol. First, the crystals were exfoliated through heat-induced sonication to 2-D nanosheets, which re-assembled through twisted stacking to form the moiré superlattices.

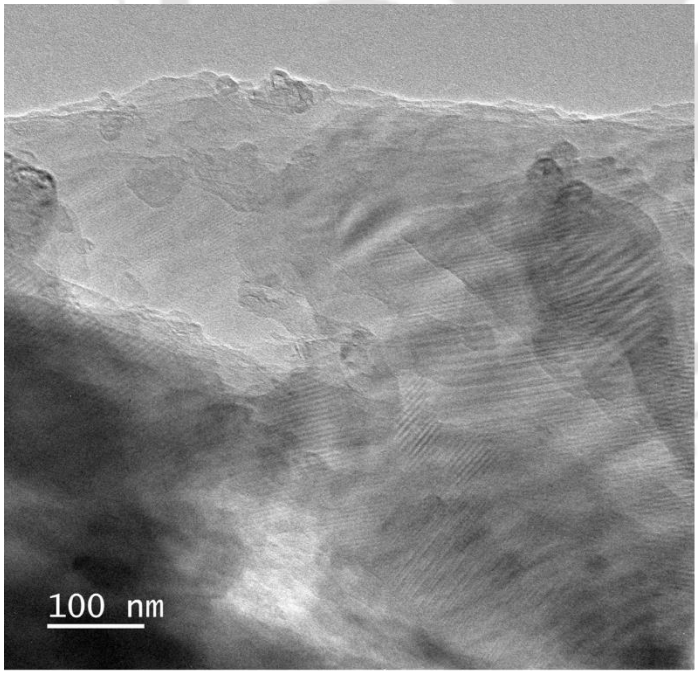

Figure 2A

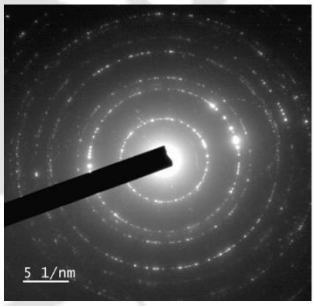

Figure 2B

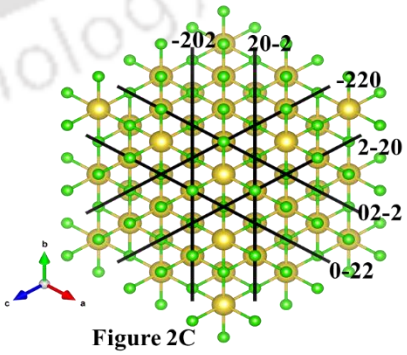

Figure 2C

Figure 6.2 (A) Transmission electron microscopy (TEM) image of moiré fringes obtained after twisted stacking of 2D nanosheets of NaCl. (B) Corresponding selected area electron diffraction (SAED) pattern. (C) Crystal structure of NaCl along 111 axis with the lattice planes participating in hexagon formation.

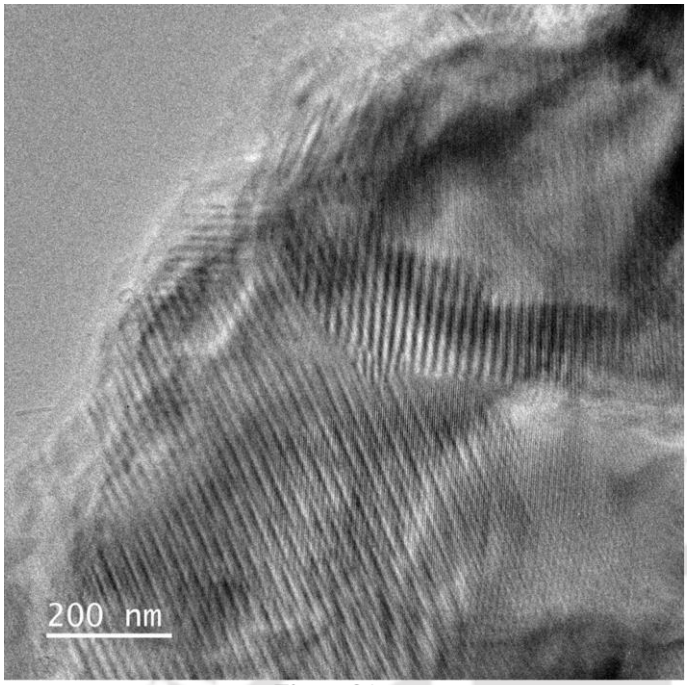

Figure 3A

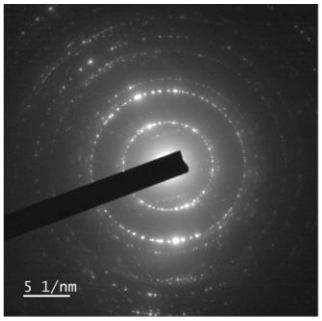

Figure 3B

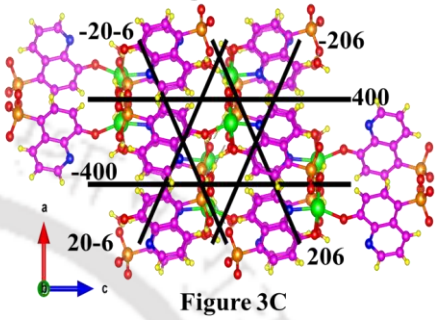

Figure 3C

Figure 6.3 (A) Transmission electron microscopy (TEM) image of moiré fringes obtained after twisted stacking of 2D nanosheets of ZQS. $2H_2O$. (B) Corresponding selected area electron diffraction (SAED) pattern. (C) Crystal structure of ZQS. $2H_2O$ along 010 axis with the lattice planes participating in hexagon formation.

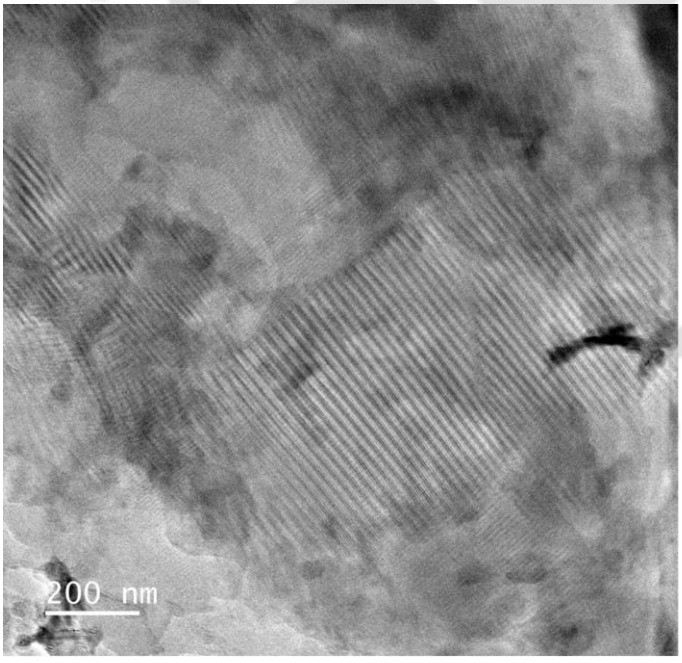

Figure 4A

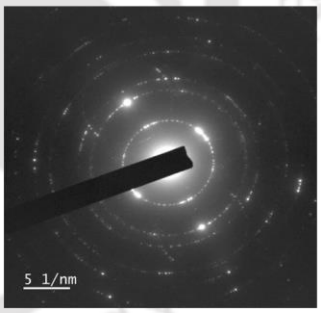

Figure 4B

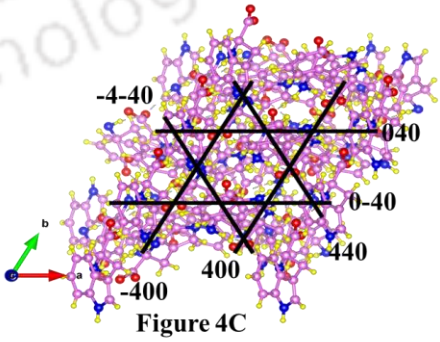

Figure 4C

Figure 6.4 (A) Transmission electron microscopy (TEM) image of moiré fringes obtained after twisted stacking of 2D nanosheets of L-tryptophan. (B) Corresponding selected area electron diffraction (SAED) pattern. (C) Crystal structure of L-tryptophan along 001 axis with the lattice planes participating in hexagon formation.

Appendix 1

The content in this appendix has been filed as an Indian patent at Kolkata office.

Indian Patent Application No : 202431027351

Filing Date : April 2, 2024

Inventor list – 1. Prof. Arun Chattopadhyay 2. Arin Bhakat 3. Ujjala Dey.

METHOD FOR SYNTHESIZING MOIRÉ SUPERLATTICES FROM CRYSTALS

FIELD OF THE INVENTION

The present invention relates to the field of crystal engineering producing innovative molecular crystals designs especially at the nanoscale two-dimensions and method of designing thereof, providing new paradigm of optical, magnetic, electronic or catalytic properties of such molecules.

BACKGROUND OF THE INVENTION

Crystal engineering over the past few decades has opened a new field for the precise design of molecular crystals leading to matter with the emergence of optical, magnetic, electronic or catalytic properties. (Corpinot, M. K.; Bučar, D.-K., A Practical Guide to the Design of Molecular Crystals. Cryst. Growth Des. 2019, 19 (2), 1426-1453; Nangia, A. K.; Desiraju, G. R., Crystal Engineering: An Outlook for the Future. Angew. Chem. Int. Ed. 2019, 58 (13), 4100-4107). Most of the work has been done involving organic molecules and metal complexes where the supramolecular interactions lead to the formation of molecular crystals. Again, the progress of crystal facet engineering for the controlled growth of the crystal along any particular facet has led to observation of facet-dependent properties. For example, single-crystalline facet-controlled growth of semiconductor crystals are now being considered for photocatalytic or surface dependent properties (Liu, J.; Wei, A., Prenucleation and coalescence of cobalt nanoclusters mediated by multivalent calixarene complexes. Chem. Comm.2009, (28), 4254-4256).

In a different vein, ionic, metal complex or organic crystals can be cleaved following a top-down approach such that one of the facets is exposed and re-assembly by twisted stacking occurs along the same axis to form moiré superlattices. These twisted crystals may bring about new properties that are not present in pure 3D crystals. In that respect, a moiré superlattice gives rise to interesting

phenomena that occur when two thin layers of crystalline materials are stacked slightly out of alignment. The overlaying of these slightly misaligned lattices results in a new, wider periodic pattern known as the moiré pattern. This pattern functions as a virtual superlattice, impacting the coupled materials' electrical and optical characteristics.

Moiré superlattices are primarily synthesized from 2D van der Waals (vdW) materials, including graphene, hexagonal boron nitride (hBN), and transition metal dichalcogenides (TMDCs). The vdW transfer technique is the most often used method for creating moiré patterns (Zihao Wang et al., Composite super-moiré lattices in double-aligned graphene heterostructures. Sci. Adv.5, eaay8897(2019).DOI:10.1126/sciadv.aay8897). This approach is based on polymer transfer mechanism, first mechanical exfoliation, and then layering of thin sheets by employing a polymer stamp. Intriguing properties have been studied in TBG (twisted bilayer graphene) and twisted TMDCs device using this vdW transfer approach. (Cao, Y., Fatemi, V., Demir, A. et al. Correlated insulator behaviour at half-filling in magic-angle graphene superlattices. Nature 556, 80–84 (2018).) (Zhang, J., Wang, J., Chen, P., Sun, Y., Wu, S., Jia, Z., Lu, X., Yu, H., Chen, W., Zhu, J., Xie, G., Yang, R., Shi, D., Xu, X., Xiang, J., Liu, K. and Zhang, G. (2016), Observation of Strong Interlayer Coupling in MoS2/WS2 Heterostructures. Adv. Mater., 28: 1950-1956. https://doi.org/10.1002/adma.201504631) (Mishchenko, A., Tu, J., Cao, Y. et al. Twist-controlled resonant tunnelling in graphene/boron nitride/graphene heterostructures. Nature Nanotech 9, 808–813 (2014). https://doi.org/10.1038/nnano.2014.187). Initially, graphene, or a TMDC monolayer, has been synthesized by mechanical exfoliation or CVD growth. Though these methods are popular but large-scale production of these moiré superlattices is difficult. The stacking of two sheets at an angle can generate new properties such as moiré excitons (Alexeev, E. M.; Ruiz-Tijerina, D. A.; Danovich, M.; Hamer, M. J.; Terry, D. J.; Nayak, P. K.; Ahn, S.; Pak, S.; Lee, J.; Sohn, J. I.; Molas, M. R.; Koperski, M.; Watanabe, K.; Taniguchi, T.; Novoselov, K. S.; Gorbachev, R. V.; Shin, H. S.; Fal'ko, V. I.; Tartakovskii, A. I., Resonantly hybridized excitons in moiré superlattices in van der Waals heterostructures. Nature 2019, 567 (7746), 81-86), superconductivity at 1.7 K (Cao, Y.; Fatemi, V.; Fang, S.; Watanabe, K.; Taniguchi, T.; Kaxiras, E.; Jarillo Herrero, P., Unconventional superconductivity in magic-angle graphene superlattices. Nature 2018, 556 (7699), 43-50) or ferromagnetism originating from the Hall effect (Pixley, J. H.; Andrei, E. Y., Ferromagnetism in magic-angle graphene. Science 2019, 365 (6453), 543-543).

Recently, moiré superlattices of metal clusters or organic molecules have been reported that were synthesized following bottom-up chemical procedures. For example, 2D copper nanocluster assembly has been reported which were synthesized following supramolecular chemical reaction of the nanosheets with triphenylphosphine in liquid medium. (Das, P.; Chattopadhyay, A., Moiré superlattices of two-dimensional copper nanocluster assemblies with tuneable twin emissions from hierarchical components leading to white light emission. J. Mater. Chem. C 2023, 11 (35), 12029-12036). In another aspect, molecular moiré superlattices of tryptophan were synthesized again through a chemical process where tryptophan molecules were stirred at 80 °C for 24 h which led to visible fluorescence due to moiré superlattices formed in the medium (Dey, U.; Chattopadhyay, A., Two-Dimensional Molecular Moiré Superlattices of Tryptophan with Visible Photoluminescence for Photo-activatable CO_2 Sensing and Storage. *J. Mater. Chem. C* **2024**. https://doi.org/10.1039/D4TC00050A). Moiré superlattices of BiOCl has been prepared through screw-dislocation driven growth utilizing easily hydrolyzed $Bi(NO_3)_3 \cdot 5H_2O$ and poly diallyldimethylammonium chloride (PDDA) as precursors of Bi^{3+} and Cl^-, respectively, and ethylene glycol as the solvent, which showed much enhanced photocatalytic activity when compared with bulk BiOCl (Liu, L.; Sun, Y.; Cui, X.; Qi, K.; He, X.; Bao, Q.; Ma, W.; Lu, J.; Fang, H.; Zhang, P.; Zheng, L.; Yu, L.; Singh, D. J.; Xiong, Q.; Zhang, L.; Zheng, W., Bottom-up growth of homogeneous Moiré superlattices in bismuth oxychloride spiral nanosheets. Nat. Commun. 2019, 10 (1), 4472).

Since the field involving the study of moiré superlattices is rapidly expanding as newer materials are being investigated, a generalized protocol is required for its feasible high-quality production. A generalized protocol may also be used for the synthesis of moiré superlattices of materials such as ionic crystals, organic molecules and inorganic complexes whose structure and properties are yet to be studied.

Liquid phase exfoliation has been used for the production of 2D nanosheets from its bulk counterpart at large scale with high-quality (Li, Z.; Young, R. J.; Backes, C.; Zhao, W.; Zhang, X.; Zhukov, A. A.; Tillotson, E.; Conlan, A. P.; Ding, F.; Haigh, S. J.; Novoselov, K. S.; Coleman, J. N., Mechanisms of Liquid-Phase Exfoliation for the Production of Graphene. ACS Nano 2020, 14 (9), 10976-10985).

Further, in ultrasonication, shear forces and cavitation, lead to the formation and collapse of micrometre-sized bubbles or cavities in liquids caused by pressure variations and locally high temperatures, impact the bulk crystals, causing exfoliation. Optimum choice of solvent and sonication time determine the quality and quantity of the materials thus produced.

Accordingly, there remains a need for methods which are scalable and provides high quality moiré superlattices of crystals of organic molecules, ionic salts and metal complexes.

The present inventors found that heat assisted liquid-phase exfoliation in the presence of ultrasonication provides an opportunity for a combination of such top-down and bottom-up methods for the scalable and high-quality production of moiré superlattices. Heat assisted liquid phase ultrasonic exfoliation tears the crystals in 2D-sheets along the direction where the attractive interactions are minimal, or the produced 2D-sheets can achieve more thermodynamically stable structures. In case of 2D-sheet, hexagonal lattice is the most stable conformer. After exfoliation, the solvent-sheet interaction has to reconcile the inter-sheet attraction forces. In an appropriate solvent and temperature, these sheets can rearrange them to form more thermodynamically stable twisted superlattice structure (Figure 1A). Further, sonication of crystals is often regarded as a non-invasive process. Hence, as formed 2D sheets are mostly defect free or mostly found near the edges of the 2D sheet. As a result, heat assisted sonication based liquid phase exfoliation can be used to synthesize defect free moiré superlattice in one step with bulk quantity.

Such combined approach for synthesis of moiré superlattices has not reported in any prior art.

OBJECTIVE OF THE INVENTION

Accordingly, it is an objective of the present invention to provide a generalized one-step protocol for the large scale and cost-effective production of moiré superlattices from crystals of organic molecules, ionic salts and metal complexes.

It is further an objective of the present invention to combine liquid exfoliation and ultrasonication and providing an opportunity for a combination of top-down and bottom-up method for synthesis of moiré superlattices of simple organic molecules, ionic salts and metal complexes.

It is also an objective of the present invention to provide a method for producing nanoscale 2D films from crystals for synthesizing moiré superlattices.

It is yet another objective of the present invention to determine the structure of the moiré superlattices thus formed and the properties they may offer.

It is another objective of the present invention to provide a method for cleaving 3D crystals into crystal facets and the re-assembling the same crystal facets by twisted stacking.

SUMMARY OF THE INVENTION

Accordingly, in an aspect of the present invention there is provided a method for synthesizing moiré superlattice from molecular crystals comprising the steps of:

i. finely grounding bulk crystals, and

ii. sonicating the grounded crystals in ultrasonic bath at moderate temperature in presence of a low boiling point solvent system to obtain a dispersion of moiré superlattice of the molecules in the solvent system.

In one aspect of the present invention there is provided a method for synthesizing moiré superlattices of organic crystals comprising the steps of:

i. finely grounding organic crystals, and

ii. sonicating the grounded crystals in ultrasonic bath at 45±2 ºC for 100-120 min. in presence of a methanol-acetone mixture.

In another aspect of the present invention there is provided a method for synthesizing moiré superlattices of metal complex crystals comprising the steps of:

i. finely grounding metal complex crystals, and

ii. sonicating the grounded crystals in ultrasonic bath at 45±2 ºC for 100-120 min. in presence of a solvent system selected from water and water-hexane mixture.

In another aspect of the present invention there is provided a method for synthesizing moiré superlattices of ionic crystals comprising the steps of:

i. finely grounding ionic crystals, and

ii. sonicating the grounded crystals in ultrasonic bath at 45±2 ºC for 100-120 min. in presence of ethanol and ethanol-methanol mixture.

BRIEF DESCRIPTION OF THE DRAWINGS

Figure1. Schematic representation of the invented protocol. First, the crystals were exfoliated through heat-induced sonication to 2-D nanosheets, which re-assembled through twisted stacking to form the moiré superlattices.

Figure 2. (A) Transmission electron microscopy (TEM) image of moiré fringes obtained after twisted stacking of 2D nanosheets of NaCl. (B) Corresponding selected area electron diffraction (SAED) pattern. (C) Crystal structure of NaCl along 111 axis with the lattice planes participating in hexagon formation.

Figure 3. (A) Transmission electron microscopy (TEM) image of moiré fringes obtained after twisted stacking of 2D nanosheets of KCl. (B) Corresponding selected area electron diffraction (SAED) pattern. (C) Crystal structure of KCl along 111 axis with the lattice planes participating in hexagon formation.

Figure 4. (A) Transmission electron microscopy (TEM) image of moiré fringes obtained after twisted stacking of 2D nanosheets of. (B) Corresponding selected area electron diffraction (SAED) pattern. (C) Crystal structure of $NH_4Fe(III)(SO_4)_2.6H_2O$ along 001 axis with the lattice planes participating in hexagon formation.

Figure 5. (A) Transmission electron microscopy (TEM) image of moiré fringes obtained after twisted stacking of 2D nanosheets of $(NH_4)_2Fe(II)(SO_4)_2.6H_2O$. (B) Corresponding selected area electron diffraction (SAED) pattern. (C) Crystal structure of $(NH_4)_2Fe(II)(SO_4)_2.6H_2O$ along 001 axis with the lattice planes participating in hexagon formation.

Figure 6. (A) Transmission electron microscopy (TEM) image of moiré fringes obtained after twisted stacking of 2D nanosheets of $(NH_4)_2Zn(II)(SO_4)_2.6H_2O$. (B) Corresponding selected area electron diffraction (SAED) pattern. (C) Crystal structure of $(NH_4)_2Zn(II)(SO_4)_2.6H_2O$ along 001 axis with the lattice planes participating in hexagon formation.

Figure 7. (A) Transmission electron microscopy (TEM) image of moiré fringes obtained after twisted stacking of 2D nanosheets of $(NH_4)_2Mn(II)(SO_4)_2.6H_2O$. (B) Corresponding selected area

electron diffraction (SAED) pattern. (C) Crystal structure of $(NH_4)_2Mn(II)(SO_4)_2.6H_2O$ along 001 axis with the lattice planes participating in hexagon formation.

Figure 8. (A) Transmission electron microscopy (TEM) image of moiré fringes obtained after twisted stacking of 2D nanosheets of ZQS. $2H_2O$. (B) Corresponding selected area electron diffraction (SAED) pattern. (C) Crystal structure of ZQS. $2H_2O$ along 010 axis with the lattice planes participating in hexagon formation.

Figure 9. (A) Transmission electron microscopy (TEM) image of moiré fringes obtained after twisted stacking of 2D nanosheets of $Fe(acac)_3$. (B) Corresponding selected area electron diffraction (SAED) pattern. (C) Crystal structure of $Fe(acac)_3$ along 001 axis with the lattice planes participating in hexagon formation.

Figure 10. (A) Transmission electron microscopy (TEM) image of moiré fringes obtained after twisted stacking of 2D nanosheets of L-tryptophan. (B) Corresponding selected area electron diffraction (SAED) pattern. (C) Crystal structure of L-tryptophan along 001 axis with the lattice planes participating in hexagon formation.

DETAILED DESCRIPTION OF THE INVENTION

The present invention is directed to provide a generalized procedure for facile, scalable and cost-effective synthesis of molecular two-dimensional (2D) films leading to moiré superlattices from their molecular crystals.

The following description with reference to the accompanying drawings is provided to assist in a comprehensive understanding of various embodiments of the present disclosure as defined by the claims and their equivalents. Even so, the detailed description should not be construed to unduly limit the present invention as modifications and verifications in the embodiments discussed herein may be made by those of skill in the art with the help of the foregoing description and accompanying figures without departing from the spirit or scope of the present inventive discovery.

It is to be understood that the singular forms "a", "an", and "the" include plural referents unless the context clearly dictates otherwise.

The terminology used herein is for the purpose of describing particular various embodiments only and is not intended to be limiting to various embodiments. It will be further understood that the terms "comprises" and/or "comprising" used herein specify the presence of stated features, integers, steps, operations, members, components, and/or groups thereof, but do not preclude the presence or addition of one or more other features, integers, steps, operations, members, components, and/or groups thereof. Also, expressions such as "at least one of," when preceding a list of elements, modify the entire list of elements and do not modify the individual elements of the list. In an embodiment of the present invention there is provided a bulk synthesis of moiré superlattices of molecular crystals.

The synthesis of moiré superlattices of crystals are achieved through a top-down method where the bulk molecular crystals are broken down into 2D films through heat-assisted sonication, which re-assemble through twisted stacking to form the superlattices.

The synthesis of moiré superlattices of crystals comprises steps of:

i. finely grounding bulk crystals, and

ii. sonicating the grounded crystals in ultrasonic bath at moderate temperature in presence of a solvent system to obtain a dispersion of moiré superlattice of the molecules in the solvent system.

A crystal can be of different nature based on its constituent atoms and types of bonds. A crystal is divided on the basis of its nature as organic molecular crystal, metal complexes and ionic crystals.

The present invention provides a common method for synthesis of moiré superlattices of organic crystals, metal complexes crystal and ionic crystals.

The method involves heat assisted sonication induced liquid phase exfoliation which leads to the synthesis of moiré superlattices from their corresponding 3D crystals in large scale. The synthesis of moiré superlattices of molecular crystals is obtained by sonicating the grounded crystals for 100-120 min in ultrasonic bath at 40 kHz frequency and a temperature of 45±2 ºC in presence of appropriate solvent.

The said moiré superlattices are synthesized following a top-down method where the bulk molecular crystals are broken down into 2D films through heat-assisted sonication, which re-assemble through twisted stacking to form the superlattices.

During sonication the crystals were exfoliated in 2D films by solvent molecules which rearrange themselves in more thermodynamically stable twisted moiré superstructures.

Choice of solvent system plays an essential part in the step of sonication in restricting the exfoliated sheets to recrystallize and at the same time it manages the inter-sheet attraction such that a few sheets can recombine to form local stable twisted moiré superlattices.

The appropriate solvent is a low boiling point solvent system. Low boiling point solvent system as used in the synthesis of moiré superlattices is selected from ethanol-methanol mixture, ethanol, water, water-hexane mixture and methanol-acetone mixture.

In an embodiment of the present invention there is provided a method for synthesizing moiré superlattices of organic crystals, which comprises the steps of:

i. finely grounding organic crystals, and

ii. sonicating the grounded crystals in ultrasonic bath at 45±2 ºC for 100-120 min. in presence of a methanol-acetone mixture.

The covalent crystals for which moiré superlatticec can be prepared by the method is L-tryptophan.

The present invention provides a method for synthesizing moiré superlattices of L-tryptophan crystals comprising the steps of:

i. finely grounding L-tryptophan crystals, and

ii. sonicating the grounded crystals in ultrasonic bath at 45±2 ºC for 100 min. in presence of a methanol-acetone mixture having methanol and acetone at a ratio of 5:1.

In an embodiment of the present invention there is provided a method for synthesizing moiré superlattices of metal complex crystals. The method for synthesizing moiré superlattices of metal complex crystals comprises the steps of:

i. finely grounding metal complex crystals, and

ii. sonicating the grounded crystals in ultrasonic bath at 45±2 ºC for 100-120 min. in presence of a solvent system selected from water and water-hexane mixture.

The metal complex crystals for which moiré superlattices can be prepared by the method is selected from diaqua-8-hydroxyquinolinyl-5-sulfonato zinc(II) (ZQS. $2H_2O$), tris(acetylacetonato)iron(III) ($Fe(acac)_3$).

A method is provided for synthesizing moiré superlattices of diaqua-8-hydroxyquinolinyl-5-sulfonato zinc(II) (ZQS. $2H_2O$) crystals comprises the steps of:

i. finely grounding diaqua-8-hydroxyquinolinyl-5-sulfonato zinc(II) (ZQS. $2H_2O$) crystals, and

ii. sonicating the grounded crystals in ultrasonic bath at 45±2 ºC for 100 min. in presence of water.

A method is provided for synthesizing moiré superlattices of tris(acetylacetonato)iron(III) ($Fe(acac)_3$) crystals comprises the steps of:

i. finely grounding tris(acetylacetonato)iron(III) ($Fe(acac)_3$) crystals, and

ii. sonicating the grounded crystals in ultrasonic bath at 45±2 ºC for 100 min. in presence of water-hexane (1/1) bilayer solvent system.

In an embodiment of the present invention there is provided a method for synthesizing moiré superlattices of ionic crystals.

The method for synthesizing moiré superlattices of ionic crystals comprises the steps of:

i. finely grounding ionic crystals, and

ii. sonicating the grounded crystals in ultrasonic bath at 45±2 ºC for 100-120 min. in presence of ethanol and ethanol-methanol mixture.

The ionic crystals for which moiré superlattices can be prepared by the method is selected from NaCl, KCl, ammonium iron (III)-sulphate, hexahydrate ($NH_4Fe(III)(SO_4)_2.6H_2O$), ammonium iron (II)-sulphate, hexahydrate ($(NH_4)_2Fe(II)(SO_4)_2.6H_2O$), ammonium manganese (II)-sulphate, hexahydrate ($(NH_4)_2Mn(II)(SO_4)_2.6H_2O$) and ammonium zinc (II)-sulphate, hexahydrate ($(NH_4)_2Zn(II)(SO_4)_2.6H_2O$).

There is provided a method for synthesizing moiré superlattices of Sodium Chloride (NaCl) crystals comprising the steps of:

i. finely grounding Sodium Chloride (NaCl) crystals, and

ii. sonicating the grounded crystals in ultrasonic bath at 45±2 ºC for 100-120 min. in presence of ethanol-methanol mixture.

There is further provided a method for synthesizing moiré superlattices of Potassium Chloride (KCl) crystals comprising the steps of:

i. finely grounding Potassium Chloride (KCl) crystals, and

ii. sonicating the grounded crystals in ultrasonic bath at 45±2 ºC for 100-120 min. in presence of ethanol-methanol mixture.

In a preferred embodiment the method for synthesizing moiré superlattices of ionic crystals is obtained in a solvent system containing ethanol-methanol mixture at a ratio of 2:1.

There is provide a method for synthesizing moiré superlattices of ammonium iron (III)-sulphate, hexahydrate crystals comprises the steps of:

i. finely grounding ammonium iron (III)-sulphate, hexahydrate crystals, and

ii. sonicating the grounded crystals in ultrasonic bath at 45±2 ºC for 100 min. in presence of ethanol.

Also provided a method for synthesizing moiré superlattices of ammonium iron (II)-sulphate hexahydrate crystals comprises the steps of:

i. finely grounding ammonium iron (II)-sulphate, hexahydrate crystals, and

ii. sonicating the grounded crystals in ultrasonic bath at 45±2 ºC for 100 min. in ethanol.

A method is provided for synthesizing moiré superlattices of ammonium zinc-(II)-sulphate hexahydrate crystals comprises the steps of:

i. finely grounding ammonium zinc-(II)-sulphate hexahydrate crystals, and

ii. sonicating the grounded crystals in ultrasonic bath at 45±2 ºC for 100 min. in ethanol.

Also a method is provided for synthesizing moiré superlattices of ammonium manganese-(II)-sulphate hexahydrate crystals comprises the steps of:

i. finely grounding ammonium manganese-(II)-sulphate hexahydrate crystals, and

ii. sonicating the grounded crystals in ultrasonic bath at 45±2 ºC for 100 min. in ethanol.

The methods are highly effective, versatile, efficient, scalable and inexpensive for making moiré 2D superlattices with intriguing properties.

ADVANTAGE OF THE INVENTION

The present invention provides a general one step protocol for the synthesis of 2D moiré superlattices from the macroscopic crystals via the formation of 2D films. This method is general, highly effective, versatile, efficient, scalable and inexpensive for making moiré 2D superlattices with intriguing properties. Such approach can be applicable to vast range of crystals in synthesizing moiré superlattices form versatile precursors.

Further embodiments of the present invention have been disclosed in Examples. The following examples serve to illustrate certain embodiments and aspects of the present disclosure and are not to be considered as limiting the scope thereof.

Example 1: PREPARATION OF MOIRÉ SUPERSTRUCTURE FROM NaCl CRYSTALS

NaCl crystals were finely ground using mortar and pestle and 40 mg of the finely ground crystals were taken in a vial with 20 mL (2:1) ethanol/methanol solvent mixture. Then it was exfoliated via sonication in 40 kHz frequency at 45±2 ºC for 120 min. Then the as-obtained dispersion was allowed to settle down for 2 min and from the upper layer 100 µL solution was taken and diluted 5 times and was drop-cast in a TEM grid.

Transmission emission microscope (TEM) images of the dispersion after exfoliation showed that a large number of twisted multi-layered 2D nanosheets formed with moiré periodicity (Figure. 2A). NaCl crystallises into cubic lattice with space group Fm-3m having cell parameter a= 5.6 Å. Figure 2A depicts the TEM image of the moiré superlattices created by the twisted stacking of single crystalline hexagonal NaCl nanosheets at specific angles. The selected area electron diffraction (SAED) pattern in Figure 2B also shows a ring-like pattern with a six-fold symmetric set of defined bright diffraction spots, which could be attributed to twisted stackings of several single-crystalline nanosheets, as if many layers of hexagons were placed while rotating at various angles. By careful observation of SAED diffraction spot in Figure 2B it is revealed that moiré patterns are created by superimposing sixteen hexagonal sheets rotated at certain angles having a

cell parameter of 2.1 ± 0.1 Å. The shortest angle between two neighbouring hexagons is 0.9º. The angles between two hexagons forming patterns range from 0.9-9º, with lower angles resulting in higher order moiré periodicity. The complicated diffraction spot of a multi-layer rotating hexagonal sheet with a lattice constant of 2.1 Å was used to determine probable moiré periodicities for all noted twist angles employing the usual rotational moiré superlattice theoretic equation 1.

$$D = a/(2\mathrm{Sin}(\theta/2)) \quad (1)$$

where a = basal lattice constant (the lattice constant for the hexagonal array of 2D NaCl sheet, i.e., 2.1 Å), D = period of moiré lattice, and θ = twisted angle. Interestingly, the experimentally observed moiré periods, of values 4.6 nm, 5.14 nm, 6.43 nm, 7.25 nm and 12.65 nm in Figure. 2A, matched with some of the values calculated for twist angle (measured from Figure. 1B) superpositions of hexagonal lattices using eqn (1). The observed moiré lattice spacing in TEM and SAED analysis and inter-sheet twisted angle are listed in Table 1.

Table 1. Twist angles measured from the SAED image in the Figure 2B and the calculated values of the corresponding moiré periods and measured moiré period form real space image of NaCl moiré superlattice.

	Twist angle in SAED (θ)(degree)	Moiré period from SAED (D) (nm)	Moiré period from Real space image (nm)
1	0.96	12.53	12.65
2	1.6	7.52	7.25
3	1.85	6.50	6.43
4	2.2	5.46	5.14
5	2.46	4.8	4.6
6	3.6	3.34	3.5
7	4.6	2.61	-
8	7.9	1.52	1.4
9	9.2	1.30	1.24

Sonication and heat induced exfoliation cleaved the NaCl crystals along 111 axis i.e., crystals were cut by a plane perpendicular to 111 axis into 2D sheets, as there is a general tendency of 2D-sheets to arrange in a more stable hexagonal lattice. Set of six (2-20) planes were involved in the formation of hexagonal sheet depicted in Figure 2C supported by the SAED analysis of the obtained moiré superlattice (Figure 2B). Set of six (2 -2 0) planes having a distance of 1.9 Å forms

hexagonal lattice of individual sheet which ultimately were twisted to generate moiré periodicity, supported by the first layer of moiré diffraction spot with a distance of 2.1 Å in SAED analysis.

Example 2: Preparation of Moiré Superstructure from KCl Crystals

KCl crystals were finely ground in a mortar pestle and 40 mg of finely ground crystals were taken in a vial with 20 mL (2:1) ethanol/methanol solvent mixture. Then it was exfoliated via sonication in 40 kHz frequency at 45±2 °C for 120 min. Then the as obtained dispersion was allowed to settle down for 2 min and from the upper layer 100 µL solution was taken and diluted 5 times and drop cast in a TEM grid. Transmission emission microscope (TEM) images of the dispersion after exfoliation showed that a large number of twisted multi-layered 2D sheets formed with moiré periodicity (Figure 3A). KCl crystallises into cubic lattice with space group Fm-3m having cell parameter a= 6.3 Å. Figure 3A depicts moiré superlattices created by the twisted stacking of single crystalline hexagonal KCl nanosheets at specific angles. The selected area electron diffraction (SAED) pattern in Figure 3B also showed a ring-like pattern with a six-fold symmetric set of defined bright diffraction spots, which could be attributed to twisted stackings of numerous single-crystalline nanosheets, as if many layers of hexagons were placed while rotating at various angles. By careful observation of SAED diffraction spot in Figure 3B revealed that moiré patterns are created by superimposing nineteen hexagonal sheets rotated at certain angles having a cell parameter of 2.1 ± 0.1 Å. The shortest angle between two neighbouring hexagons is 0.85º. The angles between two hexagons forming patterns range from 0.85-8º, with lower angles resulting in higher order moiré periodicity. The complicated diffraction spot of a multi-layer rotating hexagonal sheet with a lattice constant of 2.1 Å was used to determine probable moiré periodicities for all noted twist angles employing the usual rotational moiré theory equation 1. Interestingly, the experimentally observed moiré periods, of values 4.14 nm, 5.70 nm, 9.25 nm, 9.76 nm, 10.48 nm, 12.44 nm and 13.08 nm in Figure 3A, matched with some of the values calculated for twist angle (measured from Figure 3B) superpositions of hexagonal lattices using eqn (1). The observed moiré lattice spacing in TEM and SAED analysis and inter-sheet twisted angle was listed in Table 2.

Table 2. Twist angles measured from the SAED image in the Figure 3B and the calculated values of the corresponding moiré periods and measured moiré period form real space image of KCl moiré superlattice.

	Twist angle in SAED (θ) (degree)	Moiré period from SAED (D) (nm)	Moiré period from Real space image (nm)
1	0.85	14.15	-
2	0.9	13.3	13.08
3	0.98	12.27	12.44
4	1.14	10.55	10.48
5	1.3	9.04	9.25
6	1.41	8.5	8.8
7	1.93	6.2	6
8	2.93	4.1	4.1
9	2.45	4.9	5.04
10	4.3	2.8	2.5
11	5.7	2.1	2.39
12	8	1.5	1.8

Sonication and heat induced exfoliation cleaved the KCl crystals along 111 axis i.e., crystals were cut by a plane perpendicular to 111 axis into 2d sheets, as there is a general tendency of 2D-sheets to arrange in a more stable hexagonal lattice. Set of six (2-20) planes were involved in the formation of hexagonal sheet depicted in Figure 3C supported by the SAED analysis of the obtained moiré superlattice (Figure 3B). Set of six (2 -2 0) planes having a distance of 2.21 Å forms hexagonal lattice of individual sheet which ultimately twisted to generate moiré periodicity, supported by the first layer of moiré diffraction spot with a distance of 2.1 Å in SAED analysis.

Example 3: Preparation of Moiré Superstructure from $NH_4Fe(III)(SO_4)_2.6H_2O$ Crystals

$NH_4Fe(III)(SO_4)_2.6H_2O$ crystals were finely ground in a mortar pestle and 30 mg of finely ground crystals were taken in a vial with 20 mL ethanol solvent. Then it was exfoliated via sonication in 40 kHz frequency at 45±2 °C for 100 min. Then the as-obtained dispersion was allowed to settle down for 2 min and from the upper layer 100 uL solution was taken and diluted 5 times and drop cast in a TEM grid.

Transmission emission microscope (TEM) images of the dispersion after exfoliation showed that a large number of twisted multi-layered 2D sheets formed with moiré periodicity (Figure 4A). $NH_4Fe(III)(SO_4)_2.6H_2O$ crystallises into trigonal lattice with space group R-3 having cell

parameter a= 4.82 Å, c=24.4 Å, α=β=90°, γ= 120°. Figure 3A depicts moiré superlattices created by the twisted stacking of single crystalline hexagonal $NH_4Fe(III)(SO_4)_2.6H_2O$ nanosheets at specific angles. The selected area electron diffraction (SAED) pattern in Figure 4B also showed a ring-like pattern with a six-fold symmetric set of defined bright diffraction spots, which could be attributed to twisted stackings of numerous single-crystalline nanosheets, as if many layers of hexagons were placed while rotating at various angles. By careful observation of SAED diffraction spot in Figure 4B revealed that moiré patterns are created by superimposing eighteen hexagonal sheets rotated at certain angles having a cell parameter of 2.1 ± 0.1 Å. The shortest angle between two neighbouring hexagons is 0.57º. The angles between two hexagons forming patterns range from 0.57-8.67º, with lower angles resulting in higher order moiré periodicity. The complicated diffraction spot of a multi-layer rotating hexagonal sheet with a lattice constant of 2.1 Å was used to determine probable moiré periodicities for all noted twist angles employing the usual rotational moiré theory equation 1. Interestingly, the experimentally observed moiré periods, of values 20.8 nm, 15.1 nm, 13.8 nm, 13 nm, 8.39 nm, 4.61 nm and 3.77 nm in Figure 4A, matched with some of the values calculated for twist angle (measured from Figure 4B) superpositions of hexagonal lattices using eqn (1). The observed moiré lattice spacing in TEM and SAED analysis and inter-sheet twisted angle was listed in Table 3.

Table 3. Twist angles measured from the SAED image in the Figure 4B and the calculated values of the corresponding moiré periods and measured moiré period form real space image of $NH_4Fe(III)(SO4)_2.6H_2O$ moiré superlattice.

	Twist angle in SAED (θ)(degree)	Moiré period from SAED (D) (nm)	Moiré period from Real space image (nm)
1	0.57	21.1	20.8
2	0.77	15.62	15.1
3	0.87	13.83	13.8
4	0.95	12.66	13
5	1.43	8.41	8.39
6	2.63	4.57	4.61
7	3.23	3.72	3.77
8	4.52	2.66	2.9
9	5.81	2.07	2.09
10	8.67	1.38	1.26

Sonication and heat induced exfoliation cleaved the $NH_4Fe(III)(SO_4)_2.6H_2O$ crystals along 001 axis i.e. crystals were cut by a plane perpendicular to 001 axis into 2d sheets, as there is a general tendency of 2D-sheets to arrange in a more stable hexagonal lattice and interaction is also minimal along this axis. Set of two (110) and set of four (2-10) planes were involved in the formation of hexagonal sheet depicted in Figure 4C supported by the SAED analysis of the obtained moiré superlattice (Figure 4B). Set of two (110) and set of four (2-10) planes having a distance of 2.41 Å forms hexagonal lattice of individual sheet which ultimately twisted to generate moiré periodicity, supported by the first layer of moiré diffraction spot with a distance of 2.1 Å in SAED analysis.

Example 4: Preparation of Moiré Superstructure from $(NH_4)_2Fe(II)(SO4)_2.6H_2O$ Crystals

$(NH_4)_2Fe(II)(SO_4)_2.6H_2O$ crystals were finely ground in a mortar pestle and 30 mg of finely ground crystals were taken in a vial with 20 mL ethanol solvent. Then it was exfoliated via sonication in 40 kHz frequency at 45±2 °C for 100 min. Then the as obtained dispersion was allowed to settle down for 2 min and from the upper layer 100 µL solution was taken and diluted 5 times and drop cast in a TEM grid.

Transmission emission microscope (TEM) images of the dispersion after exfoliation showed that a large number of twisted multi-layered 2D sheets formed with moiré periodicity (Figure 5A). $NH_4Fe(II)(SO4)_2.6H_2O$ crystallises into monoclinic lattice with space group P21/c having cell parameter a= 9.32 Å, b= 12.65 Å, c=6.24 Å, $\alpha= \gamma=90°$, $\beta = 106.8°$. Figure 5A depicts moiré superlattices created by the twisted stacking of single crystalline hexagonal $(NH_4)_2Fe(II)(SO_4)_2.6H_2O$ nanosheets at specific angles. The selected area electron diffraction (SAED) pattern in Figure 5B also showed a ring-like pattern with a six-fold symmetric set of defined bright diffraction spots, which could be attributed to twisted stackings of numerous single-crystalline nanosheets, as if many layers of hexagons were placed while rotating at various angles. By careful observation of SAED diffraction spot in Figure 5B revealed that moiré patterns are created by superimposing twenty hexagonal sheets rotated at certain angles having a cell parameter of 2.1 ± 0.1 Å. The shortest angle between two neighbouring hexagons is 0.82º. The angles between two hexagons forming patterns range from 0.82-9.3º, with lower angles resulting in higher order moiré periodicity. The complicated diffraction spot of a multi-layer rotating hexagonal sheet

with a lattice constant of 2.1 Å was used to determine probable moiré periodicities for all noted twist angles employing the usual rotational moiré theory equation 1. Interestingly, the experimentally observed moiré periods, of values 14.88 nm, 13.58 nm, 11.57 nm, 8.48 nm, 7.58 nm, 5.6 nm and 4.8 nm in Figure 5A, matched with some of the values calculated for twist angle (measured from Figure 5B) superpositions of hexagonal lattices using eqn (1). The observed moiré lattice spacing in TEM and SAED analysis and inter-sheet twisted angle was listed in Table 4.

Sonication and heat induced exfoliation cleaved the $(NH_4)_2Fe(II)(SO_4)_2.6H_2O$ crystals along 001 axis i.e. crystals were cut by a plane perpendicular to 001 axis into 2d sheets, as there is a general tendency of 2D-sheets to arrange in a more stable hexagonal lattice and interaction is also minimal along this axis. Set of two (060) and set of four (420) planes were involved in the formation of hexagonal sheet depicted in Figure 5C supported by the SAED analysis of the obtained moiré superlattice (Figure 5B). . Set of two (060) and set of four (420) planes having a distance of 2.1 Å forms hexagonal lattice of individual sheet which ultimately twisted to generate moiré periodicity, supported by the first layer of moiré diffraction spot with a distance of 2.1 Å in SAED analysis.

Table 4. Twist angles measured from the SAED image in the Figure 5B and the calculated values of the corresponding moiré periods and measured moiré period form real space image of $(NH_4)_2Fe(II)(SO_4)_2.6H_2O$ moiré superlattice.

	Twist angle in SAED (θ)(degree)	Moiré period from SAED (D) (nm)	Moiré period from Real space image (nm)
1	0.82	14.67	14.88
2	0.91	13.22	13.58
3	1.03	11.68	11.57
4	1.43	8.41	8.48
5	1.6	7.52	7.58
6	2.23	5.4	5.6
7	2.6	4.62	4.8
8	4.4	2.73	2.9
9	5.64	2.13	2.12
10	9.3	1.3	1.6

Example 5: Preparation of Moiré Superstructure from $(NH_4)_2Zn(II)(SO_4)_2.6H_2O$ Crystals

$(NH_4)_2Zn(II)(SO_4)_2.6H_2O$ crystals were finely ground in a mortar pestle and 30 mg of finely ground crystals were taken in a vial with 20 mL ethanol solvent. Then it was exfoliated via sonication in 40 kHz frequency at 45±2 °C for 100 min. Then the as obtained dispersion was allowed to settle down for 2 min and from the upper layer 100 µL solution was taken and diluted 5 times and drop cast in a TEM grid.

Transmission emission microscope (TEM) images of the dispersion after exfoliation showed that a large number of twisted multi-layered 2D sheets formed with moiré periodicity (Figure 6A). $NH_4Zn(II)(SO_4)_2.6H_2O$ crystallises into monoclinic lattice with space group P21/c having cell parameter a= 9.27 Å, b= 12.56 Å, c=6.25 Å, $\alpha = \gamma = 90°$, $\beta = 106.82°$. Figure 6A depicts moiré superlattices created by the twisted stacking of single crystalline hexagonal $(NH_4)_2Zn(II)(SO_4)_2.6H_2O$ nanosheets at specific angles. The selected area electron diffraction (SAED) pattern in Figure 6B also showed a ring-like pattern with a six-fold symmetric set of defined bright diffraction spots, which could be attributed to twisted stackings of numerous single-crystalline nanosheets, as if many layers of hexagons were placed while rotating at various angles. By careful observation of SAED diffraction spot in Figure 6B revealed that moiré patterns are created by superimposing fifteen hexagonal sheets rotated at certain angles having a cell parameter of 2.1 ± 0.1 Å. The shortest angle between two neighbouring hexagons is 0.64º. The angles between two hexagons forming patterns range from 0.64-10.23º, with lower angles resulting in higher order moiré periodicity. The complicated diffraction spot of a multi-layer rotating hexagonal sheet with a lattice constant of 2.1 Å was used to determine probable moiré periodicities for all noted twist angles employing the usual rotational moiré theory equation 1. Interestingly, the experimentally observed moiré periods, of values 18.88 nm, 9.78 nm, 5.9 nm, 5.27 nm, 4.88 nm, 4.16 nm and 3.12 nm in Figure 6A, matched with some of the values calculated for twist angle (measured from Figure 6B) superpositions of hexagonal lattices using eqn (1). The observed moiré lattice spacing in TEM and SAED analysis and inter-sheet twisted angle was listed in Table 5.

Table 5. Twist angles measured from the SAED image in the Figure 6B and the calculated values of the corresponding moiré periods and measured moiré period form real space image of $(NH_4)_2Zn(II)(SO_4)_2.6H_2O$ moiré superlattice.

	Twist angle in SAED (θ)(degree)	Moiré period from SAED (D) (nm)	Moiré period from Real space image (nm)
1	0.64	18.8	18.8
2	1.21	9.9	9.78
3	2.05	5.86	5.9
4	2.24	5.37	5.27
5	2.6	4.6	4.88
6	2.9	4.14	4.16
7	3.85	3.12	3.12
8	5.64	2.13	2.08
9	8.49	1.42	-
10	10.23	1.17	-

Sonication and heat induced exfoliation cleaved the $(NH_4)_2Zn(II)(SO_4)_2.6H_2O$ crystals along 001 axis i.e. crystals were cut by a plane perpendicular to 001 axis into 2d sheets, as there is a general tendency of 2D-sheets to arrange in a more stable hexagonal lattice and interaction is also minimal along this axis. Set of two (060) and Set of four (420) planes were involved in the formation of hexagonal sheet depicted in Figure 6C supported by the SAED analysis of the obtained moiré superlattice (Figure 6B). Set of two (060) and set of four (420) planes having a distance of 2.09 Å forms hexagonal lattice of individual sheet which ultimately twisted to generate moiré periodicity, supported by the first layer of moiré diffraction spot with a distance of 2.1 Å in SAED analysis.

Example 6: Preparation of Moiré Superstructure from $(NH4)_2Mn(II)(SO_4)_2.6H_2O$ Crystals

$(NH_4)_2Mn(II)(SO_4)_2.6H_2O$ crystals were finely ground in a mortar pestle and 30 mg of finely ground crystals were taken in a vial with 20 mL ethanol solvent. Then it was exfoliated via sonication in 40 kHz frequency at 45±2 ºC for 100 min. Then the as obtained dispersion was allowed to settle down for 2 min and from the upper layer 100 µL solution was taken and diluted 5 times and drop cast in a TEM grid.

Transmission emission microscope (TEM) images of the dispersion after exfoliation showed that a large number of twisted multi-layered 2D sheets formed with moiré periodicity (Figure 7A). $NH_4Mn(II)(SO_4)_2.6H_2O$ crystallises into monoclinic lattice with space group P21/c having cell parameter a= 9.39 Å, b= 12.74 Å, c=6.25 Å, α= γ=90°, β = 106.98°. Figure 7A depicts moiré superlattices created by the twisted stacking of single crystalline hexagonal $(NH_4)_2Mn(II)(SO_4)_2.6H_2O$ nanosheets at specific angles. The selected area electron diffraction (SAED) pattern in Figure 7B also showed a ring-like pattern with a six-fold symmetric set of defined bright diffraction spots, which could be attributed to twisted stackings of numerous single-crystalline nanosheets, as if many layers of hexagons were placed while rotating at various angles. By careful observation of SAED diffraction spot in Figure 7B revealed that moiré patterns are created by superimposing thirteen hexagonal sheets rotated at certain angles having a cell parameter of 2.1 ± 0.1 Å. The shortest angle between two neighbouring hexagons is 0.49º. The angles between two hexagons forming patterns range from 0.49-13.4º, with lower angles resulting in higher order moiré periodicity. The complicated diffraction spot of a multi-layer rotating hexagonal sheet with a lattice constant of 2.1 Å was used to determine probable moiré periodicities for all noted twist angles employing the usual rotational moiré theory equation 1. Interestingly, the experimentally observed moiré periods, of values 24.6 nm, 7.28 nm, 5.38 nm, 4.52 nm, 3.13 nm, 2.43 nm and 1.74 nm in Figure 7A, matched with some of the values calculated for twist angle (measured from Figure 7B) superpositions of hexagonal lattices using eqn (1). The observed moiré lattice spacing in TEM and SAED analysis and inter-sheet twisted angle was listed in Table 6.

Table 6. Twist angles measured from the SAED image in the Figure 7B and the calculated values of the corresponding moiré periods and measured moiré period form real space image of $(NH_4)_2Mn(II)(SO_4)_2.6H_2O$ moiré superlattice.

	Twist angle in SAED (θ)(degree)	Moiré period from SAED (D) (nm)	Moiré period from Real space image (nm)
1	0.49	24.55	24.6
2	1.66	7.24	7.28
3	2.25	5.34	5.38
4	2.64	4.55	4.52
5	4	3	3.13
6	5.46	2.2	2.43
7	6.18	1.94	1.74

8	8.18	1.47	-
9	13.4	0.89	-

Sonication and heat induced exfoliation cleaved the $(NH_4)_2Mn(II)(SO_4)_2.6H_2O$ crystals along 001 axis i.e. crystals were cut by a plane perpendicular to 001 axis into 2d sheets, as there is a general tendency of 2D-sheets to arrange in a more stable hexagonal lattice and interaction is also minimal along this axis. Set of two (060) and Set of four (420) planes were involved in the formation of hexagonal sheet depicted in Figure 7C supported by the SAED analysis of the obtained moiré superlattice (Figure 7B). Set of two (060) and set of four (420) planes having a distance of 2.11 Å forms hexagonal lattice of individual sheet which ultimately twisted to generate moiré periodicity, supported by the first layer of moiré diffraction spot with a distance of 2.1 Å in SAED analysis.

Example 7: Preparation of Moiré Superstructure from ZQS. $2H_2O$ Crystals

ZQS. $2H_2O$ crystals were finely ground in a mortar pestle and 30 mg of finely ground crystals were taken in a vial with 20 mL water solvent. Then it was exfoliated via sonication in 40 kHz frequency at 45±2 ºC for 100 min. Then the as obtained dispersion was allowed to settle down for 2 min and from the upper layer 100 µL solution was taken and diluted 5 times and drop cast in a TEM grid.

Transmission emission microscope (TEM) images of the dispersion after exfoliation showed that a large number of twisted multi-layered 2D sheets formed with moiré periodicity (Figure 8A). ZQS. $2H_2O$ crystallises into orthorhombic lattice with space group Pbca having cell parameter a= 9.29 Å, b= 15.21 Å, c=16.10 Å, $\alpha=\beta=\gamma=90°$. Figure 8A depicts moiré superlattices created by the twisted stacking of single crystalline hexagonal ZQS. $2H_2O$ nanosheets at specific angles. The selected area electron diffraction (SAED) pattern in Figure 8B also showed a ring-like pattern with a six-fold symmetric set of defined bright diffraction spots, which could be attributed to twisted stackings of numerous single-crystalline nanosheets, as if many layers of hexagons were placed while rotating at various angles. By careful observation of SAED diffraction spot in Figure 8B revealed that moiré patterns are created by superimposing sixteen hexagonal sheets rotated at certain angles having a cell parameter of 2.1 ± 0.1 Å. The shortest angle between two neighbouring hexagons is 0.52º. The angles between two hexagons forming patterns range from 0.49-7.15º, with lower angles resulting in higher order moiré periodicity. The complicated diffraction spot of a

multi-layer rotating hexagonal sheet with a lattice constant of 2.1 Å was used to determine probable moiré periodicities for all noted twist angles employing the usual rotational moiré theory equation 1. Interestingly, the experimentally observed moiré periods, of values 23.31 nm, 10.27 nm, 8.1 nm, 5.82 nm, 2.65 nm, 2.59 nm and 1.75 nm in Figure 8A, matched with some of the values calculated for twist angle (measured from Figure 8B) superpositions of hexagonal lattices using eqn (1). The observed moiré lattice spacing in TEM and SAED analysis and inter-sheet twisted angle was listed in Table 7.

Table 7. Twist angles measured from the SAED image in the Figure 8B and the calculated values of the corresponding moiré periods and measured moiré period form real space image of ZQS. $2H_2O$ moiré superlattice.

	Twist angle in SAED (θ)(degree)	Moiré period from SAED (D) (nm)	Moiré period from Real space image (nm)
1	0.52	23.13	23.31
2	1.19	10.11	10.27
3	1.5	8	8.1
4	2.02	5.95	5.82
5	4.35	2.76	2.65
6	4.8	2.50	2.59
7	6.17	1.95	1.75
8	7.15	1.68	1.59

Sonication and heat induced exfoliation cleaved the ZQS. $2H_2O$ crystals along 010 axis i.e. crystals were cut by a plane perpendicular to 010 axis into 2d sheets, as there is a general tendency of 2D-sheets to arrange in a more stable hexagonal lattice and interaction is also minimal along this axis. Set of two (400) and set of four (206) planes were involved in the formation of hexagonal sheet depicted in Figure 8C supported by the SAED analysis of the obtained moiré superlattice (Figure 8B). Set of two (400) and Set of four (206) planes having a distance of 2.3 Å forms hexagonal lattice of individual sheet which ultimately twisted to generate moiré periodicity, supported by the first layer of moiré diffraction spot with a distance of 2.1 Å in SAED analysis.

Example 8: Preparation of Moiré Superstructure from $Fe(acac)_3$ Crystals

$Fe(acac)_3$ crystals were finely ground in a mortar pestle and 40 mg of finely ground crystals were taken in a vial with 20 mL water/hexane (1:1) bilayer solvent system. Then it was exfoliated via sonication in 40 kHz frequency at 45±2 ºC for 100 min. Then the as obtained dispersion was allowed to settle down for 2 min and from the water part 100 µL solution was taken and diluted 5 times with water and drop cast in a TEM grid.

Transmission emission microscope (TEM) images of the dispersion after exfoliation showed that a large number of twisted multi-layered 2D sheets formed with moiré periodicity (Figure 9A). $Fe(acac)_3$ crystallises into orthorhombic lattice with space group Pbca having cell parameter a= 16.56 Å, b= 15.43 Å, c=13.57 Å, α=β=γ=90°. Figure 9A depicts moiré superlattices created by the twisted stacking of single crystalline hexagonal $Fe(acac)_3$ nanosheets at specific angles. The selected area electron diffraction (SAED) pattern in Figure 9B also showed a ring-like pattern with a six-fold symmetric set of defined bright diffraction spots, which could be attributed to twisted stackings of numerous single-crystalline nanosheets, as if many layers of hexagons were placed while rotating at various angles. By careful observation of SAED diffraction spot in Figure 9B revealed that moiré patterns are created by superimposing five hexagonal sheets rotated at certain angles having a cell parameter of 4.4 ± 0.1 Å. The shortest angle between two neighbouring hexagons is 0.73º. The angles between two hexagons forming patterns range from 0.73-12.41º, with lower angles resulting in higher order moiré periodicity. The complicated diffraction spot of a multi-layer rotating hexagonal sheet with a lattice constant of 0.44 Å was used to determine probable moiré periodicities for all noted twist angles employing the usual rotational moiré theory equation 1. Interestingly, the experimentally observed moiré periods, of values 11.8 nm, 4.51 nm, 2.79 nm, 2.68 nm and 2.12 nm in Figure 9A, matched with some of the values calculated for twist angle (measured from Figure 9B) superpositions of hexagonal lattices using eqn (1). The observed moiré lattice spacing in TEM and SAED analysis and inter-sheet twisted angle was listed in Table 8.

Table 8. Twist angles measured from the SAED image in the Figure 9B and the calculated values of the corresponding moiré periods and measured moiré period form real space image of $Fe(acac)_3$ moiré superlattice.

	Twist angle in SAED (θ)(degree)	Moiré period from SAED (D) (nm)	Moiré period from Real space image (nm)
1	0.73	34.53	-
2	2.2	11.45	11.8
3	5.31	4.74	4.51
4	8.88	2.84	2.79
5	9.33	2.70	2.68
6	12.41	2.03	2.12

Sonication and heat induced exfoliation cleaved the $Fe(acac)_3$ crystals along 001 axis i.e. crystals were cut by a plane perpendicular to 001 axis into 2d sheets, as there is a general tendency of 2D-sheets to arrange in a more stable hexagonal lattice and interaction is also minimal along this axis. Set of two (400) and Set of four (230) planes were involved in the formation of hexagonal sheet depicted in Figure 9C supported by the SAED analysis of the obtained moiré superlattice (Figure 9B). Set of two (400) and set of four (230) planes having a distance of 4.3 Å and 4.1 Å respectively forms hexagonal lattice of individual sheet which ultimately twisted to generate moiré periodicity, supported by the first layer of moiré diffraction spot with a distance of 4.4 Å in SAED analysis.

Example 9: Preparation of Moiré Superstructure from L-tryptophan Crystals

L-tryptophan crystals were finely ground in a mortar pestle and 30 mg of finely ground crystals were taken in a vial with 20 mL (5:1) methanol/acetone solvent mixture. Then it was exfoliated via sonication in 40 kHz frequency at 45±2 ºC for 100 min. Then the as obtained dispersion was allowed to settle down for 2 min and from the upper layer 100 µL solution was taken and diluted 5 times and drop cast in a TEM grid.

Transmission emission microscope (TEM) images of the dispersion after exfoliation showed that a large number of twisted multi-layered 2D sheets formed with moiré periodicity (Figure 10A). L-tryptophan crystallises into triclinic lattice with space group P1 having cell parameter a= 11.43 Å, b= 11.46 Å, c=35.60 Å, α=84.42°, β=87.69°, γ=60.10°. Figure 10A depicts moiré superlattices created by the twisted stacking of single crystalline hexagonal L-tryptophan nanosheets at specific

angles. The selected area electron diffraction (SAED) pattern in Figure 10B also showed a ring-like pattern with a six-fold symmetric set of defined bright diffraction spots, which could be attributed to twisted stackings of numerous single-crystalline nanosheets, as if many layers of hexagons were placed while rotating at various angles. By careful observation of SAED diffraction spot in Figure 10B revealed that moiré patterns are created by superimposing twenty-four hexagonal sheets rotated at certain angles having a cell parameter of 2.1 ± 0.1 Å. The shortest angle between two neighbouring hexagons is 0.6º. The angles between two hexagons forming patterns range from 0.6-4.32º, with lower angles resulting in higher order moiré periodicity. The complicated diffraction spot of a multi-layer rotating hexagonal sheet with a lattice constant of 2.1 Å was used to determine probable moiré periodicities for all noted twist angles employing the usual rotational moiré theory equation 1. Interestingly, the experimentally observed moiré periods, of values 20.8 nm, 10.4 nm, 6.28 nm, 4.6 nm, 3.52 nm and 2.82 nm in Figure 10A, matched with some of the values calculated for twist angle (measured from Figure 10B) superpositions of hexagonal lattices using eqn (1). The observed moiré lattice spacing in TEM and SAED analysis and inter-sheet twisted angle was listed in Table 9.

Table 9. Twist angles measured from the SAED image in the Figure 10B and the calculated values of the corresponding moiré periods and measured moiré period form real space image of L-tryptophan moiré superlattice.

	Twist angle in SAED (θ)(degree)	Moiré period from SAED (D) (nm)	Moiré period from Real space image (nm)
1	0.6	20.05	20.8
2	1.19	10.11	10.4
3	1.93	6.23	6.28
4	2.8	4.29	4.6
5	3.41	3.53	3.52
6	4.32	2.78	2.82

Sonication and heat induced exfoliation cleaved the L-tryptophan crystals along 001 axis i.e. crystals were cut by a plane perpendicular to 001 axis into 2d sheets, as there is a general tendency of 2D-sheets to arrange in a more stable hexagonal lattice. Set of two (400), Set of two (040) and Set of two (440) planes were involved in the formation of hexagonal sheet depicted in Figure 10C supported by the SAED analysis of the obtained moiré superlattice (Figure 10B). Set of two (400),

set of two (040) and set of two (440) planes having a distance of 2.4 Å forms hexagonal lattice of individual sheet which ultimately twisted to generate moiré periodicity, supported by the first layer of moiré diffraction spot with a distance of 2.1 Å in SAED analysis.

We claim:

1. A method for synthesizing moiré superlattices from molecular crystals comprising the steps of:

i. finely grounding bulk crystals, and

ii. sonicating the grounded crystals in ultrasonic bath at moderate temperature in presence of a solvent system to obtain a dispersion of moiré superlattices of the molecules in the solvent system.

2. The method as claimed in claim 1, wherein the solvent system is a low boiling point solvent system.

3. The method as claimed in claim 1, wherein the molecular crystals are selected from organic crystals, metal complexes and ionic crystals.

4 The method as claimed in claim 1, wherein the moderate temperature at which sonication is performed is 45±2 ºC.

5. The method as claimed in claim 1, wherein the sonication is performed for 100-120 minutes.

6. The method as claimed in claim 1, wherein the sonication is performed at 40 kHz frequency.

7. The method as claimed in claim 2, wherein the low boiling point solvent system is selected from ethanol-methanol mixture, ethanol, water, water-hexane mixture and methanol-acetone mixture.

8. A method for synthesizing moiré superlattices of organic crystals comprising the steps of:

i. finely grounding organic crystals, and

ii. sonicating the grounded crystals in ultrasonic bath at 45±2 ºC for 100-120 min. in presence of a methanol-acetone mixture.

9. The method as claimed in claim 8, wherein the methanol-acetone mixture contains methanol and acetone at a ratio of 5:1.

10. The method as claimed in claim 8, wherein the organic crystal is L-tryptophan.

11. A method for synthesizing moiré superlattices of metal complex crystals comprising the steps of:

i. finely grounding metal complex crystals, and

ii. sonicating the grounded crystals in ultrasonic bath at 45±2 ºC for 100-120 min. in presence of a solvent system selected from water and water-hexane mixture.

12. The method as claimed in claim 11, wherein the water hexane mixture contains water and hexane at a ratio of 1:1.

13. The method as claimed in claim 10, wherein the metal complex crystals are diaqua-8-hydroxyquinolinyl-5-sulfonato zinc(II) (ZQS. $2H_2O$) and $Fe(acac)_3$

14. A method for synthesizing moiré superlattices of ionic crystals comprising the steps of:

i. finely grounding ionic crystals, and

ii. sonicating the grounded crystals in ultrasonic bath at 45±2 ºC for 100-120 min. in presence of ethanol and ethanol-methanol mixture.

15. The method as claimed in claim 14, wherein the ethanol-methanol mixture contains ethanol and methanol at a ratio of 2:1.

16. The method as claimed in claim 13, wherein the ionic crystals are NaCl, KCl, $NH_4Fe(III)(SO_4)_2.6H_2O$, $(NH4)_2Fe(II)(SO_4)_2.6H_2O$, $(NH4)_2Mn(II)(SO_4)_2.6H_2O$ and $(NH4)_2Zn(II)(SO_4)_2.6H_2O$.

DRAWINGS

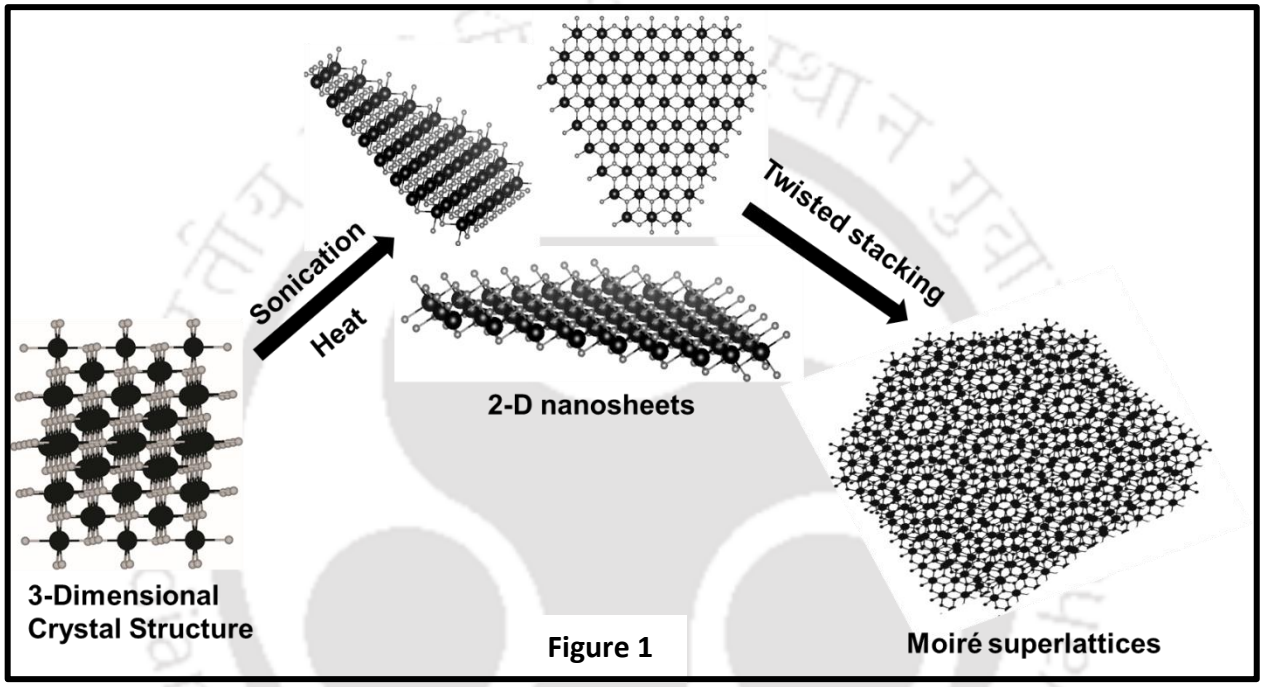

Figure 1

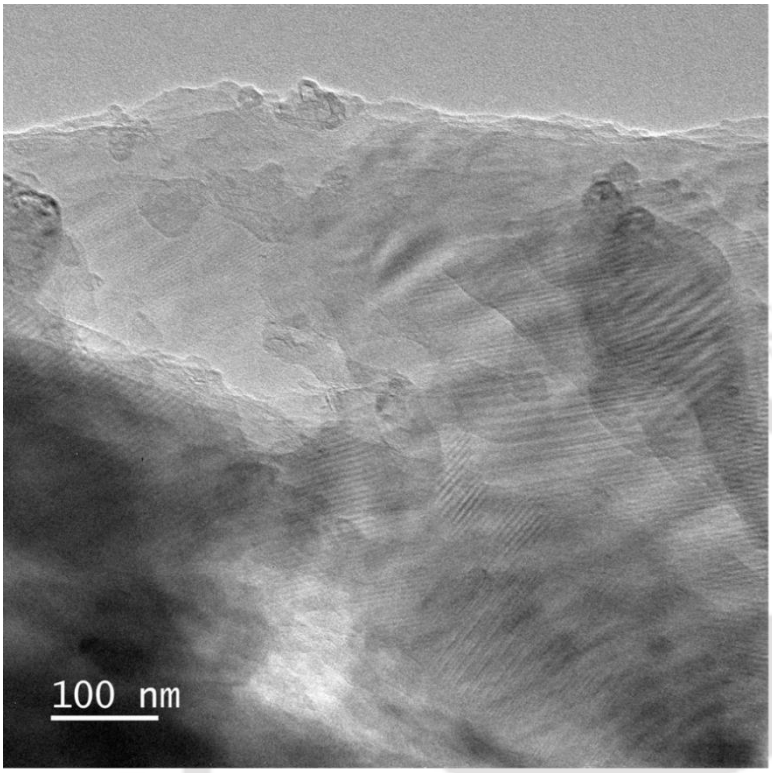

Figure 2A

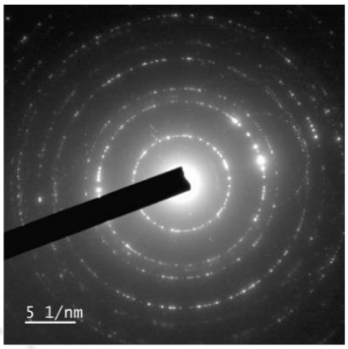

Figure 2B

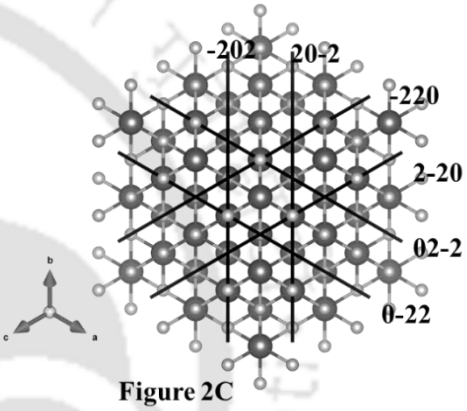

Figure 2C

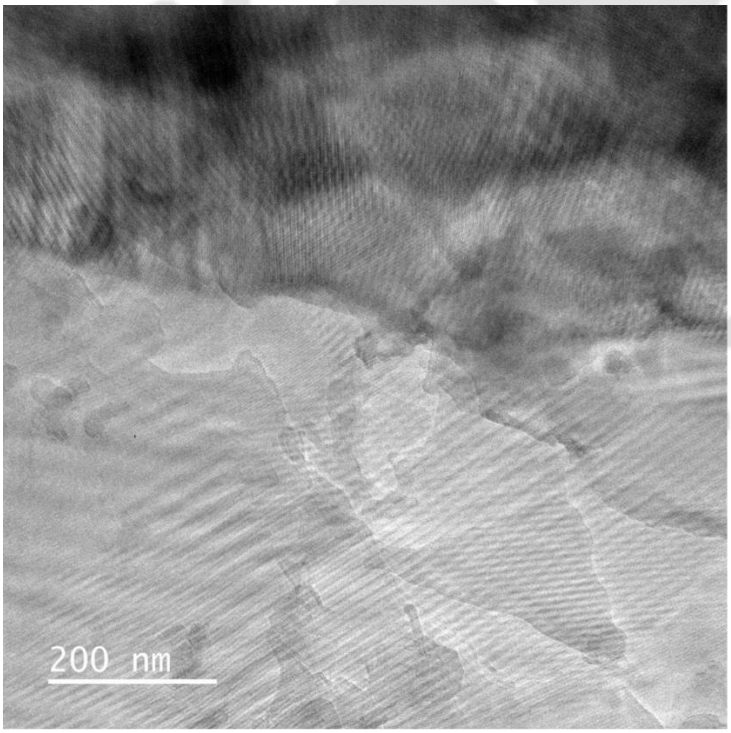

Figure 3A

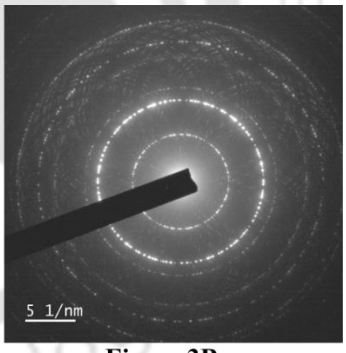

Figure 3B

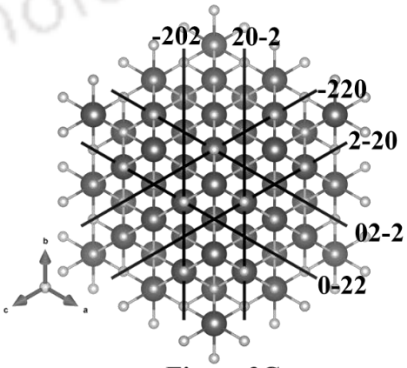

Figure 3C

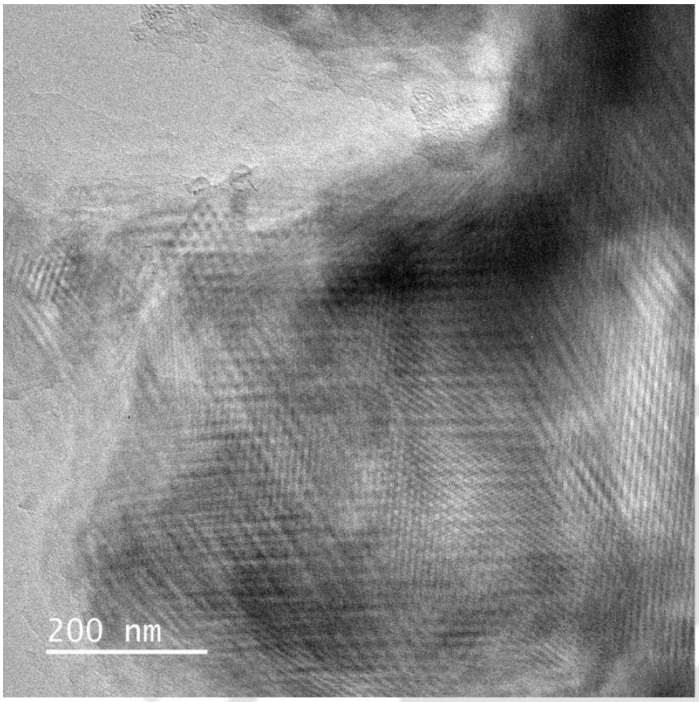

Figure 4A

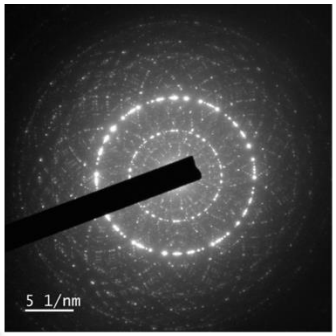

Figure 4B

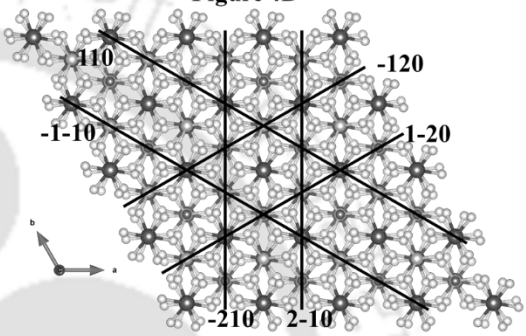

Figure 4C

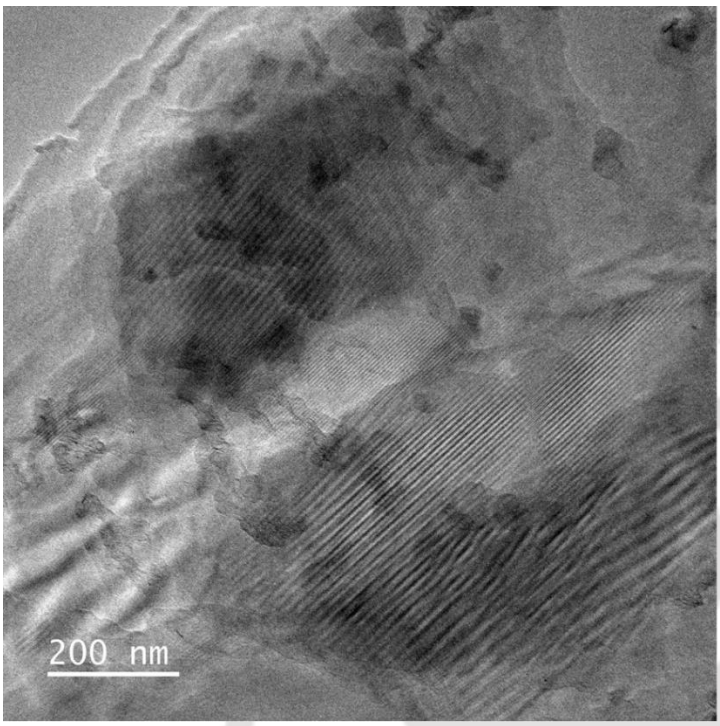

Figure 5A

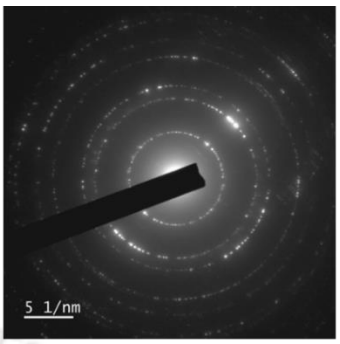

Figure 5B

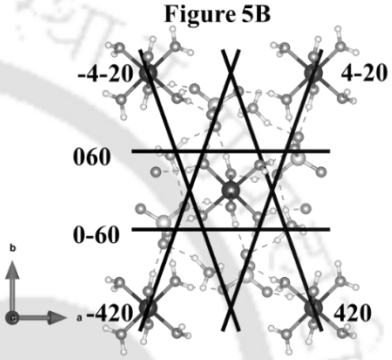

Figure 5C

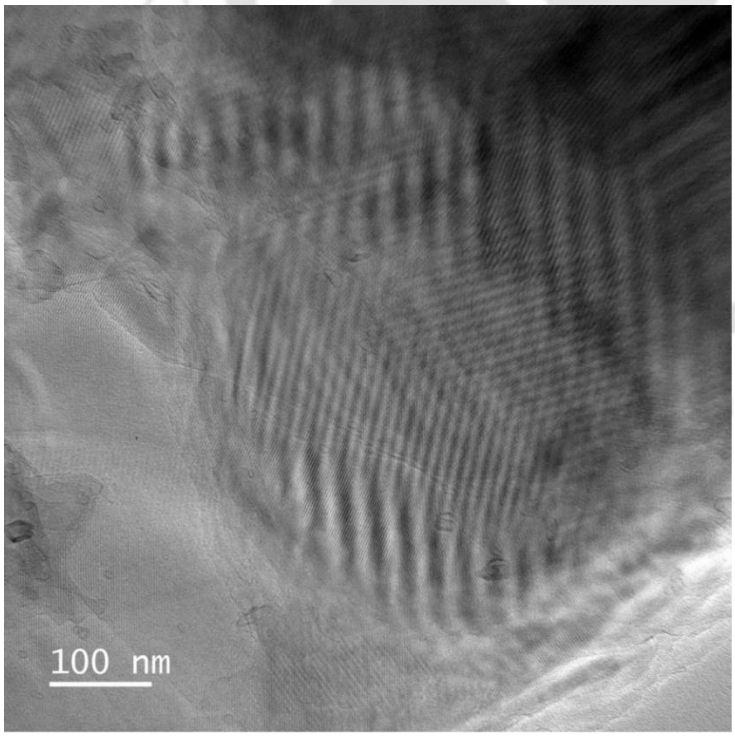

Figure 6A

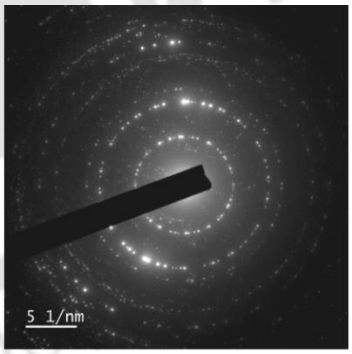

Figure 6B

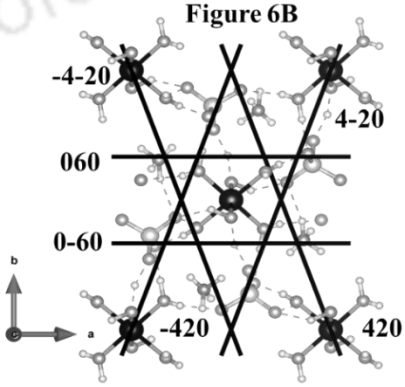

Figure 6C

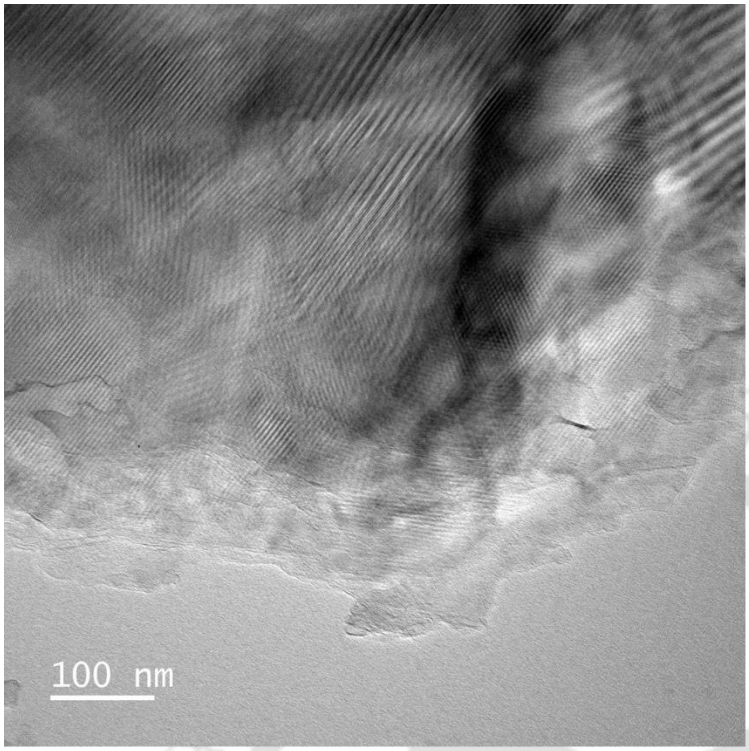

Figure 7A

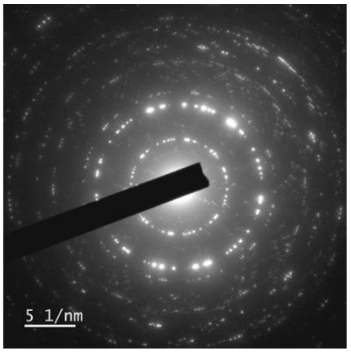

Figure 7B

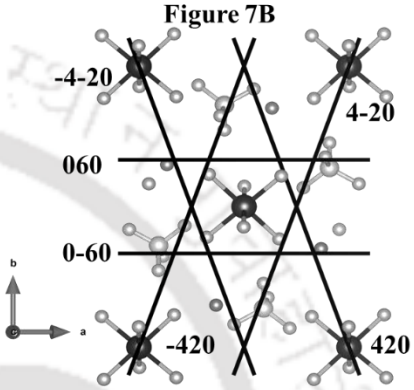

Figure 7C

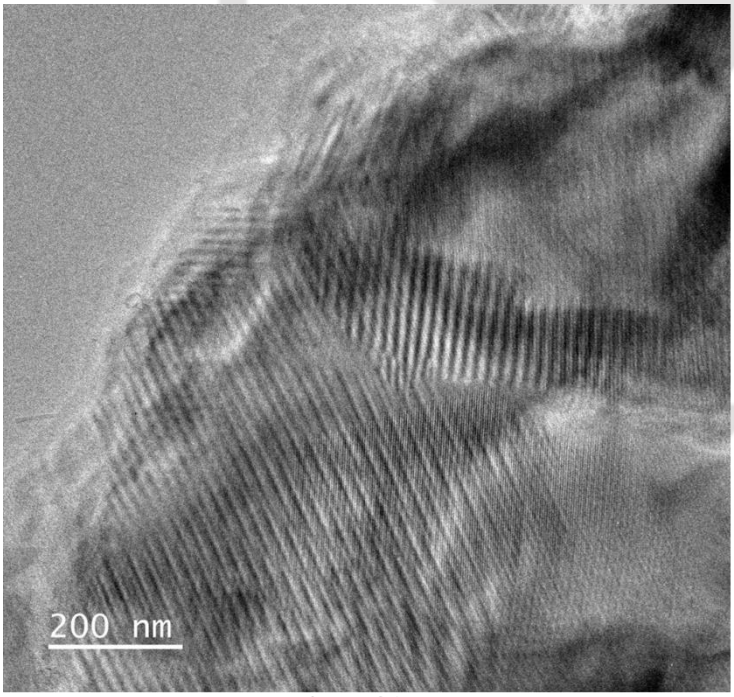

Figure 8A

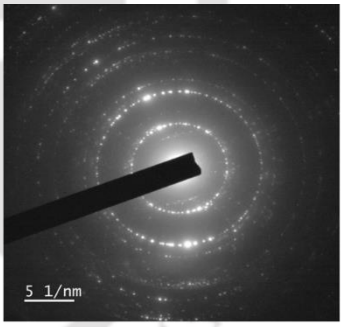

Figure 8B

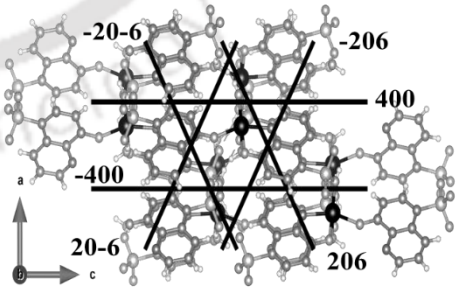

Figure 8C

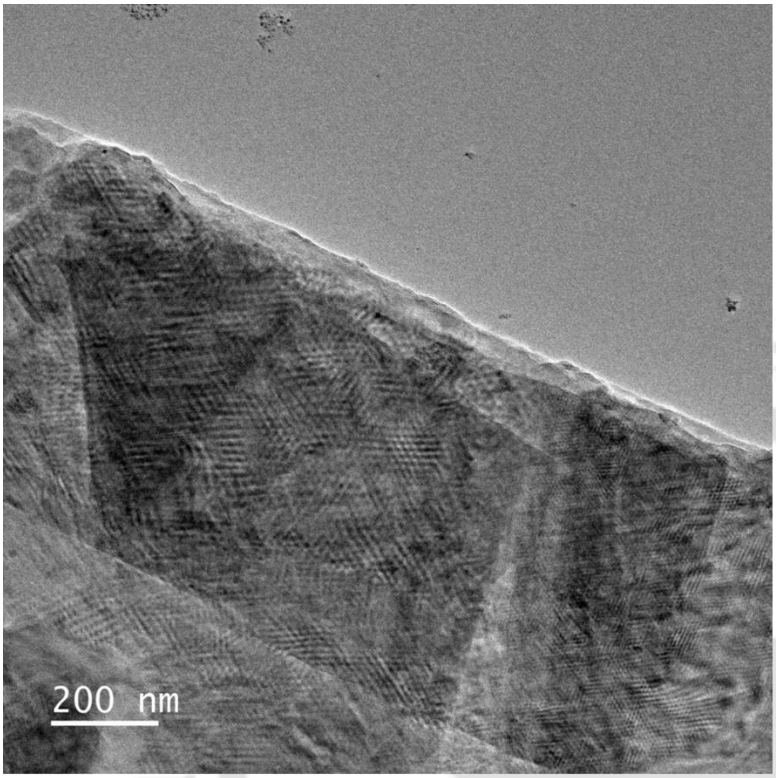

Figure 9A

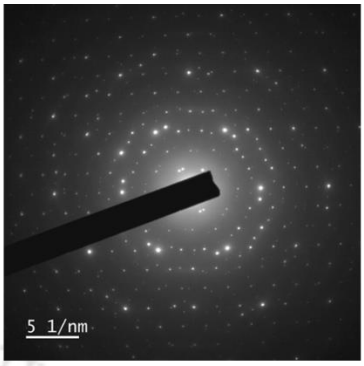

Figure 9B

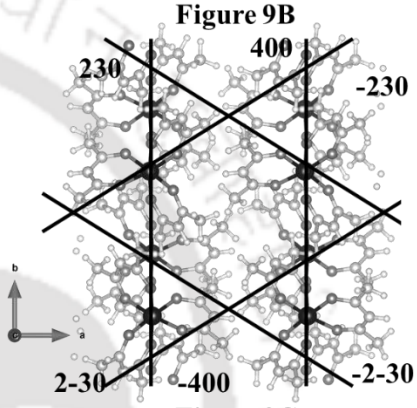

Figure 9C

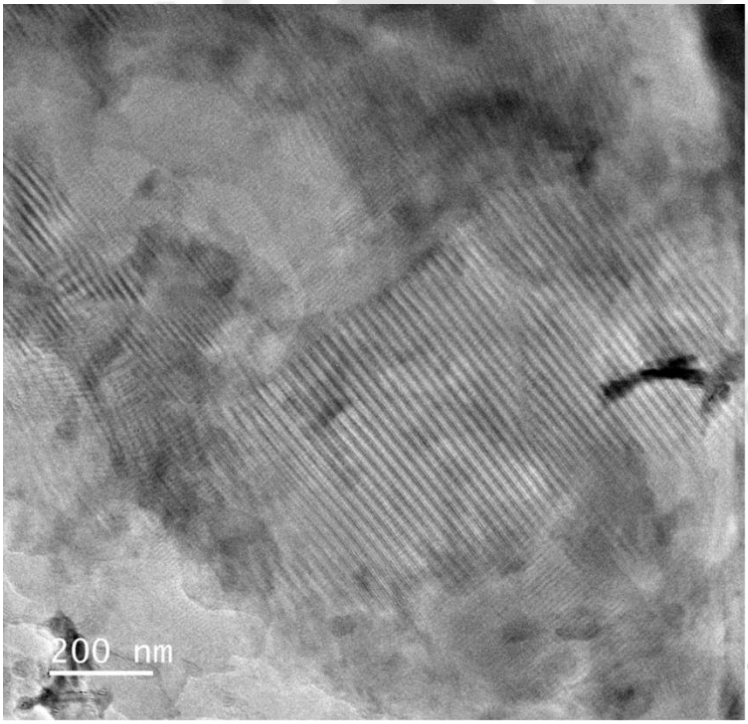

Figure 10A

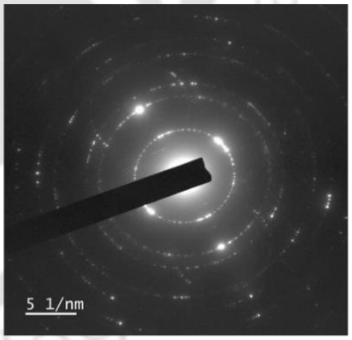

Figure 10B

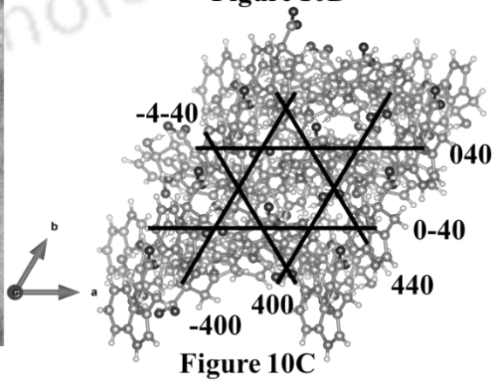

Figure 10C

ABSTRACT

METHOD FOR SYNTHESIZING MOIRÉ SUPERLATTICES FROM CRYSTALS

The present invention provides a generalized method for synthesizing moiré superlattices from covalent molecular crystals, ionic crystals and metal complex crystals which comprises the steps of finely grounding bulk crystals, and sonicating the grounded crystals in ultrasonic bath at moderate temperature in presence of a solvent system to obtain a dispersion of moiré superlattices of the molecules in the solvent system.

INTELLECTUAL PROPERTY INDIA
PATENTS | DESIGNS | TRADE MARKS | GEOGRAPHICAL INDICATIONS

सत्यमेव जयते

Application Filing Receipt

Goverment of India
Patent Office
Intellectual Property Office Building,
CP-2, Sector V, Salt Lake City,
Kolkata- 700091
Phone- 033-2367145-46,87
Fax: 033-2367198
e-mail: kolkata-patent@nic.in

CBR Number : 6722 **CBR date: 02-04-2024**

Application Type: ORDINARY APPLICATION
Priority Number:
Priority Date:
Priority Country: Not Selected

To,

INDIAN INSTITUTE OF TECHNOLOGY GUWAHATI

S. MAJUMDAR & CO., 5 Harish Mukherjee Road, Kolkata – 700 025, West Bengal, India

Received documents purporting be to an application for patent numbered 202431027351 dated 02-04-2024 by INDIAN INSTITUTE OF TECHNOLOGY GUWAHATI of Guwahati – 781039, Assam, India relating to METHOD FOR SYNTHESIZING MOIRÉ SUPERLATTICES FROM CRYSTALS together with the Complete and fee(s) of ₹5600 (Five Thousand Six Hundred only).

Note:

1. In case of Patent Application accompanied by a Provisional Specification, a complete Specification should be filed within 12 months from the date of filing of the Provisional Specification, failing which the application will be deemed to be abandoned under Section 9(1) of the Patent Act, 1970.
2. You may withdraw the application at any time before the grant of patent, if you with so. If, in addition to withdrawal, you also wish to prevent the publication of application in the Patent Office Journal, the application should be withdrawn within fifteen months from the date of priority of date of filing, whichever earlier.
3. If not withdrawn, your application will be published in the Patent Office Journal after eighteen months from the date of priority of date of filing, whichever is earlier.
4. If you with to get your application examined, you should file a request for examination in Form-18 within 48 months from the date of priority or date of filing, whichever is earlier, failing which the application will be treated as withdrawn by the applicant under Section 11(B)(4) of the Patent Act, 1970.

(For Controller of Patents)

List of Publication

1. **Bhakat, A**.; Dey, U.; Chattopadhyay, A., Room Temperature Persistent Phosphorescence of Aggregated Gold Nanoclusters under Molecular crystal confinements. (Manuscript communicated 2024).
2. Bhattacharya, D.; **Bhakat, A**.; Debnath, T., Localized Surface Plasmon Resonance in AgInTe2 based Quantum Dots and Core-shell Nanocrystals. (Manuscript communicated 2023)
3. **Bhakat, A**.; Chattopadhyay, A., Molecular Cooperativity in the Intense Raman Scattering on the Surface of an Organic Molecular Microcrystal. *Adv. Optical Mater.* **2023**, 2301776.
4. **Bhakat, A**.; Paul, S.; Chattopadhyay, A., Molecular Specificity in the Intense Surface-Enhanced Raman Scattering on Copper(II) 8-Hydroxyquinoline Microcrystals. *J. Phys. Chem. C* **2023,** *127* (10), 5169-5177.
5. **Bhakat, A**.; Pal, A.; Siddaramaiah, R.; Chattopadhyay, A., Complexation-Based Super Crystalline Assembly of Zinc Oxide Quantum Dots for Sensitive Carbon Dioxide Gas Sensing. *J. Phys. Chem. C* **2021,** *125* (22), 12316-12323.
6. Bhattacharya, D.; **Bhakat, A**.; Debnath, T., Breaking $AgInTe_2$ Quantum Dot Chain to Fabricate $AgInTe_2$-ZnS Janus Nanocrystals. *Inorg. Chem.* **2023**, 62 (49), 20219-20227.
7. Pal, A.; **Bhakat, A**.; Chattopadhyay, A., Zinc Ion-Induced Assembly of Crystalline Carbon Dots with Excellent Supercapacitor Performance. *J. Phys. Chem. C* **2019,** *123* (32), 19421-19428.

List of Patent

1. Chattopadhyay, A.; **Bhakat, A**.; Dey, U., Method for Synthesizing Moiré Superlattices From Crystals. (**Indian patent filed 2024**).

Conferences Attended

1. Research and Industrial Conclave Integration held at IIT Guwahati (2023).
2. North-East Research Conclave conducted by IIT Guwahati (2022).

Permissions

Facet-Engineered Surface and Interface Design of Photocatalytic Materials

Author: Yujie Xiong, Zhengquan Li, Lili Wang, et al
Publication: Advanced Science
Publisher: John Wiley and Sons
Date: Aug 17, 2016

Seeking copyright permission

ACS Publications <acs@service-now.com>
Thu 28-03-2024 15:57
To:ARIN BHAKAT <arin@iitg.ac.in>

Dear Dr. Bhakat,

Thank you for contacting ACS Publications Support.

Your permission requested is granted as long as your thesis won't be sold, and there is no fee for this reuse.
In your planned reuse, you must cite the ACS article as the source, add this direct link:
https://pubs.acs.org/doi/10.1021/acs.chemrev.6b00196

Please let me know if you need any further assistance.

Sincerely,

Vojin Vucic
ACS Publications Support
Customer Services & Information
Website: https://acs.service-now.com/acs
Email: support@services.acs.org
Phone: 800-227-9919 | 202-872-(HELP) 4357

Case Info:

Case Number : CSCSI0199654

Created On: 03-28-2024 05:26:05 AM EDT

Short Description: Seeking copyright permission

Description: Dear ACS support,
I am Arin Bhakat, a PhD student at the Indian Institute of Technology, Guwahati. For my thesis, I want to reuse Figure 2 of a review article by Michael A Boles. entitled ' Self-assembly of Colloidal Nanocrystals: From Intricate Structure to Functional Materials'. The link to the article is given below:
https://pubs.acs.org/doi/10.1021/acs.chemrev.6b00196

Please give me copyright permission to include this figure in my PhD thesis.
Thank you.
Regards
Arin Bhakat.
SRF at IITGuwahati

TH-3405_186122002

Ref:MSG1565003_DbPx9zVGPuFGP3iYob8X

TH-3405_186122002

Glycerol-Assisted Construction of Long-Life Three-Dimensional Surface-Enhanced Raman Scattering Hot Spot Matrix

Author: Yongkang Wang, Zhiyong Wei, Yan Zhang, et al
Publication: Langmuir
Publisher: American Chemical Society
Date: Dec 1, 2019

PERMISSION/LICENSE IS GRANTED FOR YOUR ORDER AT NO CHARGE

This type of permission/license, instead of the standard Terms and Conditions, is sent to you because no fee is being charged for your order. Please note the following:

- Permission is granted for your request in both print and electronic formats, and translations.
- If figures and/or tables were requested, they may be adapted or used in part.
- Please print this page for your records and send a copy of it to your publisher/graduate school.
- Appropriate credit for the requested material should be given as follows: "Reprinted (adapted) with permission from {COMPLETE REFERENCE CITATION}. Copyright {YEAR} American Chemical Society." Insert appropriate information in place of the capitalized words.
- One-time permission is granted only for the use specified in your RightsLink request. No additional uses are granted (such as derivative works or other editions). For any uses, please submit a new request.

If credit is given to another source for the material you requested from RightsLink, permission must be obtained from that source.

BACK CLOSE WINDOW

RightsLink

Molecular Specificity in the Intense Surface-Enhanced Raman Scattering on Copper(II) 8-Hydroxyquinoline Microcrystals

Author: Arin Bhakat, Sujay Paul, Arun Chattopadhyay
Publication: The Journal of Physical Chemistry C
Publisher: American Chemical Society
Date: Mar 1, 2023

PERMISSION/LICENSE IS GRANTED FOR YOUR ORDER AT NO CHARGE

This type of permission/license, instead of the standard Terms and Conditions, is sent to you because no fee is being charged for your order. Please note the following:

- Permission is granted for your request in both print and electronic formats, and translations.
- If figures and/or tables were requested, they may be adapted or used in part.
- Please print this page for your records and send a copy of it to your publisher/graduate school.
- Appropriate credit for the requested material should be given as follows: "Reprinted (adapted) with permission from {COMPLETE REFERENCE CITATION}. Copyright {YEAR} American Chemical Society." Insert appropriate information in place of the capitalized words.
- One-time permission is granted only for the use specified in your RightsLink request. No additional uses are granted (such as derivative works or other editions). For any uses, please submit a new request.

If credit is given to another source for the material you requested from RightsLink, permission must be obtained from that source.

BACK CLOSE WINDOW

RightsLink

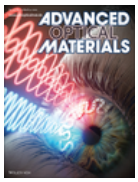

Molecular Cooperativity in the Intense Raman Scattering on the Surface of an Organic Molecular Microcrystal

Author: Arin Bhakat, Arun Chattopadhyay
Publication: Advanced Optical Materials
Publisher: John Wiley and Sons
Date: Sep 28, 2023

Review Order

Please review the order details and the associated terms and conditions.

No royalties will be charged for this reuse request although you are required to obtain a license and comply with the license terms and conditions. To obtain the license, click the Accept button below.

Licensed Content

Licensed Content Publisher	John Wiley and Sons
Licensed Content Publication	Advanced Optical Materials
Licensed Content Title	Molecular Cooperativity in the Intense Raman Scattering on the Surface of an Organic Molecular Microcrystal
Licensed Content Author	Arin Bhakat, Arun Chattopadhyay
Licensed Content Date	Sep 28, 2023
Licensed Content Volume	12
Licensed Content Issue	5
Licensed Content Pages	10

Order Details

Type of use	Dissertation/Thesis
Requestor type	Author of this Wiley article
Format	Print and electronic
Portion	Full article
Will you be translating?	No

About Your Work

Title of new work	Crystalline molecular and nanoparticles assemblies with optoelectronic application potential
Institution name	Indian Institute of Technology Guwahati
Expected presentation date	Jun 2024

Additional Data

Requestor Location

Requestor Location	Mr. ARIN BHAKAT B4-326,KAMENG HOSTEL,IIT GUWAHATI NORTH GUWAHATI, Assam 781039 India Attn: IIT Guwahati

Tax Details

Publisher Tax ID	EU826007151

TH-3405_186122002

I agree to these terms and conditions.

I understand this license is for reuse only and that no content is provided.

Total: 0.00 USD

BACK DECLINE SAVE QUOTE ACCEPT

Please click accept only once.

RightsLink

Complexation-Based Super Crystalline Assembly of Zinc Oxide Quantum Dots for Sensitive Carbon Dioxide Gas Sensing

Author: Arin Bhakat, Ayan Pal, Raveesh Siddaramaiah, et al
Publication: The Journal of Physical Chemistry C
Publisher: American Chemical Society
Date: Jun 1, 2021

PERMISSION/LICENSE IS GRANTED FOR YOUR ORDER AT NO CHARGE

This type of permission/license, instead of the standard Terms and Conditions, is sent to you because no fee is being charged for your order. Please note the following:

- Permission is granted for your request in both print and electronic formats, and translations.
- If figures and/or tables were requested, they may be adapted or used in part.
- Please print this page for your records and send a copy of it to your publisher/graduate school.
- Appropriate credit for the requested material should be given as follows: "Reprinted (adapted) with permission from {COMPLETE REFERENCE CITATION}. Copyright {YEAR} American Chemical Society." Insert appropriate information in place of the capitalized words.
- One-time permission is granted only for the use specified in your RightsLink request. No additional uses are granted (such as derivative works or other editions). For any uses, please submit a new request.

If credit is given to another source for the material you requested from RightsLink, permission must be obtained from that source.

BACK CLOSE WINDOW